HAL
open science

Arbre de partition binaire : un nouvel outil pour la représentation hiérarchique et l'analyse des images hyperspectrales

Silvia Valero

▶ **To cite this version:**

Silvia Valero. Arbre de partition binaire : un nouvel outil pour la représentation hiérarchique et l'analyse des images hyperspectrales. Traitement du signal et de l'image [eess.SP]. Université de Grenoble; Universitat politècnica de Catalunya - BarcelonaTech, 2011. Français. NNT : 2011GRENT123 . tel-01561781v2

HAL Id: tel-01561781

https://theses.hal.science/tel-01561781v2

Submitted on 13 Jul 2017

HAL is a multi-disciplinary open access archive for the deposit and dissemination of scientific research documents, whether they are published or not. The documents may come from teaching and research institutions in France or abroad, or from public or private research centers.

L'archive ouverte pluridisciplinaire **HAL**, est destinée au dépôt et à la diffusion de documents scientifiques de niveau recherche, publiés ou non, émanant des établissements d'enseignement et de recherche français ou étrangers, des laboratoires publics ou privés.

UNIVERSITÉ DE GRENOBLE

THÈSE

Pour obtenir le grade de

DOCTEUR DE L'UNIVERSITÉ DE GRENOBLE et L'UNIVERSITAT POLITÈCNICA DE CATALUNYA

Spécialité : **Signal, Image, Parole et Télécom**

Arrêté ministériel : 7 août 2006

Présentée par

Silvia, VALERO VALBUENA

Thèse dirigée par **Jocelyn CHANUSSOT** et
codirigée par **Philippe SALEMBIER**

préparée au sein du **Grenoble Images Parole Signal Automatiue Laboratoire (Gipsa-Lab)**

dans **l'École Doctorale « Electronique , Electrotechnique, Automatique, Traitement du Signal »**

Arbre de partition binaire : Un nouvel outil pour la représentation hiérarchique et l'analyse des images hyperspectrales

Thèse soutenue publiquement le **9 decembre 2011**
devant le jury composé de :

M. Jean, SERRA
Professeur Emerite, ESIEE Paris, Président du jury
M. Antonio, PLAZA
Associate Professor, Escuela Politecnica de Caceres-University of Extremadura, Rapporteur
Mme. Josiane, ZERUBIA
DR INRIA, INRIA Sophia Antipolis Méditerranée, Rapportrice
M. Carlos, LOPEZ-MARTINEZ
Assistant Professeur, Universitat Politecnica de Catalunya, Examinateur
M. Hugues, TALBOT
Professeur associé, ESIEE Paris, Examinateur
M. Jesus, ANGULO
Chargé de recherche, Centre de Morphologie Mathématique, MINES-ParisTech, Examinateur

A mis padres, a mi hermano y a Xavi.
Por su apoyo, comprensión y paciencia durante todos estos años.

Acknowledgements

Mes remerciements vont tout d'abord aux membres du jury qui ont eu l'amabilité et la gentillesse d'évaluer mon travail. Je souhaite aussi remercier mes deux directeurs de thèse, Philippe Salembier et Jocelyn Chanussot.
Merci Jocelyn de m'avoir fait confiance dès le départ de cette course. Merci Philippe, sans toi la réalisation de ce projet n'aurait également pas été envisageable. Merci pour ces ans pendant lesquels j'ai beaucoup appris à votre côté.
Gracias a mi padres, por educarme y enseñarme a ser como soy. Gracias a mi hermano, con quien tanto he compartido. Gracias a Xavi, por estos ocho años a mi lado.
Por último, gracias a todos mis amigos por ser mi segunda familia.

Abstract

The optimal exploitation of the information provided by hyperspectral images requires the development of advanced image processing tools. Therefore, under the title **Hyperspectral image representation and Processing with Binary Partition Trees**, this PhD thesis proposes the construction and the processing of a new region-based hierarchical hyperspectral image representation: the Binary Partition Tree (BPT). This hierarchical region-based representation can be interpreted as a set of hierarchical regions stored in a tree structure. Hence, the Binary Partition Tree succeeds in presenting: (i) the decomposition of the image in terms of coherent regions and (ii) the inclusion relations of the regions in the scene. Based on region-merging techniques, the construction of BPT is investigated in this work by studying hyperspectral region models and the associated similarity metrics. As a matter of fact, the very high dimensionality and the complexity of the data require the definition of specific region models and similarity measures. Once the BPT is constructed, the fixed tree structure allows implementing efficient and advanced application-dependent techniques on it. The application-dependent processing of BPT is generally implemented through a specific pruning of the tree. Accordingly, some pruning techniques are proposed and discussed according to different applications. This Ph.D is focused in particular on segmentation, object detection and classification of hyperspectral imagery. Experimental results on various hyperspectral data sets demonstrate the interest and the good performances of the BPT representation.

Contents

1 Introduction **9**
1.1 Hyperspectral imaging . . . 10
1.2 Binary Partition Trees . . . 11
1.3 Objectives . . . 15
1.4 Thesis Organization . . . 17

2 State of the art **19**
2.1 Hyperspectral image processing . . . 20
2.1.1 Classification techniques incorporating spatial constraints . . . 21
2.1.2 Traditional imagery techniques extended to HSI . . . 25
2.2 Hierarchical region-based processing using trees . . . 33
2.2.1 Definition of the tree structure . . . 35
2.2.2 First hierarchical tree representations . . . 36
2.2.3 BPT Literature . . . 38
2.3 Conclusions . . . 39

3 BPT construction **41**
3.1 Introduction . . . 42
3.2 Region Model . . . 45
3.2.1 First-order parametric model . . . 46
3.2.2 Non parametric statistical Region Model . . . 47
3.3 Merging Criterion . . . 55
3.3.1 Measures associated to the first-order parametric model . . . 59
3.3.2 Measures associated to the non parametrical statistical region model . . . 61
3.3.3 Similarity measure via Multidimensional Scaling . . . 64
3.4 Experimental Evaluation . . . 71
3.4.1 Quality measures between partitions . . . 71
3.4.2 Data Sets Definition . . . 73
3.4.3 Experiment 1: Evaluation of BPT hierarchical levels . . . 78
3.4.4 Experiment 2: Evaluation of D_s selection . . . 93
3.5 Conclusions . . . 94

4 BPT Pruning Strategies **97**
4.1 Introduction . . . 98
4.2 Supervised Hyperspectral Classification . . . 103
4.2.1 Populating the BPT . . . 103
4.2.2 Pruning Decision . . . 105
4.2.3 Experimental results . . . 107
4.3 Segmentation by Energy Minimization Strategy . . . 115
4.3.1 The $D(\mathcal{N})$ definition . . . 118
4.3.2 Homogeneity measure . . . 118
4.3.3 Experimental Results . . . 119
4.4 Segmentation by recursive spectral graph partitioning . . . 124
4.4.1 The BPT node weight $\mathcal{W}_{\mathcal{N}}$ . . . 124
4.4.2 Local Branch partitioning . . . 126
4.4.3 Experimental Results . . . 130
4.5 Object detection . . . 135
4.5.1 Detection of roads . . . 136
4.5.2 Detection of buildings . . . 137
4.5.3 Experimental Results . . . 138
4.6 Conclusions . . . 140

5 Conclusions **143**

6 Résumé en français **147**

7 Appendix **153**
7.1 Tree complexity . . . 154
7.2 Acronyms . . . 159
7.3 Mathematical Appendix: Association measures . . . 161
7.4 Hierarchical levels obtained by Pavia University data set . . . 164
7.5 List of Publications . . . 165

1
Introduction

Hyperspectral imaging, also known as imaging spectroscopy, corresponds to the acquisition of a set of images representing the information contained in a large portion of the electromagnetic spectrum. In contrast to human vision which is restricted to some wavelengths, these spectral imaging systems have the capability of viewing electromagnetic radiation ranging from ultraviolet to infrared. With this additional spectral (or color) information, these images exhibit greatly improved color differentiation as compared to conventional color imaging. This new source of information implies an important difference between hyperspectral and traditional imagery. The main difference is that hyperspectral images are composed by hundreds of bands in the visible range and other portions of the electromagnetic spectrum. Therefore, hyperspectral imagery allows sensing radiation in a spectral range where human eyes cannot.

Hyperspectral imaging is related to multispectral imaging, however, it exists an important difference between the number of spectral bands. Multispectral images usually contain a set of up to ten spectral bands that moreover are typically not contiguous in the electromagnetic spectrum. Contrarily, hyperspectral images have a large number of narrow spectral bands (usually several hundreds) being captured by one sensor in a contiguous spectral range. Hence, hyperspectral imaging often provides results not achievable with multispectral or other types of imagery. The characterization of images based on their spectral properties has led to the use of this type of images in a growing number of real-life applications.

In remote sensing, many applications such as mineralogy, biology, defense or environmental measurements have used of the potential of these images. In a different field, some techniques have

used hyperspectral data in order to study food quality, safety evaluation and inspection. Also, in medical research, these images are used to analyze reflected and fluorescent light applied to the human body. In this context, hyperspectral imaging is an emerging technique which serves as a diagnostic tool as well as a method for evaluating the effectiveness of applied therapies. In planetary exploration these data are also used to obtain geochemical information from inaccessible planetary surfaces within the solar system.
The traditional hyperspectral image representation involves an array of spectral measurements on the natural scene where each of them corresponds to a pixel. This most elementary unit on the image, provides an extremely local information. Furthermore, besides the scale issue, the pixel-based representation also suffers from the lack of structure. As a result, hyperspectral image processing at the pixel level has to face major difficulties in terms of scale: the scale of representation is most of the time far too low with respect to the interpretation or decision scale.
Hence, the general aim of this thesis is the construction and the exploitation of a new hyperspectral image representation. The goal of this new representation is to describe the image as a set of connected regions instead of as a set of individual pixels. This abstraction from pixels to regions is achieved by Binary Partition Trees. These region-based image representations are presented in this thesis as an attractive and promising solution to handle the low level representation problem. In this framework, this first chapter is starting by the basic background concerning this Phd research. Firstly, a brief description of the hyperspectral imagery and the Binary Partition Tree representation is presented in the following. Afterward, the main objectives and the organization of this thesis are described.

1.1 Hyperspectral imaging

Hyperspectral sensors collect multivariate discrete images in a series of narrow and contiguous wavelength bands. The resulting datasets contain numerous image bands, each of them depicting the scene as viewed with a given wavelength λ. This whole set of images can be seen as a three dimensional data cube where each pixel is characterized by a discrete spectrum related to the light absorption and/or scattering properties of the spatial region that it represents. Fig. 1.1 shows an illustration of a hyperspectral image.

Definition 1. (Hyperspectral Image) *An hyperspectral image $\mathbf{I}_\lambda$ is a set of N_z discrete 2D images $\mathbf{I}_\lambda = \{I_{\lambda_j},\ j = 1, ..., N_Z\}$. Each I_{λ_j} is formed by a set of N_p pixels where each pixel p represents the spatial coordinates in the image. Consequently, given a specific wavelength λ_j, , $I_{\lambda_j}(p)$ is the radiance value of the pixel p on the waveband I_{λ_j}.*

The spectrum of a pixel as a function of wavelength λ is called the spectral radiance curve or spectral signature and it provides insightful characteristics of the material represented by the pixel.

Definition 2. (Spectral signature) *The spectral radiance curve or spectral signature denoted by $\mathbf{I}_\lambda(\mathbf{p})$ is the vector pixel $\mathbf{p}$ containing all the radiance values along the N_z wavelenghts.*

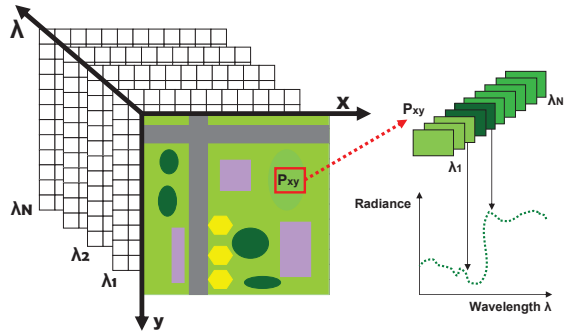

Figure 1.1: Illustration of a hyperspectral image

The price of the wealth of information provided by hyperspectral images is a huge amount of data that cannot be fully exploited using traditional imagery analysis tools. Hence, given the wide range of real-life applications, a great deal of research is devoted to the field of hyperspectral data processing [1]. A hyperspectral image can be considered as a mapping between a $2D$ spatial space to a spectral space of dimension N_z. The spectral space is important because it contains much more information about the surface of target objects than what can be perceived by human vision. The spatial space is also important because it describes the spatial variations and correlation in the image and this information is essential to interpret objects in natural scenes. Hyperspectral analysis tools should take into account both the spatial and the spectral spaces in order to be robust and efficient. However, the number of wavelengths per pixel and the number of pixels per image, as well as the complexity of jointly handling spatial and spectral correlation explain why this approach is still a largely open research issue for effective and efficient hyperspectral data processing.

Hyperspectral image processing highly desired goals include automatic content extraction and retrieval. These aims to obtain a complete interpretation of a scene are addressed by supervised or unsupervised pixel level analysis which still requires a remote sensing analyst to manually interpret the pixel-based results to find high-level structures. This is because there is still a large semantic gap between the outputs of commonly used models and high-level user expectations. The limitations of pixel-based models and their inability in modeling spatial content motivated the research on developing algorithms for region-based analysis.

1.2 Binary Partition Trees

Binary Partition Tree (BPT)[15] is a hierarchical region-based representation, which can be interpreted as a set of hierarchical regions stored in a tree structure. A tree structure is well suited for representing relationships among data in a hierarchical way.

An easy example of the hierarchical organization is the structure followed by the files and folders

in a computer. The hierarchy between the folders clearly offers to the user the ability to efficiently manage filesand the stored information.
In image analysis, tree structures can be used as a hierarchical data organization in a similar way. An example of such tree representations is the Binary Partition Tree, where the tree nodes represent image regions and the branches represent the inclusion relationship among the nodes. Fig. 1.2 is an illustration of a BPT which shows the hierarchical representation offered by this representation.
In this tree representation, three types of nodes can be found: Firstly, leaves nodes representing the original regions of the initial partition; secondly, the root node representing the entire image support and finally, the remaining tree nodes representing regions formed by the merging of their two child nodes corresponding to two adjacent regions. Each of these non leaf node has at most two child nodes, this is why the BPT is defined as binary.

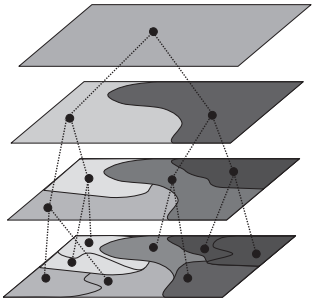

Figure 1.2: Example of hierarchical region-based representation using BPT

The BPT construction is often based on an iterative bottom-up region merging algorithm. Starting from individual pixels or any other initial partition, the region merging algorithm is an iterative process in which regions are iteratively merged. Each iteration requires three different tasks: 1) the pair of most similar neighboring regions is merged, 2) a new region containing the union of the merged regions is formed, 3) the algorithm updates the distance between the new created region with its neighboring regions.
Working with hyperspectral data, the definition of a region merging algorithm is not straightforward. Theoretically, a pixel in an hyperspectral image is a spectrum representing a certain ground cover material. Consequently, regions formed by pixels belonging to the same material are expected to be formed by an unique reflectance curve. Unfortunately, this assumption is not true since it exists a large spectral variability in a set of spectra formed by one given material. In the case of remote sensing images, this variability is introduced by several factors such as the noise resulting from atmospheric conditions, the sensor influence, non direct reflexion or the illumination effects.
Fig.1.3(a) shows an example of variability of 4 adjacent spectra forming a region belonging to the same material. Some important variability effects are found in this example. The first important difference between radiance values can be seen in the first wavelengths since they are strongly

corrupted by some noise. Besides these noisy bands, a non constant variability along the wavelength dimension is also found in this example. Because of this variability, special care has to be taken in modeling hyperspectral regions (it cannot be assumed that the spectra of pixels belonging to a given region are strictly homogeneous). Besides the intra-variability, the characteristics of the image features exhibit a majority of irregular and complex patterns. Thus, a region model taking into account the analysis of the textured regions, such as vegetation areas, has to be carefully designed.

Another important issue is the definition of a spectral similarity measure to establish the merging order between regions. The main difficulty in defining a spectral similarity measure is that most of the spectral signatures cannot be discriminated broadly along all the wavebands. The reason of this difficulty is the redundancy of the spectral information or equivalently the correlation between consecutive values of the spectral signature curve. It should be remembered that the difference between two consecutive wavelengths is usually very small, therefore, the radiance values have not important changes in consecutive positions.

Let us consider that the discrimination between the three different spectral signatures plotted in Fig.1.3(b) wants to be addressed. These three spectral signatures belong to three different classes: tree, bare soil and meadows. In it, the red curve can be strongly discriminated between the blue one across all the wavelength domain. Contrarily, this discrimination difference between the red and the green spectral signatures is only found in the last 30 bands. This fact explains why the most effective similarity measure between spectral signatures are characterized by taking into account the overall shape of the spectral signatures instead of local radiance differences.

These last characteristics of the spectral signatures make the definition of a region model and a similarity metrics, defining a good merging order for the BPT construction, an opened research problem.

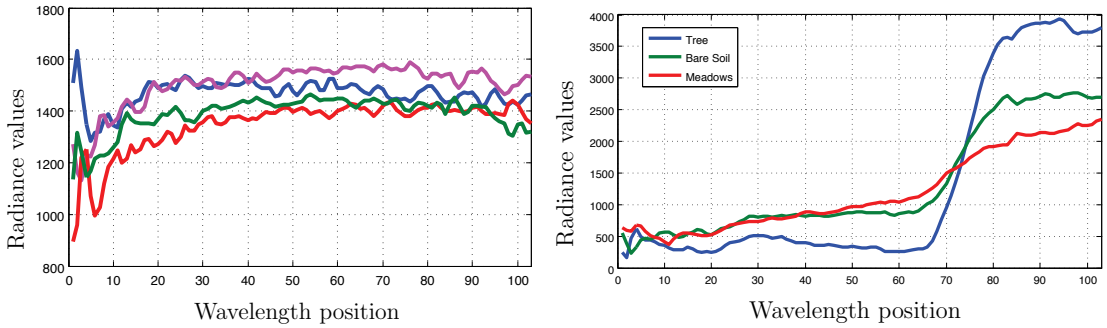

Figure 1.3: Examples of spectral signatures

On the other hand, it can be noticed that once the BPT representation has been computed, this tree is a generic representation which can be used for many different purposes. Therefore,

different processing techniques can be defined in order to process the tree. The processing of BPT, which is highly application dependent, generally consists in defining a pruning strategy. This is true for filtering (with connected operators), classification, segmentation, object detection or in the context of data compression.
Fig.1.4 illustrates an example of image representation by using a BPT structure. The images shown at the top of Fig.1.4 correspond to the set of regions represented by the BPT example. The whole image is represented by region R_9, whereas tree leaves correspond to R_1,R_2,R_3,R_4 and R_5, respectively. The inclusion relationship can be easily corroborated by the tree representation of Fig.1.4. For instance, R_6 corresponds to the union of R_3 and R_4.

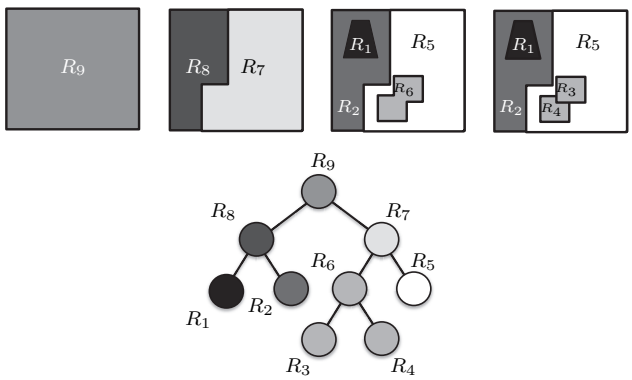

Figure 1.4: Binary Partition Tree example

The tree processing of Fig.1.4 according to a specific application can be done by a pruning. The pruning of the tree can be seen as a process aiming to remove subtrees composed of nodes which are considered to be homogeneous with respect to some criterion of interest (homogeneity criterion, e.g., intensity or texture). This task can be performed by analyzing a pruning criterion along the tree branches to retrieve the nodes of largest area fulfilling the criterion. Given the example of Fig.1.4 , a pruning example is shown in Fig.1.5 . The pruning is defined by the green line which cuts the tree into two parts. In this case, the pruning strategy has removed the green nodes corresponding to regions R_1,R_2,R_3 and R_4. The definition of this pruning gives us the partition shown on the right of Fig.1.5. This partition has been obtained by selecting the leaf nodes of the pruned tree. Note that Fig.1.5(b) only corresponds to one possible pruning result from the BPT shown in Fig.1.4. Thus, different hyperspectral image processing aims can lead to different pruning results. This can be understood as the BPT pruning is the application dependent step regarding the BPT hyperspectral image processing framework.

The hyperspectral image processing framework based on BPT then relies on two steps illustrated in Fig.1.6. The first one corresponds to the construction of the BPT in the case of hyperspectral data, enabling the exploitation of the spectral/spatial correlation. Accordingly, the second step is a pruning strategy which is completely linked to a specific application.
The work developed in this thesis deals with the discussion of BPT image processing frame-

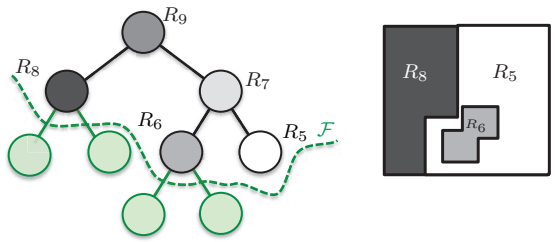

Figure 1.5: BPT pruning example

work for the case of hyperspectral imaging. As Fig.1.6 has shown, this discussion is split in two parts: the construction and the pruning of the BPT, respectively. The usefulness of this tree representations will be demonstrated in particular through the development of efficient tree based algorithms for some specific applications. In this Phd, the studied applications in hyperspectral context relies on the classification, the segmentation and the object detection.

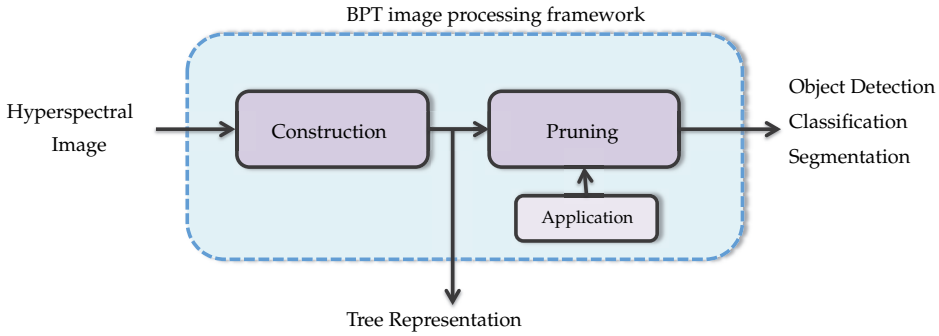

Figure 1.6: Diagram of BPT processing framework

1.3 Objectives

Two different objectives have been addressed in this thesis. The first goal consists in developing the Binary Partition Tree representation for hyperspectral data, thus improving the performances of the state of the art which relies on a pixel-based representation. The second goal is the definition of some pruning techniques to process the tree structure for different applications. To achieve both objectives, this thesis plans to face a wide range of problems, such as:

1. **BPT contstruction**

   The BPT construction is often based on an iterative region merging algorithm. Region merging techniques are usually based on local decisions, directly based on the region features. Starting from an initial partition or from the collection of pixels, neighboring regions are

iteratively merged. Thus, region merging algorithms are specified by: 1) a merging criterion, defining the similarity between pair of neighboring regions; and 2) a region model that determines how to represent a region and the union of two regions. Working with hyperspectral data, the definition of a region model and a merging criterion is not straighforward. Thus, the study of both notions is going to be the first step in this PhD work.

- Region Model definition

  In our case, the Region Model defines how to characterise a set of spectra forming an hyperspectral region. The simplest solution is to use a first order model: the mean. Hence, classical spectral distances between the mean of each region can be used as merging criterion. Unfortunately, some limitations may come from the poor modeling based on the mean. The first limitation comes from the fact that high intra-class spectral variability can be found in an image region from the same material. The second important issue is that, with the mean model, regions are assumed to be homogeneous. This assumption is rarely true in natural scenes where textured regions are often observed. Therefore, this PhD investigates alternative models which provides a general strategy with less assumptions about the nature of the regions [17].

- Similarity Measure as Merging Criterion

  Following the classical literature, the radiance values along all the wavebands should be taken into account in order to discriminate two spectra. Consequently, the best classical distances between spectra are based on the overall shape of the reflectance curve [16]. However, all the bands in the hyperspectral images are not equally important in terms of discrimination. In particular, some materials can only be discriminated in some hyperspectral bands of the spectral range. This issue is related to the strong correlation existing between consecutive bands. Therefore, a good similarity metric in the hyperspectral space should take into account the following issues: 1) the correlation between bands in order to remove the redundant information and 2) a multivariate similarity measure taking into account the most important bands should be established. During this PhD, similarity measures between hyperspectral regions will be studied in order to define a good merging criterion for BPT construction.

2. **BPT Pruning strategies**

As mentioned before, the pruning strategy completely depends on the application of interest. Accordingly, some pruning techniques will be proposed and discussed according to different applications. We will focus in particular on segmentation, object detection and classification of hyperspectral imagery.

- Classification application

  The goal of this pruning is to remove subtrees composed of nodes belonging to the same class. Thus, the final aim is to use the pruned BPT to construct a classification map of the whole image. Note that using the pruned tree, the classification map describing

the pixel class assignment can be easily constructed by selecting the leaf nodes of the resulting pruned tree. The method proposed here consists of two different steps. First, some specific region descriptors are computed for each node. Then, the second step involves a BPT analysis to take the pruning decision.

- Segmentation application

  The segmentation pruning consists in extracting from BPT a partition of hyperspectral image where the most meaningful regions are formed. Thus, the goal of such application is to remove subtrees which can be replaced by a single node. All the nodes inside a subtree can be replaced if they belong to the same region in the image space. This means that the distance between them is small and the distance between them and their BPT neighboring nodes is high.

  In this context, two different approaches are studied in this thesis. Firstly, the hyperspectral segmentation goal is tackled by a global energy minimization strategy. This approach defines an error associated to each partition contained in the BPT and then, it extracts the partition having the minimum error. The second approach focused on hyperspectral image segmentation is based on applying normalized cuts on the BPT branches. The purpose of this second approach is to study how the classical spectral graph partitioning technique can be applied on BPT structures.

- Object Detection application

  The BPT is studied here as a new scale-space of the image representation in the context of hyperspectral object detection. The recognition of the reference objects in hyperspectral images has been mainly focused on detecting isolated pixels with similar spectral characteristics. In contrast, this thesis presents the BPT hyperspectral image representation in order to perform a different object detection strategy. To this goal, the detection of two specific reference objects from an urban scene is investigated. Hence, the methodology to extract BPT nodes forming these objects is studied.

1.4 Thesis Organization

This thesis proposes the construction and the processing of BPT image representation in the case of hyperspectral images. The major goals are, on the one hand, to develop the construction of BPT region-based representation and, on the other hand, to propose some pruning strategies according to three different applications. To tackle these points, this PhD dissertation is divided into five major parts:

1. In this first chapter, the context of this thesis is introduced. After briefly presenting hyperspectral imagery and, the Binary Partition Tree representation, the objectives and the thesis organization are described.

2. The second chapter provides the background for hyperspectral image processing and hierarchical tree representations. The basic terms used in this Phd are introduced and the

techniques proposed in the state of the art are reviewed.

3. In the third chapter, the BPT construction for hyperspectral images is investigated. Different merging orders are defined by combining different region models and merging criteria. The different merging orders result in different BPT constructions. Thus, some experiments are carried out in order to analyze the various constructed BPTs. The quantitative validation of the BPT construction has been performed based on different manually created ground truth data. Also in this chapter, a comparison against the classical state of the art technique that is typically used for hierarchical hyperspectral image segmentation is presented.

4. Different BPT pruning strategies are examined in the fourth chapter. The different applications and their corresponding pruning strategies are presented in the different sections. First, a supervised classification of hyperpectral data is described. Afterward, two different sections tackle the supervised and unsupervised image segmentation goals by performing two different approaches. A strategy based on energy minimization is firstly proposed based on a constrained lagrangian function. This approach is supervised because the number of regions that wants to be obtained at the partition result is previously known. Concerning the unsupervised approach, this chapter presents a pruning strategy based on normalized cut and spectral graph partitioning theory.
   Finally, this chapter introduces a hyperspectral object detection procedure using BPT image representation. Two different examples are described respectively detailing the recognition of roads and buildings in urban scenes. Each of the aforementioned parts describing the different application begins with a short introduction to the problems to be addressed. Besides, experimental results are reported on various real data sets according to the distinct application goals.These results are conducted to assess and validate the interest of the proposed algorithms. Furthermore, each of these sections present the main conclusions of the approach as well as future perspective.

5. The last chapter summarizes the main points discussed along the thesis and highlights the major conclusions.

This thesis is concluded by a series of appendices describing different aspects related to the topics discussed along this work. First, the characteristic of tree performances are discussed. Then, the acronyms used in this PhD dissertation and a mathematical appendix is presented. Finally, more results and the list of publications are included.

2

State of the art

Contents

2.1 Hyperspectral image processing **20**

2.1.1 Classification techniques incorporating spatial constraints 21

2.1.2 Traditional imagery techniques extended to HSI 25

2.2 Hierarchical region-based processing using trees **33**

2.2.1 Definition of the tree structure 35

2.2.2 First hierarchical tree representations 36

2.2.3 BPT Literature 38

2.3 Conclusions **39**

This chapter provides the background for hyperspectral image processing and hierarchical tree region-based representations. The first section details the hyperspectral image analysis state of the art, stressing the importance of the spectral-spatial hyperspectral information. The second section explains the interest of studying hierarchical region-based representations, and also the importance of using tree-based structures. The basic terms and the current state of the art of tree image representations are detailed, justifying the choice of the Binary Partition Tree. Finally, a review of the BPT related literature is presented.

2.1 Hyperspectral image processing

Particular attention has been paid in the literature to hyperspectral image processing in the last ten years. A large number of techniques have been proposed to process hyperspectral data. As a matter of fact, the processing of such images not straightforward [72].

The first important drawback is the high dimensionality of the space which contains a lot of redundant information and requires a tremendous computational effort. In order to manage it, an important number of hyperspectral techniques have focused on transforming the data into a lower dimensional subspace without losing significant information in terms of separability among the different materials. In this context, several supervised and unsupervised dimension reduction techniques have been proposed for hyperspectral imaging.

Based on image statistics, Principal Component Analysis (PCA) and Independent Component Analysis (ICA) [74] are the two most used unsupervised techniques. Regarding supervised techniques, some examples are the Discriminant Analysis Feature Extraction (DAFE)[75], Decision Boundary Feature Extraction (DBFE), and Non-parametric Weighted Feature Extraction (NWFE) [76][77]. These supervised methods reduce the high dimensionality by minimizing a classification criterion by using some ground truth data.

The second important challenge in hyperspectral image techniques corresponds to the processing of the data in a joint spectral-spatial space. Early analysis techniques are traditionally focused on the spectral properties of the hyperspectral data using only the spectral space. These pixel-based procedures analyze the spectral properties of each pixel, without taking the spatial or contextual information related to the pixel of interest into account. Thus, these techniques are quite sensitive to noise and lack of robustness. In this framework, many different supervised and semi-supervised techniques have been proposed to perform pixelwise classification [2],[3],[4],[5],[6]. Without taking the spatial location of the pixels into consideration (i.e: only studying spectral proprerties), these techniques assign to each pixel the label corresponding to its predicted class.

In the last few years, the importance of the spatial space and, in particular, of taking into account the spatial correlation has been demonstrated in different contexts such as classification [10] [**?**], image segmentation [11] [12] [13] or unmixing [8]. With this approach, hyperspectral images are viewed as arrays of ordered pixel spectra which enables to combine the spatial and the spectral information. For instance, in a classification context, pixels are classified according to the spectral information and according to the information provided by their spatial neighborhood.

The spatial contextual information in hyperspectral image processing has been introduced in different ways in the literature. This has led to divide hyperspectral techniques using spatial information in two important groups as shown on Fig.2.1. The separation between these two families of techniques has been previously defined in [78].

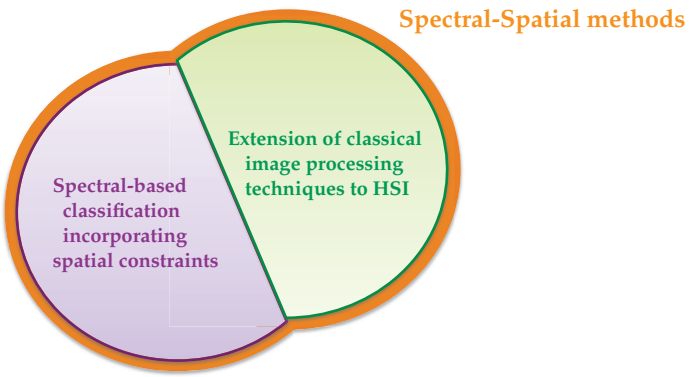

Figure 2.1: Spectral-Spatial Hyperspectral processing techniques

1. *Classification with spatial constraints*: This family of techniques corresponds to all the supervised and unsupervised classification methods incorporating spatial constraints.

2. *Extension of classical techniques to HSI*: This second group of hyperspectral methods is formed by all the techniques which are the extension of classical image processing techniques to high dimensional spaces.

According to this classification, the aim of the next subsections is to review some of the techniques related to each category. In 2.1.1, different methodologies introducing the spatial information in different stages of the classification process are presented. The other category of techniques is reviewed in 2.1.2. It deals with methods involving the extension of some classical image processing tools to hyperspectral imaging.

2.1.1 Classification techniques incorporating spatial constraints

Classification is one of the most studied applications in hyperspectral imagery. The goal is to label each pixel with the label corresponding to the class or the object that it belongs to. In the literature, the best classification results have been obtained by techniques incorporating the spatial information to the spectral space. The incorporation of the spatial or contextual information improves pixel-wise classification results which usually present an important *salt and pepper* noise (misclassification of individual pixels).
Thus, it seems clear that spatial knowledge should be incorporated during the classification methodology, the main question is then at which stage and how it should be included.

- Is it better to incorporate spatial information as an input data before classifying the data?

- Should the spatial information be included in the classification decision?

- Is the incorporation of the spatial information a post-processing stage of the classification process?

The incorporation of the spatial information has been suggested in different manners. This work reviews three groups of techniques according to these three discussed questions.

Spatial information as an input parameter

Some methods include the use of the spatial domain in an early stage. These techniques are characterized by computing in a first step some spatial image measurements which are later used by a classifier. The flowchart describing this approach is shown in Fig.2.2

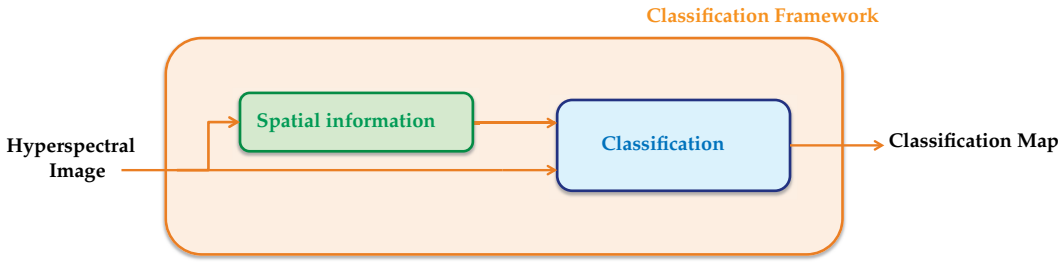

Figure 2.2: Spatial information as an input parameter

In some strategies following this scheme, this first step consists in constructing a spectral and spatial feature vector for each pixel which is later used as an input parameter in a pixel-wise classication task. An example is found in [79] , where the Gray Level Co-occurrence Matrix (GLCM) image measurements (Angular Second Moment, Contrast, Entropy and Homogeneity) are computed as a first step. These four texture measurements form a set of images which is decomposed by a Principal Component Analysis (PCA) to obtain its Principal Components (PCs). This last information is then used as an input feature for a Maximum Likelihood classifier.
Using another image reduction technique such as the Non-negative Matrix Factorization MNF, these GLCM texture measurements were also studied in [80]. They are used jointly with some spectral features to propose a supervised classification using the well-known Support Vector Machine (SVM) classifier.
Other strategies try to classify hyperspectral data by using a segmentation map as an input parameter. These approaches start by partitioning the image into homogeneous regions and then classifying each region as a single object. Most of these methods are based on the work presented in [81] which is the first standard approach proposed to join spectral and spatial domain in multispectral imagery. It corresponds to the ECHO (Extraction and Classification of Homogeneous Objects) classifier. In this method, an image is segmented into statistically homogeneous regions by the following recursive partitioning algorithm:

- First, an image is divided by a rectangular grid into small regions, each region containing an initial number of pixels.
- Then, following an iterative algorithm, an homogeneity criterion is tested between adjacent regions. If the test does not fail, these regions are merged forming a new region which will

be evaluated in the next iteration. In the other case, the minimal required homogeneity is not achieved, the region is then classified by using a ML classifier.

A recent work in [87] has extended this algorithm to an unsupervised version, where an image is also divided into different homogeneous regions according to their spatial-spectral similarities.
The classical ECHO classification methodology has also been followed in [82]. This technique proposes as a first step the extraction of some image features to reduce the image dimension. A merging algorithm similar to ECHO is then applied on the reduced image to construct a partition. Then, a SVM classifier is used to classify each region of the partition map. The SVM classifier has largely demonstrated its effectiveness in hyperspectral data. Thus, it has been also used in [83]. This work defines a neighborhood by using a segmentation result before applying a SVM classifier for every region. The segmentation map is obtained by a region growing segmentation performed by the eCognition software[84].
In the context of hyperspectral classification, a study of the pixel neighborhood definition to be used with SVM classifier can be found in [85] , where techniques as watershed [86] and Recursive hierarchical segmentation software [**?**] have been studied. In these last techniques, the classification map plays a different role in the classification decision. Instead of classifying a partition region by considering its spectral mean values, a majority voting decision is studied within the classification map regions.
One of the most critical aspects for the methods using partition maps as an input parameter is that they are very sensitive to the initial segmentation settings. For instance, the number of regions and the regions edges from the spatial partition of the image are critical parameters to achieve a good classification in the later step.

Spatial information inside the classification decision

The second important group of spatial-spectral classification techniques have considered that the spatial information should be included in the classification decision rule. Fig.2.3 describes the framework of this methodology.

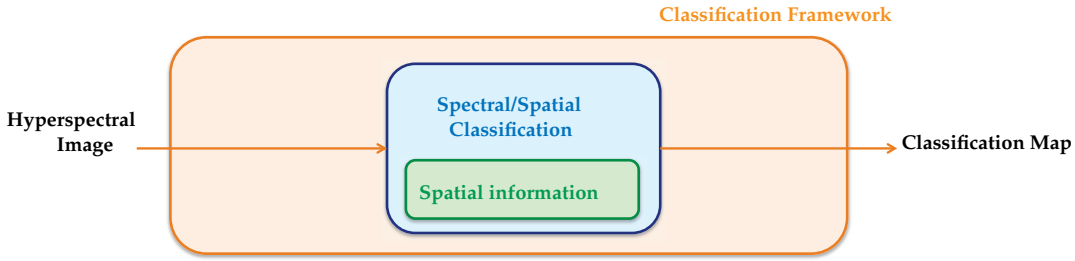

Figure 2.3: Spatial information inside the classification decision

Following this strategy, some methods have proposed to introduce the spatial constraints inside the SVM classifier decision. The approach of such methods proposed by [88] consists in

introducing the spatial information through the kernel functions. It has been demonstrated in [88] that any linear combination of kernels actually is a kernel $K = K_1 + K_2$: if K_1 and K_2 are two kernels functions fulfilling Mercer's conditions [88]. The interest is then to construct a combination of spatial and spectral kernel as $K(x, y) = \mu K_{spectral}(x, y) + (1 - \mu)K_{spatial}(x, y)$ where μ weights the relative importance of the spectral and spatial information.
The work presented in [88] proposes a gaussian kernel as $K_{spectral}$ by using the euclidean distance. Concerning the contextual information, $K_{spatial}$ introduces information about the local mean and variance for each pixel using a fixed square neighborhood. As mentioned by the authors, some problems can be found in this spatial kernel because of the fixed neighborhood window. In order to overcome the phenomena of edge effect (misclassifications in the transition zones), the method presented in [89] proposes an adaptive spatial neighborhood for $K_{spatial}$. Morphological filters are used to extract the connected components of the image which are assigned to each pixel as its adaptive neighborhood. The vector median value is computed for each connected component and this value is then used as the contextual feature for $K_{spatial}$.
Other approaches, not using SVM classifier, also include spatial information in the classification decision. For instance, in [91] and [90], authors have proposed unsupervised and supervised classification by estimating the class probability of each pixel through a defined spatial-spectral similarity function. Concerning the spectral decision, the Spectral Angle Mapper (SAM) is used as a discriminative measure showing its effectiveness in [92] . Concerning spatial discrimination, a stochastic watershed algorithm is proposed for segmenting hyperspectral data.

Spatial information as a post-processing stage

The third and last familiy of hyperspectral classification techniques reviewed here performs a post-processing in order to incorporate the spatial information. This regularization step avoids possible errors obtained by classification methods using only the spectral information. The followed methodology is represented by Fig.2.4.

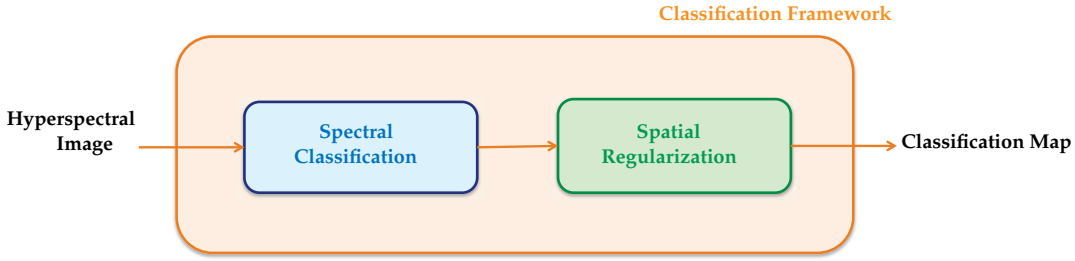

Figure 2.4: Spatial information as a post-processing stage

An important number of techniques are characterized by proposing the Markov Random Field MRF model [93] as the spatial post-processing task. The methodology of such approaches relies on three different steps. Firstly, hyperspectral data are classified in order to assign to each pixel its class-conditional PDFs. Secondly, using the classification results, an energy function composed

by one spectral and one spatial term is defined. For this energy function, the spectral energy term is usually derived from its class-conditional probability whereas the spatial energy term is computed by evaluating the class-probability of the neighborhood. Finally, the last step consists in labeling each hypespectral pixel with one class. This is done by the minimization of the energy function which has been formulated as a *maximum a posteriori* (MAP) decision rule.
In hyperspectral literature, different classifiers have been used for assigning class-conditional PDFs before constructing an energy function. In [96] , a DAFE dimension reduction used by a Bayesian classifier has been proposed. Another class-Pdfs estimation is proposed in [94] where the pixelwise ML classifier is used. The integration of the SVM technique within a MRF framework has been used in [100] [98] [99]. Also, in [97] class-conditional PDFs are estimated by the Mean Field-based SVM regression algorithm. Recent works have proposed to estimate the posterior probability distributions by a multinomial logistic regression model[101] [102]. For instance, the method presented in [101] first proposes a class-PDFs estimation by using a MLR classification step and then a MAP classification by minimizing the energy function using the α-Expansion min-cut algorithm.
Besides of these studies, some other works have been proposed in the literature involving hyperspectral image processing by MRF (See [78]).

2.1.2 Traditional imagery techniques extended to HSI

Traditional imagery techniques commonly used to process gray-scale, RGB or multispectral images are not suited to the dimensionality of the data present in a hyperspectral image. In order to address the high dimensionality issue, two different approaches have been mainly suggested. One solution consists in reducing considerably the hyperspectral data dimension in order to work with classical techniques. The other procedure is based on the extension of certain operations or image processing fundamentals into this new multi-dimensionality.
Following both approaches, classical techniques such as morphological filters, watershed transformations, hierarchical segmentation, diffusion filtering or scale-space representation, have been extended for HSI imaging. Within this large group of algorithms, this section will focus on two groups: the morphological transformations and the hierarchical segmentation techniques (See Fig.2.5). In order to increase the knowledge about the extension of other classical techniques, a review of diffusion filtering techniques is presented in [78].

Transformations based on Mathematical Morphology

The first group of techniques reviewed here are the works concerning mathematical morphology transformations. In traditional imagery, the importance of mathematical morphology has grown and it has become a popular and solid theory over the past decades [103]. This nonlinear methodology has lead to the definition of a wide range of image processing operators. Based on lattice theory, the morphological operator are based on *maxima* and *minima* operations. This implies the definition of an ordering relation between the image pixels. In the case of hyperspectral image,

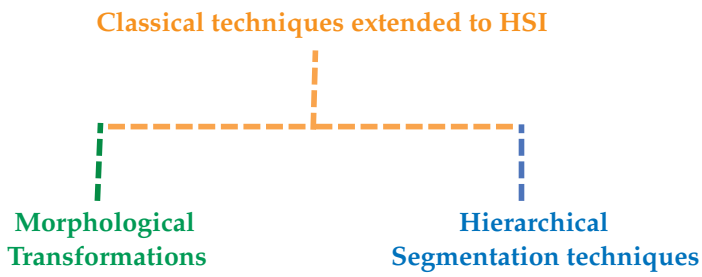

Figure 2.5: Division between the different reviewed works

as the pixels are multidimensional variables, the definition of a vector ordering is not straightforward.

The easiest solution is to use a marginal ordering where each hyperspectral band is processed individually. This ordering approach has been discussed in the past for RGB images where the main problem is the appearance of false colors [104]. In hyperspectral domain, this order is not appropriate given that, in order to preserve the actual spectral information, hyperspectral bands must not be processed individually. To address these problems, different vector orderings have been recently proposed for hyperspectral images.

From our knowledge, the first extension of morphological operators to hyperspectral images has been proposed in [105] for endmember extraction purpose. The suggested operators correspond to the extension of the most well-known operators, namely dilation and erosion. In order to compute the *maxima* and the *minima* between the studied pixel and its neighborhood defined by the structuring element (SE), two vector orderings are defined by computing min/max cumulated distance. The first approach proposes to define a D-order which is given by a metric that calculates the cumulative distance between one particular pixel and all the other pixels of the SE. The second approach is a R-order relying on the calculation of a spectral similarity between every spectral pixel in the SE and the centroid (mean spectral value) of the SE. The pseudo-distance used in [105] is the spectral angle distance and the SE corresponds to a square. Besides this distance, different non linear measures such as SID [7], have been proposed by the same authors in more recent works [114]. These operators have been proposed in some works leading to interesting results in classification.

Beside that, recent works [106] have remarked that these morphological operators cannot be used to define morphological filters since they are not adjunct operators (the self-dual property does not hold). For this reason, a supervised reduced ordering is proposed in [106] by defining two reference vector pixels: a target spectrum and a target background. These two reference pixels, namely foreground f and background g, are used to define a function h where $h(f)$ is the smallest (contrarily, $h(g)$ is the largest) element in the complete lattice defined by h. It induces a supervised h -ordering where h is constructed with a positive kernel function. Different semi-supervised and supervised kernels and consequently different h functions have been extensively studied in

[107]. The definition of the h-ordering has allowed authors to define different morphological operators such as the top-hat transformation which extracts contrasted components with respect to the background.

Other well-known operators of mathematical morphology are morphological profiles MPs [108]. These operators are computed by successively applying classical geodesic opening and closing operations. At each operation, the structuring element size is increased gradually. These operators have been studied in HSI in several works mostly focusing on data classification. Most of these studies have addressed the huge dimensionality issue by first reducing the hyperspectral image dimension. Hence, hyperspectral dimension reduction techniques are usually proposed as a first step before constructing MPs.

One of the first work introducing these operators for HSI images can be found in [109] where PCA is proposed as a first step to reduce the hyperspectral image dimension. The first principal component band, describing the *maximum* data variance direction, is then used as a gray scale image for computing classical MPs.

Following this approach, the work in [110] has also proposed the use of the gray scale first principal component image for constructing MPs. The resulting MPs are used here to classify the data by using the fuzzy ARTMAP method.

These two last works have only considered a single band image from PCA to perform Morphological Profiles. Consequently, the dimensionality reduction applied for these techniques can lead to a significant loss of information. To manage this issue, Extended Morphological Profiles EMP have been proposed in [111]. In this work, PCA technique is also proposed to reduce the image dimensionality. However, more components are taken to form the reduced space. The number of components is given by comparing the total cumulated variance of the data associated to the PCs with a threshold usually set to 99%. The resulting PCs are used to build individual morphological profiles (one for each PC), which are combined together in one extended morphological profile. In [111], EMPs are then single stacked vectors which are classified with a neural network, with and without feature extraction.

Another classification works [89] has further investigated the EMP construction for applying SVM classification. Concerning the image reduction technique, some techniques have considered ICA instead of PCA for computing the EMP [112]. Instead of the conventional PCA, a Kernel Principal Component Analysis is proposed in [115] as supervised feature reduction technique for computing the EMP.

Although most techniques have proposed to reduce the dimensionality of the image, the work presented in [114] has proposed the MPs construction by using the full spectral information. Using the morphological operators defined in [105] , the authors proposed in [114] different morphological profiles without any dimensionality reduction stage. In a SVM classification background, this new multi-channel MPs are compared with MPs computed in a reduced space.

The extraction of spatial features from hyperspectral images by using MPs or EMPs have shown their good performances in a large number of applications as classification or unmixing. However, these transformations cannot fully provide the spatial information of an image scene. This is

because they are based on morphological geodesic opening and closing filters which only act on the *extrema* of the image. Consequently, MPs only provide a partial analysis of the spatial information analyzing the interaction of a set of SEs of fixed shape and increasing size with the image objects. In order to solve these limitations, morphological attribute filters have been proposed instead of the conventional geodesic operators to construct Extended Attribute Profiles EAPs[113]. The application of attribute filters in a multilevel way leads to describe the image by other features such as shape, texture or homogeneity. EAPs have been also proposed for hyperspectral data classification and they have been constructed after applying different dimensionality reduction techniques such as PCA or ICA[113].

As can be seen, most of the techniques concerning MP, EMP or EAP are focused on hyperspectral classification. Thus, they could be also included in the first group of classification techniques reviewed in Sec.2.1.1. In fact, these morphological operators have been used to estimate in different manners the spatial information which is lately used in a classification stage.

Going on with morphological operators, another important algorithm extended to hyperspectral image is the watershed. This transformation is based on considering each frequency band image as a topographic relief, whose elevation depends on the pixel values. In this topographic relief, the local *minima* are considered as catchment basins. In the first step, some image *minima* are defined as markers which are the sources of the catchment basins. Then, a flooding process of the catchment basins is performed by a region growing step starting from each marker. The flooding process finalizes when two different catchment basins meet, hence defining a watershed line(edge). The resulting image partition of watershed algorithm is obtained by these edges.

In the case of color image, the classical watershed algorithm is computed by interpreting the height of the image color gradient as the elevation information. Thus, the extension of watershed algorithm to HSI relies on defining how to extract the gradient in the multidimensional space.

One of the first works involving watershed in HSI data can be found in [116]. In this study, different gradient functions have been proposed to construct a stochastic watershed algorithm. The aim of stochastic watershed is to define an algorithm that is relatively independent of the markers by introducing a probability density function of contours. This pdf gives the edge strength which can be interpreted as the probability of pixels of belonging to the segmentation contour. The pdf of contours can be estimated by assigning to each pixel the number of times that it appears as an edge in a series of segmentations. In the hyperspectral case, the construction of such pdf has been studied taking into account all the hyperspectral bands or only using some of them after a dimensionality reduction [116]. In this last work, the contour pdf function is used to construct watershed algorithm in two different manners. The first approach consists in using the contour pdf function instead of the classical color gradient. The second approach is to used the contour pdf to construct a new probabilistic gradient based on the sum of the color gradient and the contour pdf.

Following the first strategy, a vector approach has been proposed where the pdf is computed by a similarity distance taking into account all the bands (with or without reduction). A marginal approach has also been proposed by computing one marginal pdf for each channel. The resulting

pdf is then defined by a linear weighted combination of all marginal pdfs (the weights are for example the inertia axes).
The second approach consists in performing watershed algorithm by using a probabilistic gradient based on the sum of color gradient and the contour pdf. The strategy of constructing a probabilistic gradient has been pursued in recent works [91] for hyperpsectral image segmentation. In this case, the proposed gradient is also a sum between a gradient distance and a pdf contour function. However, some new pdf contour estimators are proposed using different multiscale segmentations and introducing spectral information.
Besides stochastic watershed, other color gradient functions (without introducing pdfs of contours) have been proposed for hyperspectral classification. In [85] , robust color morphological gradient and color morphological gradient have been proposed to perform the watershed algorithm. These gradient functions have been performed after reducing the dimensionality of the hyperspectral image. The result of the watershed algorithm has been used to define an image adaptive neighborhood for a SVM classification purpose.

Hierarchical segmentation techniques

Image segmentation is interpreted as an exhaustive partitioning of an image. Each region is considered to be homogeneous with respect to some criterion of interest. The aim of segmentation is the extraction of image regions as primary visual components that can be used later to identify and recognize objects of interest. The main problem is that it is very difficult to directly construct the best image partition (if there is any) given the huge number of applications potentially considered for one given image.
Let us consider for instance a high-resolution aerial image which is formed by an urban and a vegetation areas. Working at coarse scales, some applications can be defined to separate between fields and cities. However, applications focusing on individual tree or building detection should work for the same image at a much lower scale.
The interpretation of an image at different scales of analysis has led some authors to deal with multi-scale image segmentations. A multi-scale image segmentation relies on the construction of hierarchy of partitions mainly based on an iterative region merging algorithm (See Def.3). The result of the hierarchical segmentation technique is then an image partition representing a hierarchical level obtained after a region merging procedure.
Fig.2.6 shows an example of multi-scale segmentation where a region merging algorithm has been performed on the image *Iteration 0*. The partitions created during the iterative procedure are shown consecutively from the left to the right. Note that once these five hierarchical partitions are computed, a criterion related to the addressed application is needed in order to select the appropriate level of the hierarchy. Consequently, the segmentation result obtained for this example will be one of the following partitions: *Iteration 0*, *Iteration 1*, *Iteration 2*, *Iteration 3* or *Iteration 4*.

Hierarchical segmentation techniques have been also studied for hyperspectral data. Some of them are mentioned in Section2.1.1. In this framework, ECHO was the first proposed hierarchical segmentation technique [81]. As previously explained, ECHO proposes a region merging

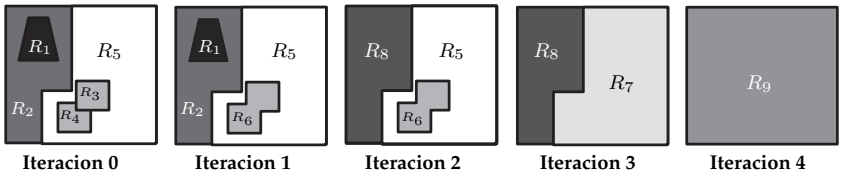

Figure 2.6: Example of multiscale segmentation

algorithm whose merging criterion is based on a likelihood test measuring if two regions are homogeneous or not. The decision to assess if the homogeneity test is true or false requires to set a threshold. Thus, the accuracy of segmentation results strongly depends on the selected threshold. Furthermore, the ECHO method is based on statistical computations and involves estimation of covariance matrices. The computation of covariance matrices may not be suited for hyperspectral data because these matrices are highly unstable (negative eigenvalues).

Following the ECHO methodology, the work presented in [82] has proposed a region merging algorithm to create a hierarchical segmentation. The aim consists in constructing a segmentation map of the image which is used to perform an object-based classification. The region merging algorithm is called Fractal Net Evolution Approach FNEA and it is executed after a subspace feature extraction. The FNEA has been proposed as a bottom-up region merging technique using a merging criterion defined as $h = w \cdot h_{spatial} + (1-w) \cdot h_{spectral}$ where w is a weight controlling two spectral/spatial distances. Concerning the spectral criterion $h_{spectral}$, the sum for all the channels of a dissimilarity homogeneity distance is proposed. This homogeneity measure is the difference between the standard deviation of two regions before and after the merging. In the case of $h_{spatial}$, it has been defined as a measure comparing the compactness and the smoothness of the region before and after the merging. The smoothness coefficient corresponds to the ratio between the perimeter of the region and the perimeter of the minimal bounding box containing the region. As compactness descriptor, the relation between the region perimeter and the square root of the region area is proposed. Therefore, the h value is used to evaluate the merging of pair of regions iteratively. Accordingly, the merging is performed if h value is below a given threshold. The result of the merging process is a segmentation map which is used as an object-based representation to classify the image. Afterward, the features computed in the first step are used to define a feature vector for the regions contained in the object-based representation. For each region, the feature vector is defined as the average of all the pixel features contained in the region.

Also close to ECHO methodology, another supervised hierarchical segmentation approach is proposed in [117] for partitioning the image into homogeneous regions. This methodology is known as "The Spatial and Spectral Classification method "(SSC). The strategy mainly consists in three different steps: 1) The extraction of homogeneous regions by computing a similarity distance as the vector norm between each pixel and its 4-connected neighborhood, 2) the classification of the homogeneous regions by a supervised classifier 3) The iterative classification of the remaining (heterogeneous) image parts by introducing a spatial distance information. In this case, the spa-

tial distance provides information about the class of the neighboring pixels around the studied pixel.
One of the most well-known hierarchical segmentation methods in hyperspectral data can be found in [120] . The proposed algorithm is based on the hierarchical sequential optimization algorithm (HSWO for Optimal Hierarchical step-Wise Segmentation) [119] and it has been adapted to hyperspectral data [22]. It relies on three steps:

1. Using the pixel-based representation of an image, a region label is assigned to each pixel (if there is no pre-segmentation step).

2. A dissimilarity criterion is computed between all pairs of adjacent regions. The fusion of two adjacent regions is performed if the distance is below a *minimum* threshold.

3. The algorithm stops if there is no more possible merging steps, otherwise it returns to step 2.

For the second step, the dissimilarity vector norm, the spectral information divergence SID, the spectral angle mapper SAM or the normalized vector distance NVD have been proposed. Recently, in order to mitigate the important computational cost of the initial approach, an algorithm called recursive approximation RHSEG ("Recursive Hierarchical Segmentation") has been proposed [121]. It has been recently used in a classification context [**?**].
Another generic hierarchical segmentation is presented in [78] based on an iterative process and a cross analysis of spectral and spatial information.The hierarchical segmentation algorithm is implemented by using a split and merge strategy. First, the image is over-segmented by a series of splits based on spectral and spatial features following a strategy called butterfly. Secondly, setting a stopping criterion, as for instance the number of regions, a region merging procedure based on split and merge operations is performed until the stopping criterion is fulfilled. The construction of a split and merge operations is carried out by the diagonalization of the matrices describing the intra- and inter-region variance,respectively.
The general conclusion of this review on hierarchical segmentation for hyperspectral data is that these techniques perform an iterative region merging algorithm based on certain similarity criteria, until the predefined termination criterion is achieved. One of the main problems of such strategy is that they assume that the "best" partition corresponds to one hierarchical segmentation level. Unfortunately, this assumption is rarely true and it can lead to some issues when the coherent objects are found at different levels of the hierarchy.
For instance, assume that for the hierarchical segmentation of Fig.2.6 the optimal partition from a given segmentation goal is formed by R_7 and R_8. It can be noticed that in this case, the optimal partition is contained in the hierarchy at level corresponding to *iteration 3*. However, it should be also remarked that an application looking for an optimal partition formed by R_7, R_1 and R_2 will never reach its purposes. This is because a large amount of information is lost in the hierarchical segmentation techniques. They actually provide a rather limited number of partitions. This also shows that these multiscale segmentations are not generic representations, in the sense that they

cannot be further processed according to different applications. The processing of a hierarchical representation can offer various advantages as compared to the strategy of creating a segmentation map following a region merging procedure. For this reason, some recent works try to process results contained in the hierarchy [122], [118] .

The work presented in [118] has proposed an example of processing hierarchical segmentation to find coherent objects in the image. In order to process the partition hierarchy, segmentation results are represented by a tree structure. In a first step, this work constructs a hierarchical segmentation of the image after reducing the dimensionality of the image performing a PCA reduction. The hierarchical segmentation is performed by constructing an opening and closing profile [108]. It is carried out by applying morphological operators on each individual spectral bands using SE of increasing sizes. These granulometry series produce a set of connected components forming a hierarchy of segments in each band. Each pixel can then be assigned to more than one connected component at each SE scale. The aim of constructing such a hierarchy is to look for connected components which correspond to objects. To this end, authors have then proposed to structure the hierarchical segmentation by a tree representation where each connected component is a node. Concerning the edges of the tree, they represent the link between two consecutive scales of the hierarchy. Thus, the edges correspond to the inclusion relationship where each node is inherently contained in its parent node. In this case, the processing of a tree representing hyperspectral data has started showing the advantages of hierarchical representations by using trees. Given the object detection goal, the tree is used to select homogeneous regions contained in the nodes by using the standard deviation of the spectral information of each region. The proposed criterion corresponds to the difference between standard deviation of a node and its descendants.

Besides this last work, in parallel of this thesis, another tree image representation has been studied for processing hyperspectral images. This representation is the max-min tree [135] which has been studied in hyperspectral context in [113] (See Fig.Fig.2.11). Working in a reduced PCA hyperspectral space, this work shows another important benefit of tree structures: their scalability. This property allows to compute region descripors on the nodes to perform EAP by using the inclusion hierarchy of the tree. As mentioned before, these morphological transformations, that can be easily defined using tree, have corroborated their performances in hyperspectral image classification.

Both hyperspectral tree image representations proposed in [113] and [118] are based on morphological construction tools. Therefore, the segmentation results stored in the hierarchy corresponds to the connected components associated to a merging order performed by granulometry series. Merging orders constructed by an iterative morphological filtering have some difference with region merging segmentation algorithms. The work in [123] has shown how the merging order constructed by iterative morphological filters does not efficiently represent objects as a connected components.

Given a one-band image, by using region merging segmentation algorithm, objects correspond to connected components that are homogeneous in their gray level. Thus, the merging criterion of these techniques consists in a measure evaluating this homogeneity notion. Instead, in the case

of morphological filters, objects are only assumed to be either bright or dark parts of the image. Hence, the merging order is based on the succession of gray level values. Thus, the stopping criterion is generally based on a different notion such as size.
The main drawback of using connected filter to create a hierarchical representation is that they just deal with the regional *maxima* and *minima* of the image (the *extrema*).
This can be understood looking at the result obtained after merging two regions by applying a morphological filter. At this point, the operator assign to the resulting connected component the lowest (or highest) value of the pixels contained in the region. This gray level assignation strategy means that these filters model a region by only using a local maximal or minimal gray level value. Thus, this model can be very simple and not very realistic. To address this issue, region merging segmentation algorithm proposes to model regions by using more realistic descriptors of the region. For instance, instead of a maximal or minimal gray level, the set of pixels belonging to a region are modeled by their mean value or by using a probability distribution.
This optimal strategy can be performed by a tree image representation such as Binary Partition Trees [15]. This explains why this thesis has focused on the construction of these trees representations in a hyperspectral context.
At this point, this review of techniques leads us to believe that the processing of hypespesctral images by using hierarchical tree region-based representation can be an interesting topic of research. In the literature, some tree representations have been already studied for the gray-scale or RGB images. As mentioned above, this thesis is focusing on the BPT. This choice is justified in the next sections where a review of tree image representations is detailed.

2.2 Hierarchical region-based processing using trees

Regions are aggregations of pixels which play a key role in image and scene analysis. The external relations of the regions in the image (adjacency, inclusion, similarity of properties..) as their internal properties (color, texture, shape,..) are extremely important for nearly every image analysis task. Hence, there is a wide agreement in the literature that describing images with region-based representations is beneficial to interpret information. These image representations have been proposed as an attractive solution tackling the pixel-based representation issues.
Being a more accurate image representation, the region-based approaches do not operate directly on individual pixels but on regions consisting of many spatially connected pixels. They can be represented by graph structures in which nodes are used to represent regions and the links are used to represent certain relationships between regions. In image analysis, the most well known region-based representation is the Region Adjacency Graph (RAG) [125]. The nodes of a RAG represent the connected regions of a partition image space and the links only connect adjacent regions in the image. An example of an image segmented into 4 regions and its corresponding RAG, which is highlighted in green, are shown in Fig.2.7.

The processing of the RAG mainly consists in deciding if the links connecting adjacent regions should be removed according to a cost function. Links having a minimal cost are then iteratively

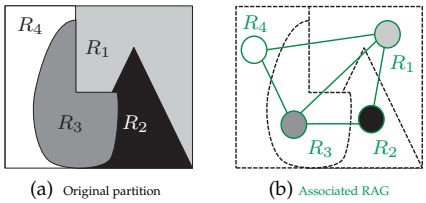

Figure 2.7: Example of Region Adjacency Graph

removed, merging adjacent regions[127]. This approach is very idealistic because it argues that at certain point in the merging process, the extracted regions would be close to the objects of the scene. This assumption is rarely true and it shows the limitations of the RAG representation.
RAG representation also suffers from another important drawback since it cannot represent the whole topological information[126]. RAG provides a "simple-connectivity view" of the image not representing the multiple adjacency nor the inclusion relations. A solution for the inclusion limitation is the hierarchical region-based representations which manage to encode a hierarchy of partitions providing a multi-resolution description of the image.

Definition 3. (Partition hierarchy) *Let $\mathcal{H}$ be a set of partitions $\{\mathcal{P}^i\}$. We say that $\mathcal{H}$ is a partition hierarchy if it is possible to define an inclusion order between each pair of elements of $\mathcal{H}$, that is, $\mathcal{P}^i \subseteq \mathcal{P}^{i+1}$*

A partition $\mathcal{P}_0$ is included in a partition $\mathcal{P}_1$, $\mathcal{P}^0 \subseteq \mathcal{P}^1$, if any region $R_J^1 \in \mathcal{P}^1$ is completely included in a region $R_J^0 \in \mathcal{P}^0$. Fig.2.8 shows a partition hierarchy example containing three partitions $\mathcal{H} = \{\mathcal{P}^0\, \mathcal{P}^1, \mathcal{P}^2\}$. The inclusion order specified in $\mathcal{H}$ is given by $\mathcal{P}^0 \subseteq \mathcal{P}^1 \subseteq \mathcal{P}^2$. The bottom layer of the hierarchy including more details than the other two layers is $\mathcal{P}^2$.

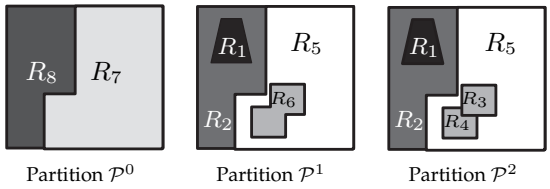

Figure 2.8: Example of partition hierarchy $\mathcal{H}$

A suitable structure for representing these hierarchical representations relies on trees as they are inherently hierarchical. In a tree representation, nodes correspond to image regions as in the RAG. However, trees edges encode the inclusion relationship between the regions: "being part of" instead of "being neighbor with".
Hierarchical region-based tree structures are attractive representations to perform an analysis of image contents at several scales simultaneously. Usually, the "best" region-based description of an

image by regions depends on the application. Therefore, it can be attractive to have a generic hierarchical image description represented by a tree, which can be processed by different algorithms typically suited to different applications. The processing of the tree is mainly based on a pruning technique which removes some of the tree branches by an application-dependant analysis algorithm.

2.2.1 Definition of the tree structure

A tree $\mathcal{T}$ is a graph formed by a set of nodes where there is a unique path connecting any pair of nodes $\mathcal{N}_i$ and $\mathcal{N}_j$. Every finite tree structure has a node called *root* establishing the hierarchical structure of the nodes. The edges connecting the nodes are called branches and each node $\mathcal{N}_i$ has exactly one entering branch. Each node without any children is called *leaf* node. Fig.2.9 shows a tree example, where the different tree notions are highlighted in different colors. For instance, root corresponds to the highest green node.

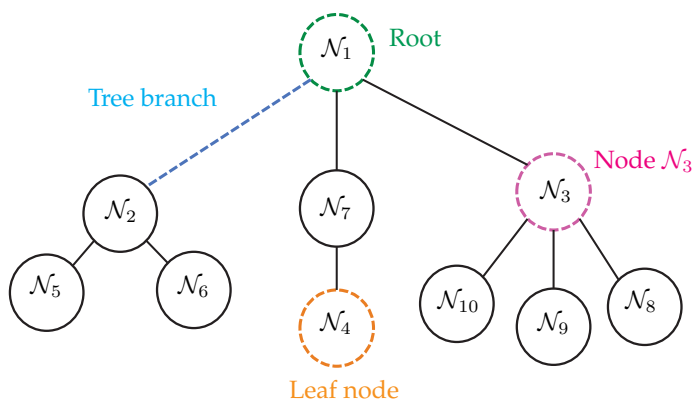

Figure 2.9: Representation of a tree $\mathcal{T}$

The *parent* of a node $\mathcal{N}_i$ is defined as the node one step higher in the hierarchy (i.e closer to the root node) and lying on the same branch. Accordingly, a *child* node is defined as the node one step lower in the hierarchy. For instance, in the case of Fig.2.9, the node $\mathcal{N}_2$ is the parent node of nodes $\mathcal{N}_5$ and $\mathcal{N}_6$ whereas these last two nodes are the children of $\mathcal{N}_2$. Nodes sharing the same parent node are called *sibling* nodes.

From every node to every other node, the set of tree branches connecting them is called *path*. If there is a path between two nodes, an ancestor-descendant relation is given when one of the two nodes is included in the path from the root node to the other node. The upper node of the two nodes is called an *ancestor* node and the lower node a *descendant* node. Considering again Fig.2.9, the ancestor nodes of $\mathcal{N}_9$ are itself, $\mathcal{N}_3$ and $\mathcal{N}_1$. On the other hand, the descendant nodes of $\mathcal{N}_3$ are $\mathcal{N}_{10}$,$\mathcal{N}_9$ and $\mathcal{N}_{11}$.

Given a tree $\mathcal{T}$, a subtree is defined as a subset of nodes of $\mathcal{T}$ whose corresponding branches form a tree. A subtree rooted at node $\mathcal{N}_i$ will be indicated with $\mathcal{T}_{\mathcal{N}_i}$. Fig.2.10 shows in red one of the

subtrees contained in $\mathcal{T}$ which is rooted at $\mathcal{N}_3$.

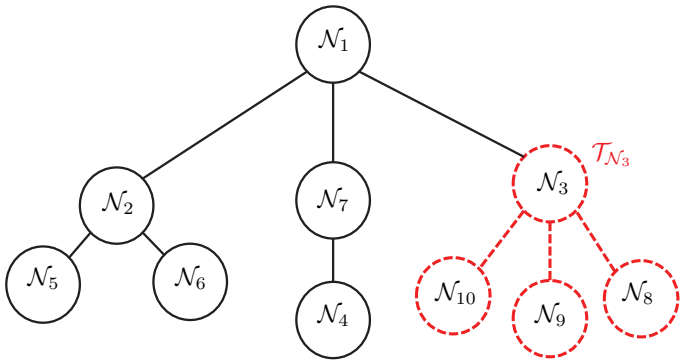

Figure 2.10: Subtree example

The work here is focused on using tree structures as hierarchical region-based representation having the following properties:

1. Each node $\mathcal{N}_i$ of $\mathcal{T}$ is associated to a region $\mathcal{R}_i$ of the image.
2. Two sibling nodes $\mathcal{N}_i$ and $\mathcal{N}_j$ are two non overlapping regions $\mathcal{R}_i \bigcap \mathcal{R}_j = \emptyset$
3. The region $\mathcal{R}_i$ associated to $\mathcal{N}_i$ is contained in the region $\mathcal{R}_k$ associated to its parent $\mathcal{N}_k$

2.2.2 First hierarchical tree representations

Hierarchical region-based representations allow to define how the different regions in a scene are organized. This idea has attracted much attention in image analysis and there are many different tree image representations in the literature. Most of these multiscale image representations are intuitively constructed by the split-and-merge [128] top-down or bottom-up methods. Starting with a partition of the image, these algorithms decrease (resp. increase) the number of regions using successive region merging (resp. splitting) operations.

One of the first hierarchical region-based representations using trees is the *quadtree* decomposition introduced by [129]. This multi-scale representation decomposes recursively the image into square blocks through a split algorithm. Each block corresponds to a tree node and it can be divided into four smaller blocks. This split decision is taken if a block does not contains pixels fulfilling a given criterion[130] [131]. Contrarily, if a block contains similar pixels, there's no reason to further divide it.

The main limitation of quadtrees is that they only allow the efficient representation of square or rectangular regions. This implies that the contour information is not preserved. In order to solve this issue, morphological trees have been proposed by studying the images as a set of connected regions.

In this context, *Critical Lake* trees were proposed in [132] based on watershed fundamentals [133].

Considering the image as a topographic surface, the tree nodes correspond to its catchment basins. Two neighboring catchment basins are merged at the lowest pass-point of the gradient along their common frontier[134].

Other important morphological trees are the *max* and *min* trees which are relatively new image representations [135]. In the case of *max* tree, leaves correspond to the *maxima* of the original image. Similarly, leaves in the *min* tree correspond to the image *minima*. The *max* tree is built by following an increasing thresholding decomposition. At each iteration, an increasing threshold evaluates the pixels contained in all the nodes created in the previous iterations. If pixels have values lower than the studied threshold, they remain in the tree node, however, pixels having higher values will form new nodes. For the construction of *min* tree, the previous algorithm has to be inverted following then a decreasing thresholding decomposition. Fig.2.11 shows an example of *max* tree representation which is obtained in two iterations given two thresholds T_1 and T_2. It can be seen how the leaves of the tree correspond to the connected components (regions) having the highest gray levels. On the other hand, root node represents the region having the lowest gray level.

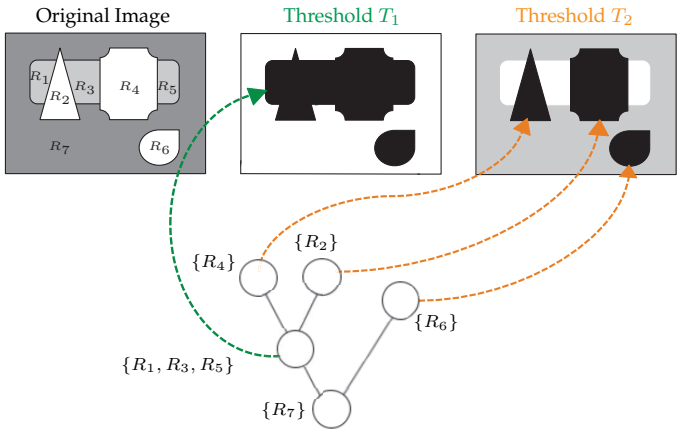

Figure 2.11: Example of Max Tree Representation

These *max*- and *min*-tree representations act separately on *maxima* and *minima* which may not be suitable in some cases because they only act on the *extrema* of the image. For instance, the same type of objects may appear brighter than their neighborhood in some parts of the image but darker in others. Thus, it should be preferable to analyze all the structures in the image, independently of their gray-level values Hence, the Inclusion Tree (also known as tree of shapes) [136] was proposed as a self-dual representation for such cases. This tree structures the family of level lines of the image by an inclusion relationship. Thus, the image connected components of upper and lower level sets are represented by a tree.

A weak point of the trees working with the image *extrema* relies on its construction by using simple fixed merging orders . For instance, the construction of *max-min* trees is completely based on

the absolute gray levels. Thus, they cannot describe easily objects that are not *extrema*. Therefore, objects appearing in transition areas between extrema can be lost in the representation.
To address such limitation, the Binary Partition Tree was proposed as a more accurate image tree representation being constructed by no fixed algorithm. This tree is a structured representation of a set of hierarchical partitions which is usually obtained through a segmentation algorithm.

2.2.3 BPT Literature

The Binary Partition Tree [15] is a hierarchy of regions representing the image at different resolution levels. The BPT allows the assignment of spatial constraints and the definition of partial orders of the regions. The hierarchy of partitions contained in BPT gives a much more natural representation of visual scenes. This addresses the weaknesses of working with the perceptually meaningless entities offered by the pixel-based representation (the pixel grid).
In the literature, BPTs have been previously studied showing their effectiveness in image filtering [15], object extraction [39] [43] [45], segmentation [44] [24], motion compensation [38], filtering [138] or contour detection [46]. Hence, the construction of BPTs has been an area of research in the last ten years in the context of multimedia images and RGB images. This construction is based on the definition of an iterative region-merging algorithm.
In image processing, the construction of a region merging order has to deal with the two following questions: 1) how to model a region and 2) how to decide if two regions are similar or not.
For the first aspect, most of the region merging algorithms proposed by BPT construction have used as region model the mean color value of the pixels belonging to the region [15] [40]. This model used also in [41] corresponds to a zero-order model which assumes color homogeneity inside the region. Because this assumption is rarely true, a model for the images formed by textured regions has been proposed in [42]. Note that this last approach assumes either color homogeneous or textured regions. In order to propose a more general strategy, a non parametric statistical region model has been proposed in [17]. This model corresponds to set of non parametric probability density functions (pdfs) with no assumptions about the nature of the regions nor the shape of the pdfs. Other important approaches have been proposed to use region models including shape information. In [47], syntactic properties directly related to the region shape description have been introduced. The use of syntactic visual features in region merging algorithm has also been used in [48] dividing the merging process into stages and using a different homogeneity criterion at each stage. Also, in [39] the perimeter of the regions is considered as a region model descriptor.
The second important aspect for constructing the merging order is how to measure the similarity between regions. The answer to this question is given by the merging criterion definition. The merging criterion corresponds to a similarity measure between the regions, which are previously modeled by the chosen region model. Thus, the merging criterion used in a region merging algorithm is completely linked to the region model definition. Using a zero-order model, merging criteria are mainly defined by classical distance based on absolute difference between colors. A complete study can be found in [40], where different measures using the classical Euclidean distance are compared. In the case of non-parametric statistical models, their use requires the

definition of a robust distance between probability distributions. In [17], some statistical similarity measures such as the Kullback-Leibler divergence rate, the Bhattacharyya coefficient and the first order Markov empirical transition matrices are proposed.
As mentioned before, the construction of BPT offers a generic representation of the image. This is very important and it is the main reason why BPT has been used in various applications. Each application is associated to a tree processing technique corresponding to the tree pruning[137]. Previous works have presented different tree pruning techniques for different purposes. A first category of the proposed pruning techniques are based on increasing criteria along the branches. A criterion C assessed on a region is increasing if: $\forall R_1 \subseteq R_2 \implies C(R_1) \leq C(R_2)$. This implies that if a criterion $C(\mathcal{N}_i)$ is associated to a node $\mathcal{N}_i$, the criterion value for the parent node of $\mathcal{N}_i$ will be higher. As a result, if a node should be removed by the pruning technique, all its descendant should also be removed. Thus, the pruning technique is straightforward by removing the subtree rooted by a node for which the criterion is below a given threshold. An example can be found in [49] where a BPT pruning by region evolution [56] is presented in an object extraction context. Increasing criteria have been frequently used because they directly lead to a pruning strategy.
Non-increasing criteria have been also proposed as the basis of the pruning strategy for some applications. These strategies are more difficult because the descendants of a node to be removed have not necessarily to be removed.
Formulating the problem as a dynamic programming issue, a pruning algorithm based on the Viterbi algorithm was presented for filtering purposes in [15] [135]. In the context of object detection, some pruning techniques are formulated as node detection[39] [43]. Defining a set of descriptors of the sought objects, these algorithms look for the nodes most likely corresponding to the sought object. More recently, a pruning technique has been proposed in [138] for filtering speckle noise. Studying a homogeneity measure along branches, this pruning follows a *max* rule which prunes the branches from the leaves up to the first node that has to be preserved.
Another family of pruning relies on a global minimization of a criterion under constraint. This problem is then formulated as a global energy minimization problem by using a Lagrangian function. In this approach, the lagrangian parameter λ is balancing the criterion and a smoothing related to the constraint. Using a gradient descent method, the optimal λ value is computed and the partition associated to the λ parameter defines the global pruning.
Setting a rate/distortion criterion, a pruning strategy following this approach has been proposed in [139]. Following this idea, a pruning algorithm by using a dynamic programming principle has been defined to compute the optimal pruning with respect to any value of λ [140].

2.3 Conclusions

In this chapter we have reviewed the work done so far in the areas of hyperspectral image processing and of hierarchical region-based tree representations. Most of the relevant work in hyperspectral imaging has been explained detailing how the main drawbacks of HSI processing are addressed. Some of these issues have been presented as the incorporation of the spatial informa-

tion to process or classify the data, the dimensionality reduction of the image before processing the extension of classical techniques to HSI context or the definition of a vector order to define morphological tools.

A large number of techniques have shown in Sec.2.1.1 how the incorporation of the spatial information can be introduced as a methodology stage from different manners. All the reviewed techniques working in the spatial-spectral domain process hyperspectral data by using their pixel-based representation.

As mentioned before, this low level representation provides extremely local information since the decisions and processing steps are applied individually to all pixels. Consequently, this low scale representation is in most cases too far from the semantic interpretation scale. To manage this issue, some of these techniques such as ECHO, have tried to introduce a description of the image, as region-based partition, as an input parameter in their strategy.

This gap between image representation and semantic interpretation has been also addressed by hierarchical segmentations described in Sec.2.1.2. In a hyperspectral framework, these techniques have been suggested to provide a region-based description of the image at different scales. Unfortunately, hierarchical segmentations cannot be considered as a generic region-based image representation which can be used to address a large number of applications.

A solution for constructing a generic representation, structuring the different regions in an organized way, relies on trees. This idea has been reviewed in Sec.2.2. This section has introduced the main advantages of processing images using tree structures. Some classical tree-based images representations previously introduced for gray-scale or RGB images have been reviewed. Morphological trees have been explained in Sec.2.2.2. They offer them a solution for the contour preservation problem related to Quad-Trees. Concerning morphological trees, some limitations have also been explained. To address such problems, BPTs have been presented as a powerful image representation that can be constructed using them by performing a region merging algorithm.

The BPT literature for classical imagery has been presented in Sec.2.2.3 where the different merging orders proposed for BPT construction have been mentioned. Also in this section, BPT pruning strategies have been reviewed showing the advantages of tree processing.

As a conclusion, this chapter has presented the framework of this thesis describing the necessity of the construction of a hierarchical region-based representation as Binary Partition Tree. The following chapters will address the construction of BPT representation for hyperspectral images and their processing for various specific applications.

3

BPT construction

Contents

3.1 Introduction **42**

3.2 Region Model **45**

3.2.1 First-order parametric model 46

3.2.2 Non parametric statistical Region Model 47

3.3 Merging Criterion **55**

3.3.1 Measures associated to the first-order parametric model 59

3.3.2 Measures associated to the non parametrical statistical region model 61

3.3.3 Similarity measure via Multidimensional Scaling 64

3.4 Experimental Evaluation **71**

3.4.1 Quality measures between partitions 71

3.4.2 Data Sets Definition 73

3.4.3 Experiment 1: Evaluation of BPT hierarchical levels 78

3.4.4 Experiment 2: Evaluation of D_s selection 93

3.5 Conclusions **94**

This chapter details the construction of BPT representation for hyperspectral imaging. In this framework, different region merging algorithms are discussed by studying various region models and merging criteria. The hierarchical partitions obtained during the BPT construction are evaluated and compared with other state-of-the-art region merging techniques[22].

3.1 Introduction

BPT is a tree-based structure representing an image by a set of hierarchical regions [15]. The tree representation provides the description of the image at different scales of resolution where the finest level of detail is given by an initial partition. As the tree is binary, each node has either two children or none (a leaf). Thus, if the initial partition involves n regions, a BPT generates a tree structure containing *2n-1* nodes.

A possible solution, suitable for a large number of cases, is to create the tree by performing an iterative region merging algorithm [57] [58]. In a bottom-up strategy starting from the leaves, the tree construction is then performed by keeping track of the merging steps. At each step, the most similar adjacent regions are merged. The strategy consists then in storing the sequence of region fusions in the tree structure. As a result, the tree represents the complete hierarchy of regions. Fig. 3.1 shows an example of BPT construction created from an initial partition. Starting from the partition illustrated on the left, the algorithm is merging at the first iteration R_3 and R_4. After this first merging, the fusion of R_3 and R_4 forms region R_5. This iterative merging step procedure is executed until an unique region contains all the pixels of the image. This last region describing all the image support is the root node which corresponds to the highest node of the tree hierarchy.

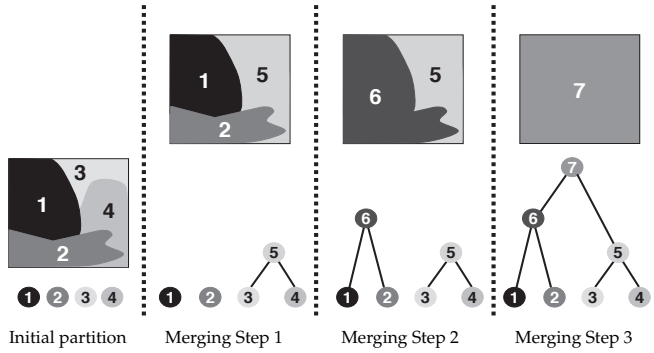

Figure 3.1: Example of BPT construction using a region merging algorithm

In this last figure, tree leaves corresponds to the regions belonging to the initial partition. However, in order to preserve as much as possible the resolution in this work, the initial partition will be a partition where each pixel is a region. Consequently, each leaf of the tree corresponds to individual pixel p of the image, i.e. a spectrum $\mathbf{I}_\lambda(p)$.

As it has been explained in Chapter 1, all the connectivity relationships between the regions of the initial partition are not represented in the tree branches. Thus, BPT only encodes a subset of possible merging. Hence, BPT offers a trade-off between the representation accuracy and the processing efficiency. On the other hand, the lost of this information cannot be an issue if BPT offers the most "likely" or "useful" merging steps. Then, BPT should be created in such a way that the most interesting or useful regions of the images are contained in BPT nodes.

The specification of a region merging algorithm to construct the BPT relies on two important

notions:

1. *Region Model* M_{R_i}: It specifies how regions are represented and how to model the union of two regions. The model should be an accurate representation of the region. Moreover, to reduce the computational time of BPT construction, M_{R_i} should be fast to compute and to update.

2. *Merging criterion* $O(R_i, R_j)$: It defines the similarity of two neighboring regions R_i and R_j. Therefore, it determines the order in which regions are going to be merged.

Both notions are used to define a region merging algorithm previously described in [141] . An example of iterative region merging procedure is shown in Fig.7.1. The implementation of this algorithm needs two different structures. The first structure is the RAG which defines the adjacency of the regions at each iteration. Concerning the second structure, hierarchical priority queue is used. The idea is that at each step the pair of most similar regions are merged. Thus, in order to do this process efficiently, a priority queue to handle the similarity values is used to access efficiently the highest similarity value. (Go to Appendix 7.1 for more details).

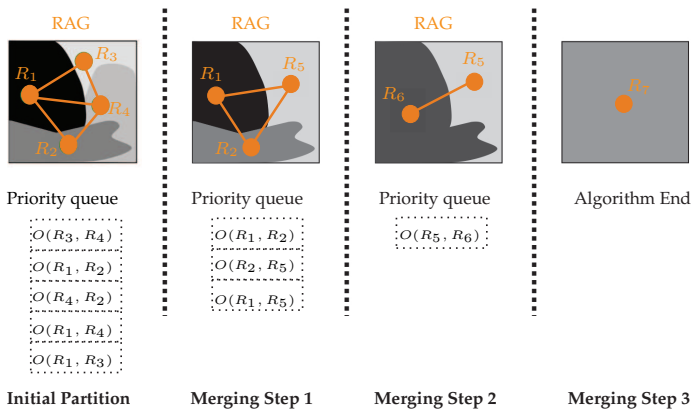

Figure 3.2: Region merging algorithm

At this point, the iterative merging process is going on with

i=0;
while i=0<Np-1 **do**
  Look for the most similar $O(R_i, R_j)$ contained in the first position of the queue
  Merge the region R_i and R_j associated to this criterion and create a new node containing the union of the regions R_{ij}.
  Update the RAG by : 1) removing the edge associated to R_i and R_j and 2) creating the new edges associated to R_{ij}.
  Update the queue list by introducing the $O(R_{ij}, R_k)$ between R_{ij} and the k old neighboring regions of R_i and R_j.
  i=i+1;

8: **end while**

Hence, the challenge related to the construction of BPT are the definition of a *region model* and the definition of a *merging criterion* for hyperspectral data. For these images, the *region model* M_{R_i} represents the set of spectra contained in region R_i, whereas the *merging criterion* $O(R_i, R_j)$ is a similarity measure between two spectrum data sets.
In the following sections, different region models and similarity metrics to construct a robust hyperspectral BPT are studied. The study can be broadly split into two important categories depending on the type of region models. The first investigated region model assumes that all pixels belonging to one region have approximately the same spectrum. This classical approach leads to the classical first-order parametric model which is used in all the region merging techniques presented in Chapter 2. The second studied region model removes the homogeneity assumption on the region. To this end, this second model relies on a non parametric statistical characterization of the region. Fig.3.3 summarizes the merging orders studied in the following sections in relations with these different region models. As shown in this figure, according to the different region models, different merging criteria have been studied.

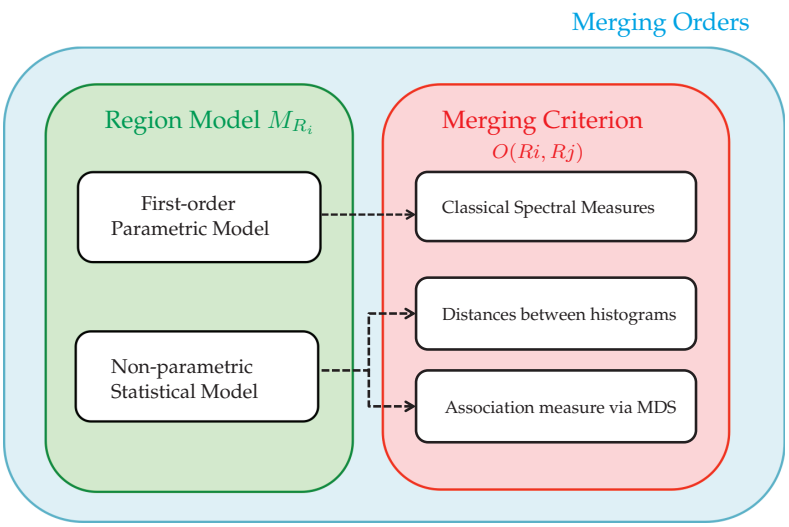

Figure 3.3: Studied hyperspectral region models and merging orders

Hence, Section 3.2 and Section 3.3 are devoted to describe in details the region models and the merging criteria illustrated in Fig.3.3, respectively.

3.2 Region Model

In hyperspectral image analysis, an image region R is defined as a set of connected N_{R_p} pixels, corresonding to spectra. In this spectrum data set $R = \{\mathbf{I}_\lambda(p_1), \mathbf{I}_\lambda(p_2), ...\mathbf{I}_\lambda(p_{N_{R_p}})\}$, each pixel is described by p_j and a spectrum $\mathbf{I}_\lambda(p_j)$ formed by N_z radiance values. The model of a region M_R is an approximate description of the N_R spectra describing the relevant information about region R.

Region modeling for hyperspectral data is challenging because the goal is to make full use of the greater discrimination provided by the high spectral resolution. The main issue is the variations of the spectral reflectance curve, within the spectra forming a region of the same class material. The spatial and spectral patterns are characteristic of the material itself, and they introduce a degree of uncertainty arising from inhomogeneities and natural variations within the material. For example, if the goal is to model a large vegetation region formed by healthy and stressed grass. In this case, all the spectra forming the region may be in fact almost identical, however, this region will not have an unimodal behavior.

Past hyperspectral works focusing on spectral classification and hierarchical segmentation have presented different strategies to model a set of spectra [19] [22][9]. Although these classification and segmentation algorithms have tried to model spectral data sets, there is an important difference between them. In hierarchical segmentation methods, each modeled spectrum data set forms a region, i.e. the spectra are connected in the spatial domain. Contrarily, in the case of spectral classification techniques, spectrum data sets are sets of unconnected spectra. Therefore, in this last case, spectrum data sets are only groups of spectra having "similar behaviors" in the spectral domain.

In the case of hierarchical segmentations [82] [117] [22], the most popular solution to describe a set of spectra is the first-order parametric model, that is the mean spectrum. As detailed in the following, the key of this model's popularity is its simplicity which allows to define merging orders in a simple way. However, this model can have an important drawback because it assumes spatial homogeneity inside the region. In order to solve this problem, parametric models for hyperspectral data have also been studied for some approaches [81]. In this case, the strategy is to model regions by a gaussian probability density function by estimating its mean and covariance matrix. This model presents two important drawbacks: 1) the estimation of the covariance matrix is not easy, in particular for small regions and 2) this model, as in the case of first order model, is also unimodal.

The unimodality problem has been addressed in several classification (also clustering) techniques. The most well-known solution consists in modeling a spectrum data set assuming that spectra belonging to the same group (cluster) are drawn from a multivariate Gaussian probability distribution. Thus, a group of spectra can be statistically modeled by a parametric probability density function completely specified by parameters as multivariate means and covariance matrices. Note that these models are obtained through a training phase, therefore, the performances of this modeling approach largely rely on the number of training samples for each class. This implies

that a large number of training samples is required for each image in order to obtain a reliable estimation.
For all these last drawbacks, besides the first-order parametric model, a non parametric statistical region model is also studied in the following sections. This non parametric statistical region model is proposed in order to avoid making any assumption as homogeneity or gaussian probability distribution inside the regions.

3.2.1 First-order parametric model

Given a hyperspectral region R formed by N_{R_p} spectra containing N_z different radiance values, the first-order parametric model M_R is defined as a vector with N_z components which corresponds to the average of the values of all spectra $p \in R$ in each band λ_i.

$$M_R(\lambda_i) = \bar{I}^R_{\lambda_i} = \frac{1}{N_{R_p}} \sum_{j \leq N_{R_p}} I_{\lambda_i}(p_j) \qquad i \in [1, ..., N_z] \tag{3.1}$$

Fig. 3.4 shows how this region model is interpreted. The grid on the left represents the set of spectra of R. In this grid, the horizontal dimension corresponds to the labels assigned to the pixels of the spatial space whereas the vertical dimension corresponds to the spectral domain for each spectrum. Hence, each cell of the grid $I_{\lambda_i}(p_j)$ represents the radiance value in the wavenlength λ_i of the pixel whose spatial coordinates are p_j. In this same figure, the green square on the right illustrates the model M_R corresponding to the vector $\bar{\mathbf{I}}^R_\lambda$ which contains in each position $\bar{I}^R_{\lambda_i}$ the mean radiance values for each wavelength on the region.

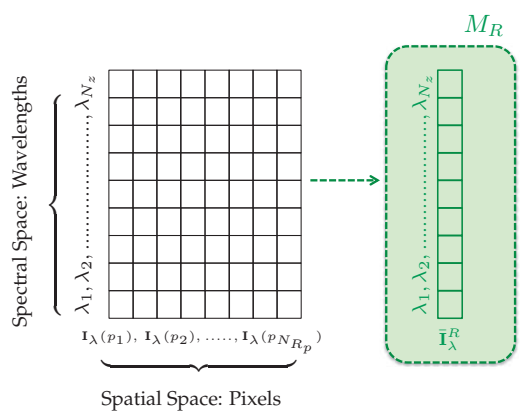

Figure 3.4: First-order parametric model

As explained at the beginning of this chapter, the simplicity of this M_R leads to simple merging orders. This is possible because the resulting M_R is also a spectrum. Consequently, classical spectral similarity measures taking into account the overall shape of the reflectance curves can be used as $O(R_i, R_j)$ [16].
On the other hand, the simplicity of the model can have some drawbacks since this model offers

a rather poor representation of the region. An example of limitation can be observed in Fig.3.5 where two different regions R_1 and R_2 form a gray scale image. In this case, M_{R_1} and M_{R_2} are the same for both regions, however, it can be noted that they are quite different. Comparing the obtained region models describing the regions of Fig.3.5, the problem is found in the region model assigned to R_1. This is because the first-order parametric model has assumed the homogeneity of the values inside the region. To address this issue, a higher order region model is proposed in the following to characterize complex regions with high intra-variability.

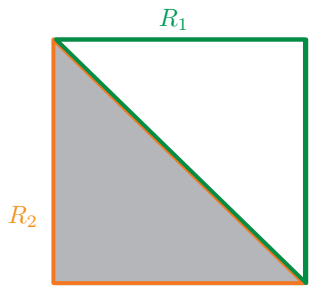

Figure 3.5: Illustrative limitation of the first order model

3.2.2 Non parametric statistical Region Model

In the context of BPT, non parametric statistical region model has been recently proposed by [17] to represent image regions in the case of gray scale or RGB images. This region model is directly estimated from the pixels of the region where neither color nor texture homogeneity are assumed. To formally tackle this idea, this M_R supposes that a region formed by a set of connected pixels is a realization of statistical variables which can be characterized by the corresponding discrete estimated probability distribution. In fact, considering region pixels as a set of independent samples, their common statistical distribution can be directly estimated. Therefore, the region model is the probability density function representing the pixels of the region. In other words, this region model corresponds to the normalized histogram of the pixel values belonging to each region.
In the case of a hyperspectral image region defined in a band λ_j, the studied variables correspond to the spectral radiance values contained in the region in the band λ_j. An optimal solution will involve to define a region model corresponding to the full multidimensional histogram. In this case, the model would have captured the full correlation between bands. However, this histogram is difficult to handle. Consequently, the region model is then represented by a set of N_z non parametric probability density functions (pdfs), one for each band $H_R^{\lambda_j}$, with no assumptions about the nature of the regions nor the shape of the pdfs. Note that although some of the correlation information is lost, this model is a trade-off between complexity and accuracy.

$$M_R = \{H_R^{\lambda_1}, H_R^{\lambda_2}, ..., H_R^{\lambda_{N_z}}\} \tag{3.2}$$

Fig.3.6 shows the non parametric statistical model interpretation. It is observed how M_R is

a matrix where each cell represents the probability of the region pixels to have a radiance value a_s in a specific band λ_k. The region model is then formed by the set of the rows $H_R^{\lambda_k}$, each one corresponding to the empirical spatial distribution (histogram) of the region R in the band λ_k. As Fig.3.6 shows each $H_R^{\lambda_k}$ is coded by N_{Bins} bins.

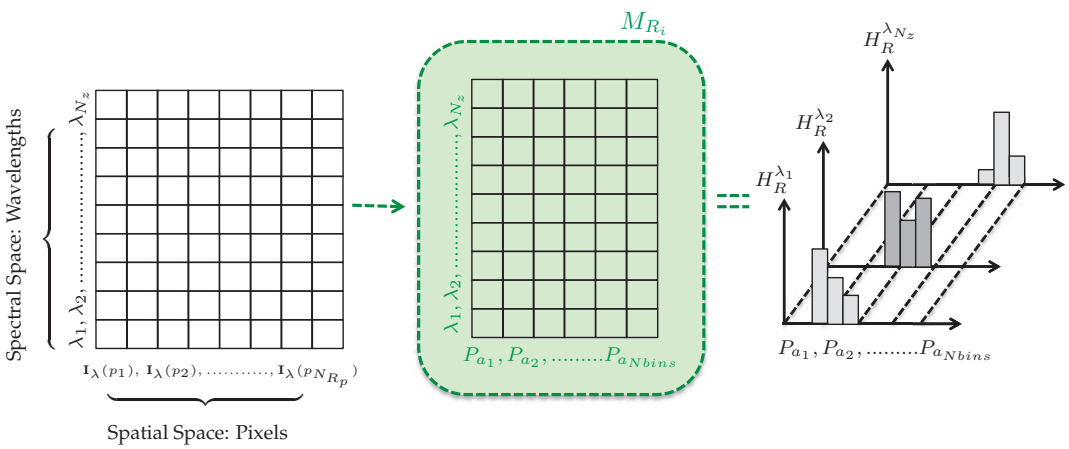

Figure 3.6: Non parametric statistical model

As explained before, the BPT construction is performed by using the pixel-based representation of the image as the initial partition. As a result, the BPT leaves are regions formed by individual pixels. Therefore, in this case, the histogram of each band λ_i is an unit impulse, as only one instance of pixel is available, defined as:

$$H_R^{\lambda_i}(P_{a_k}) = \begin{cases} 1 & a_k = I_{\lambda_i}(p) \\ 0 & otherwise \end{cases} \tag{3.3}$$

Note that in the BPT leave case, only one sample is used to estimate the pdf of the region. Therefore, in order to improve the quality of this estimation, the pdf of individual pixels $\mathbf{I}_\lambda(p)$ can be more precisely estimated by exploiting the self-similarity present in the image [24][61]. The key assumption behind the pixel pdf estimation consists in considering that the image is locally a general stationary random process and that it is possible to find many similar patches in an image. For instance, Fig.3.7 shows an example where three different patches appear several times in this image. This image is formed by the combination of three different hyperspectral bands corresponding to a portion of the ROSIS Pavia Universtiy data set described in Sec.3.4.2. The yellow and red patches correspond to reasonably homogeneous building and vegetation regions, respectively. Contrarily, blue patches represent border regions containing a building part and also a shadow area. The patch is defined as a 2D square of size $(2Wx - 1) \times (2Wy - 1)$ where each pixel has a vector value.

The idea consists in assuming that the probability distribution of $\mathbf{I}_\lambda(p)$ depends only on the values of the pixels in $P(p)$ and that it is independent of the rest of the image (Markovian model).

Figure 3.7: Patches redundancy

Hence, the probability distribution H_R^λ of each individual pixel p given its neighborhood $P(p)$, can be estimated by looking for the similar patches centered at different p_y pixels. Ideally, if two patches $P(p)$ and $P(p_y)$ are similar, their central pixel should be the same. To search for similar patches, a window space Ω_p centered at p is defined. An illustration can be seen in Fig.3.8 where the aim is to estimate the probability distribution of the orange pixel p. This size of the patch is in this example 3×3.The search window is represented in green and the green pixel indicates a pixel under consideration to estimate the pdf of p. The pdf estimation of pixel p is based on computing weights $w(p, p_y)$ to measure if there exist any $P(p_y)$ similar to $P(p)$ on Ω.

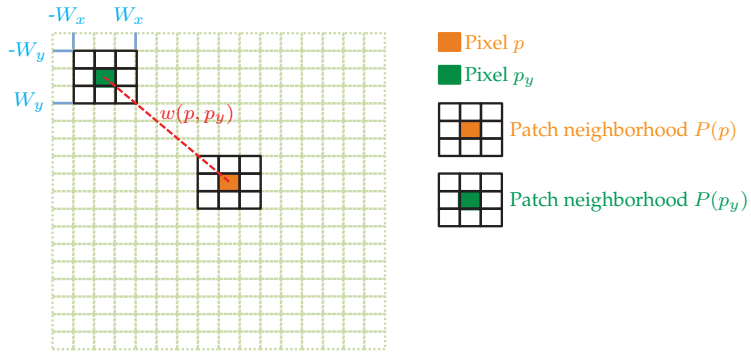

Figure 3.8: Two-dimensional illustration of the pixel probability distribution estimation. The probability of pixel value p is formed by the contributions to the histogram which depend on some weights. The weight $w(p, p_j)$ is based on the similarity of the intensities in square neighborhoods $P(p)$ and $P(p_j)$ around p and p_j.

This window Ω, such as presented in Fig.3.8, is used to look for all the $P(p_y)$ which are similar to $P(p)$. Thus, this similarity is interpreted as a weight $w(p, p_y)$ which is considered as an additive contribution to the probability of the pixel p of having the value of $\mathbf{I}_\lambda(p_y)$. Computing all $w(p, p_y)$ associated to the pixel p for all the possible pixels p_y in the search window, the function $w(p, p_y)$ can be used to estimate the probability density function for the individual pixel p. As mentioned before, this is done by considering that each $w(p, p_y)$ is an additive contribution to the probability of having the value p_y in the pdf of pixel p. Algorithm.1 summarizes the pdf estimation procedure

for pixel p. Note that with pixel p_y having the the value a_k in λ_i, the contribution $w(p, p_y)$ to the histogram of p is affected on the bin related to a_k.

Algorithm 1 Algorithm of the pdf estimation for pixel p

```
for each pixel p_y in the search window Ω do
  Compute w(p, p_y)
  for i=0 until i< N_z do
    a_k = I_{λ_i}(p_y)
    H_R^{λ_i}(P_{a_k})+=w(p, p_y)
  end for
end for
```

The computation of the weight $w(p, p_y)$ associated to all the pixels p_y in Ω in the hyperspectral context is proposed in this work as:

$$w(p, p_y) = \frac{1}{Z(p)(1 + d_{win}(p, p_y))} e^{-\sum_{t=1}^{N_z} \frac{d(P_{\lambda_t}(p), P_{\lambda_t}(p_y))}{h^2_{\lambda_t}}} \tag{3.4}$$

where $P(p_y)$ is one possible similar patch centered in p_y in the search window Ω_p and $d_{win}(p, p_y)$ is the local displacement between p and p_y in the search window. The $Z(p)$ is the normalizing factor to assure $\sum_{\forall p_y \in \Omega} w(p, p_y) = 1$. It is given by:

$$Z(p) = \sum_{\forall p_y \in \Omega} \frac{1}{(1 + d_{win}(p, p_y))} e^{-\sum_{t=1}^{N_z} \frac{d(P_{\lambda_t}(p), P_{\lambda_t}(p_y))}{h^2_{\lambda_t}}} \tag{3.5}$$

Concernig the similarity between the pixel values of a patch centered at p and a patch centered at p_y, it is computed by using the following expression:

$$d(P_{\lambda_t}(p), P_{\lambda_t}(p_y)) = \sum_{b_y=-W_y}^{W_y} \sum_{b_x=-W_x}^{W_x} \frac{((I_{\lambda_t}(p + b_x + b_y) - I_{\lambda_t}((p_y + b_x + b_y))^2}{(2 * d_p + 1)^2} \tag{3.6}$$

where $d_p = \sqrt{b_x^2 + b_y^2}$ is the local displacement on the patch regarding the central pixel.
The smoothing parameter h_{λ_t}, which stands for the typical distance between similar patches, controls for each λ_t the decay of the function w. This parameter h_{λ_t} depends on the standard deviation $\sigma_N^{\lambda_t}$ of the noise of the image band I_{λ_t}.
The standard deviation for each hyperspectral band can be automatically estimated by calculating the pseudo-residuals $\epsilon_p^{\lambda_t}$ of each pixel p as described in [23]. The pseudo-residual can be estimated as described by Fig.3.9.

Finally, the noise variance of the entire band is estimated by averaging the pseudo-residuals as described by Eq.3.7.

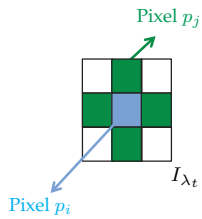

$$\epsilon_{p_i}^{\lambda_t} = \sqrt{\tfrac{4}{5}}(I_{\lambda_t}(p_i) - \tfrac{1}{4}\sum_{p_j \in F} I_{\lambda_t}(p_j))$$

Figure 3.9: Pseudo-residual $\epsilon_{p_i}^{\lambda_t}$ for the pixel p_i by using a four-neighborhood F

$$(\sigma_N^{\lambda_t})^2 = \frac{1}{N_p}\sum_{i=1}^{N_p}(\epsilon_{p_i}^{\lambda_t})^2 \tag{3.7}$$

The patch size $(2Wx-1)\times(2Wy-1)$ should a *priori* be related to the scale of objects in the image. The size of the search window Ω, which has a dramatic impact on the computation time, has also an influence on the visual quality of the results.

In the following, three different examples of the pdf estimation from three individual pixels is shown. The three pixel examples are obtained from the ROSIS Pavia University data set and their search window spaces $\Omega_{p_1}, \Omega_{p_2}$ and Ω_{p_3} are shown in Fig.3.10, respectively. The studied pixels p_1, p_2 and p_3 highlighted in red are centered at the position $(0,0)$ of their respective search windows. Note that the corresponding 2-dimensional search windows shown in Fig.3.10(a)(b)(c) only correspond to the projection of each Ω on the image band $I_{\lambda_{80}}$.

The first pixel p_1 belongs to a homogeneous round building, see Fig.3.10(a). Contrarily, p_2 of Fig.3.10(b) is a pixel situated at the transition between two different regions: a building and a shadow area. Pixel p_3 belongs to a meadow region of the complete image and it is shown in Fig.3.10(c). For these three pixels $\{p_1, p_2, p_3\}$ their corresponding values $\{I_{\lambda_{80}}(p_1), I_{\lambda_{80}}(p_2), I_{\lambda_{80}}(p_3)\}$ on the band λ_{80} of Fig.3.10 are $\{50, 38, 82\}$.

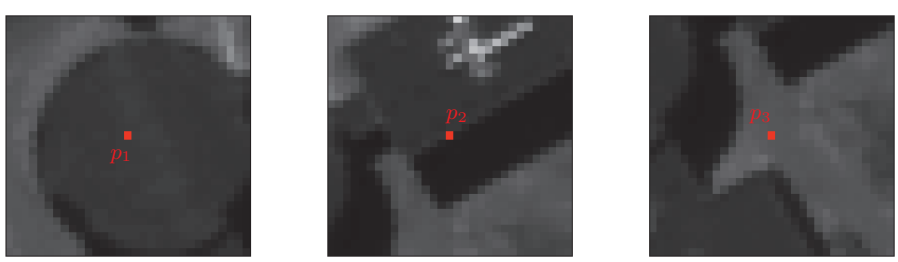

(a) Ω_1 (b) Ω_2 (c) Ω_3

Figure 3.10: Search windows Ω_{p_1}, Ω_{p_2} and Ω_{p_3} in $I_{\lambda_{80}}$

For these examples, the search window has a size of 20×20 and the smoothing parameter h_{λ_t} has been set equal to $h^2_{\lambda_{50}} \approx 10(\sigma_N^{\lambda_t})^2$ (See Eq.3.7). The estimation $\sigma_N^{\lambda_t}$ is performed by com-

puting the pseudo-residuals as described in Fig.3.9. The estimation of $(\sigma_N^{\lambda_t})^2$ for all the different hyperspectral bands of Rosis Pavia University (where N_z=103) is shown in Fig.3.11.

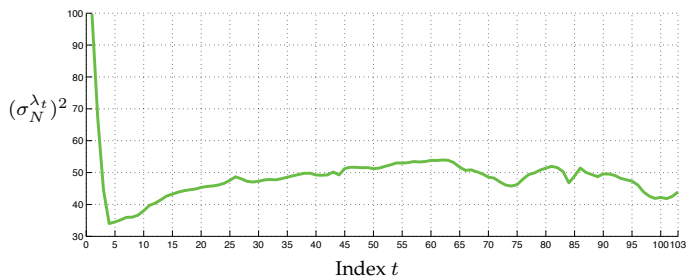

Figure 3.11: $(\sigma_N^{\lambda_t})^2$ according to the different $N_z = 103$ bands

The vertical axis of Fig.3.11 can be interpreted as the estimation of the noise standard deviation. This can be corroborated by observing the results of two different hyperspectral bands such as, for example, λ_1 and λ_{50}. Looking at the noise estimation for these two wavelengths in Fig.3.11, it can be observed that the noise in I_{λ_1} is much higher than in $I_{\lambda_{50}}$. As a result, the h value $h^2_{\lambda_1} = 99,78$ is higher than $h^2_{\lambda_{50}} = 51,2$. To verify the obtained results, Fig.3.12 shows these two corresponding hyperspectral bands I_{λ_1} and $I_{\lambda_{50}}$. Fig.3.12 corroborates that the presence of the noise is more important in I_{λ_1} than in $I_{\lambda_{50}}$.

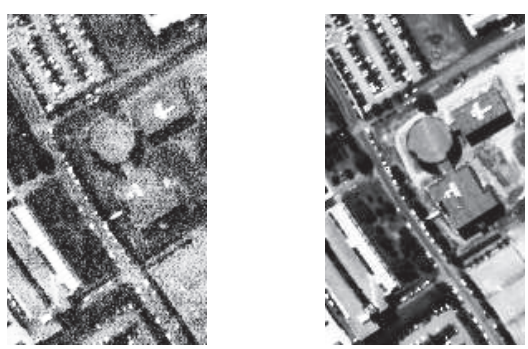

(a) I_{λ_1} (b) $I_{\lambda_{50}}$

Figure 3.12: Two different hyperspectral bands to verify noise estimation

At this point, the algorithm of Fig.1 is performed for the three pixels $\{p_1, p_2, p_3\}$ of Fig.3.10. For each pixel p, the first step consists in computing the weights $w(p, p_y)$ of Eq.3.4 for all the pixels p_y belonging to Ω_p. The weights obtained for the three different pixels are shown in Fig.3.13.

An important remark is that the weights shown in Fig.3.13 are independent of the all hyperspectral bands since Eq.3.6 has averaged the results for all bands. It means that the contribution $w(p, p_y)$ of pixel p_y to the probability distribution of pixel p is the same for all the λ_k.
Fig.3.13(a) shows how most of the pixels of Ω_{p_1} belonging to the homogeneous round object have high weight values. In the case of p_2, Fig.3.13(b) illustrates how the pixels of the Ω_{p_2} having

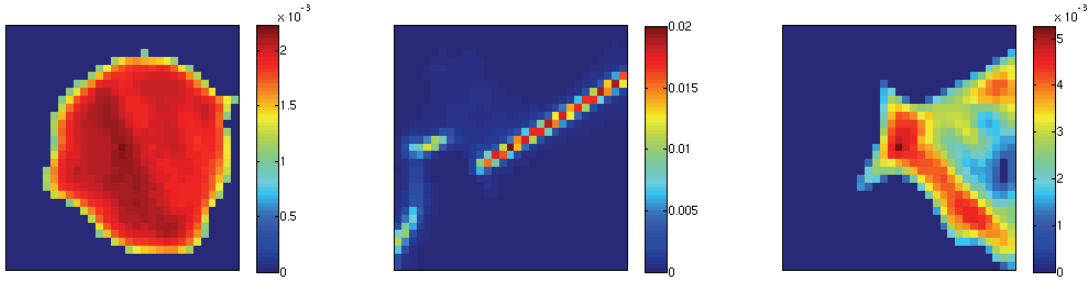

(a) $w(p_1, p_y)\ \forall\ p_y \in \Omega_{p_1}$ (b) $w(p_2, p_y)\ \forall\ p_y \in \Omega_{p_2}$ (c) $w(p_3, p_y)\ \forall\ p_y \in \Omega_{p_3}$

Figure 3.13: Weights associated to pixels p_1, p_2 and p_3

a weight contribution are only the pixels forming the border area. This point is important because it means that the initial distributions of the object border pixels are going to be the same. Concerning the last pixel p_3, an important number of weights appears with different intensities in Fig.3.13(c). Looking at Fig.3.10(c), these differences cannot be completely understood since p_3 seems to appear in a large quite homogeneous area on the right. The problem here is that the weights shown in Fig.3.13(c) are obtained according to all the hyperspectral bands, whereas Fig.3.10(c) is only the projection of the Ω_{p_3} on the image $I_{\lambda_{80}}$. Therefore, the weight intensities differences in all the right area of Fig.3.13(c) can be understood by looking at other bands such as the bands shown in Fig.3.14. In this figure, it can be seen that some differences appears in another λ of the hyperspectral image.

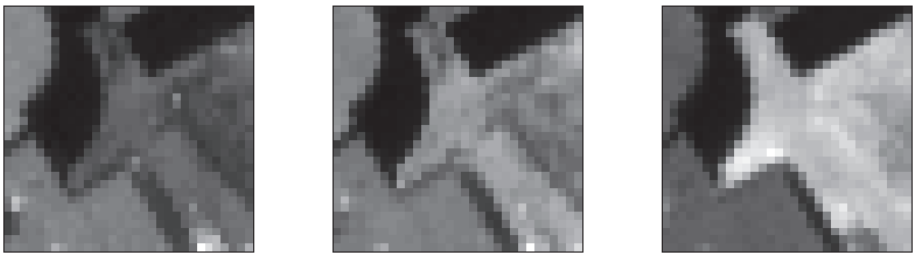

(a) $I_{\lambda_{20}}$ (b) $I_{\lambda_{50}}$ (c) $I_{\lambda_{100}}$

Figure 3.14: Ω_{p_3} projection on some hyperspectral bands

Going on with the algorithm of Fig.1, the obtained weights of Fig.3.13 are used to estimate the probability distributions of the three pixels p_1, p_2 and p_3. In this case, the $H_{p_1}^{\lambda_{80}}$,$H_{p_2}^{\lambda_{80}}$ and $H_{p_3}^{\lambda_{80}}$ are estimated only in hyperspectral band $I_{\lambda_{80}}$ by using the weights of Fig.3.15. These distributions are obtained by adding the weights of Fig.3.13 to the bins associated to the gray levels values of Fig.3.10.

Fig.3.15(a) shows the probability of the pixel p_1 belonging to the homogeneous area. It can be observed that $H_{p_1}^{\lambda_{80}}$ is quite narrow which can be explained by the homogeneity of the round object. Regarding Fig.3.15 (b), the shape of the distribution looks similar to the sum of two gaussian

distributions centered around two values. This can be interpreted by the border position of this pixel p_2 situated between two different regions. For the last distribution $H_{p_3}^{\lambda_{80}}$, a *maximum* of probability is observed around the value 80. Note that this is explained because the value of p_3 in $I_{\lambda_{80}}$ is equal to 82.

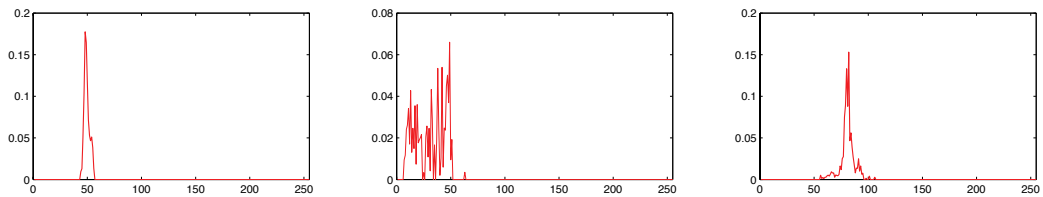

(a) $H_{p_1}^{\lambda_{80}}$ (b) $H_{p_2}^{\lambda_{80}}$ (c) $H_{p_3}^{\lambda_{80}}$

Figure 3.15: Probability distributions associated to weights of Fig.3.13 in $I_{\lambda_{80}}$

At this point, two different region models have been presented for modeling a hyperspectral region in this section. Thus, different merging criteria are going to be studied in the following according to these models.

3.3 Merging Criterion

In a general region merging algorithm, the merging criterion $O(R_i, R_j)$ corresponds to the similarity measure defining the order in which regions are going to merge, i.e. the merging order. In the case of BPT construction, the merging criterion computes the similarity between two neighboring regions R_i and R_j.
Theoretically, $O(R_i, R_j)$ is computed on the two models M_{R_i} and M_{R_j}. For this reason, the merging criterion strongly depends on the choice of the region model. In this study, two different region models have been introduced in Section 3.2. Consequently, different merging criteria according to these region models are studied here.
Working in a hyperspectral image context, the merging criterion is thus concentrated on the spectral characteristics of the regions. The interest of the spectral information is its tremendous capability to discriminate between different materials at very detailed level. The N_z hyperspectral image bands enable to partition the image into regions which would not be possible to find in a classical gray or RGB image. The importance of the spectral information is shown in Fig.3.16, where two different hyperspectral bands from Pavia Center data set are shown. This figure is used in order to corroborate how different bands lead to different important discriminative information. To this end, two different zones of the image : $Zone\ 1$ and $Zone\ 2$ are analyzed.

(a) $I_{\lambda_{20}}$ (c) $I_{\lambda_{100}}$

Figure 3.16: Importance of the spectral information

The $Zone\ 1$ of the image pointed by the green arrow corresponds to a vegetation area that is quite textured. Comparing the gray level values of the $Zone\ 1$ in Fig.3.16(a) with their values on Fig.3.16(b) some differences can be noted. In the case of Fig.3.16(a), the vegetation area has a low gray level value according to the low reflectance value of vegetation at λ_{20}. This is because $I_{\lambda_{20}}$ illustrates the radiance values at λ_{20} which belongs to the visible range of the electromagnetic spectrum (from 0.4 to 0.7 μm). Thus, at the visible range, it is known that the pigment in plant leaves, chlorophyll, strongly absorbs the light for use in photosynthesis. This explains then the low gray level values of $Zone\ 1$ in Fig.3.16(a).
Looking this $Zone\ 1$ containing the same vegetation area in Fig.3.16(b), the radiance has increased (light gray levels). The gray level increase of the vegetation zone here is because λ_{100} belongs to the range of the near-infrared wavelengths (from 0.7 to 1.1 μm). Therefore, the cell structure of the leaves at the near infrared, strongly reflects near-infrared light.

Another remark comparing $Zone\ 1$ in both images of Fig.3.16, concerns in the small dark regions appearing at the borders of the vegetation area in $I_{\lambda_{100}}$. Observing in detail Fig.3.16(a), it can be corroborated that these small dark regions cannot be found looking at $I_{\lambda_{20}}$ whereas $I_{\lambda_{100}}$ permits their discrimination.

The second important difference comparing both images of Fig.3.16 can also be found at the $Zone$ 2 pointed by the orange arrow. This image region has an enormous difference in its gray level values for this pair of images. In Fig.3.16(a), this region appears strongly contrasted with background formed by the terrain and matched with the dark building structure. In contrast, in Fig.3.16(b), it is observed how the same $Zone\ 2$ can be considered hidden on the background and separated from the building structure. Thus, using the spectral information contained in both images, it can be seen that $Zone\ 2$ does not belong to the building nor to the image background. Consequently, in order to extract the $Zone\ 2$ from this hyperspectral image, the spectral information contained in all the different bands should be taken into account.

This last example shows how the introduction of the spectral information into the merging criterion can be the key to decide if two hyperspectral regions are similar or not. However, the definition of a merging criterion including all the spectral information is not straightforward. The first difficulty of defining a spectral similarity measure is the strong spectral correlation throughout almost all the bands. This correlation is explained by the narrow difference between two consecutive wavelengths in which hyperspectral image bands have been captured. Consequently , the spectral information difference between two adjacent hyperspectral bands is very small. Visually, it implies that the grayscale values of two consecutive hyperspectral bands appear nearly identical. One of the main issues of the band correlations is that the spectral discrimination between materials can only be found in some bands. Hence, much of the hyperspectral data in a scene would seem to be superfluous.

An example is shown in Fig.3.17 where three different pixel spectra $\mathbf{I}_{\lambda_t}(p_1)$, $\mathbf{I}_{\lambda_t}(p_2)$ and $\mathbf{I}_{\lambda_t}(p_3)$ are plotted. In this example, $\mathbf{I}_{\lambda_t}(p_1)$ and $\mathbf{I}_{\lambda_t}(p_3)$ are two spectra belonging to the same material whereas $\mathbf{I}_{\lambda_t}(p_2)$ belongs to a different one. The spectral differences between $\mathbf{I}_{\lambda_t}(p_1)$ and $\mathbf{I}_{\lambda_t}(p_2)$ are small and approximately constant along all the wavelengths. Contrarily, in the case of $\mathbf{I}_{\lambda_t}(p_3)$, this spectrum can be only discriminated from the other two spectra, $\mathbf{I}_{\lambda_t}(p_1)$ and $\mathbf{I}_{\lambda_t}(p_2)$, in the spectral domain ranging from λ_{61} to λ_{85}. Note that if this range is small, a similarity measure evaluating separately the local spectral differences at the bands can have some problems in order to discriminate $\mathbf{I}_{\lambda_t}(p_3)$. This problem occurs because it can not be assumed that the sum of the local differences between $\mathbf{I}_{\lambda_t}(p_1)$ and $\mathbf{I}_{\lambda_t}(p_2)$ is smaller than the sum of the local differences between $\mathbf{I}_{\lambda_t}(p_2)$ and $\mathbf{I}_{\lambda_t}(p_3)$. For this reason, some classical similarity measures between spectra have taken into account the overall shape of spectra as the key of their discrimination. Following this approach, it can be seen how the discrimination between $\mathbf{I}_{\lambda_t}(p_2)$ and $\mathbf{I}_{\lambda_t}(p_3)$ may be more successful if spectral shapes is considered.

Besides the correlation, the illumination variations of the image scene introduce another important issue, which should be taken into account to define a spectra similarity measure. The lack of illumination, such as for instance in the shadow areas of the image, causes lower radiance values

which implies dark regions of the image. Consequently, two pixels of the same object having different illuminations appear in the image having different gray level values intensities.

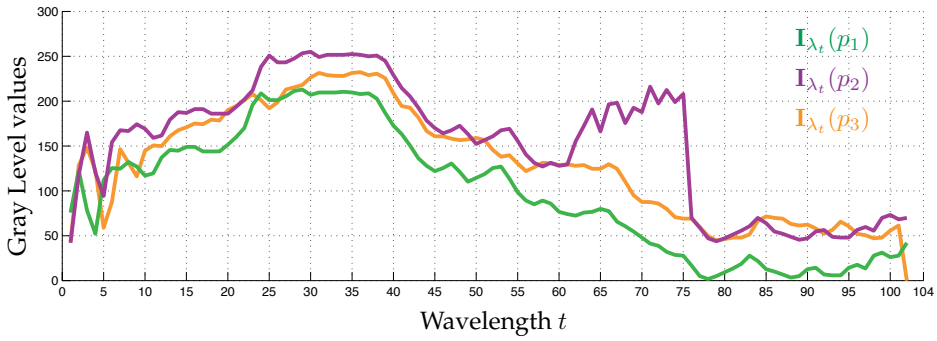

Figure 3.17: Three Spectral Signatures

The effects of the illumination variations can be observed in Fig.3.16 where the image illumination source comes from the north-west orientation. On the figure above, four aligned gable roof buildings are seen. Each of them is then formed by two sloping planes on each side of the roof ridge. According to the roof shape and the illumination of the image, each building of Fig.3.16 is divided into two regions depending whether pixels are in the shadow area or not.
With p_1 and p_2 two pixels coming from two different roof parts, their spectral signature $\mathbf{I}_{\lambda_t}(p_1)$ and $\mathbf{I}_{\lambda_t}(p_2)$ are shown in Fig.3.18. The vertical axis of this last figure shows the gray level values associated to the radiance values. In this example, $\mathbf{I}_{\lambda_t}(p_1)$ is the pixel situated in the shadow area. Comparing $\mathbf{I}_{\lambda_t}(p_1)$ with $\mathbf{I}_{\lambda_t}(p_2)$, it is observed that both pixels have the similar overall spectral curve shape, however, they appear shifted.

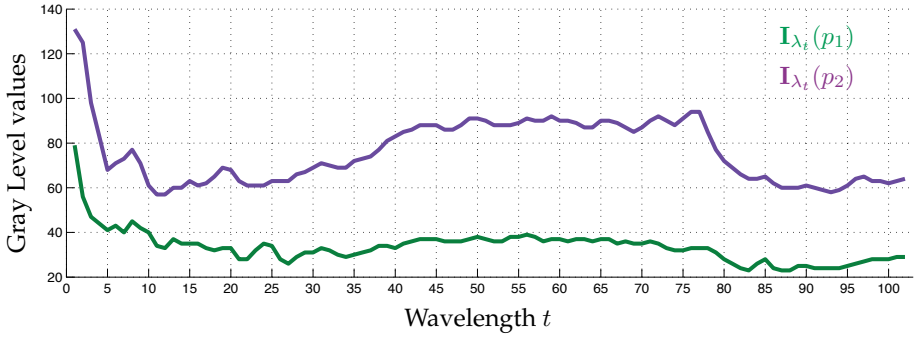

Figure 3.18: Shadow effect

From a first point of view, the shadow effect can be considered as a non-problem during the merging sequence construction. Pixels belonging to the shadow area of the roof will merge together forming an unique region whereas the other roof part will form another one. However, the roof is a single object of the image. Thus, an optimal region merging algorithm should obtain the entire roof in a single region in its last merging steps. Note that this goal can be achieved only if

the overall shape of the spectra of Fig.3.18 is taken into account in the merging criterion.
Until now, the spectral information issues regarding the definition of a similarity measure between two spectra have been detailed. Nevertheless, it should be remembered that our purpose is to define a similarity measure as merging criterion between two hyperspectral regions represented by their respective M_{R_i} and M_{R_j}. Therefore, being M_{R_j} a set of spectra, the merging criterion definition cannot always be considered as a single spectrum distance. For instance, the non parametric statistical region model represents a set of probability distributions instead of a single average spectrum, as it is done in the first-order parametric model. Hence, in order to define a general merging criterion between two hyperspectral regions, the spectral information characteristics summarized in the next three points must be taken into account.

- *A priori*, all the hyperspectral bands should be taken into account in order to measure the similarity between two hyperspectral regions.
- Since there is a high interband correlation, the discriminative spectral information cannot always be found in all the bands.
- The overall shape of the spectral information along the wavelengths is a robust descriptor of the material that it represents.

Taking into account these last three points, some different merging criteria are proposed according to the previous region models presented in Sec.3.2. The scheme illustrating all the studied merging criteria is shown in Fig.3.19. Two families of merging criteria are separately studied according to the green and purple rectangle separation. The first category corresponds to the merging criteria defined for the first order parametrical region model and which are based on classical spectral distances. Accordingly, the second category is composed of the merging criteria associated to the the non parametric statistical region model. In this second family, a sub-division between the presented merging criteria can be organized in two groups: Firstly, the similarity criteria based on distances between probability distributions which have been previously defined in the literature. Secondly, a new merging criterion is proposed in this PhD. It measures the similarity between regions taking into account the redundant hyperspectral information.
Fig.3.19 also shows that for some of the categories different similarity distances are studied. For instance, as classical spectral measures, the Spectral Angle Mapper and the Spectral Information Divergence are going to be studied for the first region model family. Concerning the category of distances between histograms, the Battacharyya distance and the diffusion distance are studied separately.
Sec.3.3.1 and Sec.3.3.2 describe the different merging criteria summarized in Fig.3.19.

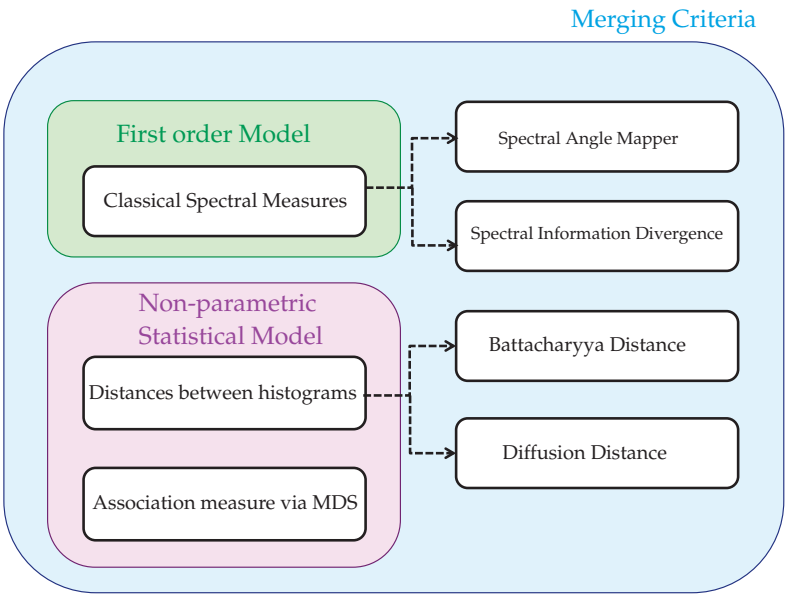

Figure 3.19: Studied merging criteria

3.3.1 Measures associated to the first-order parametric model

The merging criteria proposed here concern the first-order parametric model presented in Sec.3.3.1. It is based on the fact that the hyperspectral region has been represented by a single spectrum containing the average spectral values of each band. Consequently, classical spectral similarity measures previously introduced in the literature can be used as merging criterion.
The state of the art has defined two groups of spectral similarity measures: the *deterministic* and the *stochastic* measures. *Deterministic* measures are used to determine the geometric characteristics of spectra by either measuring the angle, or the Euclidean distance, or correlation between a set of spectra. Concerning the *stochastic* similarity measures, they evaluate statistical distributions of the spectral reflectance values. These last measures essentially define spectral variations by modeling spectral information as a probability distribution. Thus, in the *stochastic* case, the spectrum is considered by these measures as a random variable in the λ dimension.
Given the division between these two families of similarity measures between spectra, one distance of each family has been studied here as merging criterion. As a *deterministic* measure, Spectral Angle Mapper (SAM) has been chosen, whereas the Spectral Information Divergence (SID) has been selected for the *stochastic* family.

Spectral Angle Mapper

The Spectral Angle Mapper between SAM is defined as the existing angle between two spectra. This measure is based on the fact that two spectra from the same material have the same overall shape. Therefore, the smaller is the angle, the more similar the two spectra are.

Given two region models M_{R_i} and M_{R_j} representing two adjacent regions by their mean spectra $\bar{\mathbf{I}}^R_\lambda$ and $\bar{\mathbf{I}}^R_\lambda$, the use of SAM as merging criterion is given by

$$O_{SAM} = \underset{Ri,Rj}{\operatorname{argmin}} \quad \cos^{-1}\left(\frac{\sum_{z=1}^{N_z} \bar{I}^{R_i}_{\lambda_z} \bar{I}^{R_j}_{\lambda_z}}{\sqrt{\sum_{z=1}^{N_z} \bar{I}^{R_i}_{\lambda_z} \bar{I}^{R_i}_{\lambda_z} \sum_{z=1}^{N_z} \bar{I}^{R_j}_{\lambda_z} \bar{I}^{R_j}_{\lambda_z}}} \right) \tag{3.8}$$

Note that this spectral angle is relatively insensitive to changes in pixel illumination because increasing or decreasing illumination does not change the direction of the vector, only its magnitude (See Fig.3.18). This insensitivity to the illumination variations is also found in the Spectral Information Divergence which is studied as the second similarity measure.

Spectral Information Divergence

The Spectral Information Divergence computes the probabilistic discrepancy between two spectral signatures modeled by their corresponding probability distributions $P_{R_i}(\lambda)$ and $P_{R_j}(\lambda)$. The use of the SID as merging criterion then implies that the probability distribution $P_R(\lambda)$ associated to each M_R should be computed as a first step. To address the modelling of M_R as a random variable in the λ dimension, the spectrum normalization of Eq. 3.9 is applied at each λ_i

$$P_R(\lambda_i) = \bar{I}^R_{\lambda_i} \;/\; \sum_{t=1}^{N_z} \bar{I}^R_{\lambda_t} \tag{3.9}$$

where $\bar{I}^R_{\lambda_i}$ corresponds to the average of the values of all spectra $p \in R$ in each band λ_i.

The estimation of $P_{R_i}(\lambda)$ and $P_{R_j}(\lambda)$ enables the computation of a similarity measure between R_i and R_j by computing the Kullback Leibler divergence $D(R_i, R_j)$ between their probability distributions as follows:

$$D(R_i, R_j) = \sum_{k=1}^{N} P_{R_i(\lambda_k)} \log \frac{P_{R_i(\lambda_k)}}{P_{R_j(\lambda_k)}} \tag{3.10}$$

Note that this measure is not symmetric, therefore, the dual divergence must be computed in order to use $D(R_i, R_j)$ as merging criterion. Finally, the merging criterion by using the Spectral Information Divergence is given by

$$O_{SID} = \underset{Ri,Rj}{\operatorname{argmin}} \; \{ \; D(R_i, R_j) \; + \; D(R_j, R_i) \; \} \tag{3.11}$$

3.3.2 Measures associated to the non parametrical statistical region model

In the case of non parametrical statistical region model, a region is represented by a set of spatial histograms. Each histogram corresponds to the distribution of the radiance intensities at each wavelength. Given this region model, distances between histograms are studied here.
In image processing, it is well known that the design of a robust histogram distance is a challenging task because histograms are quite sensitive to changes such as the quantization effects. In the literature, two families of distances have been defined according to the type of bin correspondence: the classical *bin-to-bin* and the *cross-bin* distances. In the first group, distances just compare each bin in one histogram to the corresponding bin in the other. Some classical examples belonging to this category are the Minkowski distance (such as L1 and L2), the histogram intersection, the Kullback-Leibler metric, or the Bhattacharyya distance. The second family corresponds to the *cross-bin* distances allowing the cross-bin comparison. Consequently, this second family of distances is more robust to distortions. The Earth Mover's Distance (EMD)[60] and Diffusion distance [59] fall into this second category.
In this work, one distance of each family has been studied as merging criterion. Concerning the *bin-to-bin* distances, Battacharyya distance has been chosen to be studied. In the same context, this measure has been previously proposed and tested in [17] its effectiveness has been demonstrated compared to other distances such as the Kullback-Leibler metric. In the case of cross-bin distances, diffusion distance has been chosen due to its fast computation time compared to other measures.
These two classical distances are proposed in this section as merging criteria. Note that these distances are measured separately for each band. Accordingly, the correlation between the histograms in the spectral domain has not been taken into account by these distances. Hence, another merging criterion has been defined for the non parametrical statistical region model. The idea of this third merging criterion is to exploit the properties of the spectral information explained at the beginning of this section. To this end, it involves two steps for each pair of adjacent regions: 1) the extraction of the discriminative information contained in each region and 2) the definition of an association measure measuring the similarity between the information obtained in the first step. This last merging criterion has been called here as the association measure via Multidimensional Scaling (MDS). In the following, the three merging criterion are detailed.

Battacharyya Distance

The bin-to-bin Bhattacharyya distance between two statistical discrete distributions measures the amount of overlap between them. Given two adjacent regions R_i and R_j, modeled by their non parametrical statistical region models, the Battacharyya distance at band λ_k between the distributions $H_{R_i}^{\lambda_k}$ and $H_{R_j}^{\lambda_k}$. is defined by

$$BC(H_{R_i}^{\lambda_k}, H_{R_j}^{\lambda_k}) = -\log(\sum_{s=1}^{N_{Bins}} H_{R_i}^{\lambda_k}(a_s)^{\frac{1}{2}} H_{R_j}^{\lambda_k}(a_s)^{\frac{1}{2}}) \tag{3.12}$$

where N_{Bins} are the number of bins used to quantify the images intensities. Note that if $H_{R_i}^{\lambda_k}$ and $H_{R_j}^{\lambda_k}$ perfectly overlap, the Bhattacharyya distance is then 0. Eq-3.12 only defines the similarity between two regions in a specific hyperspectral image band.
In our case, M_{R_i} and M_{R_j} are formed by a set of N_z distributions. Therefore, the merging criterion O_{BAT} can be defined by using Eq-3.12 as the sum of the N_z dissimilarity measures obtained for the different bands:

$$O_{BAT} = \underset{R_i, R_j}{\operatorname{argmin}} \sum_{k=1}^{N} BC(H_{R_i}^{\lambda_k}, H_{R_j}^{\lambda_k}) \tag{3.13}$$

The Battacharyya distance described above assumes that the histograms are already aligned. Consequently, the merging criterion of Eq.3.13 is sensitive to distortions, and suffers from the quantization effect. Fig. 3.20 shows the problems associated to this effect. For a given spectral band λ_k, three different histograms concerning three different regions $H_{R_i}^{\lambda_k}$, $H_{R_j}^{\lambda_k}$ and $H_{R_p}^{\lambda_k}$ are shown. Looking at the three distributions, it can be observed that the red distribution of the region R_i is much closer to the green distribution than to the blue one. However, the Battacharyya distance between the $H_{R_i}^{\lambda_k}$ and the other two distributions is the same and is equal to zero. The problem is that no bin from $H_{R_j}^{\lambda_k}$ and $H_{R_p}^{\lambda_k}$ overlap the red histogram. Ideally, the similarity measure in this example should give a lower value between the red and the green than between the red and the blue.

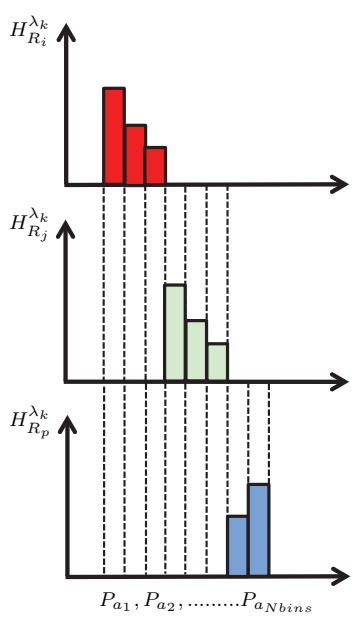

Figure 3.20: Illustration of the insensitivity of Battacharyya distance where distributions do not overlap. If the histograms do not overlap, they have the same zero distance

To address this weakness, the work in [18] has proposed a solution to avoid to estimate densi-

ties formed by too many bins with zero probability which, in practice, may decrease the value of the similarity measure between the densities. The solution consists in convolving the histograms by a triangular window. Note that this approach introduces some probability values that are not really existing in the region. Therefore, in order to solve this problem, the work presented here has proposed the use of a cross-bin measure between probability distributions as a solution. Thus, the diffusion distance is proposed as a cross-bin similarity measure [59] in the following. It defines a second merging criterion.

Diffusion Distance

The diffusion distance D_K is a cross-bin distance defined to measure the similarity between two discrete probability distributions, which cannot be overlapped. The main idea of this distance is to measure the difference between two histograms at various resolution scales through a diffusion process. Therefore, the goal is to measure at the different scales how the histogram are different. If the histograms are different, the difference between them will exist in several scales.
The diffusion process is computed by convolving the histogram difference $d_l(a_s)$ with a Gaussian filter $\phi_{\sigma_G(a_s)}$,where $a_s \in \mathbb{R}^m$ is a vector. Thus, each diffusion scale l is computed by a convolution task and a downsampling step as:

$$d_0(a_s) = H_{R_i}^{\lambda_k}(a_s) - H_{R_j}^{\lambda_k}(a_s) \tag{3.14}$$

$$d_l(a_s) = [d_{l-1}(a_s) * \phi_{\sigma_G(a_s)}] \downarrow_2 \quad l \in [1, ..., L] \tag{3.15}$$

The notation $\downarrow_2$ denotes downsampling by a factor of two. L is the number of pyramid layers and σ_G is the constant standard deviation for the Gaussian filter ϕ. From the Gaussian pyramid constructed by Eq.3.15, a distance D_K between the histograms can be computed summing up the L1 norms of the various levels:

$$D_K(H_{R_i}^{\lambda_k}, H_{R_j}^{\lambda_k}) = \sum_{l=0}^{L} \sum_{s=1}^{N_B} |d_l(a_s)| \tag{3.16}$$

Consequently, the proposed merging criterion using the diffusion distance defined in previous equations is derived as:

$$O_{DIF} = \underset{Ri,Rj}{\operatorname{argmin}} \sum_{k=1}^{N} D_K(H_{R_i}^{\lambda_k}, H_{R_j}^{\lambda_k}) \tag{3.17}$$

Before concluding on merging criteria using classical histogram distances, it should be remembered that hyperspectral bands are processed separately by the last two criteria: O_{BAT} and O_{DIF} . As a result, the correlation between bands is not taken into account in these merging criteria. Moreover, the overall spectral shape of the spectra is another unused information. Note that in order to include all of these notions, the non parametric statistical region model should be processed entirely. Ideally, this could be done if the region model was the full multidimensional

histogram. Unfortunately, the computational complexity of this histogram is not realistic for the huge hysperspectral data.

Taking this issue into account, a last merging criterion is proposed in Sec.3.3.3. This merging criterion exploits the inter-distances between the different probabilistic distributions contained in each individual region model. The goal is then to remove redundant information contained in each region model. Consequently, the hyperspectral band correlations and the sparsity problem are eliminated and then, a similarity measure jointly taking into account the overall shape of the spectral information can be defined. Besides, this last proposed measure based on distances between observations can be expressed in canonical correlations [33].

3.3.3 Similarity measure via Multidimensional Scaling

The merging criterion presented here for the non parametrical statistical region model is based on the distances between wavebands and canonical correlations [31]. The merging criterion is divided in two steps summarized in Fig.3.21.

The first step, pointed by the blue rectangle, corresponds to a local dimensionality reduction by analyzing the inter-waveband similarity relationships for each data set M_R. The purpose of this stage is to remove the redundant hyperspectral information via multidimensional metric scaling (MDS). As a result, the principal components of the regions containing the most relevant information are obtained.

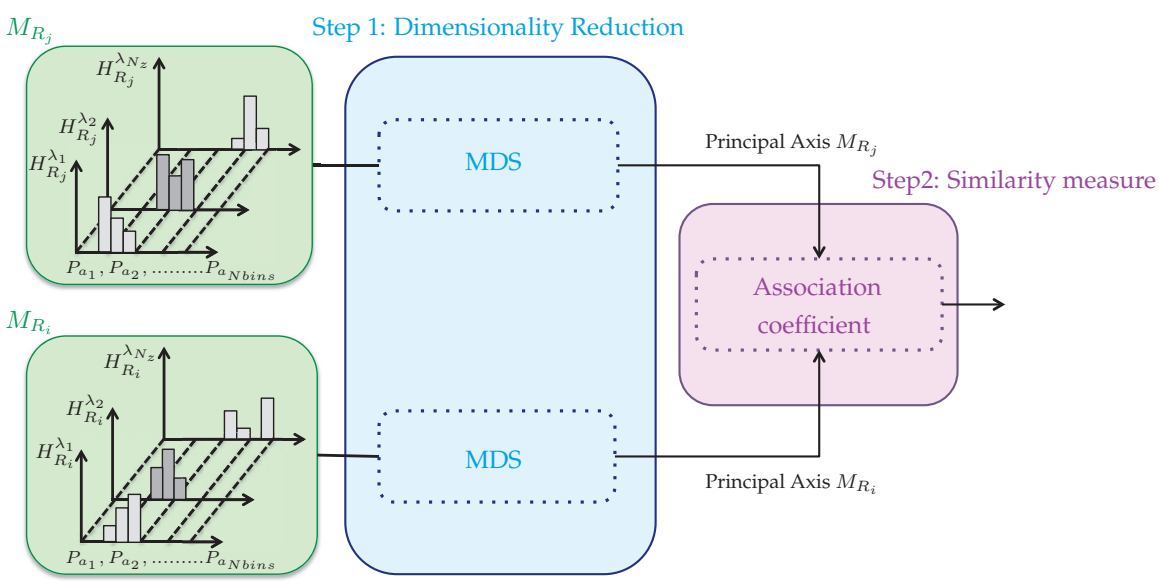

Figure 3.21: Methodology for similarity measure via Multidimensional Scaling

Afterwards, a similarity measure correlating the principal axis of both data sets obtained via multidimensional scaling is performed. This similarity measure, which is highlighted in purple in

Fig.3.21, relies on a statistical test based on the multivariate analysis of variance (MANOVA). The goal is to test whether there is a dependence (or correlation) between the principal components of the regions or not.

Step1: Dimensionality Reduction

Multidimensional scaling (MDS) [28] represents a set of objects as a set of points in a map of chosen dimensionality, based on their interpoint distances. The objective is to maximize the agreement between the displayed interpoint distances and the given ones. Thus, MDS attempts to locate N_o objects as points in an Euclidean space E where the geometric differences between pairs of points in E agree, as closely as possible, with the true differences between the N_o objects. In our case, the N_o objects correspond to the N_z probability distributions of each M_R. Hence, the probability distribution similarities (or dissimilarities) of M_R can be represented by a N_z x N_z distance matrix Δ_R= (δ_{kl}), where $\delta_{kl} = \delta_{lk} \geq$0 is the diffusion distance value computed by Eq. 3.16. Hence, being A the matrix with entries $A = -(\frac{1}{2})\delta_{kl}^2$ and the centering matrix $H = I_N - \frac{1}{N}11^t$, the so-called inner product matrix B_R associated to Δ_R can be computed by $B_R = HAH$ for each M_R [28]. B_R is also called Gower's centered matrix which is computed by centering the elements of A [32].
The inner product matrix B_R is an N_zxN_z symmetric matrix which can be spectrally decomposed as $B_R = U_R\Lambda_R^2U_R^t$. Assuming that the eigenvalues in Λ_R^2 are arranged in descending order, the matrix $U_R\Lambda_R$ and U_R contains the principal and the standard coordinates of region R, respectively.
As mentioned above, the aim of MDS is to represent M_R in a lower dimensional space, by taking the first D_s most representative principal or standard coordinates. Therefore, given two regions defined by M_{R_i} and M_{R_j}, this first step computes the first D_s standard coordinates of M_{R_i} and M_{R_j}. That is, two distance matrices Δ_{R_i} and Δ_{R_j} to find $B_{R_i} = U_{R_i}\Lambda_{R_i}^2U_{R_i}^t$ and $B_{R_j} = U_{R_j}\Lambda_{R_j}^2U_{R_j}^t$ are computed using the explained procedure.

Selection of the number of dimension D_s

The number of dimensions D_s is an important aspect in most multivariate analysis methods. Classically, the number of dimensions is based on the percentage of variability accounted for by the first dimensions. Therefore, a popular criterion consists in selecting the first eigenvectors corresponding to the highest eigenvalues. In this case, the D_s components represent the *maximum* possible proportion of the variance in D_s dimensions. Applying this strategy with N_z possible eigenvalues arranged in descending order, the dimension D_s is then given by Eq.3.18.

$$\frac{\sum_{t=1}^{D_s} \lambda_{tR}}{\sum_{t=1}^{N_z} \lambda_{tR}} \approx 1 \tag{3.18}$$

where $\lambda_{N_z R}$ and λ_{1R} correspond to the smallest and the highest eigenvalues, respectively. This criterion has been the only criterion used in hyperspectral methods performing dimensionality reduction techniques as PCA [10] [36] [116]. Note that PCA corresponds to the special case of multidimensional scaling metric when the euclidean distance is used as δ. For these works, the criterion according to Eq.3.18 has allowed to extract the first D_s uncorrelated components.
Unfortunately, this criterion can have some issues in our case. The problem is that the D_s principal coordinates representing two different regions can be correlated between themselves. For example, let us consider that D_s is equal to 5 for two neighboring regions which leads to the result of 5 different eigenvectors. If these 5 eigenvectors give different information, i.e. are uncorrelated, the choice of D_s is correct. However, if the first eigenvector of the first region is highly correlated with the fourth component of the second region, the choice of $D_s = 5$ is going to introduce a bias. Therefore, it may be better to choose $D_s = 3$ in this example.
Here, in order to solve the explained limitation, a criterion which extends a sequence c defined and studied in [33] is used to set the value of D_s. Firstly, a *maximum* dimension N_s suggested by the data should be fixed, which corresponds to the *minimum* dimension for which $\frac{\sum_{t=1}^{N_s} \lambda_{tR}^2}{\sum_{t=1}^{N_z} \lambda_{tR}^2} \approx 1$ (Such as 3.18). Then, with u_i and v_i, $i = 1, ..., N_s$, being the N_s first eigenvectors of U_{R_i} and U_{R_j}, a sequence C_k is defined as:

$$C_k = \frac{\sum_{t=1}^{k} \sum_{p=1}^{k} \lambda_{tR_i}^2 (u_t' v_p)^2 \lambda_{tR_j}^2}{\sum_{t=1}^{N_s} \sum_{p=1}^{N_s} \lambda_{tR_i}^2 (u_t' v_p)^2 \lambda_{tR_j}^2} \qquad k \in [1, ..., N_s] \tag{3.19}$$

where $\lambda_{tR_i}^2$ $\lambda_{tR_j}^2$ are the eigenvalues of B_{R_i} and B_{R_j} which are proportional to the variances of the corresponding principal axes. The term $(u_t' v_p)^2$ is the correlation coefficient between the t-th and the p-th eigenvectors. Thus, the numerator in c_k can be interepreted as a weighted average of the relationships between principal axes.
Clearly $0 \leq C_1 \leq, ... \leq C_{D_s} \leq, ... \leq C_{N_s} = 1$. Hence, the dimension D_s is then chosen such that C_{D_s} is high, for instance $C_{D_s} = 0.9$. In this way, D_s represents the number of uncorrelated eigenvectors representing the largest proportion of variance.

Step2: Similarity measure between M_{R_i} and M_{R_j} principal axis

The proposed similarity measure relies on measuring the correlation, also called dependency, between the principal coordinates representing two adjacent regions. This notion of multivariate dependence test can be easily explained by the next example.
Assume that a study wants to be conducted to evaluate the students' improvements in math and physics by trying different textbooks. In that case, improvements in math and physics are the two dependent variables, and the goal is to test the following hypothesis: Are both topics jointly affected by the difference in textbooks?
As a result, if the overall multivariate test is significant, it can be concluded that the respective effect (e.g., textbook) is significant. In our case, changing the textbooks and the improvements by two different hyperspectral regions, the purpose of the dependence test still remains the same.

Hence, the goal is to measure if a multivariate test between two regions defined by their principal coordinates ($U_{R_i}\Lambda_{R_i}$ and $U_{R_j}\Lambda_{R_j}$) will be significant or not.
It is done by interpreting the D_s columns of $U_{R_i}\Lambda_{R_i}$ and $U_{R_j}\Lambda_{R_j}$ as a predictor X and a response variable Y of a multivariate linear regression model, respectively. Regression analysis helps to analyze such situations by focusing on the change in a dependent variable associated with changes in two or more independent variables. The expression of this multivariate linear regression model is given by:

$$Y = X\beta + e \tag{3.20}$$

where β is the matrix of parameters containing the regression coefficients and e is the matrix of residual errors. Given Eq.3.20, the aim is to use this model to test if Y and X are correlated or, in other words, if Y is a linear combination of X. It is clearly seen that if there is no relationship between X and Y, the matrix β is equal to 0.
The goal is therefore to measure if a significant relationship between X and Y exists by testing the multivariate general linear hypothesis $\beta = 0$.
The proposed multivariate statistical test is based on the Multivariate analysis of the variance (MANOVA) theory. The MANOVA has been largely used to measure the interactions among dependent and independent multidimensional variables. The primary objective is to assess the significance of group differences. To estimate it, MANOVA studies the covariances of the variables as well as their individual variances by the sums of squares and cross-products matrices, which are the basis for these quantities.
The sums of squares and cross-products matrices evaluates how is the residual error $\hat{e} = (Y - X\hat{\beta})$ measuring the error of the prediction matrix $\hat{Y}$ according to Y. The prediction matrix $\hat{Y} = X\hat{\beta}$ is defined by the estimation of the regression coefficients $\hat{\beta}$. In the case of multivariate data, the simplest method to estimate the matrix $\hat{\beta}$ is the ordinary least-squares method which minimizes the sum of squares residuals $tr(\hat{e}'\hat{e}) = tr[(Y - X\hat{\beta})^t(Y - X\hat{\beta})]$ [30]. The least-squares solution for $\hat{\beta}$ estimation is given by $\hat{\beta} = (X^tX)^{-1}X^tY$. Accordingly, the prediction matrix is given by $\hat{Y} = X\hat{\beta} = PY$ where $P = X(X^tX)^{-1}X^t$ is the known hat matrix [34].
The regression equation allows to find the score of an outcome, and these scores are such that $Y = \hat{Y} + \hat{e}$, so the Total Sum of Square and Cross Product SSCP is given as:

$$\begin{aligned} Y^tY &= (\hat{Y} + \hat{e})^t(\hat{Y} + \hat{e}) \\ &= \hat{Y}^t\hat{Y} + \hat{Y}^t\hat{e} + \hat{e}^t\hat{Y} + \hat{e}^t\hat{e} \\ &= \hat{Y}^t\hat{Y} + \hat{e}^t\hat{e} \end{aligned} \tag{3.21}$$

Eq. 3.21 shows how SSCP is decomposed into Sum of Square and Cross Product of scores of outcomes $\hat{Y}^t\hat{Y}$ and Sum of Square and Cross Product of errors $\hat{e}^t\hat{e}$. These two matrices denoted in the following by H and E summarize the (co)variation of the fitted values and residuals for a given predictor $\hat{Y}$. In MANOVA theory, they have been used to define different multivariate

dependences test to verify the general linear hypothesis $\beta = 0$.
The most common multivariate statistic test to measure if the hypothesis $\beta = 0$ is true or false is known as Wilks' lambda likelihood ratio test W. Besides this test, it must be remarked that other multivariate statistics tests as Roy, Lawley-Hotteling or Pillai criteria to test $\beta = 0$ have been studied.(See Appendix 7.3 for further information). Also, association measures without considering the multivariate regression model have also been taken into account as measures shown in Appendix 7.3. Comparing all these measures, Wilks' lambda test has been chosen because the association measure obtained by Wilks' lambda test A_w leads to the highest value of association. It means that the other measures can obtain very small values which could be interpreted as a null association.(See order relationship in Appendix.7.3).
The Wilks' lambda test can be interpreted as the proportion of generalized variance in the dependent variables that is accounted for by the predictors. This treatment is performed by finding the ratio of the determinant (generalized variance) of the error SSCP matrix to the determinant of the sum of the treatment and error E matrices. Mathematically, the Wilks' lambda W is expressed by:

$$W(X,Y) = \frac{det(E)}{det(E+H)} = \frac{det(\hat{e}^t\hat{e})}{det(Y^tY)} \tag{3.22}$$

where the term $\hat{e}^t\hat{e}$ is defined by:

$$\begin{aligned}
\hat{e}^t\hat{e} = & \quad (Y - X\hat{\beta})^t(Y - X\hat{\beta}) \\
= & \quad Y^tY - Y^tX\hat{\beta} - \hat{\beta}X^tY + \hat{\beta}^tX^tY + \hat{\beta}^tX^tX\hat{\beta} \\
= & \quad \hat{Y}^t\hat{Y} - Y^tX\hat{\beta} \quad (\text{ where } \hat{\beta}^tX^tY = \hat{\beta}^tX^tX\hat{\beta}\,) \\
= & \quad \hat{Y}^t\hat{Y} - Y^tX(X^tX)^-Y \\
= & \quad Y'[I - X(X^tX)^-X^t]Y
\end{aligned} \tag{3.23}$$

The Wilks' lambda test satisfies $0 \leq W(X,Y) \leq 1$. The zero value indicates that the hypothesis $\beta = 0$ is false and then X and Y are highly correlated. Contrarily, if $W(X,Y) = 1$, the hypothesis is true and then X and Y are completely independent. It must be remembered that in our case, X and Y correspond to the principal coordinates of the region represented by $Y = U_{R_j}\Lambda_{R_j}$ and $X = U_{R_i}\Lambda_{R_i}$. The predicted model $\hat{Y}$ then corresponds to

$$\hat{Y} = PY = X(X^tX)^{-1}X^tY = U_{R_i}U'_{R_i}U_{R_j}\Lambda_{R_j} \tag{3.24}$$

Hence, given Eq. 3.23 and Eq.3.24, the Sum of Square and Cross Product of errors E and the total Sum of Square and Cross Product E+H are given by:

$$E = \hat{e}^t\hat{e} = Y'[I - X(X^tX)^-X^t]Y = \Lambda_{R_j}(I - U^t_{R_j}U_{R_i}U^t_{R_i}U_{R_j})\Lambda_{R_j} \tag{3.25}$$

$$E + H = Y^tY = \Lambda_{R_j}U^t_{R_j}U_{R_j}\Lambda_{R_j} = \Lambda^2_{R_j} \tag{3.26}$$

These last two expressions re-define the Wilks' lambda test of Eq.3.22. In this context, X and Y correspond to region models representing two adjacent regions R_i and R_j. Accordingly, the Wilks' lambda test $W(R_i, R_j)$ is expressed by Eq.3.27. This last equation can be used to define an association measure as $A_w = 1 - W$, which does not depend on Λ_{R_j} neither Λ_{R_i}.

$$W(R_i, R_j) = det(I - U^t_{R_j} U_{R_i} U^t_{R_i} U_{R_j}) \tag{3.27}$$

The Wilks' lambda test of Eq. 3.22, can also be calculated from the point of view of an eigenvalue approach by $W(R_i, R_j) = \lambda^1_w \times \lambda^2_w .... \times \lambda^{D_s}_w$ where λ^i_w are the eigenvalues corresponding to:

$$det(E - \lambda_w(E + H)) = 0 \tag{3.28}$$

with $0 \leq \lambda^i_w \leq 1$. These eigenvalues are directly related to the canonical correlations which are used as a way of measuring the linear relationship between two multidimensional variables. In this context, the squared canonical correlation r^2_i is defined by $1 - \lambda^i_w$. The Wilks' criterion can thus be expressed in terms of canonical correlations as:

$$W(R_i, R_j) = \prod_{i=1}^{D_s} (1 - r^2_i) \tag{3.29}$$

Hence, the Wilks' lambda test computed in Eq.3.29 is proposed here as the similarity measure between R_i and R_j. If $W(R_i, R_j)$ is equal to 0, it means that the hypothesis $\beta = 0$ is false and then R_i and R_j are highly correlated, i.e. very similar. In contrast, $W(R_i, R_j) = 1$ implies that the adjacent regions R_i and R_j are very different and no dependency can be found. Hence, this leads to the definition of the proposed merging criterion:

$$O_{MDS} = \underset{R_i, R_j}{\operatorname{argmin}} W(R_i, R_j) \tag{3.30}$$

Before concluding this section, we would like to remark that all the proposed merging criteria shown in Fig.3.19 are size-independent. In other words, the area of the regions is not included in any proposed merging order. Thus, depending on the initial partition where the merging process is started and on the specific characteristics of the image, these approaches may suffer from small and meaningless regions into the generated partition. This limitation is found especially in the initial stages of the BPT construction process.

To overcome this issue, the combination of a scale-based merging order with the presented area-independent merging criteria is used here as it has been previously done in [17]. The benefit of this approach is that the fusion of large regions is not too penalized compared to classical approaches, where the area of the region is multiplied by the similarity measure $O(R_i, R_j)$ [40] [141] .

The problem of this approach is that the area constraint and the similarity measure $O(R_i, R_j)$ can have different magnitude orders. An example can be seen in Eq.3.31 where a weighted merging criterion has been proposed in [17] by using the Battacharyya distance of Eq.3.13. In this example,

the merging order obtained by the similarity measure is multiplied by the *minimum* area of the pair of regions. In this case, O_{BAT} and the area constraint can really have different magnitude orders. The term O_{BAT} comes from a logarithmic function , it can therefore be much more smaller than the first term concerning the area of the regions. Hence, this approach can force to obtain regions having similar sizes by strongly enforcing the area constraint.

$$O_{BAT}^{weighted} = min(N_{R_{i_p}}, N_{R_{j_p}})O_{BAT} \tag{3.31}$$

To avoid this limitation, the scale-threshold procedure is included during the construction of BPT in order to avoid meaningless regions at the different levels of the hierarchy.

Introduction of the scale-threshold in the merging criteria

The idea proposed in [17] is to define a scale threshold $T_{scale}^{L_i}$ at each merging step L_i according to the number of remaining regions in the partition. At each step L_i, the $T_{scale}^{L_i}$ is considered as the *minimum* area that regions forming the partition of this level should have.
The combination of the scale-threshold constraint with the region merging order described on Fig.3.1 can be easily performed. The strategy consists in verifying for each L_i, whether there are regions of size lower than $T_{scale}^{L_i}$.
Regions below this threshold are considered as out-of-scale and the algorithm forces their merging (following their similarity values). It should be noticed that even if the out-of-scale regions are forced to merge at a given level, they will merge with their most similar neighboring region in the partition.
The scale threshold is updated after each merging step and its definition is based on the average size of regions at a certain iteration L_i by:

$$T_{scale}^{L_i} = \frac{\alpha \cdot \text{Image Area}}{\text{Number of regions at } L_i} \tag{3.32}$$

Note that even if the out-of-scale criterion forces the fusion of the small regions, the constraint is not too restrictive because it still permits to have small regions different from their neighborhood, at that high levels of the BPT hierarchy. For instance, assuming an image containing 1000 pixels and $\alpha = 0.15$. After 980 merging steps, the resulting partition at level L_{980} is formed by 21 different regions can be composed of regions having as few as 8 pixels. Heuristically, a good trade-off was presented in [17] by using $\alpha = 0.15$

3.4 Experimental Evaluation

In this section, a complete evaluation of the BPT-based representations is provided. First experiments have been performed evaluating the different proposed merging criteria and region models.To this end, some partitions obtained during the construction of the BPT merging sequence are compared between themselves and also with the state of the art RHSEG technique [22]. The experiments aim at measuring the quality of the hierarchical partitions contained in the constructed BPT representations. The quality of the obtained results is tested by a quantitative evaluation in order to assess the accuracy and robustness of the different constructed BPTs.
The main difficulty arises from the classical image segmentation issue: *An optimum segmentation result can be very different depending on the actual application*. Hence, to perform a quantitive evaluation, a reference image partition, also called ground truth, specifying a segmentation goal is necessary. As such reference was not available in our case, the manual creation of ground truth images has been a mandatory step for the BPT evaluation. The idea is to compare these manually created ground truth partitions with the image partitions contained in BPTs in order to measure their quality. The quantitative evaluation has been carried out by two different metrics defined in [51] in the context of image segmentation. These metrics have been previously used in [39] [17]. The description of the two metrics is detailed in Sec.3.4.1.
The evaluation has been carried out on different hyperspectral images. The description of these data sets is presented in Sec.3.4.2, where the different manually created ground truth partitions are also shown. Besides the experiments evaluating the different merging orders, a second set of experiments is also described here in order to evaluate the estimation of D_s in the case of O_{MDS}. The aim is to show the importance of the intrinsic dimension of the regions D_s in order to compare their similarity.

3.4.1 Quality measures between partitions

The evaluation of BPT assumes a critical role for the selection of an appropriate merging order. A visual assessment of the partitions obtained following the merging sequence construction is a first type way to evaluate the construction of the BPT. However, in order to be objective, a quantitative evaluation measuring the quality with respect to a reference segmentation is compulsory.
In the literature, the most well-known set of quality measures between partitions has been presented in [54], and more thoroughly in [53]. Most of these measures, such as GCE, LCE and BCE measures, compute the overall distance between two partitions as the sum of the local inconsistency at each pixel. These measures have achieved excellent results in [53]. However, their behavior is not always reliable, as it has been illustrated in [52]. This is probably due to their local definition, making it also difficult to predict the performances in the case of more complex segmentations. Because of these limitations, the asymmetric d_{asym} and symmetric d_{sym} distances described in [51] have been used here. Two different examples of these metrics and their definitions are presented in the following.

Asymmetric Distance d_{asym}

The first quality measure between a partition $\mathcal{P}$ and a ground truth $\mathcal{P}_{GT}$ is the asymmetric partition distance d_{asym}. This distance measures the *minimum* number of pixels whose labels should be changed so that partition $\mathcal{P}$ becomes finer than partition $\mathcal{P}_{GT}$. A partition $\mathcal{P}$ is said to be refinement of another partition $\mathcal{Q}$ if each subinterval of $\mathcal{P}$ is contained in some subinterval of $\mathcal{Q}$.
This distance is normalized by the total number of pixels of the image minus one [1]. As a result, d_{asym} is ranging between 0 and 1.
Two different quality measures can be computed using d_{asym}, as $d_{asym}(\mathcal{P}, \mathcal{P}_{GT}) \neq d_{asym}(\mathcal{P}_{GT}, \mathcal{P})$. $d_{asym}(P, P_{GT})$ measures the degree of over-segmentation. Contrarily, changing the order of the partitions, the under-segmentation of $\mathcal{P}$ according to the ground truth partition $\mathcal{P}_{GT}$ is measured by $d_{asym}(\mathcal{P}_{GT}, \mathcal{P})$.
An example showing the computation of the d_{asym} is illustrated in Fig.3.22, where the partition $\mathcal{P}$ of Fig.3.22(a) is evaluated with respect to the ground truth image $\mathcal{P}_{GT}$ shown in Fig.3.22(b). For this example, the under-segmented pixels whose labels should change from $\mathcal{P}$ to be finer than $\mathcal{P}_{GT}$ are highligthed in green in Fig.3.22(c). This last figure leads to an under-segmentation error defined as $d_{asym}(\mathcal{P}_{GT}, \mathcal{P})$ equal to 0.006. Going on with this example, the over-segmented pixels are shown in Fig.3.22(c) leading to an over-segmentation error $d_{asym}(\mathcal{P}, \mathcal{P}_{GT}) = 0.42$.
Both results $d_{asym}(\mathcal{P}, \mathcal{P}_{GT})$ and $d_{asym}(\mathcal{P}_{GT}, \mathcal{P})$ confirm the visual evaluation that can be done for this example. The partition $\mathcal{P}$ suffers from a negligible under-segmentation whereas the over-segmentation of $\mathcal{P}$ according to $\mathcal{P}_{GT}$ is quite significant.

Symmetric distance d_{sym}

Symmetric distance d_{sym} is a global error measure to establish a trade-off between under-and over-segmentation error. The distance was originally defined in the pattern analysis field, in terms of data clustering comparison [55] and used in image segmentation in [51]. The distance is defined as the *minimum* number of pixels whose labels should be changed in $\mathcal{P}$ to achieve a perfect matching with $\mathcal{P}_{GT}$, where $\mathcal{P}$ and $\mathcal{P}_{GT}$ are then becoming identical.
Consequently, the distance is measured between a partition $\mathcal{P}$ and a ground truth $\mathcal{P}_{GT}$, both having the same number of regions. Hence, this distance holds the symmetric property $d_{sym}(\mathcal{P}_{GT}, \mathcal{P}) = d_{sym}(\mathcal{P}, \mathcal{P}_{GT})$. As in the case of d_{asym}, the symmetric distance is also normalized by the total number of pixels of the image minus one. Therefore, d_{sym} is also ranging between 0 and 1.
Fig.3.23 illustrates an example of d_{sym} evaluation, where two different partitions $\mathcal{P}_1$ and $\mathcal{P}_2$ are evaluated according to the $\mathcal{P}_{GT}$ shown in Fig.3.22(b). In this example, note that the partitions $\mathcal{P}_1$ and $\mathcal{P}_2$ have the same number of regions as $\mathcal{P}_{GT}$ (N_R=2).
The first d_{sym} is computed between $\mathcal{P}_1$ and $\mathcal{P}_{GT}$. The pixels which must be changed from $\mathcal{P}_1$ to perfectly match $\mathcal{P}_{GT}$ are shown in green in Fig.3.23(c). These green pixels involve a $d_{sym}(\mathcal{P}_{GT}, \mathcal{P}_1)$ equal to 0.08. Following the same procedure, $d_{sym}(\mathcal{P}_{GT}, \mathcal{P}_2) = 0.17$. The pixels causing this error are highlighted in Fig.3.23(d). Comparing the obtained d_{sym} values with a visual evaluation, it

[1] With the N number of pixels in the image, d_{asym} is normalized by $N - 1$, which is the *maximum* number of pixels whose label may be changed in the worst case, since at least one of the pixels would remain with its own label

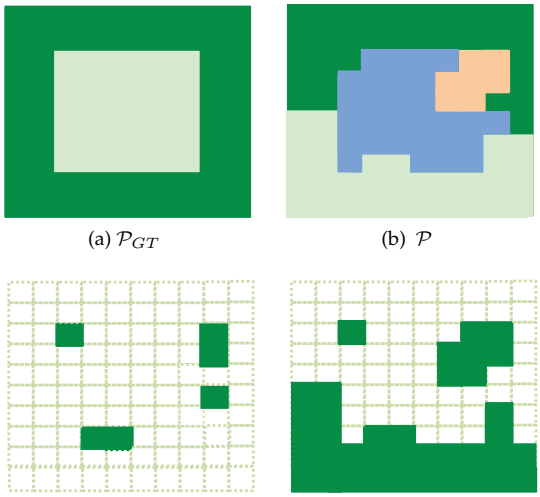

(a) $\mathcal{P}_{GT}$ (b) $\mathcal{P}$

(c) Under-segmented pixels (d) Over-segmented pixels

Figure 3.22: Illustrative example of asymmetric partition distance for an image having 10×10 pixels. (a) Partition $\mathcal{P}$ to be evaluated . (b) Ground truth partition $\mathcal{P}_{GT}$. (c) and (d) are binary images showing in green the pixels whose labels must be changed in each case to compute the under- ($d_{asym}(\mathcal{P}_{GT}, \mathcal{P})$) and the over-segmentation($d_{asym}(\mathcal{P}, \mathcal{P}_{GT})$) errors, respectively.

can be seen that both distances provide objective results between the evaluated partitions. Both evaluations result in the same conclusion, the partition $\mathcal{P}_1$ is closer to the ground truth segmentation than the partition $\mathcal{P}_2$.

3.4.2 Data Sets Definition

The experimental evaluation is carried out by using five different hyperspectral images captured by two different sensors. Accordingly, the different data sets have different spectral and spatial resolutions. The five hyperspectral images can be split in three categories: three images from Pavia University, an image from Pavia Center both acquired by the ROSIS sensor and finally, an image acquired by HYDICE sensor. Five different ground truth partitions have been manually created.

Due to the low resolution of hyperspectral data, the creation of ground truth partitions is not straightforward. Therefore, as these images present complex structures, the creation of a complete ground truth is an important challenge. A second important issue is related to the scene intrepretation. This problem is related with the different information contained in the different hyperspectral bands. In particular, composing two RGB images by using 6 different hyperspectral bands, two completely different ground truths can be created.

In order to minimize this problem, the RGB image composition used to create the ground truth partitions has been obtained by the first PCA components. Concretely, it corresponds to the three

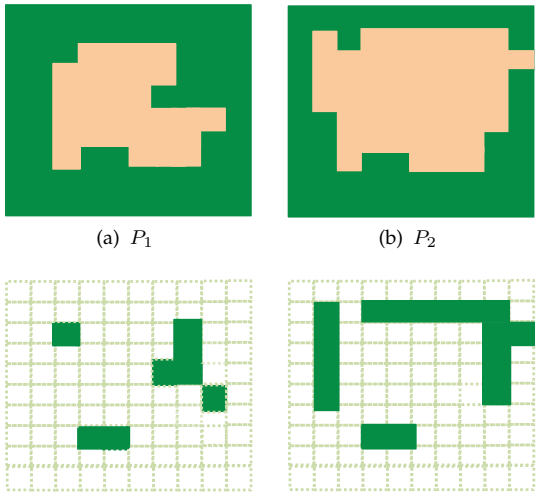

(a) P_1 (b) P_2

(c) $d_{sym}(\mathcal{P}_{GT}, \mathcal{P}_2) = 0.08$ (d) $d_{sym}(\mathcal{P}_{GT}, \mathcal{P}_2) = 0.17$

Figure 3.23: Illustrative example of symmetric partition distance for an image having 10×10 pixels. (a)-(b) Partitions $\mathcal{P}_1$ and $\mathcal{P}_2$ to be evaluated. (c) and (d) are binary images showing in green the pixels whose labels must be changed for partition $\mathcal{P}_1$ and $\mathcal{P}_2$ to perfectly match with $\mathcal{P}_{GT}$ shown in Fig.3.22(b).

components associated to the 3 highest eigenvalues. The generated ground truth partitions and the characteristics of the five hyperspectral data sets are detailed in the following.

Pavia University

The first studied hyperspectral image is acquired over the city of Pavia (Italy) by the $ROSIS-03$ (Reflective Optics Systems Imaging Spectrometer) hyperspectral sensor operated by DLR out of Oberpfaffenhofen (Germany). The spatial dimension of the image is 610×340. The geometrical resolution is 1.3 m. The original data are composed of 115 spectral bands, ranging from 0.43 to 0.86 μm with a band width of 4 nm. However, typical noisy bands corresponding to the water absorption were previously discarded leading to 103 channels. A RGB composition of the entire Pavia University data set is shown in Fig.3.24.

For this image, the experimental results aiming at the BPT evaluation are not performed by using the complete image. Indeed, the creation of a ground truth image labeling all the pixels is too complex. Fig.3.24 shows the complexity of the structures forming this image. Thus, in order to create an accurate ground truth image, three different portions of hyperspectral Pavia University have been used. The three different portions studied for the Pavia University data set are boxed by the red, the orange and the yellow rectangles.

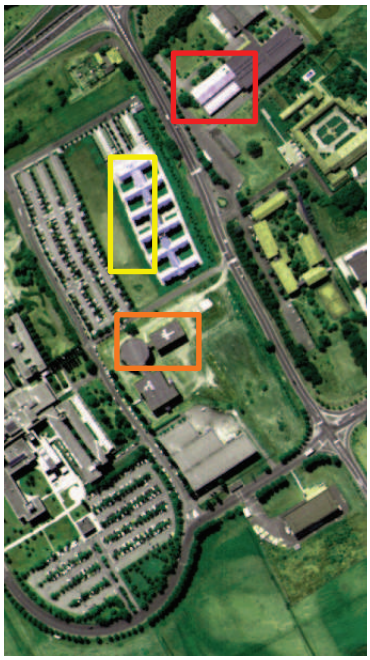

Figure 3.24: RGB composition of ROSIS Pavia University image

The three data sets have been named as Pavia-uni-Z_1, Pavia-uni-Z_2 and Pavia-uni-Z_3 and they can be seen in more details in Fig.3.25. Fig.3.25(a) corresponding to Pavia-uni-Z_1 has a spatial dimension of 39×95 pixels. The dimension of Fig.3.25(b) and Fig.3.25(c) corresponding to Pavia-uni-Z_2 and Pavia-uni-Z_3 are in this case 69×46 and 61×66.

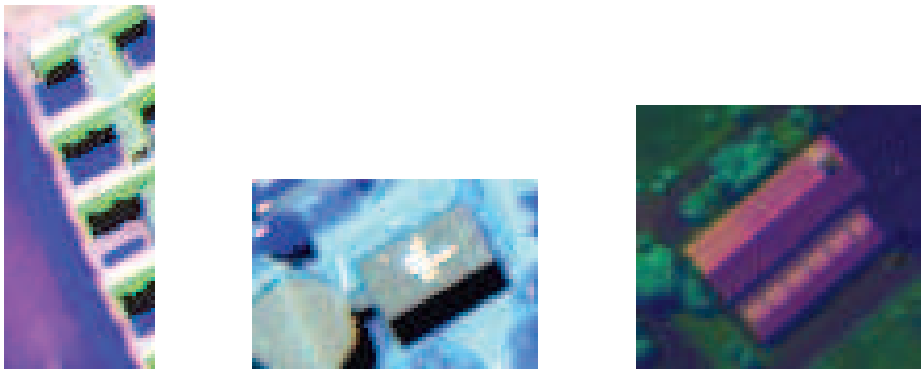

(a) Pavia-Uni-Z_1 (b) Pavia-Uni-Z_2 (c) Pavia-Uni-Z_3

Figure 3.25: RGB composition showing the three different studied zones of ROSIS Pavia University image

For these last images, three manually ground truth partitions $\mathcal{P}_{GT}$ have been created. These reference partitions are shown in Fig.3.26(a)(b)(c). The corresponding numbers of regions N_R are $N_R = 33$, $N_R = 11$ and $N_R = 42$, respectively.

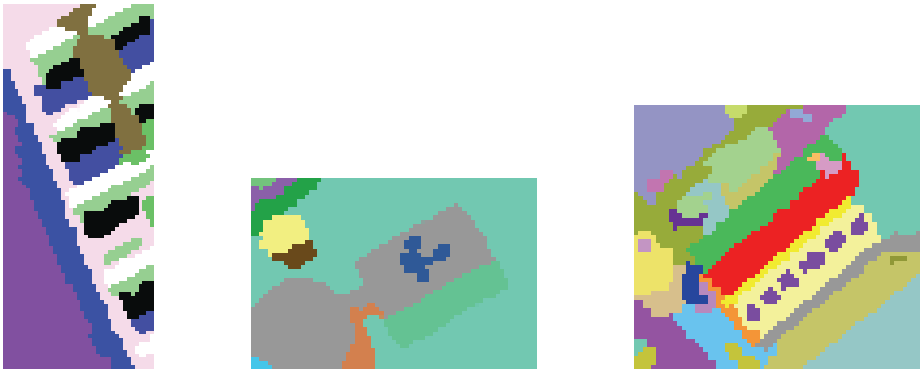

(a) $\mathcal{P}_{GT}$ from Pavia-Uni-Z_1 (b) $\mathcal{P}_{GT}$ from Pavia-Uni-Z_2 (c) $\mathcal{P}_{GT}$ from Pavia-Uni-Z_2

Figure 3.26: Manually created $\mathcal{P}_{GT}$ partitions of the three different studied zones of ROSIS Pavia University image

Pavia Center

The second studied hyperspectral data has also been captured by the hyperspectral ROSIS sensor. The entire image has 492 by 1096 pixels, collected over Pavia city centre, Italy. It contains 102 spectral channels after removal of noisy bands. From the same reasons as Pavia University, a portion of this image has been selected in order to evaluate the BPT construction. The RGB composition describing the image scene is shown in Fig.3.27(a). The corresponding ground truth containing $N_R = 23$ regions is shown in Fig.3.27(b).

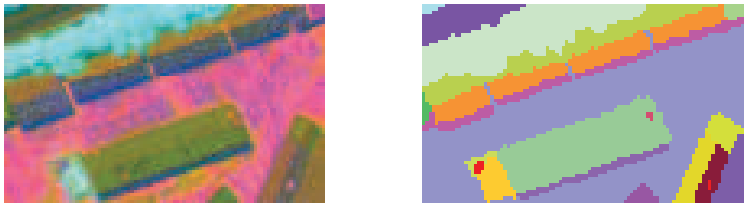

(a) RGB Composition (b) Manually created $\mathcal{P}_{GT}$

Figure 3.27: Pavia Center Data Set

Urban Hydice

The third hyperspectral data set is given by a publicly available HYDICE hyperspectral image from an urban area. Originally, the entire image is 307 $\times$ 307 pixels in size and has 210 spectral channels from $\approx$ 0.4 to 2.5 μm. After removing water absorption and noisy bands, the data contain 167 spectral bands. The scene is cluttered with a large retail store and parking lot, a residential neighborhood, and a roadway. Consequently, the majority of this scene is qualitatively complex. Hence, a portion of this image has been studied. It is 60x60 pixels and has a spatial resolution of 3 meters approximately. The ground truth and the RGB composition for this last data set is found on Fig.3.28. The corresponding number of regions involves in $\mathcal{P}_{GT}$ is 56.

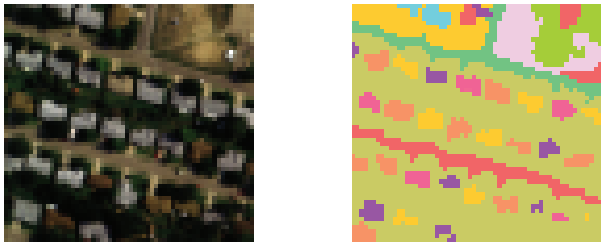

(a) RGB Composition (b) Manually created $\mathcal{P}_{GT}$

Figure 3.28: HYDICE Data Set

3.4.3 Experiment 1: Evaluation of BPT hierarchical levels

The purpose of this experiment is to evaluate the different image partitions created during the BPT construction by the different merging criteria. Starting from the pixel-based representation of an image containing N_p pixels, partitions having a number of regions equal to N_R are studied. These partitions are obtained by doing the N_p - N_R merging steps over the initial partition. The quality of the obtained partitions having N_R regions is evaluated in two different ways: Visually and by using the two different partition distances described in Sec.3.4.1.

This complete evaluation is carried out on the five different images presented in Sec.3.4.2. For each image, different BPTs according to the different merging orders proposed in Fig.3.3 have been constructed.

To perform this experiment, some parameters for the different region models and merging criteria should be set. In the case of O_{SID} ad O_{SAM}, no parameter is required. Note that the region model corresponding to these merging orders is only the average of the spectral values of the region. Contrarily, in order to construct the non parametric statistical region model presented in Sec.3.3.2, some parameters should be defined. The first important parameter is the number of bins N_{bins} used to construct the histogram of each region at each hyperspectral band. Ideally, N_{bins} should be equal to the number of possible radiance values contained on the image. For instance, if the radiance value is an integer encoded over 8 bits, their range is $[0, 255]$. Therefore, the ideal number of bins used to represent the spatial histograms of the region corresponds to $N_{bins} = 256$. The main problem is that having hundred of N_z channels, thousands of N_p pixels and $2 \times N_p - 1$ merging steps, a high N_{bins} value can be computationally critical. On the other hand, radiance values can also be coded with 16 bits ranging from $[0, 65535]$, therefore, the parameter is even more critical. Consequently, a moderate quantization is used for the computation of the non parametric statistical model.

Another consideration concerning N_{bins} is the possible histogram misalignment problem previously shown in Fig.3.20. This problem is mainly found because O_{BAT} is not robust with regards to this point. The robustness of N_{bins} parameters is sought with the merging order O_{DIF}. For this criterion, different results can be obtained by changing the value of N_{bins}, however, their differences are not very significant. The diffusion distance O_{DIF} needs to set two parameters: the standard deviation for the Gaussian filter σ_G and the number of layers. In our work, these parameters have been set according to [59]. Thus, σ_G is equal to 0.5 and the number of layers is set to 3.

Another important parameter concerning the non parametric statistical region model is the value D_s used in O_{MDS}. The procedure to extract D_s has been explained in Sec.3.3.3. Before concluding, it should be remembered that other parameters for the case of non parametrical statistical region model have been defined at the beginning of Sec.3.6. These are the parameters described to estimate the pdf's of the individual pixels. In the experiments presented in this section, the pixel pdf estimation has been performed as it has been previously done on the pixels of Fig.3.10.

At this point, the following sub-sections describe the obtained experimental results for the visual and quantitive evaluation.

Visual Evaluation of the hierarchical BPT levels

The visual evaluation of the partitions obtained by the different merging criteria is carried out here. A set of partitions obtained during the BPT construction having different number of regions are shown.

Starting from the hyperspectral image illustrated in Fig.3.24, five different BPTs have been constructed for each of the three zones: Pavia-uni-Z_1 ,Pavia-uni-Z_2 and Pavia-uni-Z_3. N_{bins} is set to 120 for these three images and D_s is set to 3.

The first results correspond to the BPT construction for Pavia-uni-Z_1, whose RGB composition has been previously shown in Fig.3.25 (a). Fig.3.29 illustrates the different partitions for the five different merging orders. In this figure, each column corresponds to a different merging order, and each row shows a partition formed by a specific number of regions N_R. From the first to the third rows, N_R values correspond to $N_R = 15$, $N_R = 35$ and $N_R = 45$. The five different merging criteria are ordered as : O_{SID}, O_{SAM}, O_{BAT}, O_{DIF}, O_{MDS}. The last column of Fig.3.29 shows the results obtained by the RHSEG algorithm [22], which is widely used in the context of hyperspectral image segmentation. The parameters used by RHSEG algorithm are the SAM similarity criterion with a spectral clustering weight of 0.1 as has been previously done in [20]. The RHSEG parameters have been kept identical for the five hyperspectral images.

Fig.3.29 shows how the merging criteria using the non parametric statistical region model (O_{BAT}, O_{DIF} and O_{MDS}) provide the best results. Comparing the methods processing hyperpsectral bands jointly or separately, some differences can be noticed. For instance, looking at the last rows where $N_R = 45$, the brown region on the left of the figure appears entirely for the case of O_{MDS}, O_{SID}, O_{SAM} and RHSEG. Contrarily, the merging orders O_{BAT} and O_{DIF} which process separately the different channels, have some problems forming this region. As a conclusion of this first visual evaluation, O_{MDS} seems to perform better than the other used criteria.

The next results in Fig.3.30 correspond to the partitions obtained for the Pavia-uni-Z_2 data. In this case, given the dimension of the image, the configuration of this figure according to Fig.3.29 has been transposed. Thus, a row contains the partitions with different N_R for a specific merging order. Correspondingly, each column shows the partitions associated to the different merging orders but with the same number of regions. This configuration is going to be kept for the remaining hyperspectral data sets. For this data set, the number of regions forming the partitions correspond to $N_R = 11$, $N_R = 25$ and $N_R = 44$.

Looking at this last figure, the results obtained by O_{MDS} and O_{DIF} lead to the best partitions. Despite of some meaningless regions, it can be seen how the main structures of the $\mathcal{P}_{GT}$ appear in these results. The difference between jointly or not taking into account all the spectral information can also be noticed in this data set by comparing Fig.3.30(j) with Fig.3.30(m). In Fig.3.30(j), a tree located on the left of the figure is split in two regions because of the shadow effect described in Sec.3.3.

Concerning the pdf estimation of the initial pixels, an interesting behavior can be seen in Fig.3.30(m). In this case, pixels forming the edge of an object have merged together forming a single region. The brown region at the figure bottom is an example of this effect. This fact is very interesting

since it allows the segmentation to achieve clean borders.
Partition results achieved on the third data set Pavia-uni-Z_3 are illustrated in Fig.3.31, where the number of regions is given by $N_R = 22$, $N_R = 43$ and $N_R = 64$. The results obtained from this hyperspectral portion are not easily interpretable. This third data set seems to be more complicated than Fig.3.25. For instance, it can be found that this portion of hyperspectral data appears in very different ways in proposed classifications published in [21] [10]. In these papers, the reported classification maps have high classification accuracies but look very different.
In our case, comparing the different images of Fig.3.31, O_{MDS} and O_{DIF} seem to provide the best results. Results obtained with the first order region model are quite poor, as presented on Fig.3.31(a)(b)(c) and (d)(e)(f). The main problem is the formation of the large blue region on the top-right part of the figure. In order to avoid this formation, a solution could be to increase the α parameter of Eq.3.32. Thus, small regions will be firstly merged and the large blue region could be formed later. The problem is that the different merging criteria should be evaluated under the same conditions in this experimental evaluation. Therefore, it can be concluded that the need of a high α value for a merging criterion is a weakness.
The partitions obtained during the BPT construction of Pavia Center hyperspectral images are shown in Fig.3.32. Here, N_{bins} is set to 100 whereas the value of D_s has been estimated as $D_s = 2$. The number of regions forming the partitions of this figure are $N_R = 13$, $N_R = 25$ and $N_R = 39$. The first two rows show the results obtained by the first order region model. In these results, it is seen that the background of the image is entirely formed at level $N_R = 39$. Unfortunately, this background region (appearing in light purple) is too large in cases of O_{SID} where the row of buildings at the top of the image has completely disappeared. An important remark about the merging orders related to the non parametric statistical region model is that O_{MDS}, O_{DIF} and O_{BAT} also obtain in this data set clear border definition in their results. As mentioned above, this is because the non parametrical statistical region model gives a more accurate region representation, which leads to the formation of regions defining the object borders.
The effect of shadow can also be noticed in results shown in Fig.3.27. Looking at the central building of the image, it has been split in two regions in the case of O_{BAT} and O_{DIF} whereas the other merging orders obtain the entire object in a single region. Comparing all the results, O_{MDS} is achieving the best result for Pavia center hyperspectral data. For instance, Fig.3.27(o) shows how O_{MDS} having $N_R = 39$ has found a small square red region in the right part of the central building. Looking at Fig.3.27(a), it is seen that this small square actually corresponds to a small object which is not found by the other merging criteria.
The last visual evaluation is performed on the hyperspectral data captured by HYDICE sensor (See Fig.3.28). In this case, 256 bins are used to quantify this image. The local dimensionality reduction performed by O_{MDS} has taken into account 3 dimensions. For this data set, results can be seen in Fig.3.33, where the shown partitions contain $N_R = 27$, $N_R = 37$ and $N_R = 56$ regions. It can be observed that O_{MDS} obtains clearly the best results. This differences between O_{MDS} and the other merging criteria is not so clear in the case of ROSIS sensor. This is because the discrimination between different materials is less difficult in the case of ROSIS sensor. The problem

is that there is a lower discrimination along all the spectral range in the Hydice image.
Also for this image, it can be seen that the merging orders O_{SID} and O_{SAM} have some problems. For these two merging orders, buildings appear connected with roads. This can be observed at the two first rows of Fig.3.33.
Comparing all the different results shown in Fig.3.29, Fig.3.30, Fig.3.31,Fig.3.32 and Fig.3.33, it is not evident to perform an accurate classification of the merging orders according to their performances. O_{DIF} and O_{MDS} seem to obtain the best results followed by O_{BC}. However, in order to evaluate more precisely the merging orders a quantitive evaluation should be done. This evaluation is carried out in the following.

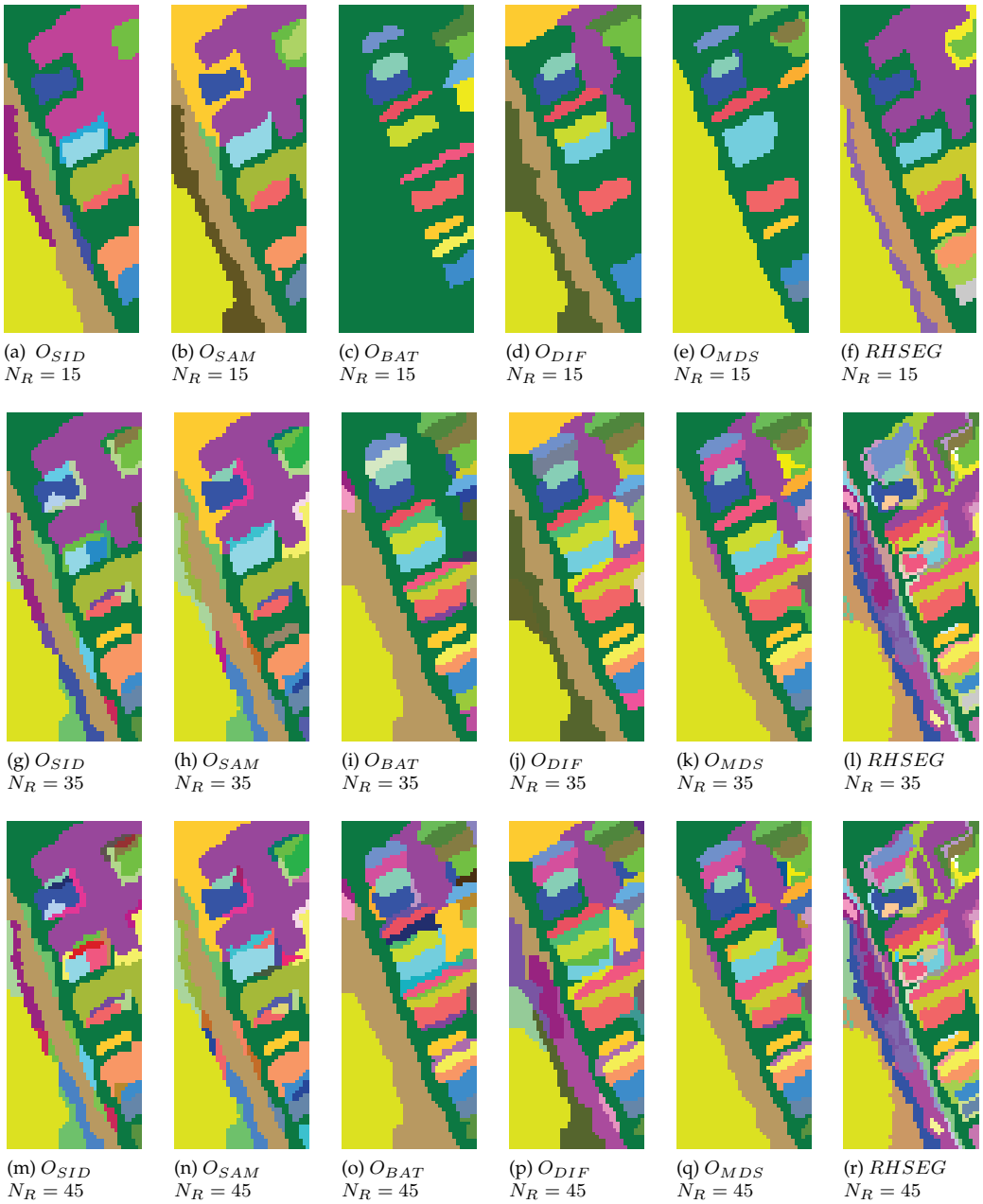

(a) O_{SID} $N_R = 15$ (b) O_{SAM} $N_R = 15$ (c) O_{BAT} $N_R = 15$ (d) O_{DIF} $N_R = 15$ (e) O_{MDS} $N_R = 15$ (f) $RHSEG$ $N_R = 15$

(g) O_{SID} $N_R = 35$ (h) O_{SAM} $N_R = 35$ (i) O_{BAT} $N_R = 35$ (j) O_{DIF} $N_R = 35$ (k) O_{MDS} $N_R = 35$ (l) $RHSEG$ $N_R = 35$

(m) O_{SID} $N_R = 45$ (n) O_{SAM} $N_R = 45$ (o) O_{BAT} $N_R = 45$ (p) O_{DIF} $N_R = 45$ (q) O_{MDS} $N_R = 45$ (r) $RHSEG$ $N_R = 45$

Figure 3.29: Visual Evaluation of the results over the Pavia-uni-Z_1 data set

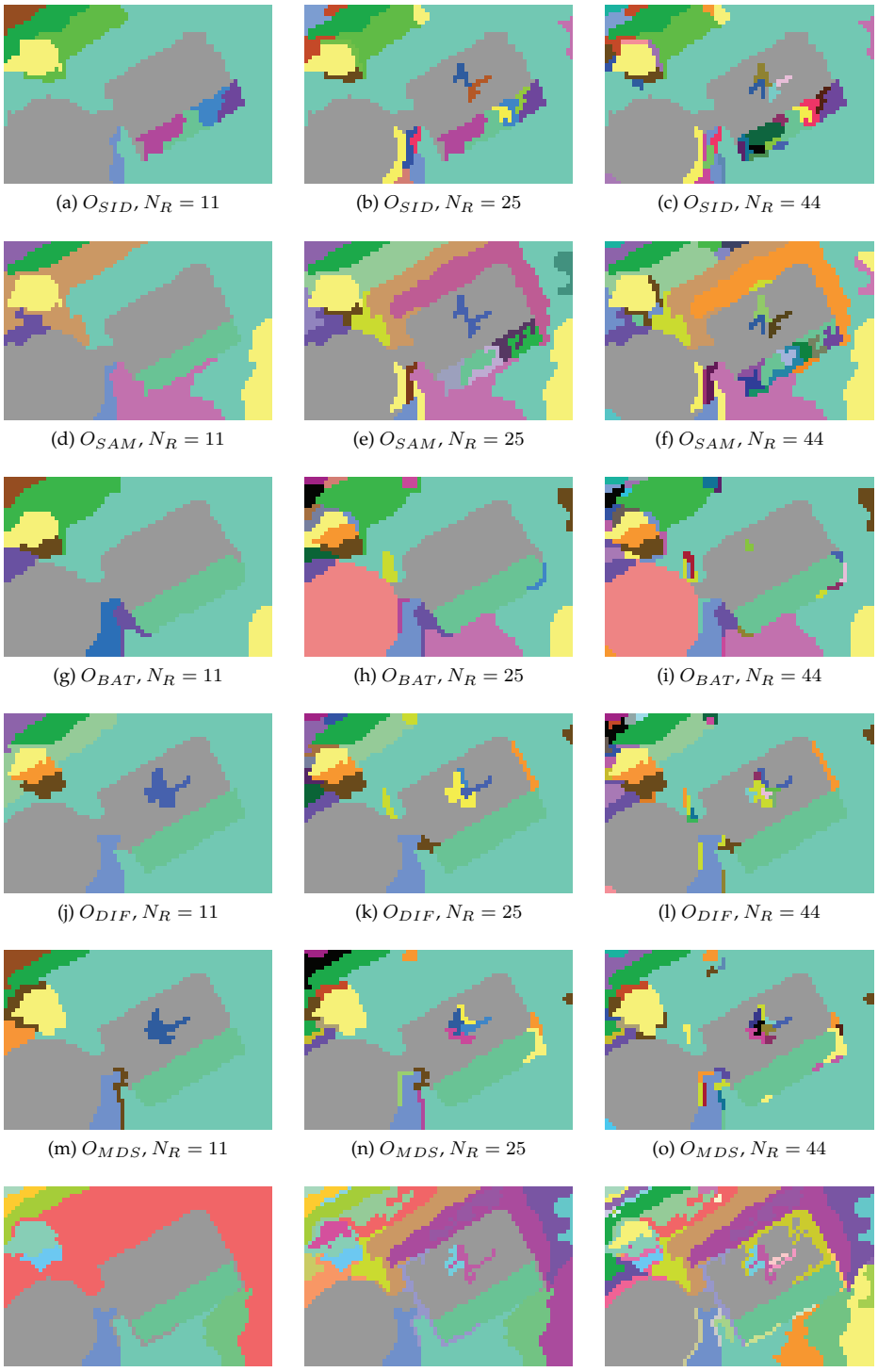

(a) O_{SID}, $N_R = 11$ (b) O_{SID}, $N_R = 25$ (c) O_{SID}, $N_R = 44$

(d) O_{SAM}, $N_R = 11$ (e) O_{SAM}, $N_R = 25$ (f) O_{SAM}, $N_R = 44$

(g) O_{BAT}, $N_R = 11$ (h) O_{BAT}, $N_R = 25$ (i) O_{BAT}, $N_R = 44$

(j) O_{DIF}, $N_R = 11$ (k) O_{DIF}, $N_R = 25$ (l) O_{DIF}, $N_R = 44$

(m) O_{MDS}, $N_R = 11$ (n) O_{MDS}, $N_R = 25$ (o) O_{MDS}, $N_R = 44$

(p) $RHSEG$, $N_R = 11$ (q) $RHSEG$, $N_R = 25$ (r) $RHSEG$,, $N_R = 44$

Figure 3.30: Visual Evaluation of the results over the Pavia-uni-Z_2 data set

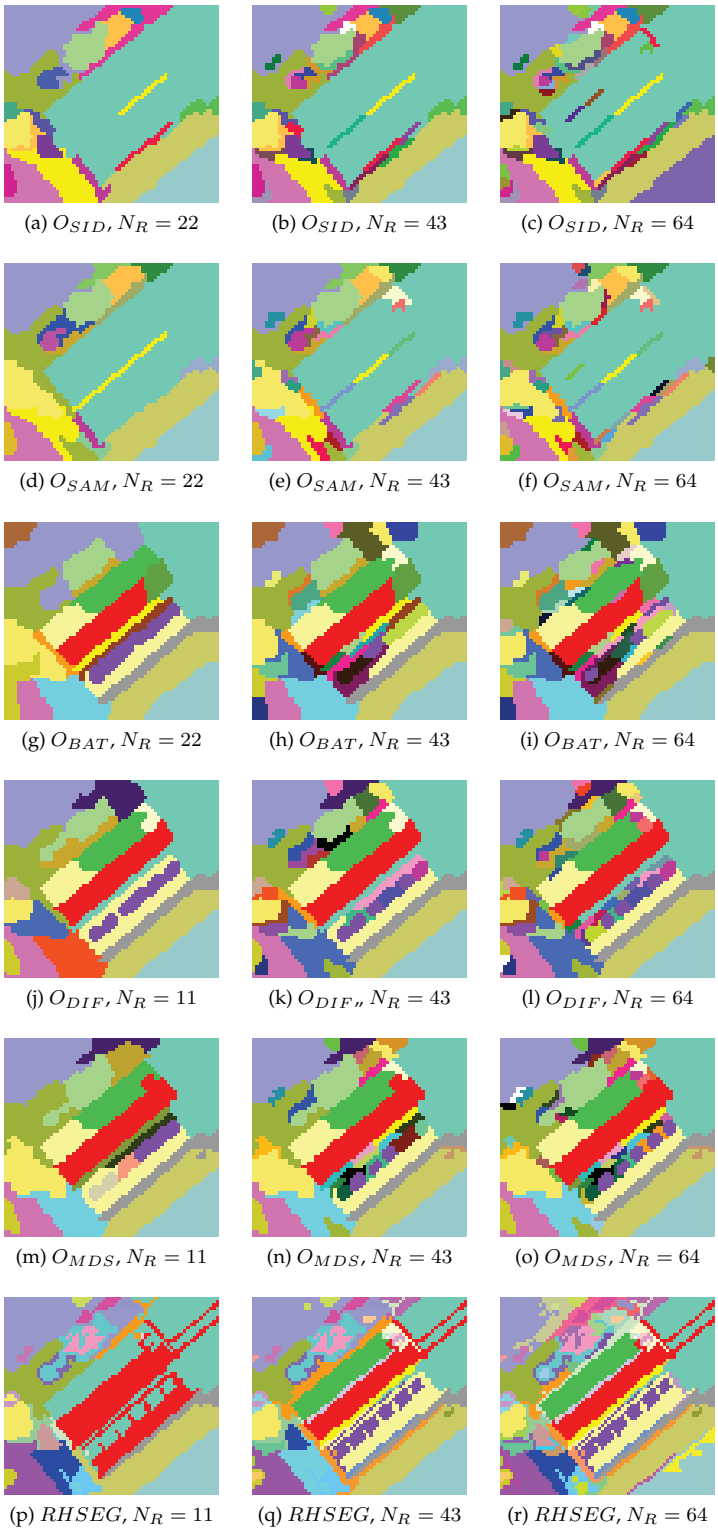

(a) O_{SID}, $N_R = 22$ (b) O_{SID}, $N_R = 43$ (c) O_{SID}, $N_R = 64$

(d) O_{SAM}, $N_R = 22$ (e) O_{SAM}, $N_R = 43$ (f) O_{SAM}, $N_R = 64$

(g) O_{BAT}, $N_R = 22$ (h) O_{BAT}, $N_R = 43$ (i) O_{BAT}, $N_R = 64$

(j) O_{DIF}, $N_R = 11$ (k) O_{DIF},, $N_R = 43$ (l) O_{DIF}, $N_R = 64$

(m) O_{MDS}, $N_R = 11$ (n) O_{MDS}, $N_R = 43$ (o) O_{MDS}, $N_R = 64$

(p) $RHSEG$, $N_R = 11$ (q) $RHSEG$, $N_R = 43$ (r) $RHSEG$, $N_R = 64$

Figure 3.31: Visual Evaluation of the results over the Pavia-uni-Z_3 data set

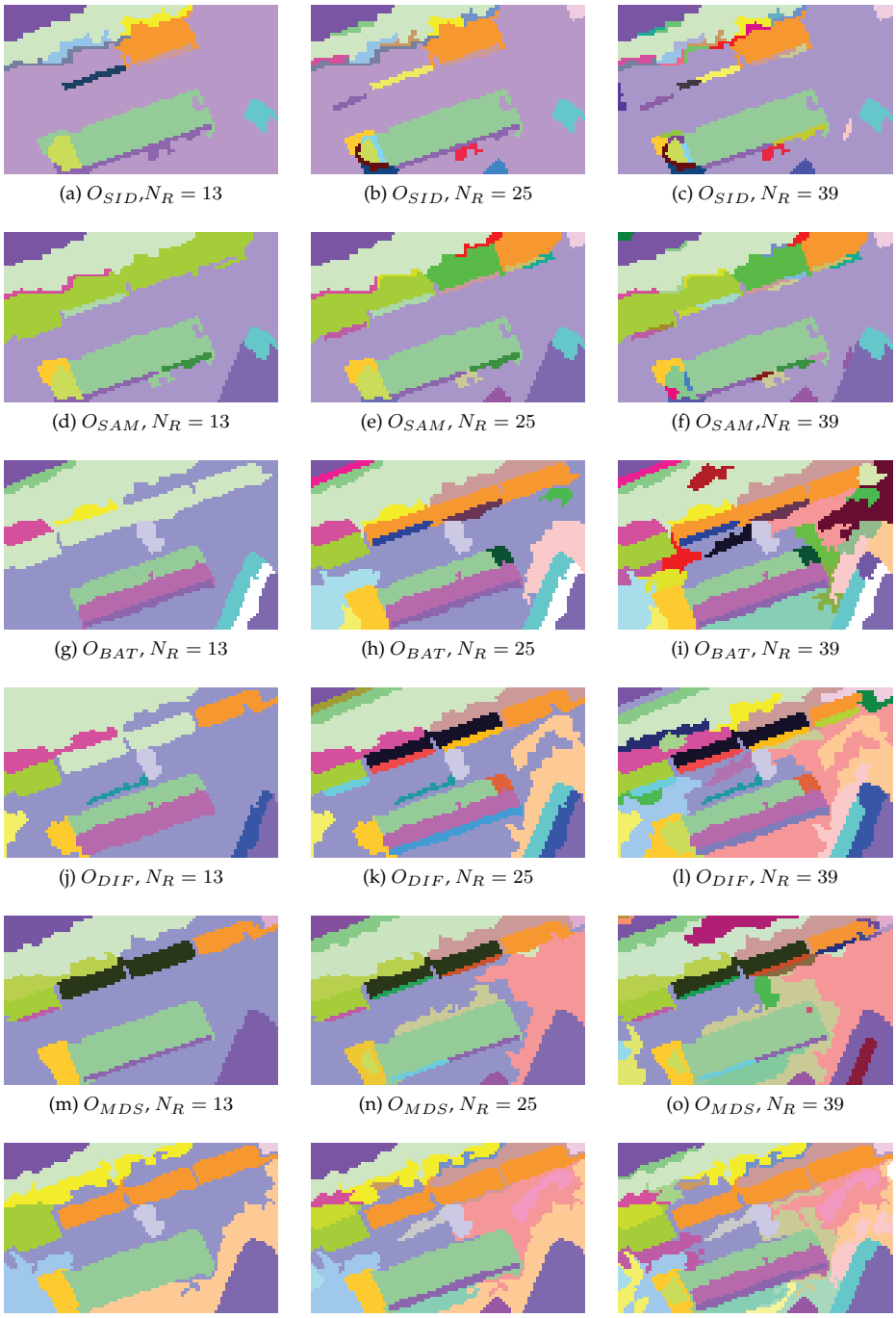

(a) O_{SID},$N_R = 13$ (b) O_{SID}, $N_R = 25$ (c) O_{SID}, $N_R = 39$

(d) O_{SAM}, $N_R = 13$ (e) O_{SAM}, $N_R = 25$ (f) O_{SAM},$N_R = 39$

(g) O_{BAT}, $N_R = 13$ (h) O_{BAT}, $N_R = 25$ (i) O_{BAT}, $N_R = 39$

(j) O_{DIF}, $N_R = 13$ (k) O_{DIF}, $N_R = 25$ (l) O_{DIF}, $N_R = 39$

(m) O_{MDS}, $N_R = 13$ (n) O_{MDS}, $N_R = 25$ (o) O_{MDS}, $N_R = 39$

(p) $RHSEG$, $N_R = 13$ (q) $RHSEG$, $N_R = 25$ (r) $RHSEG$, $N_R = 39$

Figure 3.32: Visual Evaluation of the results over the Pavia Center data set

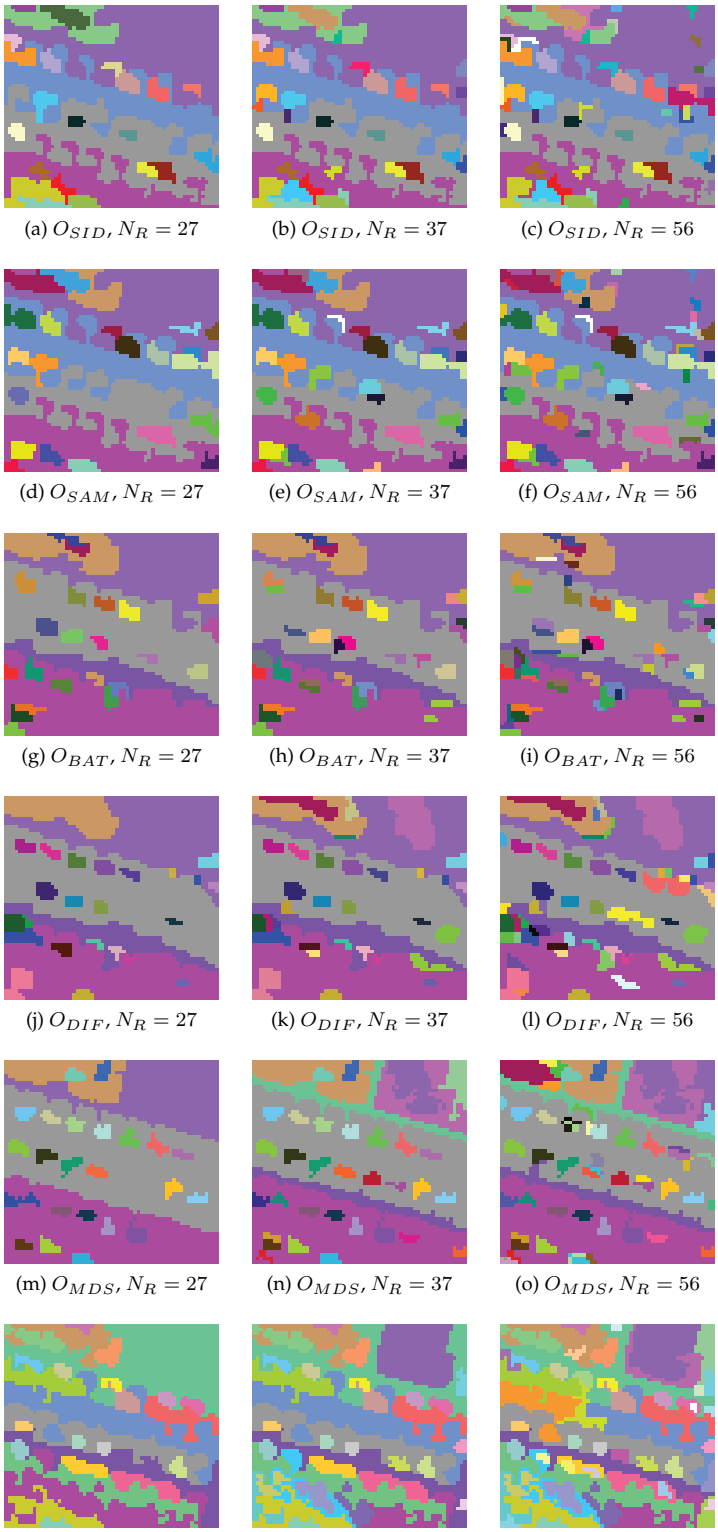

(a) O_{SID}, $N_R = 27$ (b) O_{SID}, $N_R = 37$ (c) O_{SID}, $N_R = 56$

(d) O_{SAM}, $N_R = 27$ (e) O_{SAM}, $N_R = 37$ (f) O_{SAM}, $N_R = 56$

(g) O_{BAT}, $N_R = 27$ (h) O_{BAT}, $N_R = 37$ (i) O_{BAT}, $N_R = 56$

(j) O_{DIF}, $N_R = 27$ (k) O_{DIF}, $N_R = 37$ (l) O_{DIF}, $N_R = 56$

(m) O_{MDS}, $N_R = 27$ (n) O_{MDS}, $N_R = 37$ (o) O_{MDS}, $N_R = 56$

(p) $RHSEG$, $N_R = 27$ (q) $RHSEG$, $N_R = 37$ (r) $RHSEG$, $N_R = 56$

Figure 3.33: Visual Evaluation of the results over the HYDICE data set

Hierarchical BPT evaluation by using Symmetric Distance

To quantitatively evaluate the partitions obtained during the BPT construction, the merging sequence is stopped when the resulting partition has the same number of regions N_{R_o} as the ground truth partition. Then, the symmetric distance described in Sec.3.4.1 is computed. Thus, performing $N_p - N_{R_o}$ merging steps over the image pixel-based representation, the partition $\mathcal{P}$ having the same number of regions than $\mathcal{P}_{GT}$ is obtained and evaluated for all the merging orders.
The different BPT constructions have been carried out with the same parameter adjustment as described in the previous section. The d_{sym} obtained for the five hyperpsectral data presented in Sec.3.4.2 are shown in the Tab.3.1, Tab.3.2, Tab.3.3, Tab.3.4 and Tab.3.5. In these tables, the different merging criteria and their corresponding d_{sym} are shown.
Tab.3.1 reports the results obtained for the Pavia-Uni-Z_1 image. In this case, the number of regions N_{R_o} forming the $\mathcal{P}_{GT}$ is equal to 33. This first table shows how O_{MDS} clearly obtains the best results. Also, it is seen how the merging criteria using non parametrical statistical region model achieved d_{sym} values smaller than O_{SID} and O_{SAM}. These two merging orders obtain the worst results jointly with RHSEG. Comparing the stochastic O_{SID} and the deterministic O_{SAM} merging criteria, the best result is given by O_{SID}. Regarding O_{DIF} and O_{BAT}, d_{sym} is not very different. This implies that the partition obtained by O_{DIF} is better for only a few pixels.

Table 3.1: Symmetric distance for Pavia-Uni-Z_1

Merging Criterion	d_{sym}
O_{SID}	0.383
O_{SAM}	0.425
O_{BAT}	0.279
O_{DIF}	0.274
O_{MDS}	0.138
$RHSEG$ [22]	0.48

The results obtained for the Pavia-Uni-Z_2 image are displayed in Tab.3.2 where $N_{R_o} = 11$. The high d_{sym} values obtained by O_{SAM} and RHSEG can be corroborated by looking at Fig.3.30. In both cases, the light blue background region is not found as a single region. Thus, the over-segmentation of the background region leads to this high d_{sym} value. The table also shows how O_{MDS} and O_{DIF} obtain low values as the corresponding partitions are very similar to $\mathcal{P}_{GT}$. Note that even if these partitions suffer from small irrelevent regions, the d_{sym} value is not strongly affected. This is explained by the fact that d_{sym} is related to the number of $wrong$ pixels. Thus, it penalizes more in this case the over-segmentation problem.

Tab.3.3 shows the results obtained for the Pavia-Uni-Z_3 image. The number of regions evaluated here is equal to $N_{R_o} = 43$. In contrast to the other tables, O_{DIF} criterion obtains the best results. As previously mentioned, it is not evident to interpret the results of this image. In this case, the merging criteria O_{DIF}, O_{MDS} and RHSEG obtain similar results. Concerning the other merging orders, the stochastic O_{SID} is also better than O_{SAM} in this case. This table also corroborates that non parametrical statistical region model outperforms the classical first order model.

Table 3.2: Symmetric distance for Pavia-Uni-Z_2

Merging Criterion	d_{sym}
O_{SID}	0.175
O_{SAM}	0.303
O_{BAT}	0.186
O_{DIF}	0.132
O_{MDS}	0.108
$RHSEG$ [22]	0.202

The robustness of O_{DIF} to N_{bins} lead to better results as compared to the O_{BAT} criterion.

Table 3.3: Symmetric distance for Pavia-uni-Z_3

Merging Criterion	d_{sym}
O_{SID}	0.427
O_{SAM}	0.434
O_{BAT}	0.303
O_{DIF}	0.239
O_{MDS}	0.269
$RHSEG$ [22]	0.272

Results obtained for the Pavia Center image are presented in Tab.3.4. The number of regions contained in $\mathcal{P}_{GT}$ are in this case equal to 23. As in the first two tables, O_{MDS} achieves also here the best result. However, the second best result is achieved by O_{SAM} in this case. It is observed how the partition of Fig.3.32 (e) is close to the $\mathcal{P}_{GT}$ of Fig.3.27(b). For this example, one of the main problems of O_{BAT} and O_{DIF} is the division of the central building of the image. Concerning the background region, the over-segmentation error is also important in O_{MDS}, O_{BAT}, O_{DIF} and RHSEG. Thus, these merging orders increase their d_{sym} value.

Table 3.4: Symmetric distance for Pavia Center

Merging Criterion	d_{sym}
O_{SID}	0.336
O_{SAM}	0.225
O_{BAT}	0.286
O_{DIF}	0.274
O_{MDS}	0.227
$RHSEG$ [22]	0.48

Finally, the d_{sym} evaluation by Hydice image is reported in Tab.3.5. The obtained results evaluate partitions containing 56 regions with the $\mathcal{P}_{GT}$ partition shown in Fig.3.28(b). The table corroborates the visual results illustrated on Fig.3.33.
O_{MDS} is also here the best merging criterion which can also be seen in Fig.3.33(m)(n)(o). For this criterion, the different zones of the images as building, roads and background are correctly separated. As in the previous data sets, merging orders which rely on the non-parametric statistical region model obviously outperforms the O_{SID} and O_{SAM} criteria. Comparing O_{DIF} and O_{BAT},

the first one achieves a better partition in this case, however, the difference is not very high.

Table 3.5: Symmetric distance for Hydice

Merging Criterion	d_{sym}
O_{SID}	0.54
O_{SAM}	0.474
O_{BAT}	0.35
O_{DIF}	0.33
O_{MDS}	0.236
$RHSEG$ [22]	0.65

The evaluation based on d_{sym} leads to the same conclusions as the one provided by the visual evaluation. Taking into account all experiments, O_{MDS} is the best merging order. The results obtained by the non parametrical statistical region model (O_{MDS}, O_{DIF} and O_{BAT}) outperform the results achieved by the simple first order region model (O_{SAM} and O_{SID}). Finally, comparing with the state of the art, it can be concluded that the partitions contained in the different BPTs are most similar to the different $\mathcal{P}_{GT}$ than the classical RHSEG.
In order to confirm this first quantitative evaluation, another evaluation is performed on the same five hyperspectral images by using d_{asym}.

Hierarchical BPT evaluation by using Asymmetric Distance

A quantitative evaluation of the different BPTs constructed in Sec.3.4.3 is carried out here. The asymmetric distance described in Sec.3.4.1 is used as a measure to perform an evaluation similar to the d_{sym} assessment. The main difference is that the number of regions N_R is not adjusted here to an unique value.
Thereore, the aim is to evaluate the BPT construction by observing the different partitions constructed in a specific range $[N_{Rmin}, N_{Rmax}]$. Note that in the case of the d_{asym} distance, it is not mandatory that $\mathcal{P}$ and $\mathcal{P}_{GT}$ have the same number of regions. Another difference with respect to d_{sym} is that d_{asym} can determine two different quality measures concerning over- and under-segmentation issues. Hence, the different merging orders have been evaluated in three different ways:

1. $d_{asym}(\mathcal{P}_{GT}, \mathcal{P}_{N_R})$ measures the under-segmentation of a partition $\mathcal{P}$ having N_R regions according to $\mathcal{P}_{GT}$

2. $d_{asym}(\mathcal{P}_{N_R}, \mathcal{P}_{GT})$ measures the over-segmentation of a partition $\mathcal{P}$ having N_R regions according to $\mathcal{P}_{GT}$

3. $d^T_{asym} = \frac{d_{asym}(\mathcal{P}_{N_R}, \mathcal{P}_{GT}) + d_{asym}(\mathcal{P}_{GT}, \mathcal{P}_{N_R})}{2}$ measures the trade-off between the under- and the over-segmentation

Fig.3.34 shows the experimental results obtained on the Pavia-uni-Z_1 data set. The number of regions is ranging from $N_{Rmin} = 6$ to $N_{Rmax} = 50$ approximately. These figures show

the evolution of the d_{asym} distances as a function of the number of regions. Fig.3.34(a) shows the over-segmenation, whereas Fig.3.34(b) illustrates the under-segmentation and Fig.3.34(c) the mean d^T_{asym} error. In each figure, various merging orders are identified by different colors.
In Fig.3.34, the various curves present a slope break around $N_R \approx 25$. This is because the partitions at these levels are formed by too few regions in order to be similar to $\mathcal{P}_{GT}$. Note that $\mathcal{P}_{GT}$ has been defined with 33 regions. Thus, the smallest d^T_{asym} for all the merging orders must be around this value. For instance, the O_{DIF} curve shows a minimum range of d^T_{asym} around $N_R > 23$ and $N_R < 38$
Comparing the curves, it is observed how the *minimum* d^T_{asym} evolution is given by O_{MDS}. Fig.3.34(c) can be easily related with Tab.3.1. Both evaluations, lead to classify the merging orders according to their performances as O_{MDS}, O_{DIF}, O_{BAT}, O_{SID} and O_{SAM}. This ordering can be interpreted in Fig.3.34(c) as the elevation of the curves concerning d^T_{asym} value. Comparing the merging orders with RHSEG, it is seen how its yellow d^T_{asym} curve obtains the highest values when N_R is close to the number of regions of the ground truth.
This d^T_{asym} curves can be also related to the visual evaluation. For instance, the high d^T_{asym} value obtained by O_{BAT} is given because the main building of Fig.3.25(a) has disappeared in Fig.3.29(c).

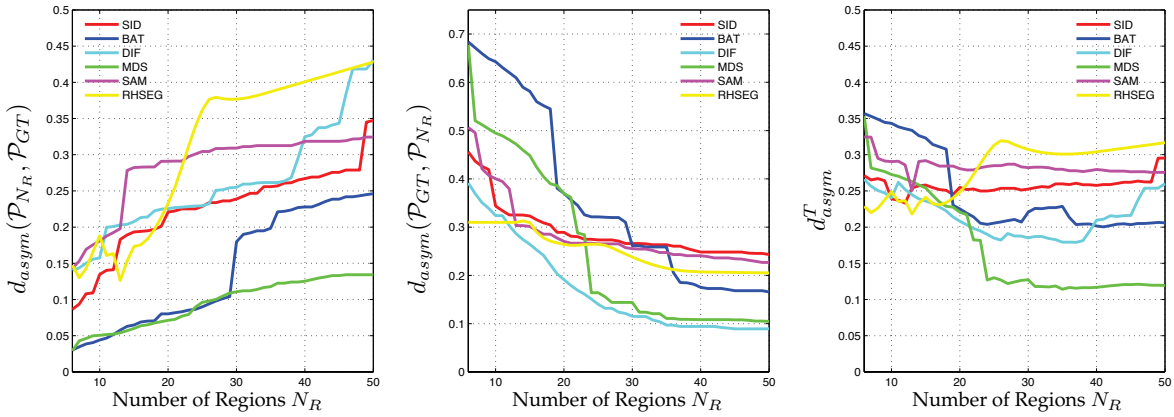

Figure 3.34: Asymmetric distances for Pavia-uni-Z_1

The asymmetric distance results achieved on the Pavia-Uni-Z_2 data set can be seen in Fig.3.35. In this case, the merging orders leading to the best results are O_{MDS}, O_{DIF} and O_{SID}. The results corroborate the d_{sym} evaluation of Tab.3.2. It is seen how the high values of d^T_{asym} comes from the over-segmentation error. This can be observed in the visual evaluation since the main structures of the image have been formed in the high hierarchy levels (where is $N_R \approx 40$) for these three best criteria. Only some small irrelevant regions are found in the partitions ranging from $N_{Rmin} = 6$ to $N_{Rmax} = 50$. This explains the low d^T_{asym} values obtained by O_{MDS}, O_{DIF} and O_{SID} in Fig.3.35(a). Note that for these curves, a *minimum* d^T_{asym}value is found when N_R is similar to the number of regions forming the ground truth.

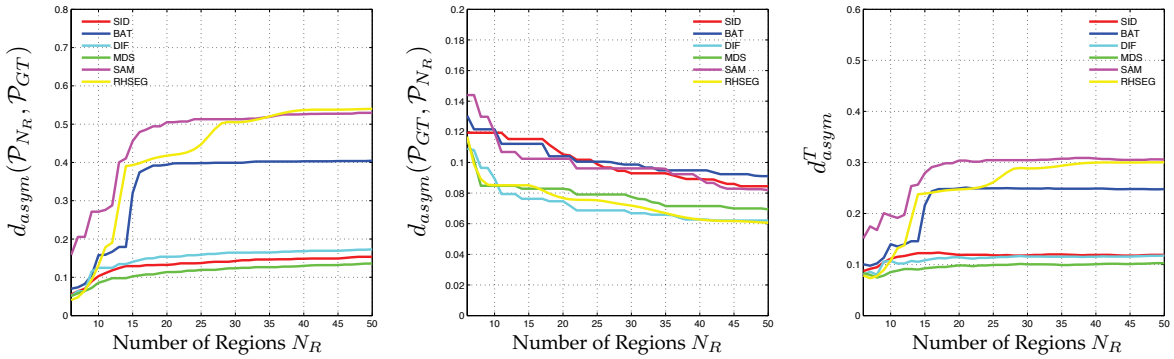

Figure 3.35: Asymmetric distances for Pavia-uni-Z_2

The results on Pavia-uni-Z_3 data set are shown in Fig.3.36. In this case, O_{MDS} and O_{DIF} outperform the other criteria. However, it must be remarked that RHSEG obtains similar results to these criteria when N_R is close to the optimal number of regions $N_R \approx 43$. This example shows how the merging orders O_{SID} and O_{SAM} obtain the worst results. This comes from the under-segmentation error obtained in Fig.3.31(a)(b)(c) and (d)(e)(f). Note that O_{BAT} and O_{DIF} have similar behavior, however, O_{DIF} provides better results.

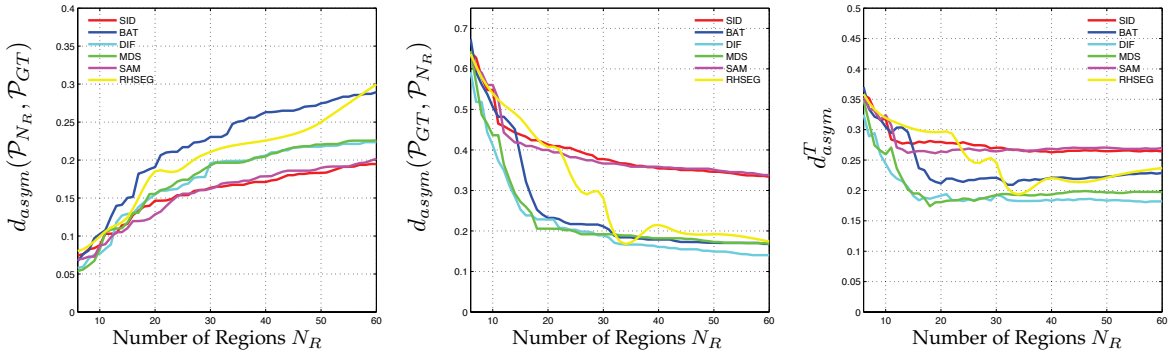

Figure 3.36: Asymmetric distances for Pavia-uni-Z_3

Going on with the evaluation, Fig.3.37 shows the results of Pavia Center. In this case, O_{MDS} is also the best criterion. However, O_{SAM} and O_{SID} obtain similar good d^T_{asym} values. It is explained by the fact that the background of the image is found in a single region in an early stage for these merging criteria. Thus, the other merging criteria suffer from over-segmentation. The curves in this example show how the d_{asym} leads to a *minimum* range of values when N_R is similar to N_{R_o}.

Finally, HYDICE image is evaluated by using d_{asym} in Fig.3.38. The best results are obtained by the merging criteria using the non parametrical statistical region model O_{MDS}, O_{DIF} and O_{BAT}.

Comparing these three criteria in Fig.3.38(c), it is observed that O_{MDS} outperforms the other criteria. Fig.3.38(a) corroborates the over-segmentation problem appearing in Fig.3.33(p)(q)(r).

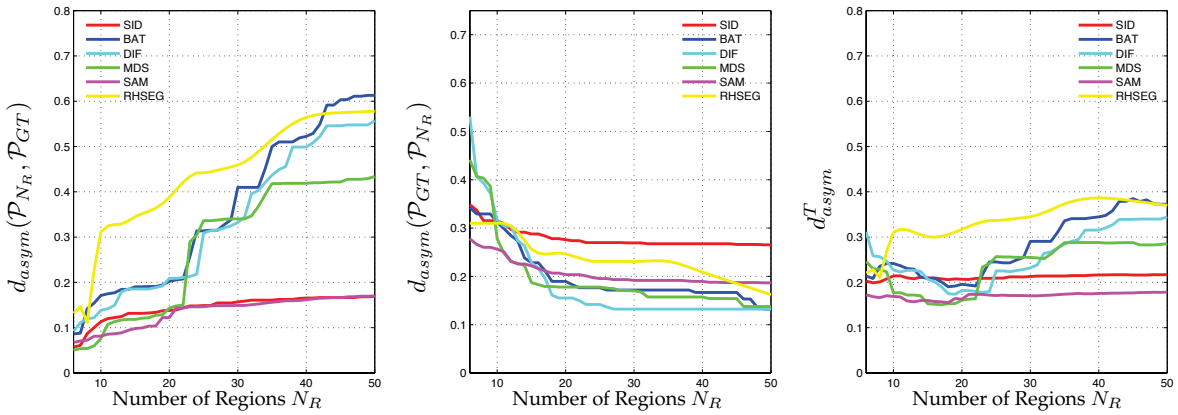

Figure 3.37: Asymmetric distances for Pavia Center

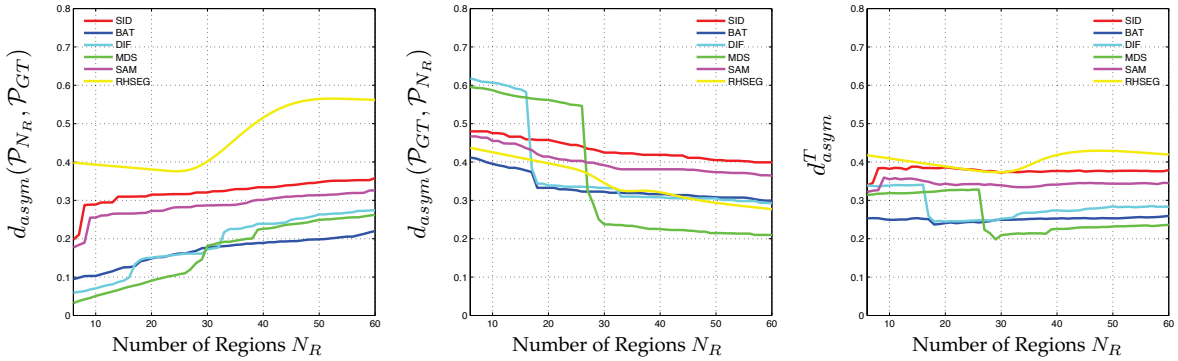

Figure 3.38: Asymmetric distances for Hydice

At this point, the three different evaluations have lead to the same conclusions about the merging orders which are completely detailed in Sec.3.5. Now, the idea is to evaluate the estimation of D_s parameter used in the O_{MDS} criterion.

3.4.4 Experiment 2: Evaluation of D_s selection

A study to evaluate the selection of D_s is detailed here. The goal is to analyze the effect of D_s concerning the obtained results for Pavia-uni-Z_1 and Pavia-uni-Z_2 examples. The presented analysis is based on the same quantitative evaluation performed by using d_{asym}. For both images, setting $N_{bins} = 120$, the idea is to construct different BPTs by using O_{MDS} criterion with different D_s.
For both images, their intrinsic dimension D_s has been estimated to 3 as described in Sec.3.4.3. Thus, the interest is to study how increasing or decreasing D_s value impacts the values of d_{asym} shown in Fig.3.34 and Fig.3.35. Hence, d_{asym} curve is plotted for each data set by using different D_s values.
In the case of Pavia-uni-Z_1, the results of this test are shown in Fig.3.39. It is observed how the estimated $D_s = 3$ value obtains the best results. The figure reveals that if only one component after the dimensionality reduction ($D_s = 1$) is used, the results are the worst ones. In fact, too much information is included in hyperspectral data to be reduced to only one component, even if this dimensionality reduction is done locally between pairs of regions. The other important point to see is how increasing D_s leads to worse results.This is expected given that increasing D_s, the similarity measure between regions is each time less discriminative. Thus, a trade-off in the choice of D_s has to be found.

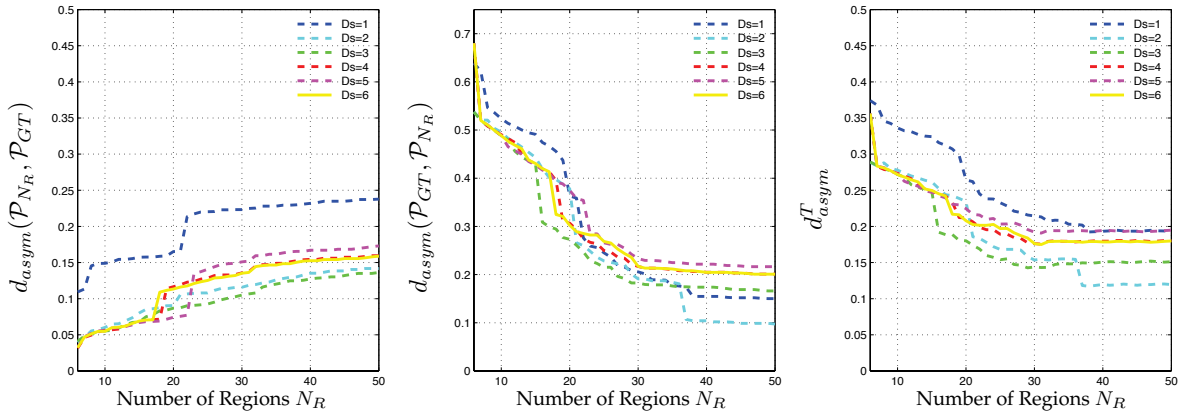

Figure 3.39: Asymmetric distances for Pavia-Uni-Z_1 with different D_s

Another example of D_s evaluation is observed in Fig.3.40 concerning Pavia-uni-Z_2. In this case, $D_s = 3$ and $D_s = 6$ provide the best results. In this example, the correlation effect explained in Sec 3.3.3 can be seen. For instance, larger D_s value ($D_s = 4$ or $D_s = 5$) correspond to higher d^T_{asym} values. However, in the case of $D_s = 6$, d^T_{asym} decreases again. This behavior results from the correlation between the sixth and the third component. As a matter of fact, this is why the D_s value has been estimated to be equal to 3 in Sec.3.4.3.

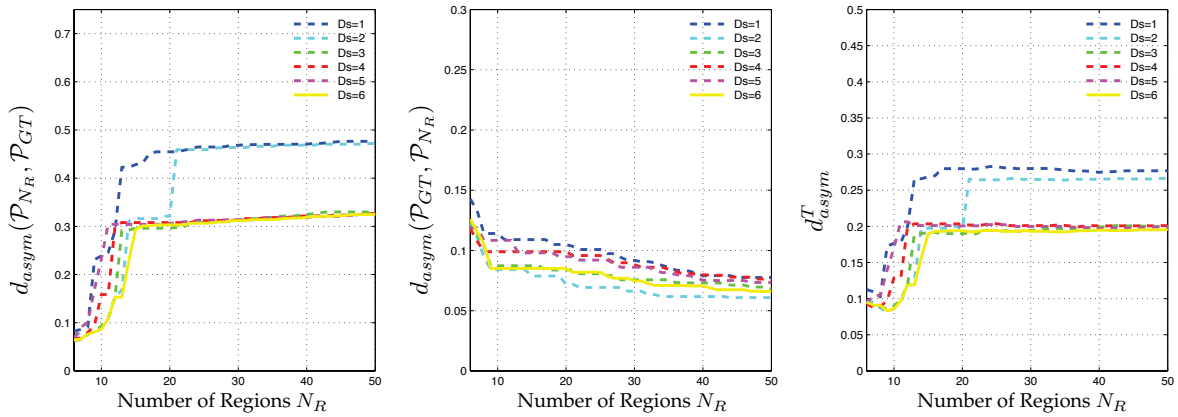

Figure 3.40: Asymmetric distances for Pavia-Uni-Z_2 with different D_s

This evaluation of the D_s estimation has shown the effectiveness of the proposed solution. Besides, it has been seen how the correlation effect between the principal coordinates representing each region is taken into account in our case.

3.5 Conclusions

In this chapter, the construction of Binary Partition Tree as a new region-based representation for hyperspectral imagery has been described. The creation of this hierarchical image description has been based on the definition of a hyperspectral region-merging algorithm.

From a conceptual point of view, an algorithm based on region adjacency graph has been detailed in order to construct BPT. Thus, the notions of region model and merging criterion have been introduced to define the merging sequence. The definition of these two notions in hyperspectral imagery context has been addressed to study different region merging orders. The proposed merging orders have been mainly categorized in two families according to their underlying region models. In this framework, first order parametric model and non parametric statistical one have been explained. The first region model has been previously used to model spectrum data sets. The extension of the non parametrical region model to the case of hyperspectral imagery is one of the major contribution of this PhD. Furthermore, using the notion of image self-similarity as in [24], a strategy to estimate the pdf of initial pixels corresponding to the BPT leaves has been described. To perform this estimation, a noise assessment in the different hyperspectral channels has also been detailed.

Various merging criteria corresponding to the two region models have been investigated in this chapter. While some criteria such as the Spectral Angle Mapper, the Spectral Information Divergence, the Battacharrya and the Diffusion distances have already been considered in the literature, a new measure has been proposed to determine the similarity between two hyperspectral regions. By extracting the first principal components of the regions, an original dependence test based on

MANOVA theory has been proposed to measure the correlation between two spectrum data sets. To our knowledge, the MDS dimensionality reduction technique proposed here introduces a novelty regarding the state of the art and is another contribution of our work. In the literature, authors have focused on the reduction of the dimensionality of hyperspectral data by studying the global image statistics. Contrarily, this Phd has proposed to extract local principal components by studying the local statistics of the regions. This local dimensionality reduction has lead to a more accurate representation of the regions.

Furthermore, a new method to extract the intrinsic dimensionality of the hyperspectral regions has also been described. The idea of correlation between the extracted principal components have been presented here.

A sensitivity study has been carried out to determine the performances of the proposed merging orders. The construction of different BPTs using the different region models and merging criteria has been investigated. Five different hyperspectral images have been selected for this study. Besides comparing the different merging orders, the partitions obtained by BPT are also compared with the state-of-the-art.

The analysis of the partitions contained in the BPT hierarchical levels has been addressed by three different evaluations. Firstly, a visual assessment of the partitions formed during the merging construction has been analyzed. Secondly, a quantitative evaluation by using different quality measures (d_{sym} and d_{asym}) has been performed. These measures have led to determine over-and under-segmentations errors committed during the BPT construction.

The results obtained by the three different evaluations lead to the same conclusions. The non-parametric statistical model clearly outperforms the simple first-order model. Given the complexity of the scene, the first-order model has shown its limitation in order to represent spectrum data sets. Contrarily, non parametrical statistical region model has shown its effectiveness in order to model the spectral variability. In particular, the obtained results have shown a high accuracy and robustness with respect to borders.

Comparing the stochastic and deterministic merging criteria used with first-order region model, SID has obtained better result than SAM.

An evaluation between the different merging criteria proposed to be used with the non parametric statistical region model has also been done. For the three presented similarity measures, Battacharyya distance obtains the worst results which is explained by its lack of robustness in case of histogram misalignment. Thus, an improvement on the results has been introduced by the cross-bin Diffusion distance. Note that this distance gives more precise information taking into account cross-bin contributions. However, the problem of Battacharrya and Diffusion distance is that the spectral information is not jointly studied. Thus, the correlation of the channels and the importance of the relevant information is not taken into account by these merging criteria. Contrarily, the similarity measure proposed via multidimensionality scaling metric has dealt with all these problems. For this reason, the merging order interpreted as the canonical correlation has achieved the best results. In all the cases, the merging criterion based on MDS and the MANOVA dependence test has constructed the best BPT image representation.

Besides the experiments aiming at the evaluation of the partitions obtained during the BPT construction, another experiment has shown the importance of the D_s choice. The number of dimensions used to measure the similarity between hyperspectral regions is an important parameter and an algorithm estimating its value has been proposed.

4

BPT Pruning Strategies

Contents

4.1 Introduction **98**

4.2 Supervised Hyperspectral Classification **103**

4.2.1 Populating the BPT 103

4.2.2 Pruning Decision 105

4.2.3 Experimental results 107

4.3 Segmentation by Energy Minimization Strategy **115**

4.3.1 The $D(\mathcal{N})$ definition 118

4.3.2 Homogeneity measure 118

4.3.3 Experimental Results 119

4.4 Segmentation by recursive spectral graph partitioning **124**

4.4.1 The BPT node weight $\mathcal{W}_{\mathcal{N}}$ 124

4.4.2 Local Branch partitioning 126

4.4.3 Experimental Results 130

4.5 Object detection **135**

4.5.1 Detection of roads 136

4.5.2 Detection of buildings 137

4.5.3 Experimental Results 138

4.6 Conclusions **140**

The aim of this chapter is to demonstrate how the Binary Partition Tree representation is suited for a large number of applications. Taking benefit of the fixed hierarchical region-based tree structure, efficient analysis techniques to process HSI images are studied as pruning strategies.
The different approaches to analyze and prune the tree are successively focused on classification, segmentation and object detection. The particularities associated to each pruning strategy are described in the different sections of this chapter. Experimental results from the different application goals demonstrate the potential of the hierarchical representation for various purposes.

4.1 Introduction

The Binary Partition Tree representation contains a set of partitions represented by a tree structure. Theoretically, the BPT nodes have been constructed in order to represent hierarchically the set of the best coherent regions. In image analysis, coherent regions play an important role in the description of the image. For instance, looking at an image describing a human face, an observer will probably remark : *"There are two eyes, a nose, a mouth...."* . Naturally, this description is mainly due to the semantic content of objects which correspond to coherent regions.
Besides, it is important to note that, in an image, a natural hierarchy seems to exist, that is a structure in its description. For example, the teeth are obviously part of the mouth, therefore in the description they are "inside" the mouth object, which is itself inside the face. BPT hyperspectral image representation meets both issues: 1) the decomposition of the image in terms of regions representing objects and 2) the inclusion relations of the regions in the scene.
The hierarchical description is important since it allows to study regions at different scales. The tree scalability can answer thus to the scale-space image analysis dilemma, where a given image has to be studied at different scales depending on the processing purpose. This highlights the major difference between BPT and classical hierarchical segmentation techniques. BPT is not an application-dependent tree structure, but it is an image representation which can be processed by several application-dependent strategies.
The processing of BPT representation can be understood as the extraction of the non-overlapping regions coded in BPT nodes according to a specific criterion. This analysis of the tree can be performed by a pruning strategy aiming at removing redundant subtrees from the original tree. A subtree is considered redundant if all its nodes can be considered homogeneous with respect to some criterion of interest (homogeneity criterion, e.g., intensity or texture).
Fig.4.1 shows an example of BPT representation for the case of a simple RGB image and assuming that the initial partition is made of regions with a constant color value. This BPT representation can be processed to achieve various application goals, leading to different pruning strategies.

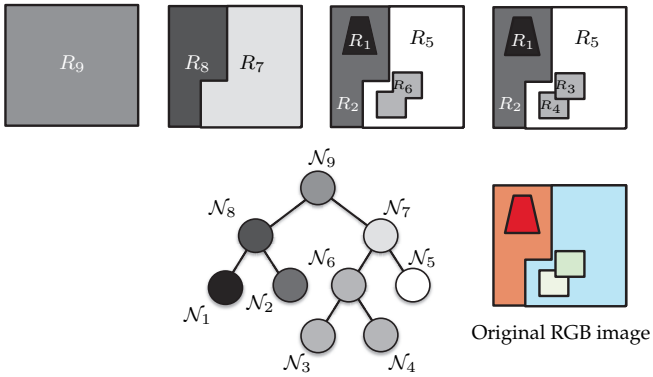

Figure 4.1: Example of Binary Partition Tree representation for RGB image

For instance, in segmentation or classification context, the main pruning goal is the spatial partition of the image by extracting a set of closed, connected (segmentation) or non necessarily connected (classification), and non-overlapping regions with respect to a criterion.
In the case of a supervised classification, the objective is to label each pixel of the image by a previously known class label. Thus, a pruning criterion could be related to the reliability of the induced classification. Concerning the goal of unsupervised segmentation, the criterion to prune the tree nodes could be different. For example, it could be the variance of the pixels forming the region. In both cases, the strategy of each of these criteria is the definition of a pruning function $\mathcal{F}$ which evaluates whether a node should be removed or not.
Fig.4.2 features a segmentation or classification pruning result of the BPT presented in Fig.4.1. In this figure, the green BPT nodes correspond to the nodes that are removed by the pruning function $\mathcal{F}$. Note that given a pruned BPT, the selection of its N_R leaves can be used to obtain an image partition $\mathcal{P}$ composed of N_R regions.
On Fig. 4.2, the leaves of the pruned tree correspond to nodes $\mathcal{N}_6$, $\mathcal{N}_8$ and $\mathcal{N}_5$, respectively. Thus, each BPT node $\mathcal{N}_i$ representing an image region R_i, the partition result $\mathcal{P} = \{R_5\} \cup \{R_6\} \cup \{R_8\}$ is formed by the 3 regions encoded in the set $\mathcal{S} = \{\mathcal{N}_5, \mathcal{N}_6, \mathcal{N}_8\}$.

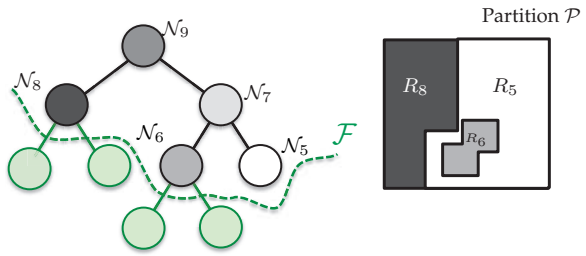

Figure 4.2: BPT pruning example concerning segmentation or classification purposes

Another application of BPT is object detection. An object is an abstract entity generally represented by a region and characterized by a set of features such as color, texture, shape, size, etc. Consequently, it is expected that objects of interest appear as individual nodes inside the BPT. This is an important advantage compared to the object detection techniques that uses pixel-based representation.

In the context of object detection with BPT, the pruning strategy consists in detecting the BPT nodes which are the most likely to be the object. Accordingly, the criterion to process the tree should be based on the specific set of features characterizing the object of interest. An example of object detection purpose is illustrated on Fig.4.1, assuming that a BPT pruning objective can be the extraction of the object formed by the largest green image region. The result of such a pruning is illustrated on Fig.4.3 where the green node corresponds to the BPT node which is detected as the sought object.

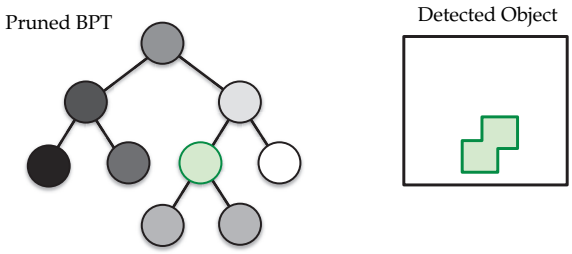

Figure 4.3: BPT pruning example for object detection

Besides segmentation, classification or object detection, other pruning strategies can be specified to process BPT. Filtering and compression are such examples. For these applications, different pruning strategies can be defined in order to minimize the error committed by the filtered or compressed image according to the original one. An example showing this purpose is illustrated on Fig.4.4 where a BPT is used to filter an image. In this example, the filtered image has been obtained by assigning the mean value of the original image to each region contained at the pruned BPT leaves. In this case, the function $\mathcal{F}$ aiming at image filtering is defined in order to minimize the inaccuracy of the filtered image with respect to the original one, by using the *minimum* number of regions.

The shown pruning examples reveal how different criteria studied on BPT nodes lead to different BPT analysis performed using a corresponding function $\mathcal{F}$. The objective of such a function is to take a set of decisions (remove or preserve) on the BPT nodes checking whether they satisfy some properties or not. Thus, in order to take these decisions, some measures should be computed first on BPT nodes before evaluating them. These measures are directly associated to the application goal describing the node characteristics and properties.

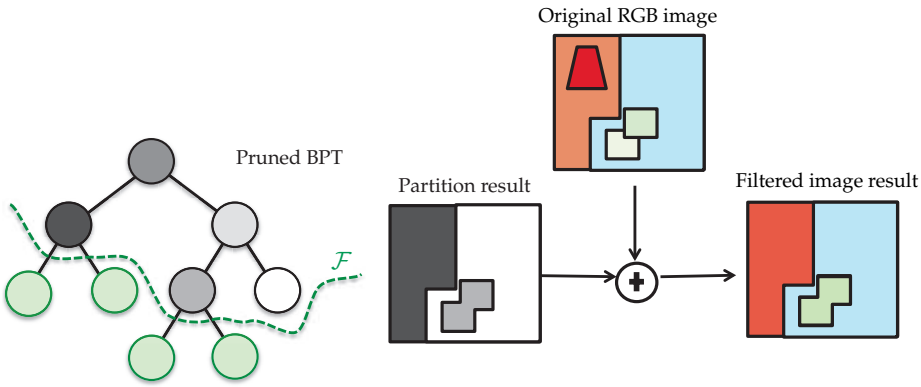

Figure 4.4: BPT pruning example given a filtering task

The BPT pruning strategy can be divided in two steps as illustrated on Fig.4.5 . Given a BPT image representation and a specific application goal, the first stage consists in populating a BPT. The purpose is to assign to each node of the BPT some measures $\mathcal{M}$ computed on the corresponding region. The measure $\mathcal{M}$ is completely defined by the application goal. This step can be done efficiently in terms of computation if the measure can be computed in a recursive manner. This means that the measure associated to a node can be computed from the criterion measured on the children nodes. An example of a recursive measure is the area of the region, i.e the number of pixels contained in a node. With non-recursive measures $\mathcal{M}$ a higher computational cost is implied.

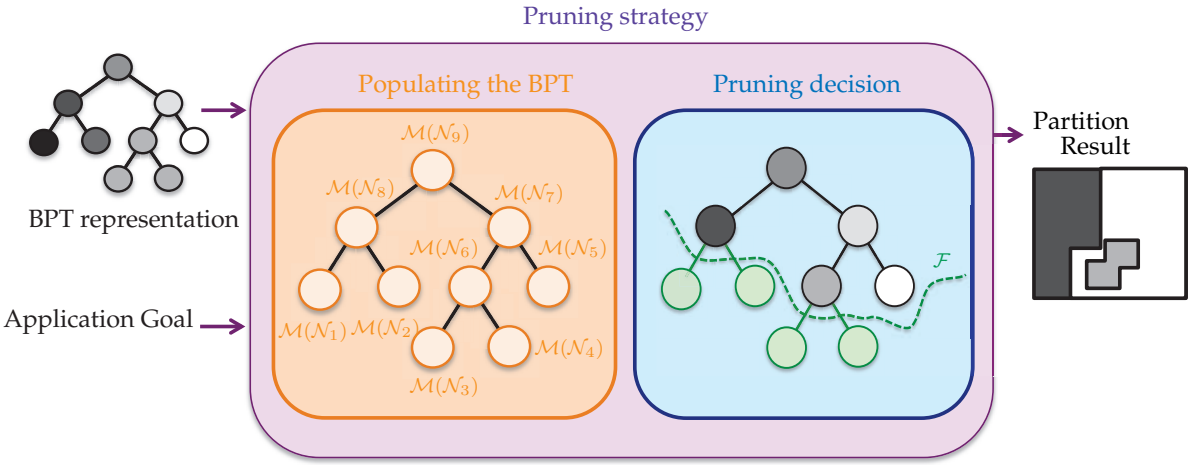

Figure 4.5: Pruning Strategy Scheme

According to this first step, the second pruning stage is the definition of a function $\mathcal{F}$ which analyzes the node measures in order to take the decision to preserve or to remove it. In the case of an increasing function $\mathcal{F}$, the pruning decision can be easily taken. An increasing function $\mathcal{F}$ assessed on a region represented by a BPT node is increasing if: $\forall R_1 \subseteq R_2 \implies \mathcal{F}(R_1) \leq \mathcal{F}(R_2)$. Consequently, if a node has to be removed, their corresponding descendant have to be removed as well. Contrarily, in the case of non-increasing $\mathcal{F}$ function, the pruning decision may be more complex. In this case, two simple strategies are known as *the minimum and the maximum decision*. In the *minimum decision*, a node is preserved if and only if all its ancestors also have to be preserved. Contrarily, the *maximum decision* corresponds to the dual behavior. Thus, a node is removed if and only if all its descendant nodes also have to be removed. The choice is also related to the tree analysis which can follow a bottom-up or a top-down strategy.

Following the strategy described in Fig.4.5, different pruning strategies are presented in the next Sections. Firstly, a supervised pruning strategy aiming at hyperspectral image classification is proposed. According to the classification goal, a specific populating of the BPT node and the corresponding pruning decision is detailed. For this application, some experimental results are shown in order to illustrate the advantage of using a region-based representation for classification.

Besides classification goal, a second purpose involving the unsupervised segmentation of hyperspectral images is proposed in Sec.4.3 and Sec.4.4. In this context, two different pruning strategies are discussed. The first approach consists in minimizing an energy function on the BPT structure to reach a global *minimum* of the cost associated to a partition. The second approach involves a local pruning decision on the BPT branches.These pruning decisions are computed by interpreting the BPT branch cut as a spectral graph partitioning problem.

Finally, an object detection pruning strategy is presented in Sec.4.5. In this last section, two examples of object recognition are proposed in an urban scene. Specifically, the roads and the building of the HYDICE urban scene are detected by the proposed technique.

4.2 Supervised Hyperspectral Classification

In this section, an example of tree processing aiming at classifying hyperspectral images is discussed. Hyperspectral image classification is the process of labeling a pixel or group of pixels on the basis of their spectral and spatial similarities. In the past, the classification of hyperspectral data has been tackled using various approaches (See Chapter 2). In the case of supervised techniques, representative samples, called training samples, are used to specify the spectral attributes of the different classes composing the scene. These class spectral features are then used by the algorithm to perform the pixel labeling. To this end, the classification algorithm compares the pixels of the image with the training samples features. Accordingly, a pixel is then labeled given its spectral characteristics by the most likely class of the training samples. The complete labeled image is known as a classification map.

According to the supervised classification objective, the goal of the pruning strategy described here aims at constructing a classification map for hyperspectral data. Note that using the pruned tree, a partition describing the pixel class assignment can be easily constructed by selecting the leaf nodes of the resulting pruned tree (See Fig.4.2). The pruning strategy discussed in this section corresponds to a bottom-up analysis of the BPT. The particular criterion used here directly depends on our classification goal.

As it has been explained at the beginning of this chapter, the analysis of the tree consists of two important steps. The first one computes and assigns specific region descriptors to each BPT node $\mathcal{N}$. The second step is the pruning decision whose task is to evaluate a cost associated to the region descriptors and eventually to decide where to prune the tree. In this classification context, both steps are explained in the following sections.

4.2.1 Populating the BPT

Given the classification aim, the main information, or node descriptor, to define our pruning involves the class probability distribution $P_{\mathcal{N}}$. This probability distribution is a vector containing the probabilities that the node belongs to each class $\mathcal{C}_i$. The reliable estimation of these probabilities is a very challenging task [3]. This is due to the small number of training samples and the high number of features.

To address this issue, class probabilities are estimated in a supervised way by using a multi-class classifier. From our knowledge, the most popular discriminative classifier in the hyperspectral image community is the support vector machines classifier (SVM), which is characterized by its ability to effectively deal with large input spaces (and to produce sparse solutions) using limited training samples. This classifier has proved to be well suited for the classification of hyperspectral data [1] [4][5] [6].

As SVMs is a supervised algorithm [68], the kernel parameters should be computed first using a training step. Here, the SVM training is done by using some leaf nodes which correspond to single spectra. The selection of these nodes directly depends on the available ground truth. The kernel function constructed during the training process enables to map an input spectrum to a

high-dimensional feature space, in which a SVM is used to give the classification result.
Once the kernel function is constructed, it is used to classify all the BPT nodes by assigning to each of them their $P_{\mathcal{N}}$. Fig.4.6 shows the process of populating BPT. On the left, the orange leaves are used to train the SVM classifier. Therefore, the SVM classifier uses the constructed kernel function to populate all the BPT nodes with their class probability distribution.

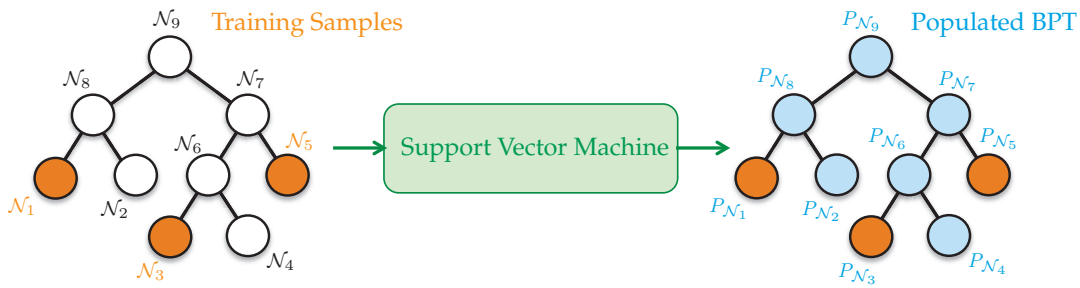

Figure 4.6: How BPT is populated using SVM Classifier

In order to classify the data, the kernel function usually uses a spectrum as input parameter. However, note that in our case, each BPT node represents a region formed by a set of spectra, not by a single spectrum. For this reason, instead of using the spectrum of the pixel itself, each BPT node $\mathcal{N}$ should be modeled by its mean spectrum before applying the kernel function on the node.
At this point, the goal is to use $P_{\mathcal{N}}$ in order to evaluate the misclassification rate $\mathcal{R}_{\mathcal{N}}$ of the nodes. Misclassification rate can be understood as the error of assigning a wrong class to a node. The use of misclassification rates has been previously studied in classification based on decision trees[50]. In these decision trees, the misclassification $\mathcal{R}_{\mathcal{N}}$ is totally linked to the class probability distribution $P_{\mathcal{N}}$. Therefore, a reliable classification result of $\mathcal{N}$ implies a likely *minimum* misclassification rate. Thus, the misclassification rate for a node $\mathcal{N}$, having an area composed of $\mathcal{A}_{\mathcal{N}}$ pixels, can be expressed as:

$$\mathcal{R}(\mathcal{N}) = \mathcal{A}_{\mathcal{N}}(1 - \max_i \mathcal{P}_{\mathcal{N}}(\mathcal{C}_i)) \tag{4.1}$$

The misclassification rate of Eq. 4.1 can have two important problems in our context. The first problem comes when a node is formed by merging a very large region with a small one. Assume the node $\mathcal{N}$ is formed by two sibling nodes $\mathcal{N}_L$ and $\mathcal{N}_R$ having an area relation such that $\mathcal{A}_{\mathcal{N}_L} >> \mathcal{A}_{\mathcal{N}_R}$. If $\mathcal{N}_L$ belongs to class $\mathcal{C}_i$ and $\mathcal{N}_R$ to class $\mathcal{C}_j$, the union of both regions will belong to $\mathcal{C}_i$ since the region contained in $\mathcal{N}_L$ is much larger than $\mathcal{N}_R$. Thus, the reliability of the SVM classifier for the node $\mathcal{N}$ will not significantly change even if both regions belong to two different classes.
The second important problem of Eq. 4.1 is the presence of mixed pixels in the image forming mixed regions. The mixed pixels in hyperspectral context are spectra which are formed with some materials involving different ground truth classes. Consequently, pixels belonging to these regions do not have a high probability of belonging to any given class. As a result, an important

misclassification rate can appear for this type of regions. In order to solve these problems, the misclassification rate of Eq. 4.1 for non-leave nodes has been modified as follows:

$$\mathcal{R}(\mathcal{N}) = \mathcal{A}_{\mathcal{N}}(1 - BC(\mathcal{P}_{\mathcal{N}_R}, P_{N_L})) \tag{4.2}$$

where $BC(\mathcal{P}_{\mathcal{N}_R}, \mathcal{P}_{\mathcal{N}_L})$ is the Battacharryya coefficient between the probability class distributions of the left and the right children of $\mathcal{N}$. With N_c different ground truth classes, the Battacharrya coefficient in this classification context is described by

$$BC(\mathcal{P}_{\mathcal{N}_R}, \mathcal{P}_{\mathcal{N}_L}) = \sum_{i=1}^{N_c} \mathcal{P}_{\mathcal{N}_R}(\mathcal{C}_i)\mathcal{P}_{\mathcal{N}_L}(\mathcal{C}_i) \tag{4.3}$$

Of course, this expression cannot be used for leaf nodes as they have no children. Hence, two types of misclassification rates are used : 1) Eq. 4.1 is the misclassification rate used for BPT leaves and 2) Eq.4.3 is the one used for non-leaf nodes. The modification of Eq. 4.3 solves the weak area relation problem allowing to detect if two reliable but different regions are going to be merged in an unique node. However, as this last equation is sensitive to small regions, a node formed by a very small wrongly classified region (for instance 1 pixel) can give a high $\mathcal{R}(\mathcal{N})$. Thus, this weakness should be solved setting that if a node has a very small area (for instance smaller than 3), its parent will have a very small $\mathcal{R}(\mathcal{N})$. In other words, very small regions cannot cut BPT branches since they are not considered as reliable.

4.2.2 Pruning Decision

The pruning analysis discussed in this section corresponds to a bottom-up analysis of the BPT evaluating the miss-classification rates computed in Sec.4.2.1. This evaluation is addressed in order to decide if a sub-tree $\mathcal{T}_s$ hanging from a node $\mathcal{N}$ can be pruned. The decision is taken by a *maximum decision* rule which considers that a node is removed if and only if all its descendant nodes can be removed.

This pruning decision compares the misclassification rate at node $\mathcal{N}$ with the misclassification rate corresponding to the set of leaf nodes of the sub-tree $\mathcal{T}_s$. Fig. 4.7 illustrates the concepts presented in the evaluation of a non-leaf node $\mathcal{N}$. The sub-tree $\mathcal{T}_s$ rooted at the node $\mathcal{N}$ is highlighted in red. The idea is to verify whether the three leaves l_1, l_2 and l_3 can be replaced by $\mathcal{N}$. To this goal, the misclassification rate associated to the node $\mathcal{N}$ is compared with the error associated to the 3 leaves in $\mathcal{T}_s$.

Mathematically, the function defining the pruning criterion $\mathcal{F}_c(\mathcal{N})$ is given by

$$\mathcal{F}_c(\mathcal{N}) = \frac{\mathcal{R}(\mathcal{N}) - \sum_{l_i \in T_s} \mathcal{R}(l_i)}{\mathcal{A}_{\mathcal{N}}} \tag{4.4}$$

It should be noticed that this function is not increasing and this is the reason why a *maximum decision* rule is used.

Given the definition of $\mathcal{F}_c(\mathcal{N})$, the aim is to detect when $\mathcal{F}_c(\mathcal{N})$ leads to low values implying that

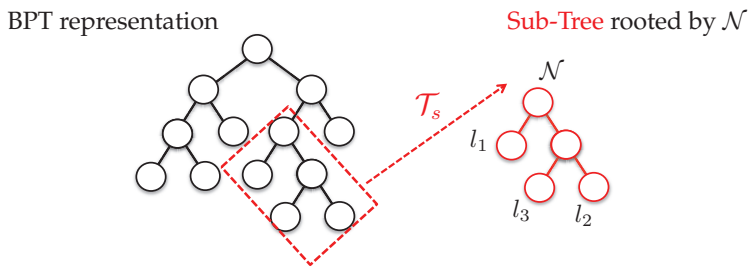

Figure 4.7: Sub-tree definition

a sub-tree can be pruned. To this end, the function $\mathcal{F}_c(\mathcal{N})$ along the BPT branches is evaluated by a bottom-up analysis. Starting from the BPT leaves, the purpose is to identify when $\mathcal{F}_c(\mathcal{N})$ is higher than an allowed threshold α_C. An example is shown in Fig.4.8.
Arising from the green BPT leaf, the $\mathcal{F}_c(\mathcal{N})$ values of its ancestor nodes situated in the blue branch are evaluated. The four obtained $\mathcal{F}_c(\mathcal{N})$ values are shown on the right. In this example, the α_C value is the *maximum* misclassification rate that can be committed at a BPT node. Considering this, Fig.4.8 shows how the $\mathcal{F}_c(\mathcal{N})$ value of the third node is higher than the allowed threshold. Consequently, according to the *maximum decision* rule, this node cannot be pruned and neither can its ancestors. As a result, the green nodes of Fig.4.8 will be pruned whereas the remaining blue nodes will form the pruned BPT.

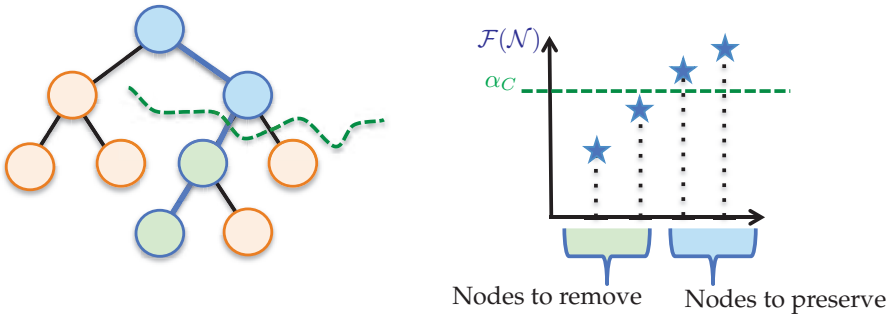

Figure 4.8: Example of *maximum* decision rule pruning decision

Note that the α_C value determines the size of the pruned BPT. When α is small, the penalty term is small, so the size of the pruned tree will be large. Contrarily, as α_C increases, the pruned BPT has fewer and fewer nodes. The pruning strategy described here has lead to the BPT simplification by removing sub-tree composed by the same class. Therefore, using the pruned BPT, a classification map of the hyperspectral image can be constructed. The idea is to use the partition formed by the leaves of the pruned BPT. Therefore, the classification map is constructed by assigning to each region of the resulting partition, the class $\mathcal{C}_j$ which has the highest probability $\mathcal{P}_{\mathcal{N}}(\mathcal{C}_j)$ determined by the SVM classifier.

4.2.3 Experimental results

Some experimental results of the classification pruning technique described above are presented in this section. The pruning evaluation is carried out on two well-known remote sensing hyperspectral images. The purpose is to perform a supervised classification of these images and to evaluate the obtained results by using their available ground truth. The assessment of the results is addressed quantitatively by evaluating the specific class accuracy and the number of nodes removed by the pruning strategy. Furthermore, a visual evaluation is carried out by analyzing the classification maps obtained by different data sets.

Indian Pines

In the first pruning experiment, Indian Pines AVIRIS hyperspectral data containing 200 spectral bands having a spatial dimension of 145 X 145 pixels is used. Fig. 4.9(a) shows a RGB composition of this data set. In this image, it can be seen how a simple RGB composition of the hyperspectral data does not allow to discriminate between the different materials. The whole image is formed by 16 different classes having an available ground truth as illustrated on Fig. 4.9(b). For this image, three different BPT are constructed using the following merging criteria O_{SID}, O_{DIF} and O_{MDS},respectively.
In the case of non parametric statistical region model, the histogram quantification is set to $N_{bins} = 150$. Concerning the merging criterion O_{MDS}, the estimated D_s value defining the number of principal components is equal to 3.

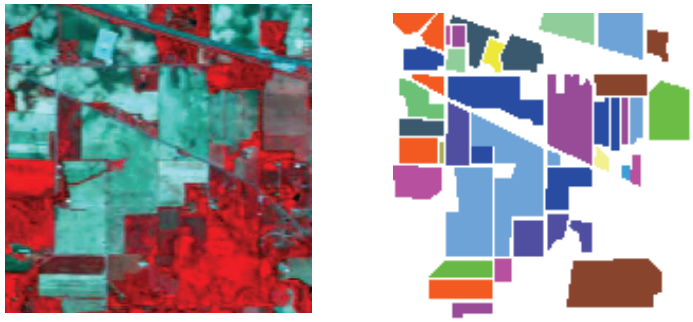

(a) (b)

Figure 4.9: (a) RGB Indian Pines Composition. (b) Available Ground Truth image

Once the three different BPT have been created, the populating BPT strategy described in Sec.4.2.1 is performed. The SVM classifier is trained by selecting randomly 20% of samples for each class from the reference data described in Fig. 4.9(b). Using the constructed SVM model and the BPT representation, the $\mathcal{P}_{\mathcal{N}}$ probability distributions are assigned to all BPT nodes in order to compute their misclassification rates.
In this example, different α_C threshold values are used to compare the different classification

maps obtained by the three BPTs. Two different evaluations are carried out for different α_C values ranging from 0 to approximately 0.4. It has been considered that α_C higher than 0.4 means a high misclassification error. The first evaluation corresponds to the number of BPT leaves obtained after the pruning. This measure gives information about the BPT construction. For a given class accuracy, if a pruning strategy removes more BPT nodes from a tree, this means that the BPT has been better constructed. The second evaluation corresponds to the overall class accuracy obtained by the classification maps achieved by the BPT pruning. Both experiments are shown in Fig.4.10.

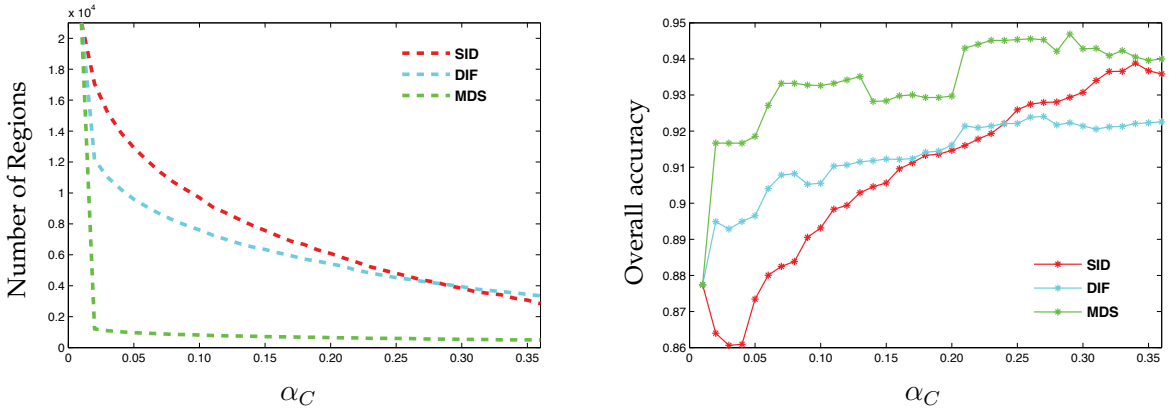

(a) Number of Regions versus α_C

(b) Overall Accuracy versus α_C

Figure 4.10: Indian Pines Pruning Evaluation

Fig.4.10(b) shows how the highest accuracies are obtained with $\alpha_C \approx 0.30$ where the results obtained by O_{MDS} outperforms the other results for all the α_C values. However, it should be noticed that in some cases, O_{SID} can lead to similar classification accuracies than O_{MDS}. Contrarily, the merging criterion O_{DIF} achieves the worst results. These results can be explained by the fact that the criterion processes separately the different bands and this turns out to be a serious drawback for classification.

Comparing the curves of O_{SID} and O_{MDS} in Eq.4.4, it could be said that both criteria have similar performances in a given α_C interval. However, comparing the results on the curves of the Fig.4.10(a), it can be remarked how O_{MDS} removes more BPT nodes in its pruning. Note that the number of regions corresponding to the pruned BPT leaves, is much lower for O_{MDS} than for the other two merging criteria.

Following this evaluation, the classification maps corresponding to the highest overall accuracy of Eq.4.4(b) are shown on Fig. 4.11. The obtained results are compared with the classical SVM pixel-wise classification of Fig. 4.11(a). The same training samples are used for all the classification results.

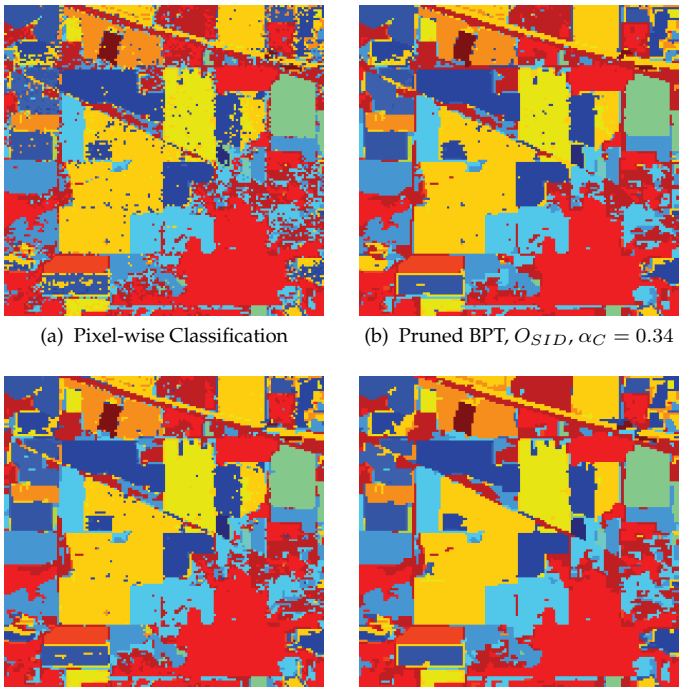

(a) Pixel-wise Classification (b) Pruned BPT, O_{SID}, $\alpha_C = 0.34$

(c) Pruned BPT, O_{DIF}, $\alpha_C = 0.27$ (d) Pruned BPT, O_{MDS}, $\alpha_C = 0.29$

Figure 4.11: Obtained Classification map using 20% of training samples

Looking at the BPT pruning results, it can be observed that the classification maps are formed by quite homogeneous regions. In particular, the BPT nodes selection according to the proposed pruning criterion provides a less noisy classification. This can be noticed in the case of Fig. 4.11(d) corresponding to the O_{MDS} merging criterion. The obtained results also corroborate the BPT performances since extracted nodes reflect semantic real-world objects of the image. It should be remarked that Indian Pines has a high spectral variability due to its low spatial resolution.
According to Fig. 4.11, Table 4.1 illustrates the corresponding class-specific and the global classification accuracies. The best class accuracies are highlighted in red. Observing these results, the proposed BPT pruning classification improves the classification accuracies for almost all the classes compared to pixel-wise classification. Studying the different merging criteria, O_{MDS} leads to the best results.

Table 4.1: Class Specific Accuracy using 20% of training samples

Class	**Simple SVM**	**Pruned BPT** O_{SID}	**Pruned BPT** O_{DIF}	**Pruned BPT** O_{MDS}
1	75.61	82.93	82.93	80.49
2	83.46	92.75	92.19	92.75
3	84.35	95.21	96.81	96.01
4	76.14	96.59	92.05	91.48
5	94.37	95.44	95.17	95.71
6	97.15	97.65	98.40	97.50
7	92.31	88.89	88.89	88.89
8	98.09	99.73	99.18	99.73
9	90	100	85.71	100
10	83.06	88.02	89.94	88.57
11	91.52	97.24	96.06	99.73
12	86.55	92.62	91.76	94.36
13	96.22	97.48	98.11	98.76
14	95.57	97.53	97.89	97.94
15	67.72	84.21	80.35	97.89
16	91.67	95.83	93.06	97.22
Overall	87.74	93.89	92.40	94.69

In order to study the influence of the number of training samples, a second experiment has been carried out by selecting now randomly 35% of samples for each class. In this second experiment, the BPT constructed by O_{MDS} is also evaluated against the pixel-wise classification. In this case, Fig.4.12 shows the classification maps obtained for this second training data set for $\alpha_C = 0.2$. The results according to the last classification map can be seen in Tab.4.2. Looking the obtained results for this second experiment, it is observed how increasing the number of training samples improves the accuracy of both schemes. In the case of the pixel-wise classification, the results have improved by around 2 percentage points as compared to Tab.4.1. Concerning the results obtained by BPT pruning, the accuracy has increased by more or less the same percentage.

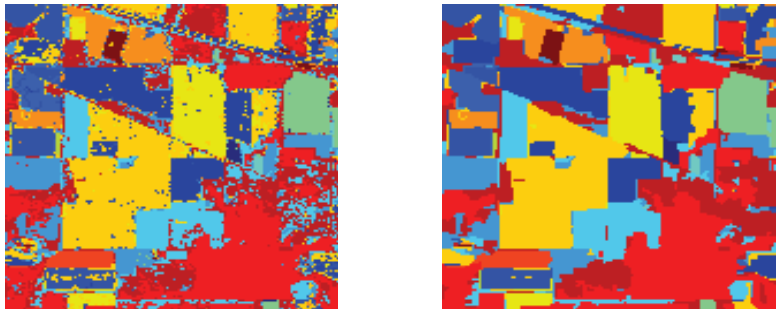

(a) Piwe-wise classification (b) Pruned BPT with $\alpha_C = 0.20$

Figure 4.12: Obtained Classification map using 35% of training samples

Table 4.2: Class Specific Accuracy using 35% of training samples

Class	Simple SVM	Pruned BPT
1	78.05	90.24
2	87.08	97.03
3	87.06	97.28
4	78.98	98.86
5	94.37	95.17
6	96.97	98.93
7	92.31	92.41
8	98.64	99.46
9	92.41	90
10	85.95	90.22
11	93.41	98.65
12	89.37	93.06
13	98.11	98.74
14	97.01	99.49
15	72.28	97.89
16	90.28	98.61
Overall	89.52	96.00

ROSIS Pavia University

The second data set used to evaluate the classification pruning corresponds to Pavia University from the ROSIS sensor. This image has been previously presented and used in Sec.3.4.2. A RGB composition for the whole image is shown in Fig.4.13. For this data set, also three different BPTs have been constructed as it has been done in the previous experiment. Accordingly, the different merging criteria O_{SID} , O_{DIF} and O_{MDS} are used for the BPT construction step. The parameters concerning the BPT construction are the same as in Sec 3.4.3 ($N_{Bins} = 100$ and $D_s = 3$). Some hierarchical levels concerning these BPT constructions can be seen in Appendix.7.4. As previously done, the purpose of this experiment is to classify this hyperspectral data by using the pruning strategy presented in Sec4.2

Figure 4.13: Pavia University RGB Composition

The pruning strategy is performed on the three different BPTs to compare the obtained results which can be used as a measure of BPT quality. Also, in order to show the BPT advantage, the different classification results obtained by the different constructed BPTs are compared with a pixel-wise classification. Firstly, a SVM classifier is trained with a training set which is further detailed in [89]. Afterward, the different BPT nodes are classified according to Fig.4.6.
After this step, the bottom-up analysis of the tree evaluating the pruning decision function $\mathcal{F}_c$ is carried out. In this experiment , the same range of α_C values is studied in order to evaluate the different results. These results are shown in Fig.4.14.

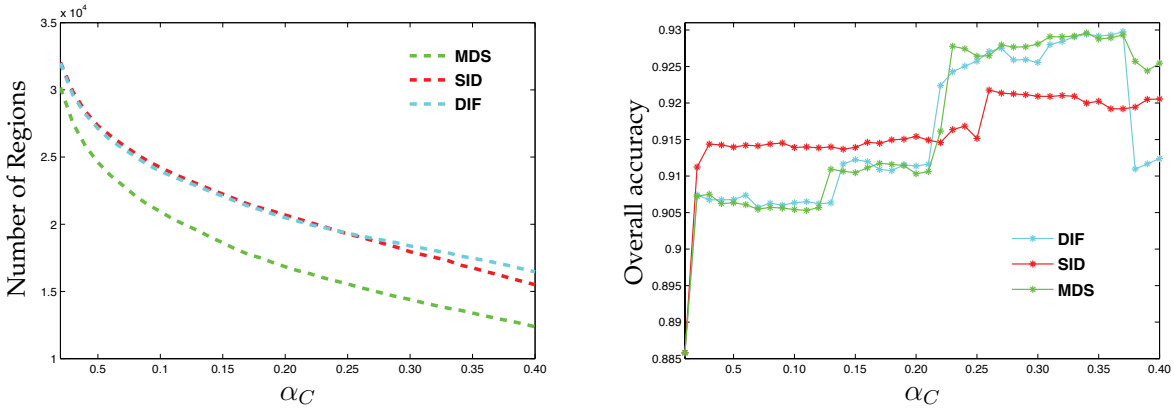

(a) Number of Regions versus α_C

(b) Overall Accuracy versus α_C

Figure 4.14: Pavia University Pruning Evaluation

First, Fig.4.14(a) shows the number of regions contained in the pruned tree versus parameter α_C. As can be seen, the number of regions decreases when α_C increases. Comparing the different merging criteria in Fig.4.14(b), it can be observed that O_{MDS} and O_{DIF} outperform the results obtained by O_{SID}. Comparing O_{MDS} and O_{DIF}, it can be noticed that the *maximum* of both curves is similar. In contrast, Fig.4.14(b) shows that O_{MDS} seems to achieve better results since, given a specific accuracy, the pruned tree contains much less regions. The classification maps associated to the *maximum* accuracy of each merging criteria are illustrated in Fig.4.15. The classification map obtained with a pixel-wise classification is also shown.
For the different constructed BPTs, Fig.4.15 shows how the results obtained by BPT pruning outperform the classical pixel-wise classification. By reducing the classification noise, BPT pruning improves the classification accuracy preserving most of the edges and shapes. Regarding the class specific accuracy of the classification maps of Fig.4.15, results can be observed in Tab.4.3. It can be observed how the hyperspectral classification by using a BPT pruning strategy improves by around 4 percentage points the results obtained by the pixel-based image representation (first column of Tab.4.3).

Table 4.3: Class Specific Accuracy by Pavia University

Class	**Simple SVM**	**Pruned BPT** O_{SID}	**Pruned BPT** O_{DIF}	**Pruned BPT** O_{MDS}
1	85.93	88.43	89.97	88.84
2	76.66	73.45	75.55	71.69
3	70.46	85.28	87.52	91.95
4	97.55	94.84	93.96	95.14
5	99.55	98.81	98.96	98.81
6	91.99	96.06	97.43	97.08
7	92.48	98.65	99.02	99.02
8	92.31	96.82	96.80	98.13
9	99.26	97.25	97.57	95.99
Overall	88.58	92.18	92.98	92.96

The classification results shown in Tab.4.3 provide the differences in terms of class accuracies but do not highlight the differences in terms of region shape and contour preservation.

Conclusions

The experimental results shown for both hyperspectral images have corroborated how a classification pruning strategy can outperform a pixel-wise classification. The two experiments have shown that O_{MDS} is the best merging order in this case. This merging criterion has achieved the best accuracy results and reduced the number of regions.
In this pruning, the *maximum* rule decision has led to a valid pruning strategy providing good results. Indeed, in the future, it may be useful to investigate alternative strategies to deal more robustly with the non increasingness of the pruning criterion.

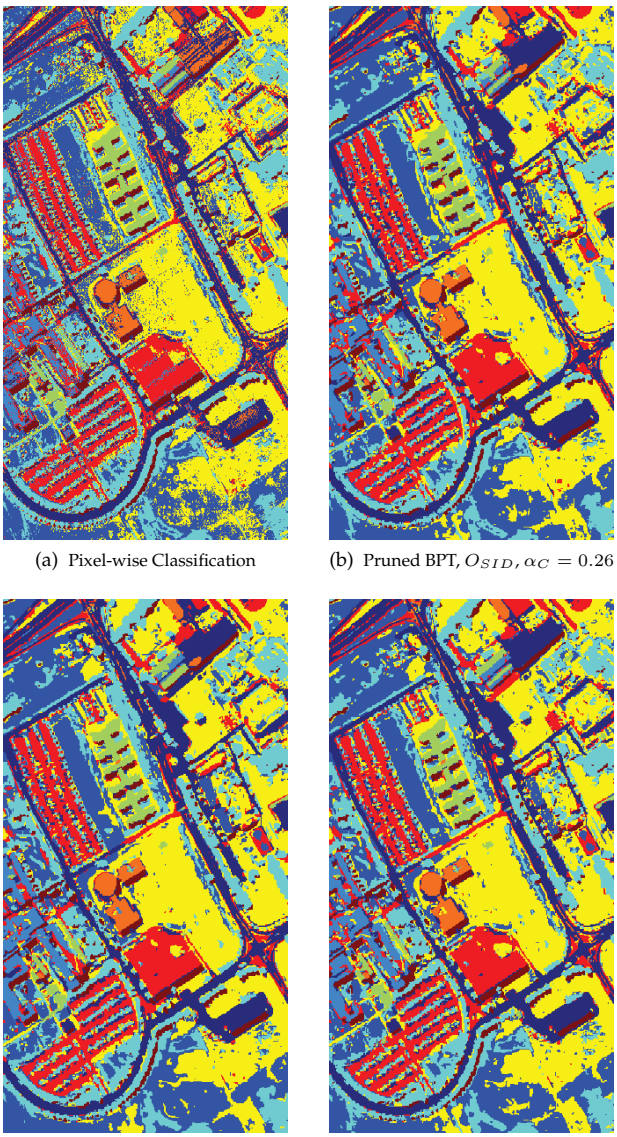

(a) Pixel-wise Classification

(b) Pruned BPT, O_{SID}, $\alpha_C = 0.26$

(c) Pruned BPT,O_{DIF},$\alpha_C = 0.37$

(d) Pruned BPT,O_{MDS},$\alpha_C = 0.34$

Figure 4.15: Obtained Classification maps

4.3 Segmentation by Energy Minimization Strategy

The segmentation of hyperspectral image using BPT representation is studied in this section. As in the case of classical hierarchical segmentation techniques, the most easy way to obtain a segmentation result from BPT representation consists in choosing a partition obtained during the merging sequence construction. In this supervised classical approach, the result is related to the desired number N_R of regions. This approach can suffer some drawbacks since depending on the value of N_R, more different or interesting regions cannot always be found during the construction of the merging sequence . This issue can be solved by the BPT scalability since regions can be obtained from the different scale levels.

Hence, the purpose of this section is to describe a supervised segmentation technique which extracts the N_R most different regions from the BPT structure. The main interest is to show that the intelligent selection of N_R BPT nodes can improve the results obtained by the $N_p - N_R$ merging steps on the initial partition (where N_p is the number of pixels in the image). To this end, a pruning strategy based on an energy minimization strategy is described in the following.

Energy minimization is an essential issue in computer vision. In the last few years, this increasing popularity has been the result of the successes of graph cut based minimization algorithms in solving many different vision problems [62] [63] [64] [65]. In computer vision the term energy minimization is popularly used to describe approaches in which the solution to the problem is determined by minimizing a function called the "energy". The solution of the minimization problem can be solved efficiently in the case of convex as well as concave functions.

The pruning is defined through the minimization of a convex function namely the *pruning cost* $E_{\mathcal{P}}$. Fig.4.16 shows an example of $E_{\mathcal{P}}$ minimization where the partition result $\tilde{\mathcal{P}} = \{R_5\} \cup \{R_6\} \cup \{R_8\}$ is formed by the three regions encoded in the set $\mathcal{S} = \{\mathcal{N}_5, \mathcal{N}_6, \mathcal{N}_8\}$.

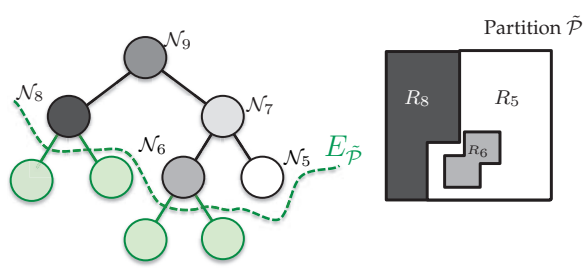

Figure 4.16: Example of pruning through $E_{\mathcal{P}}$ minimization

In mathematical optimization, the method of Lagrangian multipliers provides a strategy for finding the *minima* of a function subject to constraints. Following this approach, given a partition $\mathcal{P}$, formed by the set of BPT nodes $\mathcal{S}$, the pruning cost $E_{\mathcal{P}}$ is then formulated as follows:

$$E_{\mathcal{P}} = \underbrace{\sum_{\forall \mathcal{N}_i \in \mathcal{S}} D(\mathcal{N}_i)}_{D_{\mathcal{P}}} + \lambda \underbrace{\sum_{\forall \mathcal{N}_i \in \mathcal{S}} C(\mathcal{N}_i)}_{C_{\mathcal{P}}} \quad \text{subject to} \quad C_{\mathcal{P}} \approx C_0 \tag{4.5}$$

where λ is the so-called Lagrange parameter and $C_{\mathcal{P}}$ represents the constraints.
The first term $D_{\mathcal{P}}$ is the sum of all the errors $D(\mathcal{N}_i)$ committed at the nodes contained in $\mathcal{S}$. The error $D(\mathcal{N})$ to what has been lost if all pixels contained in the sub-tree rooted at $\mathcal{N}$ are replaced by $\mathcal{N}$. This term will be explained in details in Sec.4.3.1. The restriction parameter $C_{\mathcal{P}}$ has been defined here as the number of nodes contained in $\mathcal{S}$. According to the $C_{\mathcal{P}}$ definition, the value of the constraint on a node is given by $C(\mathcal{N}_i) = 1$. The restriction parameter is completely necessary since the algorithm is looking for an optimal partition $\tilde{\mathcal{P}}$ having a number of regions close to C_0 (optimally, the number of regions of $\mathcal{P}_{GT}$.). Note that without any restriction, the optimal partition would involve only regions made of one pixel.
Under this framework, the BPT pruning strategy aims at obtaining the partition $\tilde{\mathcal{P}}$ which minimizes $E_{\tilde{\mathcal{P}}}$ by setting *a priori* a number of regions equal to C_0. The $E_{\tilde{\mathcal{P}}}$ notion can be easily understood by looking at the pruning example shown in Fig.4.16. In this case, setting λ to 1, the error $E_{\tilde{\mathcal{P}}}$ associated to the BPT pruning highlighted in green is then $E_{\tilde{\mathcal{P}}} = D(\mathcal{N}_6) + D(\mathcal{N}_8) + D(\mathcal{N}_5) + 3$. Note that the pruning cost $E_{\mathcal{P}}$ is defined as a convex function whose minimization converges to an unique solution when the parameter $C_{\mathcal{P}}$ is equal (or very close) to C_0. Therefore, being $E_{\mathcal{BPT}}$ the set of all the possible partitions $\mathcal{P}$ contained in the BPT, the BPT pruning problem consists in finding the partition $\tilde{\mathcal{P}}$ in $E_{\mathcal{BPT}}$ such that:

$$\tilde{\mathcal{P}} = \underset{\mathcal{P} \in E_{\mathcal{BPT}}}{\operatorname{argmin}} \sum_{\forall \mathcal{N}_i \in \mathcal{S}} D(\mathcal{N}_i) + \lambda^* C_{\mathcal{P}}, \text{ with } \lambda^* \text{ such that } C_{\mathcal{P}} \approx C_0 \tag{4.6}$$

Assuming that the optimal λ^* is previously known, the pruning strategy looking for the best partition is done by a bottom-up analysis of the BPT. The analysis consists in evaluating the BPT nodes from the leaves to the root.
To perform this analysis, each BPT node $\mathcal{N}$ is evaluated against its children nodes $\mathcal{N}_r$ and $\mathcal{N}_l$. The purpose is to check if an ancestor node can replace the area represented by its children nodes with a *minimal* error. This evaluation is addressed by evaluating the $D(\mathcal{N}) + \lambda^* C(\mathcal{N})$ value against the sum of the values of $D(\mathcal{N}_r) + \lambda^* C(\mathcal{N}_r)$ and $D(\mathcal{N}_l) + \lambda^* C(\mathcal{N}_l)$. According to the result of this comparison, the pruning strategy is defined by

$$\text{if} \;\; D(\mathcal{N}) + \lambda^* C(\mathcal{N}) \leq D(\mathcal{N}_r) + \lambda^* C(\mathcal{N}_r) + D(\mathcal{N}_l) + \lambda^* C(\mathcal{N}_l) \tag{4.7}$$

$$\tag{4.8}$$

$$\text{then, } \mathcal{N} \text{ is considered as a single region} \tag{4.9}$$

$$\text{else, } \mathcal{N}_r \text{ and } \mathcal{N}_l \text{ should be considered as two independent regions} \tag{4.10}$$

Note that the bottom-up analysis of the BPT described in Eq.4.10 is addressed when the optimal parameter λ^* is *a priori* known. However, the optimal parameter λ^* is not known in practice. Therefore, the previous bottom-up BPT analysis has to be embedded in a loop searching for λ^*. The computation of the λ^* parameter can be done with a dichotomic search. The algorithm starts with a very high value $\lambda_h = 10^{20}$ and a very low value $\lambda_l = 0$ and seeks the λ^* value by following the algorithm described in Algorithm.2.
Note that the minimization of the function of Eq.4.6 can have different solutions. These solutions directly depend on the choice of $C_{\mathcal{P}}$ and $D_{\mathcal{P}}$. In our case, it has been previously stated that $C_{\mathcal{P}}$ corresponds to the number. of regions $D_{\mathcal{P}}$ is directly related to the pruning objective. A $D_{\mathcal{P}}$ function aiming at segmenting hyperspectral images is proposed in the following section.

Algorithm 2 Calculation of λ^* given a C_0 constraint

λ_{low} = 0;
BottomUpAnalysis(Input :λ_{low} , Output : $D_{\lambda_{low}}, C_{\lambda_{low}}$)
if $C_{\lambda_{low}} > C_0$ **then**
  Exit no solution
end if
λ_{high} = 1^{20};
BottomUpAnalysis(Input :λ_{high} , Output : $D_{\lambda_{high}}, C_{\lambda_{high}}$)
if $C_{\lambda_{high}} < C_0$ **then**
  Exit no solution
end if
$\lambda_M = \dfrac{\lambda_{high} + \lambda_{low}}{2}$;
BottomUpAnalysis(Input :λ_M , Output : $D_{\lambda_M}, C_{\lambda_M}$)
while $|C_{\lambda_M} - C_0| > \epsilon$ **do**
  if $C_{\lambda_M} - C_0 > C_0$ **then**
    $\lambda_{high} = \lambda_M$
  else
    $\lambda_{low} = \lambda_M$
  end if
  $\lambda_M = \dfrac{\lambda_{high} + \lambda_{low}}{2}$;
  BottomUpAnalysis(Input :λ_M , Output : $D_{\lambda_M}, C_{\lambda_M}$)
end while

4.3.1 The $D(\mathcal{N})$ definition

The $D(\mathcal{N})$ value corresponds to the error committed at node $\mathcal{N}$ when it is replaced by its two children nodes $\mathcal{N}_r$ and $\mathcal{N}_l$. Accordingly, a representative $D(\mathcal{N})$ must contain information about how is the region contained in $\mathcal{N}$ but also information about its direct descendant nodes. In general terms, the error $D(\mathcal{N})$ must be defined in order to respect the convexity of the function $E_{\mathcal{P}}$. Consequently, the $D(\mathcal{N})$ computed on a BPT node $\mathcal{N}$ whose child nodes are $\mathcal{N}_r$ and $\mathcal{N}_l$ should respect the following condition: $D(\mathcal{N}) \geq D(\mathcal{N}_r) + D(\mathcal{N}_l)$.

4.3.2 Homogeneity measure

The homogeneity measure assesses whether two sibling nodes can be substituted by their common ancestor and result in a spectrally homogeneous region. The notion of homogeneity in a hyperspectral context is not straightforward. To measure the variance of a hyperspectral region, some works have proposed to compute the variance of each band and then to sum the band contributions [19] [69]. However, these measures are not optimal since the bands of the images are individually processed.

Mathematically, the variability of a multivariate data set can be computed by the trace or the determinant of the covariance matrix representing the relations between the components of the set. In our case, the number of pixels in a region is usually not much larger than the spectral dimension of the image. Thus, the estimation of the covariance matrix is especially challenging. Consequently, in this work, in order to measure differences between the pixels values and the mean value of the region, the spectral homogeneity of the hyperspectral image region is defined by Eq.4.11. This equation corresponds to the sum of the errors committed by all the spectra of the pixels contained in the node $\mathcal{N}$. Given a spectrum, its committed error is defined as the Spectral Information Divergence measure of Sec.3.3.1 according to the average spectrum of the region $\bar{\mathbf{I}}_\lambda^R$.

$$D(\mathcal{N}) = \sum_{\forall p_j \in \mathcal{N}} SID(\ \mathbf{I}_\lambda(p_j),\ \bar{\mathbf{I}}_\lambda^R) \tag{4.11}$$

The error defined in Eq.4.11 is not normalized by the number of pixels of the region contained in $\mathcal{N}$. This property assures the increase of the attribute required by $D(\mathcal{N})$. Unfortunately, the problem of this expression is that the pruning result will be mainly formed by some large homogeneous regions. This occurs because the $D(N)$ is simply adding the contribution of each individual pixel. As a result, if one of the sibling is much larger than the other, the influence of the small sibling will be negligible in the overall $D(N)$ value.

To solve this drawback, new terms are added to Eq.4.11 as shown in Eq.4.12. Note that the purpose of the new terms of Eq.4.12 are to detect whether an ancestor node is formed by two different children regions. In these second term, $\bar{\mathbf{I}}_\lambda^{R_r}$ and $\bar{\mathbf{I}}_\lambda^{R_l}$ are the mean spectrum of the sibling nodes $\mathcal{N}_r$ and $\mathcal{N}_l$. From Eq.4.12, it can be observed how each new term corresponds to the error committed by a node $\mathcal{N}_i$ when all its pixels are replaced by the mean spectrum of its sibling node.

$$D(\mathcal{N}) = \sum_{\forall p_j \in \mathcal{N}} SID(\ \mathbf{I}_\lambda(p_j),\ \bar{\mathbf{I}}_\lambda^R) + \sum_{\forall p_k \in \mathcal{N}_r} SID(\ \mathbf{I}_\lambda(p_k),\ \bar{\mathbf{I}}_\lambda^{R_l}) + \sum_{\forall p_g \in \mathcal{N}_l} SID(\ \mathbf{I}_\lambda(p_g),\ \bar{\mathbf{I}}_\lambda^{R_r}) \quad (4.12)$$

In practice, this estimation may not be reliable for very small regions. As a result, Eq.4.12 is modified to assure that only regions having a *minimal* area are used in the last two terms. In practice, $\mathcal{A}_{min}$ has been set to 3 pixels. Hence, the final expression of $D(\mathcal{N})$ is given by the following expression:

$$D(\mathcal{N}) = \sum_{\forall p_j \in \mathcal{N}} SID(\ \mathbf{I}_\lambda(p_j),\ \bar{\mathbf{I}}_\lambda^R) + \begin{cases} 0 & \text{if } (\mathcal{A}_{\mathcal{N}_r} \text{ and } \mathcal{A}_{\mathcal{N}_l}) < \mathcal{A}_{min} \\ \sum_{\forall p_k \in \mathcal{N}_r} SID(\ \mathbf{I}_\lambda(p_k),\ \bar{\mathbf{I}}_\lambda^{R_l}) + \sum_{\forall p_g \in \mathcal{N}_l} SID(\ \mathbf{I}_\lambda(p_g),\ \bar{\mathbf{I}}_\lambda^{R_r}) & \text{else} \end{cases} \quad (4.13)$$

4.3.3 Experimental Results

Experiments are carried out here in order to test the pruning strategy defined by Eq.4.13. The BPTs constructed with O_{MDS} on the five images of Sec.3.4 are used here. For the five data sets, the N_{Bins} and D_s parameters concerning the BPT construction have been specified in Sec.3.4.3. Firstly, the $D(\mathcal{N})$ values are computed for all nodes. The minimization procedure is performed by the bottom-up analysis of the tree following the criterion presented in Eq.4.10. The value λ^* is computed according to the Algorithm 2.

The first results are shown in Fig.4.17 where the partitions are obtained from the different zones of Pavia University. The constraints C_O are set to 33 for Pavia Uni 1, $C_O = 11$ for Pavia Uni 2 and $C_O = 43$ for the last image. The first column contains the RGB composition of the different images whereas the second column shows the BPT hierarchical levels obtained during the merging sequence construction. The last column shows the results obtained by the pruning minimizing the E_P function. In order to perform a fair comparison, the partitions of the second and the third column contain the same number of regions.

For the first data set, some differences can be seen comparing Fig.4.17 (b) and (c). The pruning result does not seem to improve a lot the performance of the hierarchical BPT level, however, the results are coherent. For instance, Fig.4.17(c) has the background region divided in three regions instead of two as in the case of Fig.4.17(b). Ideally, the manually created ground truth image shown in Fig.3.26(a) has defined this background area with only two regions. However, looking at Fig.4.17(a), the green region appearing in Fig.4.17(c) and not included in the yellow background region can be discriminated in the RGB composition. Moreover, the pixel borders that appear individually instead of being merged with the large brown background region. If we look carefully these border pixels at Fig.4.17(a), it can be seen that they belong to the green building. In contrast, during the BPT construction they have been merged with the brown region. Consequently, the

pruning detects these pixels separately because it considers that they cannot be merged with the background since they are a part of the building. Comparing Fig.4.17(c) and Fig.4.17(b), another interesting difference can be noticed concerning the image illumination. In the case of Fig.4.17(c), some shadow areas are not detected as single regions. This is easily explained by the characteristics of the SID measure, which considers that pixels formed by the same material but with different illumination are identical.

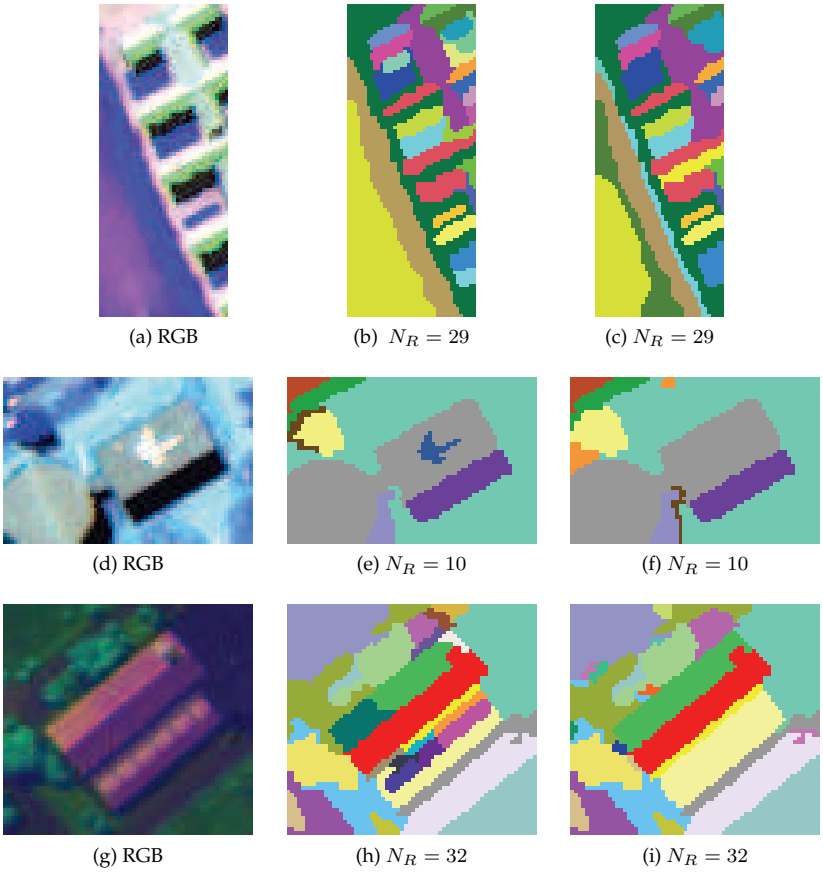

(a) RGB (b) $N_R = 29$ (c) $N_R = 29$

(d) RGB (e) $N_R = 10$ (f) $N_R = 10$

(g) RGB (h) $N_R = 32$ (i) $N_R = 32$

Figure 4.17: Comparison of Hierarchical BPT level and Pruning BPT obtained Partition

The results of the second data set Pavia Uni 2 illustrate also some differences comparing Fig.4.17(e) and Fig.4.17(c). The pruning result seems to be over-segmented as compared to the hierarchical BPT level. This can be observed on the background region since the two orange regions and the brown one are detected independently in the pruning result. The problem of these three regions is that they are in the same BPT branch. During the construction of the hierarchical levels, the small orange object situated on the top has initially merged with the large background area. After this step, the resulting background is merged with the second orange region and later,

it is merged with the brown region situated close to the building shadow. Therefore, as the small orange object has been detected separately in the pruning result, the consequence is that the other regions have not merged with the background region. This can seem an error of the pruning, however, the detection of the small orange object is not wrong since this object really exists in Fig.4.17(a). Hence, optimally, this small orange object should not be merged with the background region before the other two background regions. On the other hand, it should be noticed that the first merging concerning this small orange region during the BPT construction is explained because of the scale threshold step of Sec.3.3.3. The area of this object is too small with respect to the mean area of the regions forming its hierarchical level, then the merging of this object has been forced.

In Fig.4.17(c), a problem can be detected on the pruning results since the large metallic object situated on the building roof has disappeared in the complete gray building region. This effect is due to the definition of $D(\mathcal{N})$ that uses the Spectral Information Divergence (SID). Theoretically, the complete region of the image formed by the roof building and the large metallic object must have a large $D(\mathcal{N})$ value and consequently, these two regions should not merge. As the two regions have a strong dissimilarity, the high value of $D(\mathcal{N})$ should come from the second term of the Eq.4.13. However, after modeling the two regions by a mean spectrum, the SID between the metallic region and the roof is not very high. Note that the first term concerning the parent homogeneity is not very high because most of the pixels form the building region. Accordingly, the SID and the mean first order region model show some limitations in order to define an optimal $D(\mathcal{N})$ descriptor at this example.

Going on with Fig.4.17 evaluation, the third data set also shows how the pruning technique extracts some small regions which have been merged previously with the background at the BPT hierarchical levels. This can be observed on the right part of the figure, where some small regions appear in the background area. At the same time, the pruning result shows how the main building is formed by less regions. Visually, the pruning result seems to achieve better results for this third data set.

The same experiment is performed on the Pavia Center and HYDICE hyperspectral images. Setting the constraint equal to $C_O = 25$ for Pavia center and $C_O = 56$ for HYDICE, the obtained results are shown in Fig.4.18. Looking at the first data set, it can be noticed how the background of Pavia Center is formed by a single region in the pruning result. Besides, the pruning result shows that the small blue region on the top-right corner has been retrieved by the pruning whereas the same region does not appear in the hierarchical BPT level. The shadow effects can also be remarked for this data set and also an over-segmentation issue concerning the vegetation area. The problem of this over-segmented vegetation area is due to the fact that this region is strongly textured. In the case of hierarchical levels, the statistical region model has taken into account this texture characteristics. However, the pruning strategy is simply carried out by analyzing the mean spectrum of the region. In addition, it can also be observed in the pruning result how some small regions have cut the BPT branches because they are considered as not belonging to the large vegetation area which is reasonable.

The results obtained by HYDICE also corroborates that the use of SID it is not optimal in our strategy. For instance, this can be observed on the top left corner of the figure where only a region is detected in the pruning result. Note that because of this, the road has completely disappeared in the pruning partition result. The results shown in the first row of Fig.3.33 concerning the BPT construction by using O_{SID} help to understand the obtained pruning result. This is because O_{SID} cannot find a strong discrimination at this area on the top left corner of HYDICE data set. Accordingly, $D(\mathcal{N})$ is formed by a low value and it leads only to one large single region on the top left corner.

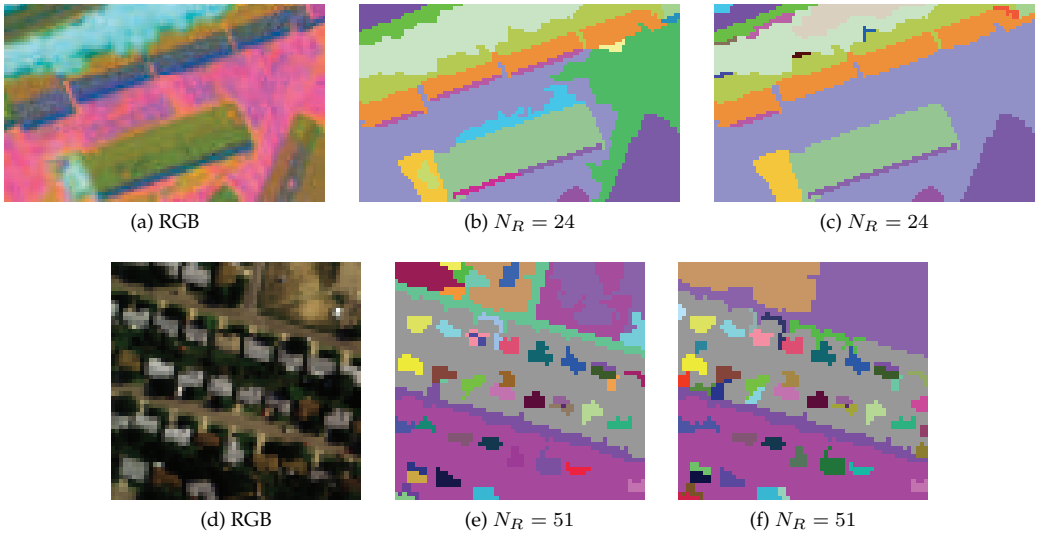

(a) RGB (b) $N_R = 24$ (c) $N_R = 24$

(d) RGB (e) $N_R = 51$ (f) $N_R = 51$

Figure 4.18: Comparison of Hierarchical BPT level and Pruning BPT obtained Partitions

In order to evaluate quantitatively the results of Fig.4.17 and Fig.4.18, the asymmetric distance is used here. The partitions from the hierarchical BPT levels and the pruning results are evaluated in comparison with the manually created ground truth presented in Chapter 2. The obtained results are shown in Tab.4.4. The last column of this table corresponds to the results obtained by the classical technique RHSEG[22]. Observing the average distance, it can be seen how the results are better in the case of the pruning strategy. However, it must be remarked that the results are similar, which proves that the quality of MDS is very high. Moreover, the obtained results largely outperform the state of the art.

Table 4.4: Asymmetric distance

Data Set	**BPT Hierarchical Level** d^T_{asym}	**Pruned Partition** d^T_{asym}	**RHSEG[22]** d^T_{asym}
Pavia Uni 1	0.182	0.178	0.310
Pavia Uni 2	0.085	0.087	0.108
Pavia Uni 3	0.182	0.156	0.204
Pavia Center	0.257	0.178	0.336
Hydice	0.232	0.237	0.4276
Average	0.1876	0.1672	0.277

Conclusions

The pruning strategy aiming at minimizing a cost function has been presented in this section. The goal of this strategy is to avoid the definition of a pruning threshold as has been previously done in the classification strategy.

Setting the number of regions as a constraint, a pruning strategy has been defined in order to extract the partition having this number of regions. The visual results obtained by the pruning strategy seem to be coherent with the RGB composition. The pruned strategy has obtained better or similar results compared to partitions generated by the merging sequence. A region descriptor measuring the spectral homogeneity has been defined in this work. This descriptor has allowed to define a promising pruning strategy which has proved its robustness compared to the merging sequence. However, although the obtained results are interesting, the error criterion measuring the spectral homogeneity of the regions has some limitations. For instance, $\mathcal{D}(N)$ assumes the homogeneity of the region by modeling the set of a spectra or each region by their mean. Moreover, the SID similarity measure may have its limitations in order to discriminate a set of spectra. Besides, $\mathcal{D}(N)$ is the addition of the error committed on the node and the error committed on their children replacement. This work has assumed that the importance of both terms is linearly weighted. However, the children information can be more important in some cases. Therefore, the pruning based on Lagrangian optimization gives promising results but improvements can certainly be made in the definition of the functional.

The most important drawback of the pruning strategy presented here is that it is still supervised. Indeed, the constraint describing the number of regions at the partition result must be known *a priori*. This is not a practical solution because the approximate number of regions is most of the time unknown. Furthermore, the constraint cannot be set as a constant parameter since different images can be formed by different number of regions. As a result, solutions that would require to set *a priori* the number of regions, as following the merging sequence or using the Lagrangian pruning technique presented here have only a limited range of applications.

For all these reasons, the main goal now is to define a completely unsupervised pruning strategy aiming at hyperspectral image segmentation. To this end, the following section discusses a pruning technique based on the spectral graph partitioning theory.

4.4 Segmentation by recursive spectral graph partitioning

The goal of this segmentation pruning is to develop an unsupervised pruning strategy to segment hyperspectral images. As previously discussed, setting *a priori* the number of regions and following the merging sequence is seldom a practical solution. Therefore, this section addresses the definition of an unsupervised algorithm which moreover aims at achieving better asymmetric distances than the previous solutions. To this end, the different BPT branches are separately studied to populate the BPT nodes with a weight $\mathcal{W}_{\mathcal{N}}$ which describes how likely is the pruning of a node.

The pruning strategy described in this section is presented in the following sub-sections. Firstly, Sec.4.4.1 is devoted to describe the interpretation of $\mathcal{W}_{\mathcal{N}}$ and its use to lead to the pruning decision. In a second step, the estimation of $\mathcal{W}_{\mathcal{N}}$ is addressed by treating the BPT branches as a graph bi-partitioning problem. The work is thus based on the well- known approach presented in [66] where a normalized cut is used to segment a graph. The complete analysis of BTP branches is described in Sec.4.4.2.

4.4.1 The BPT node weight $\mathcal{W}_{\mathcal{N}}$

We assume a BPT has been constructed in order to represent through $2N_p - 1$ nodes a hyperspectral image formed by N_p pixels. Consequently, the BPT is composed of N_p leaf nodes and $N_p - 1$ non leaf nodes. In the following, a leaf node is denoted by l whereas the non leaf nodes are designated by $\mathcal{N}$. As it has been observed in Fig.4.7, each BPT node $\mathcal{N}$ roots a sub-tree T_s which is formed by $L_{\mathcal{N}}$ leaves nodes. Note that $L_{\mathcal{N}}$ clearly corresponds in our case to the area of the region represented by the node $\mathcal{N}$. In this context, the BPT branches starting from the $L_{\mathcal{N}}$ leaves of the sub-tree rooted by $\mathcal{N}$ are analyzed to define the $\mathcal{W}_{\mathcal{N}}$ value.

The weight $\mathcal{W}_{\mathcal{N}}$ is a value assessing how likely is the pruning of a node $\mathcal{N}$. This value is computed by studying all the BPT branches starting from a different leaf $l_i \in L_{\mathcal{N}}$, which passes through the node $\mathcal{N}$ until the root. For each of these branches starting from a different leaf l_i, the idea is to assign a pruning decision $P_d^{\mathcal{N}}(l_i)$ to the node $\mathcal{N}$. Fig.4.19 shows an example where this analysis is carried out on the blue node $\mathcal{N}$. The sub-tree rooted by this node is composed by 4 leaves ($L_{\mathcal{N}} = 4$) which results in the study of 4 different branches which are drawn in orange in Fig.4.19(a)(b)(c)(d).

The analysis of each branch gives a pruning decision $P_d^{\mathcal{N}}(l_i)$ indicating whether the leaf l_i considers that the node $\mathcal{N}$ must be removed (1) or preserved (0). Therefore, starting from a specific leaf l_i, the branch analysis is going to assign the pruning decision $P_d^{\mathcal{N}_k}(l_i)$ to the $\mathcal{N}_k$ ancestors nodes of the leaf l_i.

Given a node $\mathcal{N}$, the result of its branch analysis corresponds to a set of $L_{\mathcal{N}}$ pruning decisions. These local decisions describe whether the majority of the leaves wants to prune the tree or, in other words, if they want to be represented by their ancestor node. Considering this, the weight $\mathcal{W}_{\mathcal{N}}$ can be defined as follows:

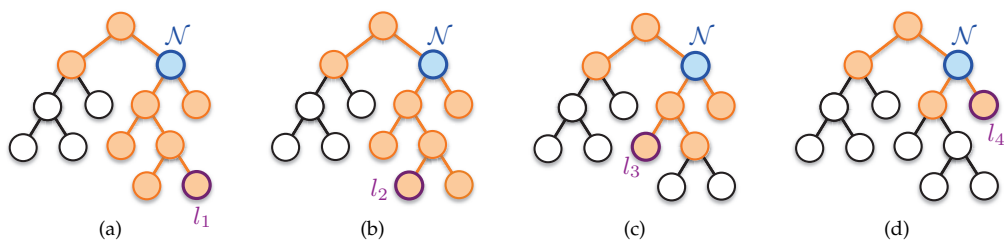

Figure 4.19: BPT branch analysis for node $\mathcal{N}$

$$\mathcal{W}_{\mathcal{N}} = \sum_{i=0}^{L_{\mathcal{N}}} P_d^{\mathcal{N}}(l_i) \tag{4.14}$$

Eq.4.14 leads to define a simple greedy algorithm by pruning the subtrees rooted by the highest BPT nodes whose condition $\mathcal{W}_{\mathcal{N}} > \frac{L_{\mathcal{N}}}{2}$ is true. An example of this pruning decision is shown in Fig.4.20 where a bottom-up algorithm evaluates the ratio $\dfrac{\mathcal{W}_{\mathcal{N}}}{L_{\mathcal{N}}}$ on the BPT nodes. In this case, the BPT node $\mathcal{N}_1$ is respecting the pruning condition, therefore, the subtree rooted by the node $\mathcal{N}_1$ can be pruned. In contrast, the condition in $\mathcal{N}_2$ is not respected and then, $\mathcal{N}_1$ must be preserved.

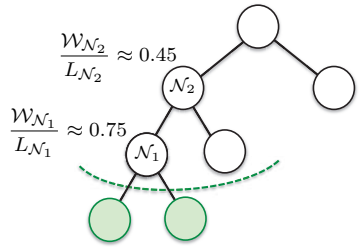

Figure 4.20: Example of Pruning decision

Another example is shown in Fig. 4.21 where a BPT is formed by four non leaf nodes and five leaf nodes. In this case, the pruned tree does not contain the branches hanging from $\mathcal{N}_1$ nor the branches hanging from $\mathcal{N}_3$. Note that these nodes are the last nodes fulfilling the criterion in their respective branches.

At that point, the branch study illustrated in Fig.4.19 must be described in order to assign the $P_d^{\mathcal{N}_k}$ values to compute the pruning weights $\mathcal{W}_{\mathcal{N}}$ involved in Eq.4.14. In this work, the study of a branch has been interpreted as the bi-partition of the branch in two disjoint sets: 1) the nodes that can be pruned according to the studied leaf and 2) the rest of the nodes of the branch. Thus, the next objective is to achieve an optimal cut in the branch dividing these two groups of nodes. The procedure is described in the following Sec.4.4.2.

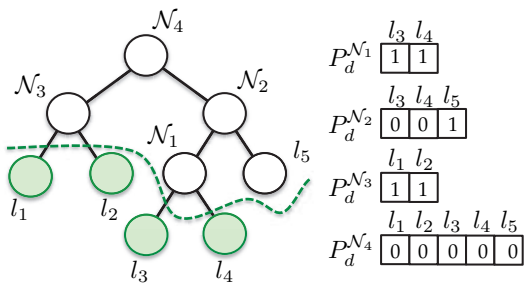

Figure 4.21: Example of BPT pruning

4.4.2 Local Branch partitioning

Let $\mathcal{P}_\mathcal{B}$ be the set of leaf and non leaf BPT nodes forming the branch $\mathcal{B}$. Given a leaf l_i, a local pruning of $\mathcal{B}$ regarding l_i consists in deciding which nodes belonging to $\mathcal{P}_\mathcal{B}$ should be removed with l_i. Fig.4.22 illustrates two examples of branch bi-partition starting from a leaf l_i.
In the case of Fig.4.22 (a), the node has been considered as not to be pruned. Contrarily, in the situation of Fig.4.22(b), the node $\mathcal{N}$ is preserved in the same group than l_i. An important difference can be remarked at this point between the branch partition technique presented in this section and the BPT pruning philosophy. For instance, as shown on Fig.4.22 (a), the result of a branch partition does not imply that two sibling nodes should belong to the same group. In contrast, the global pruning philosophy assumes that a node and its sibling are either preserved or removed (See Sec.4.4.1).

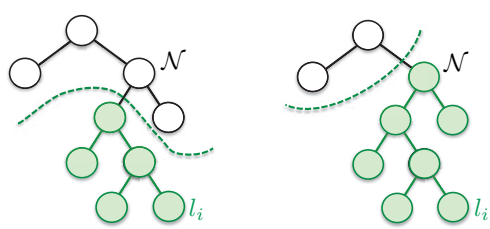

(a) $\mathcal{B}$ removing $\mathcal{N}$ (b) $\mathcal{B}$ preserving $\mathcal{N}$

Figure 4.22: Example of branch partition

Looking at Fig.4.22, it can be observed how according to the branch partition two disjoint non-empty sets $(\mathcal{U}, \mathcal{V})$ can be simply detected. The first set $\mathcal{U}$ is composed by the green node (where $l_i \subset \mathcal{U}$), whereas $\mathcal{V}$ is formed by the rest of the nodes. This interpretation is illustrated in Fig.4.23 where the resulting sets correspond to the branch partitions of Fig.4.22.
Hence, the goal of branch partitioning is to study the similarities/dissimilarities between the BPT nodes on the branch to assure a cut or bi-partitioning of the set $\mathcal{P}_\mathcal{B}$ where the similarity among nodes in $\mathcal{U}$ is high and the similarity across $\mathcal{U}$ and $\mathcal{V}$ is low. To this end, the $\mathcal{P}_\mathcal{B}$ space can be

represented as an undirected weighted graph G. Theoretically, a weighted graph G can be represented by its affinity matrix W. The advantage of these matrices is that their spectral properties (the eigenvalues and eigenvectors) provide useful information about the structure of the graph. For instance, they give practical information about how to partition the graph in different clusters in the case of (almost) regular graphs. However, the BPT branch is clearly a non regular graph, therefore, in order to define a regular graph G, the structure of a BPT branch has been slightly modified. These modifications are illustrated in Fig.4.24.

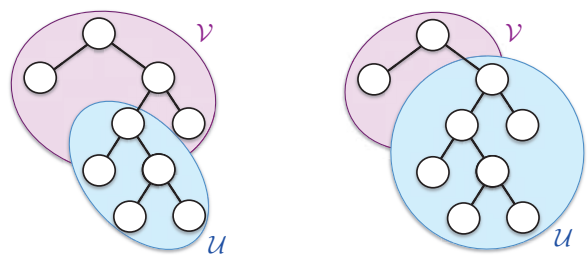

(a) Partition result (b) Partition result

Figure 4.23: Example of branch partition

The graph G representing the branch of Fig.4.24(a) is given by Fig.4.24(b). This graph contains $\mathcal{N}_{\mathcal{N}}$ nodes which correspond to the BPT nodes. The edges of G include BPT branches between parent and children nodes. However, to regularize the graph, the connection between sibling nodes has been introduced in G.

The affinity matrix is computed by all the G edges by the set of measures w_{ij} describing the similarity of each edge linking a pair of nodes $\mathcal{N}_i$ and $\mathcal{N}_j$. Note that if the edge between two nodes does not exist, w_{ij} values must be zero. Therefore, each component w_{ij} of the affinity matrix W, representing the graph G, is computed by

$$w_{ij} = \begin{cases} e^{-d(\mathcal{N}_i, \mathcal{N}_j)} & \text{if } i \neq j, \\ 0 & \text{otherwise} \end{cases} \tag{4.15}$$

The parameter $d(\mathcal{N}_i, \mathcal{N}_j)$ is the distance between regions contained in the BPT nodes $\mathcal{N}_i$ and $\mathcal{N}_j$ (if the connection exists). This distance should be low if nodes are similar and high if they are dissimilar. In order to partition the graph, the distance must be low between the nodes forming $\mathcal{U}$. the distance should theoretically also be small for nodes forming $\mathcal{V}$. In contrast, a high distance must be found on the edges separating both groups.

In our case, the definition of $d(\mathcal{N}_i, \mathcal{N}_j)$ is a challenge because the nodes forming $\mathcal{V}$ on the upper part of the branch can be very different between them. However, the set of nodes forming $\mathcal{V}$ have the property of being very different from l_0. Defining $P(\mathcal{N}_i == l_o)$ as the probability that a node $\mathcal{N}_i$ is equal to the studied leaf l_0. A distance between the nodes can be defined as follows:

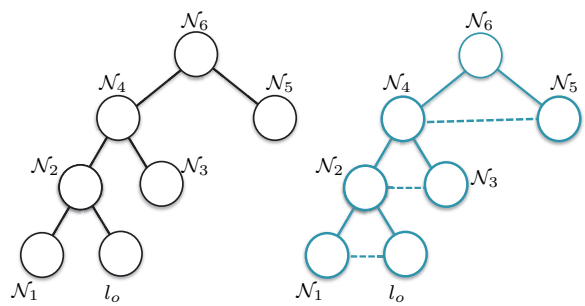

(a) Partition result (b) Partition result

Figure 4.24: Representation of G of the branch

$$d(\mathcal{N}_i, \mathcal{N}_j) = 1 - \left(\sqrt{P(\mathcal{N}_i == l_o)P(\mathcal{N}_j == l_o)} + \sqrt{P(\mathcal{N}_i \neq l_o)P(\mathcal{N}_j \neq l_o)} \right) \tag{4.16}$$

The $P(\mathcal{N}_i == l_o)$ is a value between 0 and 1, and it can for example correspond to the similarity measure computed in the $O_{MDS}(\mathcal{N}_i, l_o)$ criterion. Note that $d(\mathcal{N}_i, \mathcal{N}_j)$ will be low if two nodes are similar to l_0 (then forming $\mathcal{U}$). Besides, two nodes of $\mathcal{V}$ will also have a low distance value since both $P(\mathcal{N}_i == l_o)$ values will be low. In graph theoretic language, the optimal partition of a graph G has been defined as the one that minimizes the cut cost separating the two sets $\mathcal{U}$ and $\mathcal{V}$. The cut cost is defined as follows:

$$cut(\mathcal{U}, \mathcal{V}) = \sum_{i \in \mathcal{U},\ j \in \mathcal{V}} w_{ij} \tag{4.17}$$

The minimization of Eq.4.17 to partition a graph into k-subgraphs such that the *maximal* cut across the subgroups is minimized, was proposed in [67]. In this work, authors noticed that the *minimal* criterion of Eq.4.17 favors cutting small sets of isolated nodes in the graph. Therefore, instead of looking at the value of the total edge weight connecting $\mathcal{U}$ and $\mathcal{V}$, a normalized cut cost $Ncut(\mathcal{U}, \mathcal{V})$ was defined in [66] with the same purpose. The idea of this last approach is to compute the cut cost as a fraction of the total edge weights to all nodes in the graph. The expression of $Ncut(\mathcal{U}, \mathcal{V})$ has been then defined as

$$Ncut(\mathcal{U}, \mathcal{V}) = \frac{cut(\mathcal{U}, \mathcal{V})}{assoc(\mathcal{U}, \mathcal{N}_\mathcal{N})} + \frac{cut(\mathcal{U}, \mathcal{V})}{assoc(\mathcal{V}, \mathcal{N}_\mathcal{N})} \tag{4.18}$$

where $assoc(\mathcal{U}, \mathcal{N}_\mathcal{N}) = \sum_{i \in \mathcal{U}, j \in \mathcal{N}_\mathcal{N}} w_{ij}$. It should be remembered that $\mathcal{N}_\mathcal{N}$ is the number of nodes in G (also in our case in $\mathcal{P}_\mathcal{B}$). In practice, the optimal bi-partitioning of the graph minimizing Eq.4.18 has been presented in [66] as a spectral graph partitioning problem. Hence, the optimal cut can be found by solving the following generalized eigenvalue system:

$$D^{-\frac{1}{2}}(D - W)D^{-\frac{1}{2}}y = \lambda y \tag{4.19}$$

where W is the affinity matrix defined at Eq.4.15 and D is the diagonal matrix whose values in the diagonal are the total connections from each node i to all its neighbor nodes $d_i = \sum_{\forall j} w_{ij}$. In our context, for each BPT non leaf node this value is the sum of the similarity between their children, the direct ancestor and the sibling node. In Eq.4.19, the term $L = D^{-\frac{1}{2}}(D - W)D^{-\frac{1}{2}}$ is known as the symmetric positive semidefinite Laplacian matrix. In [66] , it has been demonstrated how the second smallest eigenvalue of the generalized eigensystem of Eq.4.19 can be used as the solution to graph partitioning problem minimizing the normalized min-cut of Eq.4.18. The strategy consists in partitioning the graph into two pieces using the eigenvector $\mathcal{E}$ of L associated to its second smallest eigenvalue. In an ideal case, the sign of the eigenvector values can tell us exactly how to partition the graph.
An example can be seen in Fig.4.25. The affinity matrix has a size of 7×7 and it is used to compute the Laplacian matrix L of Eq.4.19. Decomposing this matrix, the sign of the eigenvector associated to the second smallest eigenvalue is situated on the left. In this example, it can be seen how the eigenvector $\mathcal{E}$ partitions the graph into two pieces by the green line as: $\{l_0, \mathcal{N}_1, \mathcal{N}_2\}$ and $\{\mathcal{N}_3, \mathcal{N}_4, \mathcal{N}_5, \mathcal{N}_6\}$.

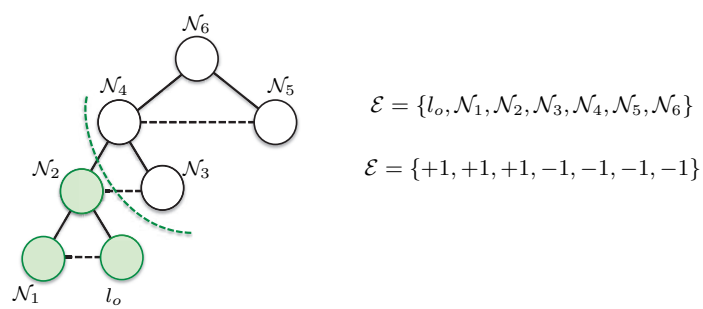

Figure 4.25: Cut according to $\mathcal{E}$

For this last example, according to the explanation of Sec.4.4.1 , the pruning decisions associated to the leaf l_o, will be $P_d^{\mathcal{N}_2}(l_o) = 1$, $P_d^{\mathcal{N}_4}(l_o) = 0$ and $P_d^{\mathcal{N}_6}(l_o) = 0$. Note that the pruning decisions of the studied branch are only taken by the ancestors of the studied leaf. Accordingly, the leaf BPT nodes have always $\mathcal{W}_{\updownarrow} = 1$.
In practice, it can not be assumed that the best cut in the branch will be performed in a first cut. Let us consider for instance a root node that is very different from the rest of the tree. In this case, it can be understood that a first cut is only going to separate the root of the tree from the rest of the branch.
For this reason, instead of a single cut, a recursive spectral graph partitioning algorithm is performed at each studied branch to detect its best cut. Given a leaf l_i, this recursive methodology is described in Algorithm 3. The main idea of the recursive strategy is that the procedure detailed in Fig.4.25 is going to be repeated iteratively. At each iteration, the set of nodes $\mathcal{U}$ containing the leaf l_i is preserved and the graph partitioning algorithm is applied on $\mathcal{U}$. At each iteration, the parti-

tion of the branch has an associated $Ncut$ value coming from the Eq.4.18. Therefore, the purpose is to perform this recursive algorithm until the $Ncut$ value is higher than a set threshold $\mathcal{T}_{Ncut}$.

Algorithm 3 Computation of recursive spectral graph partitioning of the BPT branch

$\mathcal{N}_{\mathcal{N}}$ = nodes forming the branch $\mathcal{B}$
while $\mathcal{N}_{\mathcal{N}} > 2$ and the end is not true **do**
  Compute the Laplacian matrix relating l_i with all the $\mathcal{N}_{\mathcal{N}}$ nodes of the branch
  Compute the graph cut at level k according to the closer BPT nodes on the branch having the same sign as $\mathcal{E}(l_i)$.
  Compute $Ncut$ between the first nodes arriving to level k and the remaining $\mathcal{N}_{\mathcal{N}}$
  if $Ncut <$ maximum allowed $\mathcal{T}_{Ncut}$ **then**
    L_{Cut} is equal to k
  else
    the end is true
  end if
  Next Laplacian matrix to study is given by the hanging nodes until level k, then $\mathcal{N}_{\mathcal{N}} = 2k - 1$
end while

At the end of the algorithm, the optimal cut on the branch will be retained in L_{Cut}. Thus, this information is used to populate the BPT nodes on the studied branch. Starting from a leaf l_i, all its ancestor nodes $\mathcal{N}_k$ formed in its branch until the level L_{Cut}, will have a positive pruning decision $P_d^{\mathcal{N}_k}(l_i) = 1$ (See Fig. 4.21). Contrarily, ancestor nodes formed in level higher than L_{Cut} will have a zero value in their decision $P_d^{\mathcal{N}_k}(l_i) = 0$.
Note that once the BPT is populated, the pruning decision according to the $\mathcal{W}_{\mathcal{N}}$ is applied to prune the tree. Finally, as it has been previously done, the segmentation result is obtained by selecting the leaf nodes of the pruned BPT.

4.4.3 Experimental Results

Some experiments are presented here concerning the evaluation of the pruning following the spectral graph partitioning strategy. As previously done in Sec.4.3.3, the five different constructed BPTs on Sec.3.4.3 with O_{MDS} are used here to address this evaluation. Each of these BPTs has been populated by the weights $\mathcal{W}_{\mathcal{N}}$ described at the beginning of Sec.4.4.1. To this end, the different BPT branches have been analyzed by their corresponding G interpretation. Given the representation of the BPT branches as a regular weigthed graphs, the recursive spectral graph partition algorithm described in Algorithm.3 is applied to each of them. Thus, the solution of the graph partition technique is used to assign the weights to all the BPT nodes. Finally, once all the $\mathcal{W}_{\mathcal{N}}$ of Eq.4.14 have been computed, a bottom-up evaluation on the BPT nodes is carried out. The goal of the bottom-up analysis is to verify whether the majority of the leaves forming a nodes want to prune it.

First experiments are performed on the three different zones of Pavia University Data set. The obtained results are shown in Fig.4.26 where the $\mathcal{T}_{Ncut}$ value has been set to 0.3. The first column shows the different RGB compositions of the images whereas the second column corresponds to the hierarchical BPT levels having a specific number of regions N_R. Finally, the last column shows the results obtained by the pruning strategy. The partitions shown in the second and the third columns contain the same number of regions.

Comparing the results of the third and the second column, it can be seen that the obtained results are very similar to the partitions obtained during the BPT construction and that, moreover, the number of regions is not far from the optimal region number defined in the ground truth partitions. Therefore, these results are very promising taking into account that the approach is now unsupervised. Note that the results shown in the second column are obtained by setting *a priori* a number of regions which is different at each image. In contrast, the pruning results have been obtained in unsupervised way by using the same parameters for all the images.

Some differences can be found as for example at the bottom right corner of Fig.4.26(c) and (d). In it, it is observed how a small structure has been detected in Fig.4.26(d) whereas it does not exist in Fig.4.26(c). Looking at the RGB composition of Fig.4.26(c), it is seen how the small structure really exists. Therefore, the pruning strategy has performed well in this case.

Another example is found in the roof of the gray building where a blue region is divided in two in Fig.4.26(c) and in contrast, it appears as one single region in Fig.4.26(c). In the same part of the image, another difference is seen with the appearance of the orange region in Fig.4.26(d). This region has been retrieved by our pruning, whereas in the BPT hierarchy level it appears inside the building object. If this orange region is explored in details, it is seen that it doesn't belong to the object. Therefore, it is normal that the pruning technique has decided to represent it as a single region.

Observing the pruning results, it can be thought that the obtained partitions are over-segmented. For instance, if they are compared with the partitions shown in Fig.4.18. However, it should be remarked that the appearance of the small regions seems coherent with the RGB composition and it shows some limitations regarding the BPT construction. For instance, the pink region in Fig.4.26(c) has been retrieved by the pruning strategy because it corresponds to the small white region of the Fig.4.26(a).

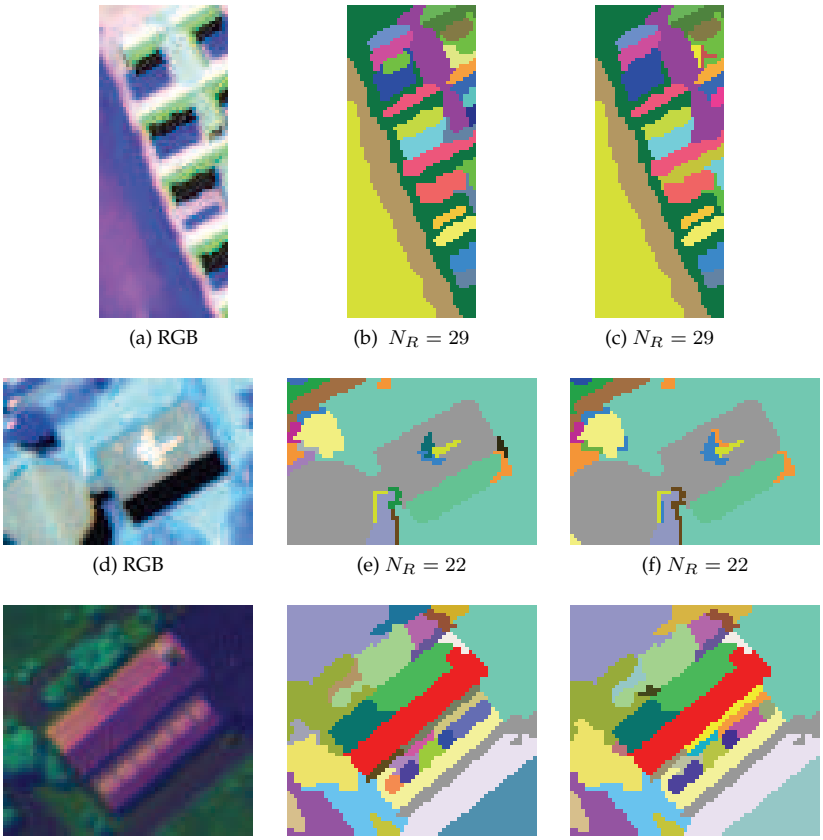

(a) RGB (b) $N_R = 29$ (c) $N_R = 29$

(d) RGB (e) $N_R = 22$ (f) $N_R = 22$

(g) RGB (h) $N_R = 34$ (i) $N_R = 34$

Figure 4.26: Comparison of Hierarchical BPT level(center) and pruned BPT(right) partitions

A second set of experiments is carried out on the Pavia Center and Hydice images. For both images, the same pruning strategy is carried out leading to the results of Fig.4.27. In the case of Pavia Center, the pruning results clearly outperform the hierarchical level since the background is only formed by a single region. An interesting phenomenon is observed in Fig.4.27(c) where 4 regions on the left part of the image have been detected individually. In all the other results obtained during this PhD on this data set, these four regions appear as a single purple region. However, looking at the RGB composition of Fig.4.27, it can be corroborated how this part of the image is formed by more than one region.

Concerning HYDICE results, both images present very similar results. A small difference can be seen as for example on the top right part of the image. The pruning results show an orange region separated from the road whereas the same region has been merged with the road in Fig.4.27(e). Looking at the RGB composition Fig.4.27(d), it seems that the pruning result is the wrong one.

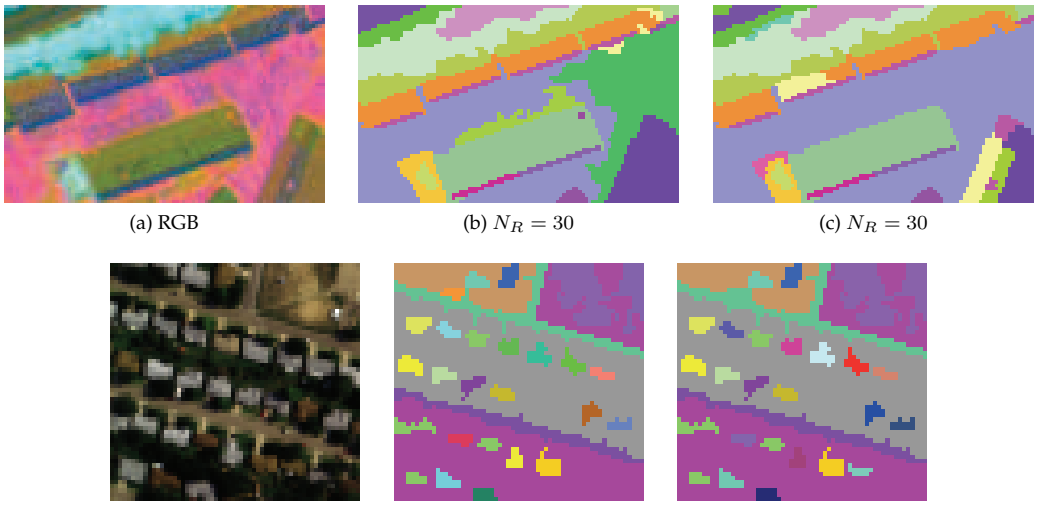

(a) RGB (b) $N_R = 30$ (c) $N_R = 30$

(d) RGB (e) $N_R = 31$ (f) $N_R = 31$

Figure 4.27: Comparison of Hierarchical BPT level(center) and pruned BPT(right) partitions

To validate our visual evaluation, the average asymmetric d^T_{asym} is computed for all the partitions shown in Fig.4.27 and Fig.4.26. The corresponding results are shown in Tab.4.5. The results assess that the obtained partitions are similar or better than the BPT hierarchical levels. This is an important achievement since, without any *a priori* knowledge, the results lead to partitions having a similar number of regions than the ground truth.
The pruning results achieved better results which is clearly seen in the case of Pavia Center. The large improvement comes from the background region which has been detected as one single region. Thus, the normalized asymmetric distance is much lower in this case. Besides, the results are compared with the state of the art [22]. In this case, the pruning results clearly outperform the results obtained by the classical RHSEG technique.

Table 4.5: Asymmetric distance

Data Set	**BPT Hierarchical Level** d^T_{asym}	**Pruned Partition** d^T_{asym}	**RHSEG[22]** d^T_{asym}
Pavia Uni 1	0.126	0.1208	0.310
Pavia Uni 2	0.096	0.091	0.249
Pavia Uni 3	0.1902	0.1907	0.1934
Pavia Center	0.255	0.1672	0.345
Hydice	0.211	0.211	0.3744
Average	0.175	0.156	0.294

Conclusions

In an unsupervised segmentation framework, the BPT pruning has been considered here as a graph cut problem. The study of the BPT branches to decide the best branch cut has been carried out by a classical technique proposed in [66]. The proposed approach has allowed to compute the affinity matrices describing the image relations by using different regions of an image. This introduces a novelty regarding the state of the art where the graph cut techniques is applied on the RAG pixel representation. Hence, classical works have computed the affinity matrix representing a region simply by studying the pixel similarities. Here, the construction of the affinity matrices using regions has been proposed. In this work, a similarity function relying on the spectrum information has been applied to weight the edges of the graph. However, note that having regions, the affinity matrix could use more information as such the shape of regions.

Looking at all the obtained results, it can be observed how the pruning strategy has lead to interesting results. The obtained partitions are coherent with the realistic RGB composition. The asymmetric distance computed on the different results has shown the improvement achieved by the BPT pruning strategy. Indeed, the obtained partitions have been obtained without any *priori* knowledge (such as a given number of regions). Comparing our asymmetric distance results with the results obtained in Sec.3.4.3 , it can be noticed that the pruning strategy has achieved partitions situated close to the *minimum* of the d_{asym} curves.

In this section as well as in Sec.4.3, it has been seen that because of the complexity of the scenes, it is sometimes difficult to define the ground truth partitions. A detailed analysis of the results reveals that some of the observed differences are subject to interpretation. On the other hand, the results have also shown that some mistakes were generated during the BPT construction. As the pruning results directly depend on the BPT construction, if a region is not perfectly represented by BPT nodes, the pruning strategy cannot retrieve it.

4.5 Object detection

In the context of many current applications, hyperspectral research is trying to develop machine vision approaches that get closer to the abilities of the human visual system. The objective is to build systems that can recognize previously seen (learnt) objects with high accuracy under varying environmental conditions. The main difficulty is that the world is rich in variability. As a result, the same object can appear with an extremely high number of different visual appearances. For this reason, object recognition needs *prior* knowledge about the object to be detected.

Hyperspectral object detection has been mainly developed in the context of pixel-wise spectral classification. This approach is seen as the individual detection of the spectra having a high similarity with the material describing the reference object $\mathcal{O}_{ref}$. The main problem of this strategy is that the objects usually cannot be only characterized by their spectral signature. Consequently, spatial features such as shape, area, orientation, etc., can also contribute significantly to the detection. Accordingly, in order to integrate the spatial and spectral information, BPT is proposed as a search space for constructing a robust object identification scheme.

The proposed strategy consists in analyzing a set of descriptors computed for each BPT node. Thus, studying these descriptors, the purpose is to recognize the possible object as one or more BPT nodes. Fig.4.28 describes the followed approach.

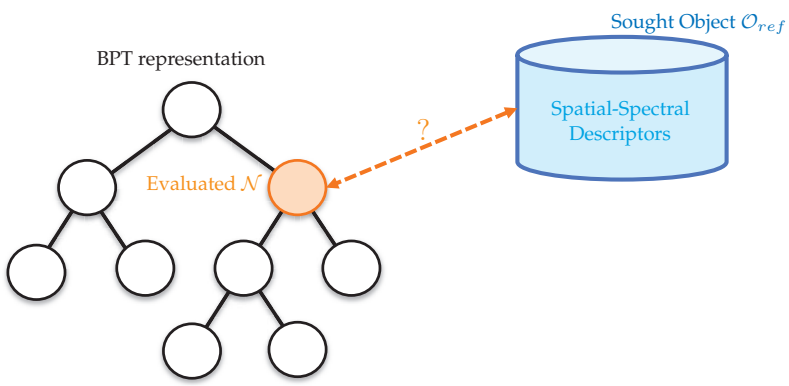

Figure 4.28: Illustration of object detection procedure

The work presented here proposes the analysis of spectral as well as spatial descriptors for each node. Spatial descriptors describe information as the shape or the area corresponding to the specific object of interest. Concerning spectral descriptors, they describe the spectra of the regions. For instance, if the material of the object $\mathcal{O}_{ref}$ is known, the spectral signature is an important spectral descriptor of the material.

Accordingly, the proposed scheme relies on the three different descriptors for the BPT nodes

$$\mathcal{O} = \{\mathcal{D}_{shape},\ \mathcal{D}_{spectral},\ \mathcal{D}_{area}\} \tag{4.20}$$

The computation of the set of descriptors for the nodes populates the BPT in this application. Thus, once the proposed descriptors $\mathcal{D}$ are computed, they are studied from the leaves to the root. The approach consists in removing all nodes that significantly differ from the characterization proposed by the reference $\mathcal{O}_{ref}$. Hence, the idea consists in considering that the sought objects are defined by the closest nodes to the root node that have a set descriptors close to the $\mathcal{O}_{ref}$ model. In order to illustrate the generality of the approach, two detection examples are presented here: road and building detection in urban scenes, respectively.

4.5.1 Detection of roads

Roads appear as elongated structures having fairly homogeneous radiance values usually corresponding to asphalt. In a classical pixel-wise classification, the detection of the roads clearly consists in detecting the possible pixels of the image that belong to the asphalt class. The main drawback is that other structures of the image can also be formed by asphalt. To solve this issue, an information is that roads appear as stretched objects. Thus, given their characteristic shape, the region elongation is used here as the shape descriptor $\mathcal{D}_{shape}$. In order to compute it, the smallest oriented rectangular bounding box must be computed for each region contained in a BPT node.
The *oriented bounding box* of the region containing $\mathcal{N}$ is the smallest rectangle including the region that is aligned with its orientation ϕ. Knowing this value, the rotation of coordinates x, y is given by

$$\alpha = xcos\phi + ysin\phi \tag{4.21}$$

$$\beta = xsin\phi + ycos\phi \tag{4.22}$$

The last transformation defines new coordinates α and β which are used to describe the points P_1, P_2, P_3 and P_4 characterizing the oriented bounding box (See Fig.4.29). Once the oriented bounding box of a region is computed, the elongation of the region, corresponding to the $\mathcal{D}_{shape}$, can be easily computed as the ratio between the width and the height of the bounding box.
The second spatial descriptor computed at BPT nodes is the area of the region $\mathcal{D}_{area}$. The idea is that a road should have at least a given number of pixels. This *minimum* required area should be set according to the spatial resolution of the image.
Concerning the spectral descriptor $\mathcal{D}_{spectral}$, it must contained the information concerning whether the region on the BPT node is formed by asphalt. Thus, given a reference spectrum of the road material, the correlation coefficient between the mean spectrum of the BPT node and a reference spectrum of the road material is used as $\mathcal{D}_{spectral}$. This coefficient can be computed by Eq.4.23 where $\bar{I}_{\lambda}^{\mathcal{N}}$ is the average spectrum contained in $\mathcal{N}$.

$$\mathcal{D}_{spectral}(\mathcal{N}) = \frac{\sum_{z=1}^{N_z}(\bar{I}^{\mathcal{N}}_{\lambda_z} - \frac{1}{N_z}\sum_{s=1}^{N_z}\bar{I}^{\mathcal{N}}_{\lambda_s})(\bar{I}^{\mathcal{O}_{ref}}_{\lambda_z} - \frac{1}{N_z}\sum_{s=1}^{N_z}\bar{I}^{\mathcal{O}_{ref}}_{\lambda_s})}{\sqrt{\sum_{z=1}^{N_z}(\bar{I}^{\mathcal{N}}_{\lambda_z} - \frac{1}{N_z}\sum_{s=1}^{N_z}\bar{I}^{\mathcal{N}}_{\lambda_s})^2}\sqrt{\sum_{z=1}^{N_z}(\bar{I}^{\mathcal{O}_{ref}}_{\lambda_z} - \frac{1}{N_z}\sum_{s=1}^{N_z}\bar{I}^{\mathcal{O}_{ref}}_{\lambda_s})^2}} \tag{4.23}$$

At this point, computing the set of three descriptors forming $\mathcal{O}$ for all BPT nodes, the idea is to select the closest nodes to the root which have a low elongation, a high correlation with asphalt material and an area higher than a given threshold.

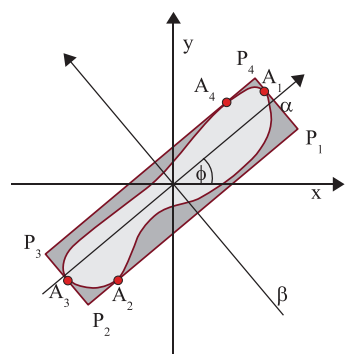

Figure 4.29: Oriented Bounding Box definition

4.5.2 Detection of buildings

The detection of buildings follows the same strategy presented above for the roads. Thus, three descriptors are also defined. Concerning $\mathcal{D}_{spectral}$, this coefficient also corresponds to the correlation coefficient measured between the mean spectrum of the BPT node and a reference spectrum of the building material. In the case of the area, the descriptor $\mathcal{D}_{area}$ is also compared with a required area to consider that a region can be a building.

The main difference with the road detection example is that the elongation of the region as $\mathcal{D}_{shape}$ is not appropriate in the case of buildings. Consequently, another spatial descriptor is used. The idea is to use the rectangularity of a region as an important characteristic. Then, a rectangularity descriptor is used as $\mathcal{D}_{shape}$. The computation of this spatial descriptor can be easily performed with the oriented bounding box definition. Thus, $\mathcal{D}_{shape}$ is computed as the ratio of the area of the BPT node and the area of the smallest oriented bounding box including the region. Theoretically, a rectangular region is going to have a value $\mathcal{D}_{shape}$=1 for perfectly rectangular regions.

The procedure of the building detection follows the same strategy as for the road case. A bottom-up analysis of the tree searches for the highest BPT nodes close to $\mathcal{O}_{ref}$.

4.5.3 Experimental Results

This section addresses the evaluation of the BPT object detection strategy proposed for the road and building detection. The goal of the experiments is to compare the results of the BPT object recognition strategy with a classical unsupervised pixel-wise classification. The experiments have been performed using the portion of HYDICE hyperspectral image of Sec.3.4.2. Fig. 4.30(a) shows a RGB combination of the image portion. The BPT has been computed with the O_{MDS}. The ground truth partition of this image illustrating the roads and buildings of the scene are shown in Fig. 4.30(b) and Fig. 4.30(c).

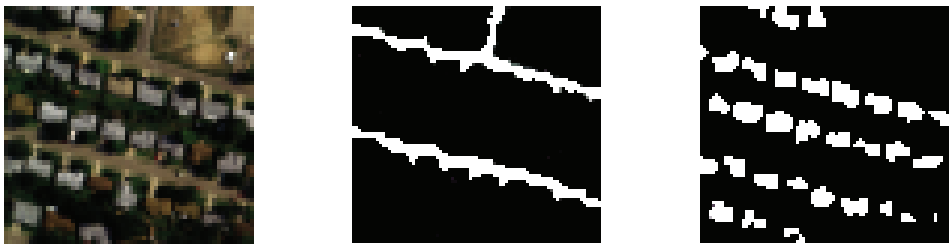

(a) RGB Composition (b) Roads $\mathcal{P}_{GT}$ (c) Buildings $\mathcal{P}_{GT}$

Figure 4.30: Hydice Data Set

The pixel-wise classification consists in detecting pixels in the image having a correlation higher than 0.9 with the reference spectrum.
To detect $\mathcal{O}_{ref}$ some reference parameters should be set. For instance, in the case of roads, the pruning strategy is looking for regions having an elongation lower than 0.3, with a correlation coefficient with asphalt higher than 0.9 and an area larger than 15 pixels. Regarding the buildings, the BPT analysis is focused on detecting regions having a rectangularity higher than 0.4, a correlation coefficient between building material higher than 0.9 and an area smaller than 15 pixels.
The first row of Fig. 4.31 shows the results of the pixel-wise classification road and building having a high correlation coefficient. The second row of Fig. 4.31 illustrates the detected BPT nodes using the two different $\mathcal{D}_{ref}$. The results obtained with the BPT corroborate the advantage of using this image representation. The use of spectral as well as spatial descriptors of BPT nodes outperforms the classical pixel-wise detection using only spectral information.

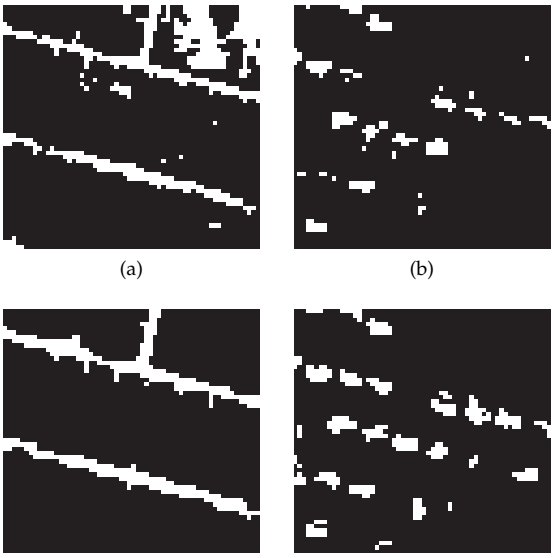

(a) (b) (c) (d)

Figure 4.31: First row: Road (a) and Building (b) detection using pixel-wise classification. Second row: Road (c) and Building (d) detection based on BPT representation

Conclusions

The hyperspectral object detection methodology by using BPT image representation has been detailed in this section. To address it, the road and building detection examples have been proposed. Some descriptors associated to the specific application have been used according to the specific goals. In order to define another object detection application, the appropriate descriptors must be detailed.

The obtained results show the interest of studying the objects of the scene by a region-based image representation. They have shown how may be possible to detect the reference object by detecting single BPT nodes. Note that in the case of Fig. 4.31 each detected component corresponds to one single BPT node. Another important remark is that in the examples shown in this section, the different descriptors have the same importance. This consideration cannot always be appropriate. Thus, in some applications, it maybe be better to give more information to the spectral descriptor.

4.6 Conclusions

This chapter has discussed different BPT processing techniques. The main purpose has been to demonstrate how different pruning strategies can be defined on the BPT structure according to specific applications. Three different applications have been studied in order to prune the tree. Firstly, a supervised hyperspectral image classification has been proposed using the SVM classifier. Then, the hyperspectral image segmentation challenge has been studied by a supervised and an unsupervised pruning strategy. Finally, the hyperspectral object detection using the BPT image representation has been explained with two different examples.

In each case, the processing of the BPT has been done in two steps. Firstly, BPT nodes are populated by computing some descriptors or features. Secondly, the analysis of the node descriptors along the BPT branches decides whether nodes should be removed or preserved.

Concerning the first step, different descriptors have been presented according to the applications. For instance, in the classification case, a descriptor related to the misclassification rate has been proposed. The goal of this descriptor is the evaluation of the error committed by removing nodes having a class different from their direct descendants. The computation of this rate has been performed by using the SVM supervised classifier. In the case of segmentation, two different approaches have been discussed. In the first approach, a supervised pruning based on an energy minimization strategy has been presented. In this context, BPT nodes have been populated by a spectral homogeneity descriptor. In this case, the idea has been to describe if the regions are spectrally homogeneous with respect to their mean spectrum. The second approach involving segmentation has been presented as an unsupervised BPT pruning technique. In this case, the BPT nodes have been populated by weights representing local pruning decisions. Studying separately each branch, the proposed methodology analyses if the ancestor nodes can replace their leaves. Finally, in the case of object detection, nodes have been populated with spatial and spectral descriptors. The descriptor choice is directly related with the road and building detection application. The elongation and the rectangularity of the regions have been proposed as spatial descriptors. Regarding the spectral descriptor, the correlation coefficient with the reference material has been used.

Once the BPT nodes have been populated, different strategies have been proposed in order to decide the pruning of the nodes. In all cases, a bottom-up analysis of the tree from the leaves to the root has been performed. Therefore, some pruning rules have been defined for the different BPT pruning strategies. In the first pruning strategy involving the hyperspectral image classification, the *maximum* decision rule has been used. In this context, the classification results have shown the benefit of using the BPT image representation. Classification accuracies have clearly outperformed the classical results obtained by the standard pixel-wise classification. Besides the quantitative results, the obtained classification maps have shown homogeneous regions without involving the classical impulsive classification noise.

For segmentation, a supervised pruning technique performing a global analysis has been proposed. This technique has been presented as an energy minimization problem subject to a constraint. The constraint corresponds to the desired number of regions. Note that because of this constraint this pruning is supervised. In this case, promising results have been obtained. However, the main drawback of this technique is that the number of regions forming the partition should be known *a priori*. Hence, this approach does not seem to be appropriate for most practical solutions. Therefore, an unsupervised pruning strategy has been proposed based on the spectral graph partitioning theory.

This last pruning technique have provided the best performances. The partition results have been compared with the partitions obtained during the merging sequence construction and with the state of the art. The quantitative evaluations have corroborated the robustness of the pruning.

In the case of object detection, two different pruning examples have been presented for two object detection examples. Setting the detection of roads and building as main goals, very interesting and promising results have been obtained.

The four pruning strategies have shown how the BPT representation can be used in different contexts. Moreover, the obtained results have corroborated the interest of studying hyperspectral images by using a region-based representation like the BPT.

5
Conclusions

In this thesis, the BPT region-based representation for hyperspectral imagery has been presented as a very promising area of research [70]. The construction and the processing of the BPT representation in a hyperspectral context have been discussed. This tree-based structure has been preferred in to other graph structures since BPT succeeds in representing : 1) the decomposition of the image in terms of regions representing objects and 2) the inclusion relations of the regions in the scene. Furthermore, given its fixed structure, BPT allows implementing efficient and advanced application-dependent techniques on it. In this framework, the work addressed in this thesis is mainly divided in two parts: the BPT construction and the BPT processing.

The BPT construction for hyperspectral imaging has been investigated in Chapter 3. Consequently, the first main challenge in this Phd has been the definition of a region merging algorithm. This task has not been straightforward. This has been explained by the complexity of the data given the variability of the spectra and the high correlation between bands. To address these issues, several regions models and merging criteria have been studied [69]. Concerning the region models, the popular region model described here as the first-order model has been compared with the non parametric statistical region model previously defined in [17] for classical imagery. The use of non parametric statistical region model has been proposed as a solution for representing a set of spectra. This region model has shown its performances to solve the spectral variability issue. Furthermore, it has proved its capabilities to represent complex or textured regions. In order to compute this model for the individual spectra of the image, robust algorithm to estimate the pdf of initial pixels based on self-similarity ideas has been proposed in Sec.3.2.2. To be able to

estimate the pdf of individual spectra, a noise estimation in the case of the hyperspectral image bands has been detailed in the same section. This noise estimation can be used in future works to define a noise reduction strategy in hyperspectral image based on a non-local mean procedure.
According to the non parametric statistical region model, different merging criteria have been proposed. The problem associated to the Battacharyya distance described in [17] has been solved by using the cross-bin Diffusion distance. The use of a cross-bin distance has corroborated its advantage showing in particular its robustness to the N_{bins} parameter. Although this distance may be less accurate than other cross-bin histogram distances known in the literature such as Earth Mover Distance L_1, it has been chosen because of its trade-off between complexity and accuracy. Despite of the interesting results provided by the metrics comparing histograms, the correlation issue was not addressed in this case.
Hence, a new merging criterion taking into account the correlation between hyperspectral bands has been proposed as one of the main contributions of the PhD in Sec.3.3.3. The idea has been to locally reduce the dimension of the region model via multidimensional scaling. Studying the similarities between the histograms of the region, the local principal coordinates of each region has been extracted. Then, a statistical test based on MANOVA theory has been proposed to measure the similarity between two adjacent regions. This test has also been directly related with the canonical correlations. In this context, an estimation of the best dimension to compare the principal coordinates of two regions has been presented in this work. In order to compare two principal components data sets representing two hyperspectral regions, a trade-off between the principal coordinates of each data set has been proposed.
To compare the different merging orders, an evaluation has been carried out by evaluating the partitions obtained during the merging sequence construction. In order to evaluate the results, a visual and a quantitative evaluation have been carried out. The quantitative assessment has been performed wiht the symmetric and the asymmetric distances presented in Sec.3.4.1. To our knowledge, this Phd has introduced the first quantitative evaluation to validate the hyperspectral image partitions concerning the whole image. Experimental results have shown the good performances of the BPT construction in comparison with the most used state of the art technique: RHSEG [22]. The obtained results have also shown the limitations of the first order region model. In contrast, the merging criterion via MDS has obtained the best results in our study. Thus, this merging criterion can be considered as a promising measure to establish similarities between spectral data sets in future works.
The second main important contribution shown in this thesis is the different BPT processing techniques which have been targeted for different applications. Four different strategies have been presented in the context of supervised hyperspectral image classification, supervised and unsupervised hyperspectral image segmentation and finally, object detection. The processing of BPT has been presented in Chapter 4 as a pruning strategy based on performing an analysis of the nodes of the tree by measuring a specific criterion . The different strategies have corroborated how the BPT is not an application-dependent tree structure, but it is an image representation which can be processed by several application-dependent strategies.

As a first example of pruning, the supervised classification of hyperspectral image has been addressed. The SVM classifier has been used to populate the BPT nodes with the probability class distribution. Then, a bottom-up analysis of the tree branches has removed the BPT nodes following a *maximum* rule decision. Experimental results have shown that the proposed method improves the classification accuracies of a standard SVM, providing classification maps with a reduced amount of noise.

The second pruning strategy was targeting a supervised segmentation. This pruning technique has been presented as a global energy minimization problem on the BPT structure. Under this framework, a constrained Lagrangian function has been proposed by using a spectral homogeneity descriptor. The constraint parameter has been set as the desired number of regions. The main goal of this pruning has been to show that if the desired number of regions is known, the partition involving this number of regions obtained following the merging sequence construction is not optimal. In other words, the pruning technique aims at extracting the same number of regions but with higher homogeneity. Experiments have been conduced to compare the partitions obtained from the merging sequence with those obtained through the pruning. The pruning results have shown some improvements in their accuracies. However, it must be remarked that the O_{MDS} criterion has constructed a quite good BPT representation, therefore, to achieve a large improvement is a challenging task. The formulation of the BPT pruning as global minimization problem offers a very promising line of work for the future leading to robust strategies.

Nevertheless, supervised segmentation cannot be widely used in practice. Indeed, the number of regions is most of the time unknown and moreover, it is strongly image-dependant. Hence, in order to tackle this problem, the segmentation of hyperspectral images with an unsupervised pruning strategy has been studied. To this end, a pruning strategy based on normalized cut has been proposed.

The analysis of BPT branches to decide the best cut has been addressed by interpreting the BPT branches as regular graphs by including the sibling node connections. Then, the spectral graph partitioning theory has been applied to obtain normalized cut. The aim of the cut has been to partition the branch in two disjoint data sets. As a result, the cut on the branch must be considered as a local pruning . Therefore, the solution of the branch cut has been used here to populate the BPT nodes using weights describing how likely is the pruning of a node. These weights have been used later to perform a bottom-up analysis of the tree according to a *maximum* decision rule. This rule has been defined as a majority vote comparing the weight of a node with its area.

The results obtained by this pruning are very positive since using the same parameters, it has been possible to extract partitions with similar number of regions as the ground truth partitions and with the highest quality compared to the remaining segmentation strategies discussed in this PhD. The results have shown how a hyperspectral image is partitioned in coherent regions compared to the ground truth. One of the possible limitations of this pruning is that the study of the branches is done locally. Thus, the application of the spectral graph theory to the complete tree structure could be envisaged as future research work. Futhermore, the computation of the affinity matrices by using BPT image representation seems to be an encouraging line of research.

Indeed, the computation of this matrices has been mainly done in the literature for classical RAG structures. Therefore, the idea of using a hierarchical image representation could lead to better results.

The last pruning example has been presented in the framework of object detection. Two examples have been proposed in order to illustrate how BPT can be a powerful representation for the object recognition applications. To this end, the road and the building examples have been shown. Such examples have described how the spectral and the spatial information can be incorporated in the search of a reference object. This work can be seen as a contribution in the hyperspectral field. Indeed, in most of the work reported in the literature, object detection has been only based on a pixel-wise classification algorithm by selecting pixels spectrally similar to a pre-defined class.

6

Résumé en français

L'Arbre Binaire de Partitions: Un nouvel outil pour la représentation hiérarchique et l'analyse des images hyperspectrales

L'imagerie hyperspectrale correspond à l'acquisition d'un ensemble d'images représentant les informations contenues dans une grande partie du spectre électromagnétique. Contrairement à la vision humaine, qui est limitée à certaines longueurs d'onde, les systèmes d'imagerie hyperspectrales ont la capacité de mesurer le rayonnement électromagnétique dans le visible et dans d'autres longueurs d'onde. Cette couche d'information spectrale (ou couleur) supplémentaire représente l'avantage principal de l'imagerie hyperspectrale par rapport à l'imagerie couleur traditionnelle. L'intérêt de cette nouvelle source d'information est la possibilité d'une caractérisation fine des objets imagés.
L'imagerie hyperspectrale est liée à l'imagerie multispectrale, cependant, il existe une différence importante entre le nombre de bandes spectrales. Les images multispectrales correspondent un ensemble d'au plus de dix bandes spectrales qui de plus ne sont pas contigues dans le spectre électromagnétique. Au contraire, les images hyperspectrales ont un grand nombre de bandes spectrales (habituellement centaines) capturées dans des longueurs d'ondes contigues. La figure 6.1 illustre un exemple d'image hyperspectrale. On peut constater qu'une image hyperspectrale peut être considérée comme une correspondance entre un espace 2D spatial et un espace spectral λ_i dont la dimension est N. Pour ces images, le spectre d'un pixel en fonction de longueur d'onde λ est appelé courbe radiance spectrale ou signature spectrale. Pour chaque pixel, la signature

spectrale fournit donc une information détaillée des propriétés spectrales du matériel et permet une identification et une discrimination précise des objets.

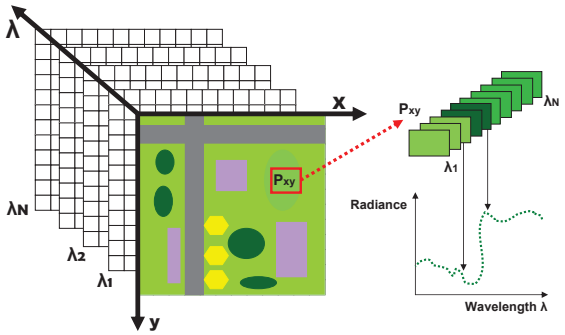

Figure 6.1: Example d'image hyperspectrale

Ainsi, l'imagerie hyperspectrale fournit souvent des résultats qui ne peuvent pas être obtenus avec des images multispectrales ou couleurs. En conséquence, la caractérisation des images à partir de leurs propriétés spectrales a conduit à l'utilisation de ce type d'image dans un nombre croissant d'applications réelles. Parmi les plus importantes, on peut citer l'identification des minéraux, l'agriculture de précision, d'études forestières (état sanitaire, identification d'espèces...) ou la gestion des milieux aquatiques.

Néanmoins, la grande dimension de ces données (typiquement chaque pixel est représenté par plusieurs centaines de valeurs, correspondant aux centaines de longueurs d'onde utilisées) conduit à l'échec des méthodes traditionnelles de traitement. Ainsi, le développement d'algorithmes avancés afin de révéler le réel potentiel de l'imagerie hyperspectrale est nécessaire.

Comme énoncé précédemment, pour ces images, l'information spectrale décrit des propriétés des objets qui ne peuvent pas être perçues par la vision humaine. Parallèlement à cela, l'information spatiale qui décrit les variations spatiales et les différents corrélations dans l'image est également importante. Dans ce cadre, cette dernière information est essentielle afin d'interpréter les objets dans les scènes naturelles. Ceci justifie la nécessité de tenir en compte à la fois les informations spatiale et spectrale dans le traitement des images hyperspectrales. Cependant, le nombre de longueurs d'onde par pixel et le nombre de pixels par image, ainsi que la complexité de l'exploitation conjointe de la corrélation spatiale et spectrale explique pourquoi le traitement des images hyperspectrales est encore un sujet de recherche largement ouvert.

L'un des principaux objectifs du traitement d'image hyperspectrale comprend la délimitation des régions cohérentes dans l'image afin d'obtenir une interprétation complète de la scène. Ceci est envisagé avec des techniques d'analyse supervisés et non supervisées qui travaillent avec la représentation traditionnelle au niveau pixel. L'analyse individuelle des spectres formant une image hyperspectrale fournit un traitement qui n'est pas optimal. En effet, les représentations plus structurées permettent, de manière générale, une analyse plus fine des objets présents dans

l'image. Dans ce cadre, il est nécessaire d'établir des connexions entre les pixels de l'image hyperspectrale afin de distinguer des formes et des objets dans l'image qui caractérisent le contenu de l'image. Les représentations à base de régions fournissent un moyen d'obtenir un premier niveau d'abstraction permettant une réduction du nombre d'éléments à traiter et une obtention des informations sémantiques du contenu de l'image. Ce type de représentations fournit une nette amélioration par rapport à la représentation classique qui repose sur les pixels individuels. En conséquence, sous le titre "L'arbre binaire de partitions: Un nouvel outil pour la représentation hiérarchique et l'analyse des images hyperspectrales", cette thèse est consacrée à la construction d'une nouvelle représentation hiérarchique d'images hyperspectrales basée sur des régions: l'Arbre Binaire de Partitions ABP (ou BPT, pour Binary Partition Tree).
Cette nouvelle représentation peut être interprétée comme un ensemble de régions de l'image structurées en arbre. L'arbre binaire de partitions peut être utilisé pour représenter : (i) la décomposition d'une image en régions pertinentes et (ii) les différentes relations d'inclusion des régions dans la scène. Une telle représentation est illustrée à la figure 6.2. Cette figure montre comment les nœuds de l'arbre représentent des zones de l'image et les branches représentent la relation d'inclusion entre les nœuds.

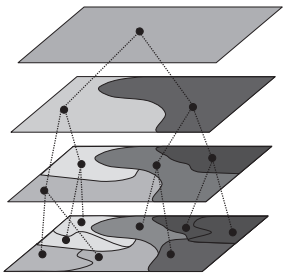

Figure 6.2: Example d'Arbre Binaire de Partitions

L'ABP est obtenu à partir d'une partition initiale de l'image dont les régions peuvent correspondre auxpixels individuels. Si la partition initiale implique n régions, l'ABP correspond à une structure contenant $2n$-1 noeuds. L'ABP doit être créé de telle manière que les régions plus intéressantes ou utiles de l'image soient représentées par des noeuds. Une solution possible, adapté à un grand nombre d'applications consiste à créer l'arbre par l'exécution d'un algorithme de fusion de régions. La figure 6.3 montre un exemple de construction.

Dans cette thèse, la construction de l'ABP a été envisagé avec l'étude de différents algorithmes itératifs de fusion de régions. Cette étude de différents algorithmes a été nécessaire pour gérer la grande dimensionnalité et complexité des données hyperspectrales. Pour définir complètement l'algorithme de fusion, deux questions doivent être analysées:

1. *Modèle de région MR* : il décrit les attributs nécessaires pour représenter une région et pour caractériser l'union de deux régions.

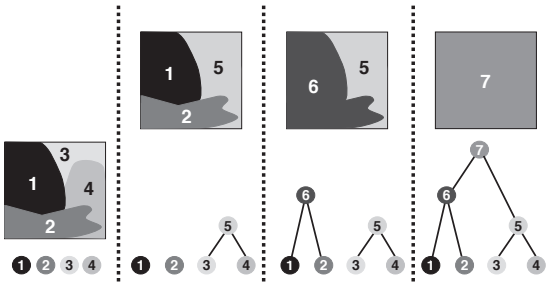

Figure 6.3: Exemple de construction d'Arbre Binaire de Partitions

2. *Critère de fusion* $O(R_i, R_j)$: il spécifie la distance à utiliser entre les attributs de deux régions voisines R_i et R_j. Le choix de cette distance détermine l'ordre de fusion des régions et donc la structure de l'arbre.

Afin de répondre à ces deux points, différents modèles de représentation d'une région hyperspectrale et différentes distances entre deux régions hyperspectrales ont été étudiés dans ce travail.
En ce qui concerne la définition du modèle région, le problème principal est la caractérisation d'un ensemble de spectres formant une région hyperspectrale. Dans ce cadre, la solution la plus simple est d'utiliser un modèle de premier ordre: la moyenne. Dans ce cas, les distances classiques entre spectres peuvent être utilisés comme critères de fusion entre deux spectre moyens représentant deux régions voisines. Malheureusement, certaines limitations existent dans la modélisation des régions par la moyenne. La première limitation est liée au fait qu'il existe une forte variabilité spectrale pour les régions formées à partir du même matériau. Une deuxième limitation de ce modèle de région est la supposition que les régions sont homogènes. Cette hypothèse est rarement vraie dans les scènes naturelles où les régions observées sont souvent texturés. En conséquence, des modèles alternatifs pour modéliser des régions hyperspectrales ont été proposés dans cette thèse.
En ce qui concerne le critère de fusion des régions hyperspectrales, suivant la littérature classique, l'ensemble des valeurs du spectre doit être pris en compte. Pour cela, les distances spectrales classiques les plus efficaces sont celles qui utilisent la forme générale de la courbe des signatures spectrales. D'autre part, tous les canaux dans les images hyperspectrales ne sont pas aussi important en terme de discrimination. Par exemple, dans certains cas, les matériaux permettent leurs discrimination dans des canaux spécifiques de l'image hyperspectrale. Cette problématique est liée à la forte corrélation existant entre bandes consécutives. En fin de compte, une bonne similitude métrique dans l'espace hyperspectral doit tenir compte des questions suivantes: 1) la corrélation entre les canaux afin d'éliminer les informations redondantes et 2) une mesure de similarité globale tenant en compte les valeurs de tous les canaux de l'image. Dans ce travail, différentes mesures de similarité entre régions hypersepctrales sont étudiées afin de définir un bon critère de fusion pour la construction de l'ABP.

Grâce à la structure en forme d'arbre, l'ABP permet la définition d'un grand nombre de techniques pour un traitement avancé des images hyperspectrales. Ces techniques sont typiquement basées sur l'élagage de l'arbre grâce auquel les régions les plus intéressantes pour une application donnée sont extraites. La figure 6.4(b) montre un exemple d'élagage de l'ABP de la figure 6.4(a).

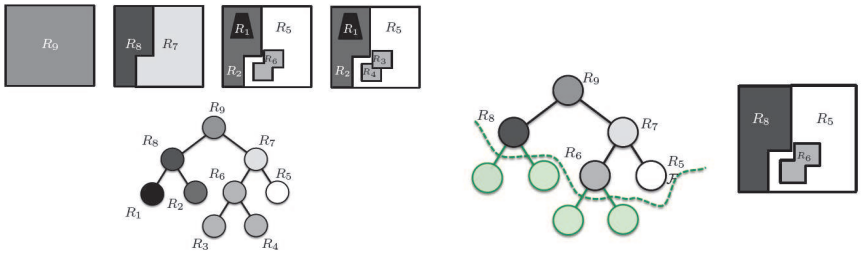

(a) Example d'Arbre Binaire de Partitions

(b) Résultat de l'élagage

Figure 6.4: Example d'élagage de l'Arbre Binaire de Partitions

L'élagage de l'arbre peut être vu comme l'extraction des sous-arbres composés de noeuds considérés comme homogènes au sens d'un certain critère (homogénéité spectrale, intensité, forme, texture,etc.). Cette tâche peut être effectuée en analysant un critère d'élagage le long des branches de l'arbre afin de trouver les noeuds de taille maximale satisfaisant le critère. Alors que la construction de l'arbre est une opération générique, le choix du critère d'élagage est défini en fonction de l'application. Dans ce cadre, cette thèse se concentre sur trois applications particulières : la segmentation, la classification et la détection d'objets dans les images hyperspectrales.
La classification supervisée des images hyperspectrales en utilisant l'ABP consiste à supprimer les sous-arbres composés de nœuds appartenant à la même classe. Ainsi, l'objectif final est d'utiliser l'ABP élagué pour construire une carte de classification complète de l'image. Cela est possible en sélectionnant les feuilles de l'ABP élagué. La méthode proposée dans cette thèse se compose de deux étapes différentes. Tout d'abord, certains descripteurs spécifiques à chaque région sont calculés pour chaque nœud de l'ABP. Puis, la deuxième étape implique une analyse des branches de l'ABP afin de prendre une décision sur l'élagage.
La deuxième application étudiée dans cette thèse est la segmentation des images hyperspectrales. Cela consiste à extraire de l'ABP une partition de l'image formée par les régions les plus significatives. Cette tâche consiste à supprimer les sous-arbres qui peuvent être remplacés par un seul nœud. Cela est possible si tous les noeuds à l'intérieur d'un sous-arbre appartiennent à la même région dans l'image. Cela signifie que la distance entre eux est faible et la distance entre eux et leurs noeuds voisins est élevé. Dans ce contexte, deux approches différentes sont étudiées dans cette thèse. Tout d'abord, la segmentation d'images hyperspectrales est abordée par une stratégie de minimisation d'énergie globale. Pour cette approche, on définit une erreur associée à chaque partition contenue dans le BPT et puis, une technique d'élagage est définie afin d'extraire la partition ayant l'erreur minimale.

La seconde approche dans l'application de segmentation d'images hyperspectrales est fondée sur l'application des coupes normalisées sur les branches de l'ABP. Cette deuxième approche consiste à étudier comment des techniques classiques de partitionnement de graphes peuvent être appliquées sur la structure de l'ABP.
La dernière application abordée dans ce travail est l'élagage de l'ABP visant à effectuer la détection de certains objets en télédétection. Afin d'intégrer l'information spatiale et spectrale, l'ABP est proposé comme un espace de recherche pour construire une identification robuste d'objets. La stratégie consiste à analyser l'ABP en utilisant un ensemble de descripteurs calculés pour chaque noeud. Nous proposons d'utiliser conjointement trois descripteurs: un descripteur de forme, un descripteur spectral, ainsi que la taille de chaque noeud. Ces trois descripteurs sont calculés pour tous les noeuds. Ensuite, les noeuds les plus proches de la racine (i.e. ceux qui sont de taille maximale pour une branche donnée), et qui respectent le prédicat défini, sont retenus pour la détection. Deux exemples de détection ont été testés dans cette thèse: la détection de routes et la détection de bâtiments.
Les résultats expérimentaux obtenus sur différents jeux de données pour les différentes applications montrent les qualités de la représentation ABP. Les résultats des trois applications améliorent clairement les résultats obtenus en utilisant la représentation de l'image hyperspectral au niveau de pixel. L'étude des différentes applications démontre la généricité de la représentation offerte par l'ABP.

7

Appendix

7.1 Tree complexity

The construction of the BPT for an image containing N_p pixels is performed by keeping track of the sequence created by a region-merging algorithm. Accordingly the performances of the BPT construction are directly related to those of the creation of the region-merging algorithm. In this work the implementation of the BPT follows the strategy presented in [141] where the BPT is constructed for classical imagery. Consequently the implementation of the region merging algorithm is based on hierarchical queues. A hierarchical queue is a queue where each element is related to a given priority. An arbitrary element can be introduced in a hierarchical queue in any order. The extraction is, however, done in descending order of priority (i.e. the elements with higher priority are extracted first). Elements having the same priority follow a First-In-First-Out (FIFO) rule. In this context the queue is used to efficiently store, update and access to the merging order distances associated to pairs of neighboring regions.
In the implementation of the region merging algorithm, two structures need to be allocated in memory, the current RAG structure and the priority queue. Both notions are illustrated in Fig. 7.1. The RAG structure (see Sec.2.2) is plotted in orange representing the adjacency of the regions forming the partition at each iteration.

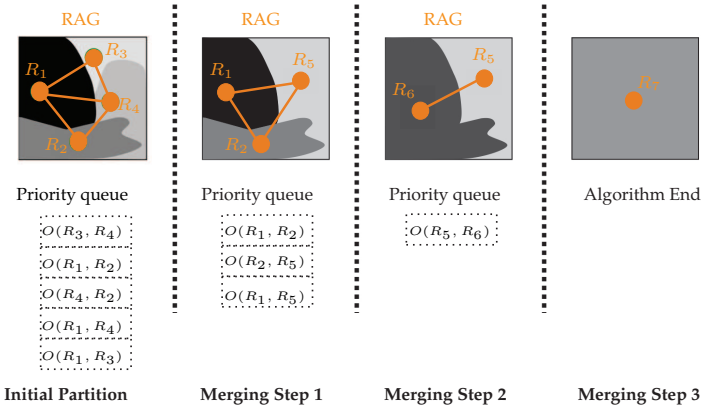

Figure 7.1: Region merging algorithm

At each step the RAG represents the regions and the four corresponding adjacencies. The priority queue is used to index and process the links according to their merging order. As shown in Fig. 7.1, this order of priority queue corresponds to the merging order. The first position of the queue therefore contains the edge of the RAG associated to the minimum $O(R_i, R_j)$ value. In the case of Fig. 7.1 it can be observed that the first position corresponds to $O(R_3, R_4)$. Accordingly this pair of regions is merged in the first iteration while $O(R_3, R_1)$ appears contrarily in the last position. This implies that the similarity of these regions is very low.
In order to initialize the RAG and the priority queue the M_{R_i} is computed for all the initial nodes of the RAG before computing the $O(R_i, R_j)$ for each pair of neighboring nodes. This distance information is introduced in the queue in a position according to its value. As a con-

sequence, whether the initial partition is made of single-pixel regions and the neighborhood is four-connected, the queue is initially formed by N_p multiplied by the all pair of regions according to the four-connectivity.

After each merging the queue is updated in two sequential steps, (i) by removing the old links concerning the merged nodes, and (ii) by updating the new links representing the adjacency of the new regions with its neighbors. The algorithm used to insert, to delete and to search the nodes relies on a balanced tree binary search. The number of steps required for searching, inserting and deleting nodes in the queue can be therefore done in $O(log2N)$ where N is the number of nodes in the tree [142] [141].

In order to construct the BPT $N_p - 1$ merging iterations are performed after which the queue is empty. Accordingly the number of operations O_{total} required by this implementation is given by

$$O_{total} = O_{initial} + (N_p - 1) * O_{update} \tag{7.1}$$

where $O_{initial}$ is the number of operations at the initialization step and O_{update} is the number of operations required for updating the new links. The former task consists of two different sub-tasks as shown in Eq.7.2. First, the N_p region models are computed where $O_{ini\ node}$ represents the number of operations required by the construction of a BPT leaf. Second, the corresponding distance $O_{merging}$ between its four neighboring pixels is computed for each leaf node.

$$O_{initial} = N_p * O_{ini\ node} + N_p * 4 * O_{merging} \tag{7.2}$$

The second term of Eq.7.1 corresponds to the $N_p - 1$ iterations that have to be performed. Note that the term $N_p * 4$ can be lower if a neighboring pixel has been previously initialized. The term $O_{updated}$ is the number of required operations after a region merging step corresponding to the update of the queue, which are described by Eq.7.3. At each iteration, a new node is formed and the corresponding region model is computed. The second term of Eq.7.3 corresponds to the update of distances between the old neighbors of the removed regions and the newly formed region. It must be noted that the number of distances to be computed at this step depends on a factor K. This factor corresponds to the number of links to be updated and it depends on the tree construction (if it is more or less balanced).

$$O_{update} = O_{node} + K * O_{merging} \tag{7.3}$$

This last equation shows the strong dependence of the complexity of the BPT construction on three factors, (i) the number of pixels of the image N_p, (ii) the operations required for the creation of a node after a merging O_{node}, and (iii) the complexity of the merging criteria $O_{merging}$ between each pair of adjacent regions.

In order to minimize the computational load the previous bottlenecks of the tree must be studied. As for parameter N_p, it is evident that the number of pixels of the image cannot be modified. However, in order to reduce the computational load in some applications it might be interesting to start where pixels are not single individual regions as it is done in Fig. 7.1. For instance, an

initial partition can be defined with regions containing three pixels. Although some accuracy will be lost in this case, the complexity of the BPT construction will strongly decrease.
Concerning the term O_{node}, the computation of the region model plays an important role. In this context the strategy of constructing a region model in a recursive manner means that the model of the union of two regions can be computed from the models of these regions. Non-recursive strategies requiring to go back to the original pixels to compute the model should be avoided.
Concerning the region models described in this dissertation the first order and the non-parametric statistical region model can be recursively computed. In the case of the first order model, this can be easily done by saving only two parameters, (i) the number of pixels of the region N_{R_p} and (ii) the accumulative sum for all the spectra for each band $\sum_{j \in N_{R_p}} I_{\lambda_i}(p_j)$. Regarding the non-parametric statistical region model, the model of a parent node can be also computed recursively since:

$$H^{\lambda_i}_{R_{i \cup j}}(P_{a_k}) = \frac{N_{R_{i_p}} * H^{\lambda_i}_{R_i}(P_{a_k}) + N_{R_{j_p}} * H^{\lambda_i}_{R_j}(P_{a_k})}{N_{R_{j_p}} + N_{R_{i_p}}} \tag{7.4}$$

where $H^{\lambda_i}_{R_i}(P_{a_k})$ and $H^{\lambda_i}_{R_j}(P_{a_k})$ are the probability of the children nodes representing the probability of having a specific radiance value at a_k histogram bin.
Hence a recursive region model O_{node} is mandatory in order to obtain better performances. However, the information concerning each model must be saved in order to get a recursive algorithm. Therefore, the allocation of the memory for each node has an increasing cost increasing the memory cost of the BPT construction.
An important remark must be done concerning the non-parametric statistical model presented in Sec. 3.2.2. For this region model, an algorithm estimating the probability distribution of a single pixel has been described. As a consequence the number of steps O_{node} required at Eq.7.2 does not correspond to the same number of operations $O_{ininode}$ needed for Eq. 7.3. In the first case the number of operations is related to the pdf estimation for each individual pixel. In the second case this region model is computed recursively as it is described by Eq. 7.4.
In a large hyperspectral image, the estimation of the pdf of individual pixels can become a bottleneck during the initialization step. Note that for each pixel the algorithm described in Fig.1 is computed by analyzing a local window. In this thesis, we have made no attempt to actually optimize the processing time. However, if this issue of pixel pdf estimation turns out to be important in the context of specific applications, simplification of the estimation algorithm will be studied.
Comparing the two proposed region models in this thesis, it can be seen that the complexity and the memory requirements are quite different. The first order model only requires the allocation of 1) a vector of N_z values where each component contains the sum of all the spectra in the region and 2) a variable describing the number of pixels of the region. In the case of non-parametric statistical region model the set of histograms per bands containing N_{Bins} must be allocated in memory for each region. In the case of O_{MDS} criterion the principal coordinates of the region must be also allocated in memory in order to avoid redundant operations. In conclusion, the memory requirements are high for the non-parametric statistical region model.

The number of operations concerning the second important term $O_{merging}$ has been also studied in this thesis. In the case of the merging criteria involving the first region model the necessary operations are quite fast. In contrast the other merging criteria require a higher computational time. The parameter N_{Bins} plays here an important role. Parameter D_s is also critical because the computation of Wilks' test involves a higher computational time in front of more principal coordinates.

Another remark concerns the number of bands in the hyperspectral images N_z, which is an important factor in terms of computational time and memory usage. In order to assess the complexity of BPT construction several tests have been performed. The BPT construction algorithm has been tested using an Intel Xeon processor running under Linux with a clock speed of 2.40GHz and 20 Gbytes of RAM. We remark that this thesis mades no attempt to minimize the computational load nor the memory requirements of our algorithms. Thus, this area can be further improved.

The first test corresponds to the first zone of Pavia university image presented in Fig.3.25. This image is formed by 3705 pixels and a spectral dimension is $N_z = 102$. The CPU time and the required memory for BPT construction is shown in Tab.7.1 comparing the different merging criteria. In the case of non-parametrical statistical region model N_{bins} is equal to 150. The O_{MDS} criterion uses an intrinsic dimension of the image $D_s = 3$.

The criteria O_{SID} and O_{SAM}, which rely on the first order region model, are much faster and requires low memory. On the other hand, the other merging criteria are based on the non-parametric statistical region model. In the case of O^1_{BAT}, the initialization of the individual pixels is made by the method proposed in [18]. Contrarily, O^2_{BAT} uses the pdf estimation explained in Chapter 3. These two different initialization steps concerning the BPT construction lead to some differences in Tab. 7.1. As it can be seen, the computational time is similar in both cases. This result is explained because, in the early stage of the BPT construction using O^1_{BAT}, the drawback concerning the histogram misalignment happens. The construction of the BPT is therefore less balanced implying more comparisons between adjacent regions. Contrarily, consuming a similar time O^2_{BAT} leads to a better initialization. Indeed, one second from the total 2.15 minutes is completely dedicated to the pdf estimation.

The differences between the initialization can also be seen in O_{DIF} and O_{MDS}. As expected, the pdf estimation used in this thesis is more time consuming. However, the BPT is better constructed in the case of pdf estimation by Alg. 1 as in the case of Battacharyya distance. Tab. 7.1 shows the price to pay for it. The merging criterion O_{MDS} is clearly the most time consuming. This is completely explained by the computation of the matrix distance used to compute the principal coordinates. In this case, almost 6 out of the 9 minutes are used to compute the principal coordinates of the individual pixels.

In terms in memory, it can be observed the difference between the two presented region models. The allocation of memory of the set of N_z histograms shows its implication in this case.

Another complexity test is shown in next Tab.7.2. This test corresponds to the second zone of Pavia University of Fig.3.25 .This second table corroborates the same conclusions as the last Table.

In order to show another example with a larger image, the next example shows the complexity

Table 7.1: Performances Pavia Uni 1: 3705 pixels

Merging Criterion	Time (minutes)	Memory (Mbytes)
O_{SID}	0.072	10.24
O_{SAM}	0.047	10.21
O^1_{BAT}	1.56	307.2
O^2_{BAT}	2.15	311.2
O^1_{DIF}	1.01	309.24
O^2_{DIF}	2.56	310.27
O^1_{MDS}	9.24	337.92
O^2_{MDS}	11.02	335.8

Table 7.2: Performances Pavia Uni 2: 3174 pixels

Merging Criterion	Time (minutes)	Memory(Mbytes)
O_{SID}	0.054	10.21
O_{SAM}	0.0532	9.82
O^1_{BAT}	1.58	247.80
O^2_{BAT}	1.53	251.90
O^1_{DIF}	0.58	290.81
O^2_{DIF}	2.29	299
O^1_{MDS}	7.50	327.68
O^2_{MDS}	10.06	317.44

in time of the BPT constructed at Fig.7.2. As in the other two examples, the number of bands is equal to $N_z = 102$ for this image. The computation times shown in Tab.7.3 shows how increasing the number of pixels, the requirements in terms of complexity and memory allocation are higher.

Table 7.3: Performances Pavia Uni: 16000 pixels

Merging Criterion	Time (minutes)	Memory (Mbytes)
O_{SID}	0.29	71.68
O_{DIF}	3.57	757.76
O_{MDS}	32.40	790.72

It must be noticed that the BPT is viewed in this work as an image representation that has to be constructed only once and that opens the door to a wide range of applications. As demonstrated in Chapter 4, different pruning strategies handle different applications. Moreover, operations such as modifying the parameters for an SVM classification, or training the classifier, or optimizing the segmentation or searching for different objects can all be performed on the constructed BP. The complexity of the pruning strategy mainly depends on the number of BPT nodes. In this thesis, the proposed pruning strategies are faster. For instance, in the case of classification, energy minimization or object detection, algorithms turn in less than one minute for a BPT containing 7409 nodes.

7.2 Acronyms

BPT	Binary Partition Tree
λ	Wavenlength
I_λ	Hyperspectral image
N_z	Number of hyperspectral bands
N_p	Number of pixels of hyperspectral image
I_{λ_j}	Hyperspectral image band given a specific wavelength λ_j
$I_{\lambda_j}(p)$	the radiance value of the pixel p on the hyperspectral image band λ_j
$\mathbf{I}_\lambda(p)$	is the vector pixel p containing all the radiance values along the N_z wavelenghts
R	Image region
$\mathcal{P}$	Image partition
N_R	Number of region containing in an image partition
RAG	Region Adjacency Graph
$\mathcal{N}$	Tree node
$\mathcal{T}_\mathcal{N}$	Subtree rooted by BPT node $\mathcal{N}$
M_R	Region Model
$O(R_i, R_j)$	Merging criterion between region R_i and R_j
N_{R_p}	Number of spectra containing in region
$\bar{I}^R_{\lambda_i}$	The average spectral value of a region R at the image band λ_i
$\bar{\mathbf{I}}^R_\lambda$	Vector containing the average spectral values of a region R for all N_z bands
$P_R(\lambda)$	The probability distribution according to λ by applying the $\bar{\mathbf{I}}^R_\lambda$ spectrum normalization
$H^{\lambda_k}_R$	Empirical spatial distribution (histogram) of the region R in the band λ_k
N_{Bins}	Number of bins
$H^{\lambda_i}_R(P_{a_k})$	Probability of the region R of having the radiance value a_k in the band λ_i
$P(p)$	Patch neighborhood centered at pixel p
W_x, W_y	Horizontal and vertical dimension of patch neighborhood
Ω_p	Search window centered at p given its individual pixel distribution initialization
$w(p, p_y)$	The additive contribution to the probability of the pixel p of having the value of $\mathbf{I}_\lambda(p_y)$.
$d_{win}(p, p_y)$	The local displacement between pixels p and p_y according to the search window space Ω_p
$Z(p)$	Normalizing factor
d_p	The local displacement on the patch regarding the central pixel
h_{λ_i}	Smoothing parameter for λ_i
$\sigma^{\lambda_i}_N$	Standard deviation of the noise in the λ_i
$P_R(\lambda)$	Probability distribution of a spectrum concerning λ dimension
SAM	Spectral Angle Mapper
SID	Spectral Information Divergence
$D(R_i, R_j)$	Kullback-Leibler Divergence between R_i and R_j
BAT	Battacharyya Distance
DIF	Diffusion Distance
MDS	Multidimensional Scaling Metric

$\mathcal{P}$	Image Partition
$\mathcal{P}_{GT}$	Ground truth Partition
d_{asym}	Asymmetric distance between partitions
d_{sym}	Symmetric distance between partitions
N_c	Number of classes of ground truth
$\mathcal{A}_{\mathcal{N}}$	Area of region contained on the node $\mathcal{N}$
$P_{\mathcal{N}}$	Class probability distribution of node $\mathcal{N}$
$L_{\mathcal{N}_i}$	Number of leaves forming the sub-tree $T_{\mathcal{N}_i}$ rooted by the node $\mathcal{N}_i$
$E_{\tilde{\mathcal{P}}}$	Minimum Pruning cost of the partition $\tilde{\mathcal{P}}$
C_0	Equaltity constraint of the Lagrangia multiplier
$E_{\mathcal{BPT}}$	the set of all the possible partitions $\mathcal{P}$ contained in the BPT
$D(\mathcal{N})$	Error commtited at node $\mathcal{N}$
$C(\mathcal{N})$	Constraint at node $\mathcal{N}$
λ^*	Optimal Lagrangian parameter
$\mathcal{N}_r$ and $\mathcal{N}_l$	Right and left children nodes sharing the same $\mathcal{N}$ father node
l	Leaf node
$\mathcal{W}_{\mathcal{N}}$	Pruning decision weight for a node $\mathcal{N}$
$P_d^{\mathcal{N}}(l_i)$	Local Pruning decision from a leaf l_i to its ancestor node on the branch $\mathcal{N}$
$\mathcal{B}$	BPT branch
$\mathcal{P}_{\mathcal{B}}$	The set containing the nodes forming the BPT branch $\mathcal{B}$
G	Weighted graph
W	Affinity matrix
$d(\mathcal{N}_i, \mathcal{N}_j$	Similarity distance between node $\mathcal{N}_i$ and$\mathcal{N}_j$
L	Laplacian matrix
$\mathcal{E}$	Second smallest eigenvalues of Laplacian matrix
$\mathcal{N}_{\mathcal{N}}$	Number of nodes forming a BPT branch

7.3 Mathematical Appendix: Association measures

Roy, Lawley-Hotelling and Pillai Criteria

For testing $\beta = 0$, another criteria as the Roy R, Lawley-Hotelling U and Pilllai's criterion V can be employed as

$$R = \frac{\lambda_1}{(1+\lambda_1)} \tag{7.5}$$

$$U = tr(E^{-1}H) = \sum_{i=1}^{D_s} \lambda_i \tag{7.6}$$

$$V = tr((E+H)^{-1}H) = \sum_{i=1}^{D_s} \frac{\lambda_i}{(1+\lambda_i)} \tag{7.7}$$

where λ are the eigenvalues associated to $E^{-1}H$. These criteria can be described in terms of canonical correlations as

$$R = r_1^2 \tag{7.8}$$

$$U = \sum_{i=1}^{D_s} \frac{r_i^2}{1-r_i^2} \tag{7.9}$$

$$V = \sum_{i=1}^{D_s} r_i^2 \tag{7.10}$$

The three different tests can be used to define three new association measures A_R, A_{LH} and A_P by

$$A_R = \frac{\lambda_1}{(1+\lambda_1)} \tag{7.11}$$

$$A_{LH} = \frac{U}{D_s}(1+\frac{U}{D_s}) \tag{7.12}$$

$$A_P = \frac{V}{D_s} \tag{7.13}$$

Other symmetric measures to measure multivariate dependence between two data sets

Vector Correlations

Given two data sets X and Y whose covariance matrices are defined by $S_{xx} = X^tX$, $S_{yy} = YY^t$ and $S_{X,y} = X^tY$, the RV coefficient [25] is given by

$$RV(X,Y) = \frac{tr(S_{xy}S_{yx})}{\sqrt{tr(S_{xx}^2)tr(S_{yy}^2)}} \tag{7.14}$$

In our case, being U_{R_i} and U_{R_j} the standard coordinates of two regions having $N_z x D_s$ dimensions, $S_{xx} = S_{yy} = I_{D_s}$ where I_{D_s} is a diagonal matrix of D_s columns and rows. Thus, the association measure A_{RV} given by the vectorial correlation between two regions R_i and R_j is

$$A_{RV}(R_i,R_j) = \frac{tr(U_{R_i}^t U_{R_j} U_{R_j}^t U_{R_i})}{\sqrt{D_s^2}} \tag{7.15}$$

which is expressed in terms of canonical correlations r_i as

$$A_{RV}(R_i,R_j) = \frac{\sum_{i=1}^{D_s} r_i^2}{D_s} \tag{7.16}$$

Note that being in our case $tr(S_{xx}^2) = tr(S_{yy}^2)$, the association measure A_{RV} is equal to A_P

Generalized multiple Correlation

Another measure of multiple correlation coefficient [31] between X and Y has been defined as

$$R^2(X,Y) = \frac{det(S_{yx}S_{xx}^{-1}S_{xy})}{det(S_{yy})} \tag{7.17}$$

Simplifying this last equation when X and Y correspond to the standard coordinates U_{R_i} and U_{R_j}, the association measure A_R by the multiple correlation coefficient is defined as

$$A_{HC}(R_i,R_j) = det(U_{R_j}^t U_{R_i} U_{R_i}^t U_{R_j}) = \prod_{i=1}^{D_s} r_i^2 \tag{7.18}$$

where notation HC refers to Hotelling and Cramer[31]

Procrustes statistics

According to [28], Procrustes analysis is a technique which matches a configuration to another, where there is a one-to-one correspondence from one set to the other set of points, and obtains a measure of the match. If both configurations are represented by two centered matrices X and Y, the Procrustes statistic PR is

$$PR^2(X,Y) = \frac{[tr(X^tYY^tX)^{\frac{1}{2}}]^2}{tr(X^tX)tr(Y^tY)} \tag{7.19}$$

This test can be expressed as the association measure A_{PR} by considering $Y = U_{R_j}\Lambda_{R_j}$ and $X = U_{R_i}\Lambda_{R_i}$ as

$$
\begin{aligned}
A_{PR}(R_i, R_j) = & \frac{[tr(\Lambda_{R_i} U_{R_i}^t U_{R_j} \Lambda_{R_j}^2 U_{R_j}^t U_{R_i} \Lambda_{R_i})^{\frac{1}{2}}]^2}{tr(\Lambda_{R_i}^2) tr(\Lambda_{R_j}^2)} \\
= & \frac{[tr(U_{R_i}^t U_{R_j} U_{R_j}^t U_{R_i})^{\frac{1}{2}}]^2}{D_s^2} \\
= & \frac{(\sum_{i=1}^{D_s} r_i)^2}{D_s}
\end{aligned} \tag{7.20}
$$

Order relationship

The association measures can be ordered as

$$
A_{HC} \leq A_{PR} \leq A_P \leq A_{LH} \leq A_R \leq A_w \tag{7.21}
$$

because, clearly,

$$
\prod_{i=1}^{D_s} r_i^2 \leq \prod_{i=1}^{D_s} (r_i^2)^{\frac{1}{s}} \leq \frac{\sum_{i=1}^{D_s} r_i^2}{D_s} \tag{7.22}
$$

7.4 Hierarchical levels obtained by Pavia University data set

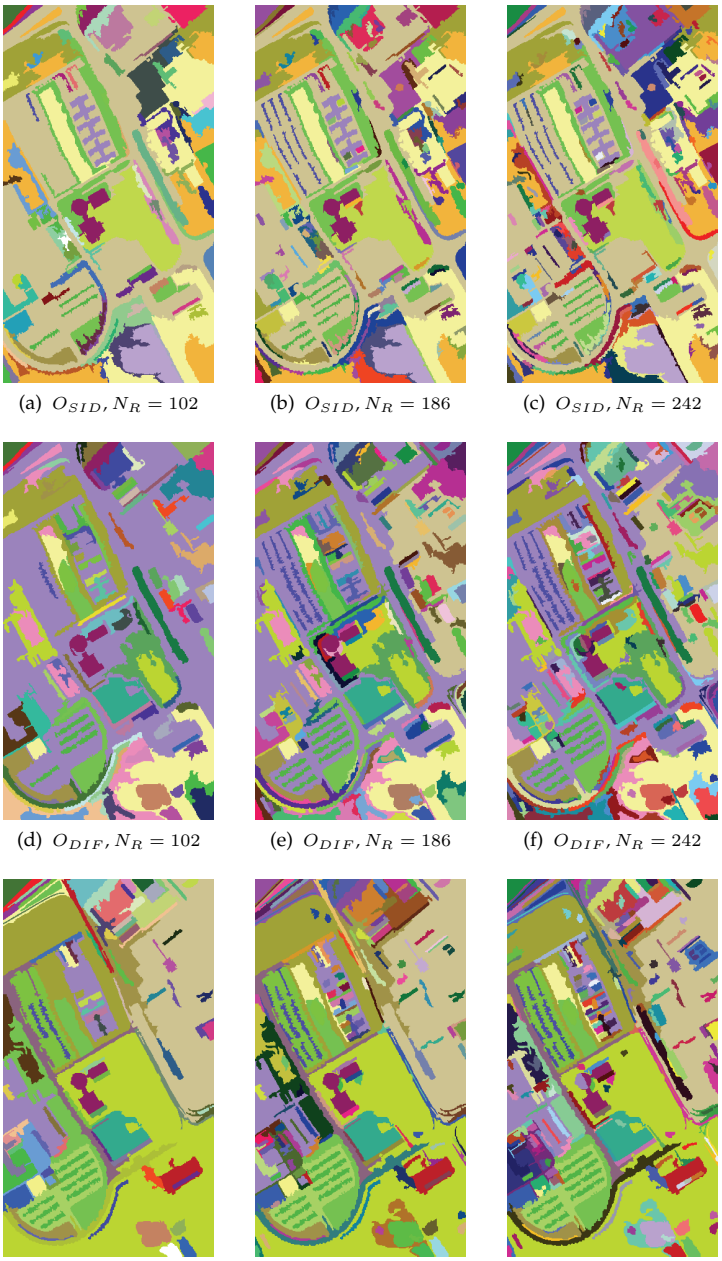

(a) $O_{SID}, N_R = 102$ (b) $O_{SID}, N_R = 186$ (c) $O_{SID}, N_R = 242$

(d) $O_{DIF}, N_R = 102$ (e) $O_{DIF}, N_R = 186$ (f) $O_{DIF}, N_R = 242$

(g) $O_{MDS}, N_R = 102$ (h) $O_{MDS}, N_R = 186$ (i) $O_{MDS}, N_R = 242$

Figure 7.2: Hierarchical Levels of Pavia University

7.5 List of Publications

International Journals

- A. Alonso-Gonzalez, S. Valero, J. Chanussot, C. Lopez-Martinez and P. Salembier,
  Processing multidimensional SAR and hyperspectral images with Binary Partition Trees,
  In reviewing process in IEEE Transactions on Geoscience and Remote Sensing, 2012

- S. Valero, P. Salembier and J. Chanussot,
  Hyperspectral image representation and processing with Binary Partition Trees,
  In reviewing process in IEEE Transactions on Image Processing, 2011

- C.M. Cuadras, S. Valero, D. Cuadras, P. Salembier and J. Chanussot,
  Distance-based measure of association with applications in relating hyperspectral images,
  Communications in Statistics: Theory and Methods,vol.41, pp. 2342–2355, 2012.

International Conferences

- S. Valero, P. Salembier and J. Chanussot,
  Hyperspectral image segmentation using Binary Partition Trees,
  IEEE ICIP'11 - International Conference on Image Processing, september 2011

- S. Valero, P. Salembier, J. Chanussot and C.M. Cuadras,
  Improved Binary Partition Tree Construction for hyperspectral images: Application to object detection
  IEEE IGARSS'11 - International Geoscience and Remote Sensing Symposium, Vancouver

- J.Benediktsson, L.Bruzzone, J.Chanussot, M.Dalla Mura, P.Salembier and S.Valero,
  Hierarchical Analysis of Remote Sensing Data: Morphological Attribute Profiles and Binary Partition Trees
  ISMM 2011, International Symposium on Mathematical Morphology, 2011

- C.M. Cuadras, S. Valero, P. Salembier, J. Chanussot
  Some measures of multivariate association relating two spectral data sets,
  COMPSTAT 2010 - International Conference on Computational Statistics, 2010, Paris

- S. Valero, P. Salembier and J. Chanussot,
  Comparison of merging orders and pruning strategies for binary partition tree in HSI data
  IEEE ICIP'10 - International Conference on Image Processing, 2010, Hong Kong

- S. Valero, P. Salembier and J. Chanussot,
  New hyperspectral data representation using binary partition tree
  IEEE IGARSS'10 - International Geoscience and Remote Sensing Symposium,2010, USA
  This paper received the Symposium Prize Best Paper Award

National Conferences

- S. Valero, P. Salembier and J. Chanussot,
  L'arbre binaire de partitions: Une nouvelle representation hierarchique d'une image hyperspectral,
  Gretsi, Symposium on Signal and Image Processing, 2011

Bibliography

[1] A. Plaza, J.A. Benediktsson, J. Boardman, J. Brazile, L. Bruzzone, G. Camps-Valls, J. Chanussot, M. Fauvel, P. Gamba, A. Gualtieri, J. Tilton and G. Trianni. Advanced Processing of Hyperspectral Images. *In Remote Sensing of Environment*, vol. 113, n° 1, pp. S110-S122, 2009.

[2] C.I. Chang. Hyperspectral Imaging: Techniques for Spectral Detection and Classification. *In Kluwer Academic Publishers*, Dordrecht, 2003

[3] D.A. Landgrebe. Signal Theory Methods in Multispectral Remote Sensing. *In John Wiley and Sons*, 2003

[4] G. Camps-Valls and L. Bruzzone. Kernel-based methods for hyperspectral image classification. *In IEEE Transactions on Geoscience and Remote Sensing*, 43(6), pp.1351-1362, 2005.

[5] L. Bruzzone, M. Chi, and M. Marconcini. A novel transductive SVM for semisupervised classification remote sensing images. *In IEEE Transactions on Geoscience and Remote Sensing*, vol.44(11), pp.3363-3373, 2006.

[6] M. Chi and L. Bruzzone. Semisupervised classification of hyperspectral images by SVMs optimized in the primal. *In IEEE Transactions on Geoscience and Remote Sensing*, vol.45(6), pp.1870-1880, 2007.

[7] C.-I Chang. Spectral information divergence for hyperspectral image analysis. *in IEEE Proceedings of IGARSS*, pp.509-511, Germany, 1999.

[8] A. Plaza, P. Martinez, R. Perez and J. Plaza. Spatial/spectral endmember extraction by multidimensional morphological operations. *in IEEE Transactions on Geoscience and Remote Sensing*, vol.40, pp.2025-2041, 2002.

[9] N. Gorretta, J.M Roger, G. Rabatel and V. Bellon-Maurel, C. Fiorio and C. Lelong. Hypersectral image segmentation: The butterfly approach. *In IEEE Proceedings of Workshop on Hyperspectral Image and Signal Processing: Evolution in Remote Sensing*, 2009.

[10] M. Fauvel, J.A. Benediktsson, J. Chanussot and J.R. Sveinsson. Spectral and Spatial Classification of Hyperspectral Data Using SVMs and Morphological Profiles. *In IEEE Transactions on Geoscience and Remote Sensing*, vol.46 (11), pp.3804-3814, 2008.

[11] A. Farag, R. Mohamed and A. El-Baz. A unified framework for map estimation in remote sensing image segmentation. *In IEEE Transactions on Geoscience and Remote Sensing*, vol.43(7), pp.1617-1634, 2005.

[12] J. Li, J. Bioucas-Dias and A. Plaza. Semi-Supervised Hyperspectral Image Segmentation Using Multinomial Logistic Regression with Active Learning. *In IEEE Transactions on Geoscience and Remote Sensing*, vol.48(11), pp.4085-4098, 2010

[13] J. Angulo and S. Velasco-Forero. Semi-supervised hyperspectral image segmentation using regionalized stochastic watershed. *In Proceedings of the SPIE*, vol.7695, 2010.

[14] A. K. Jain, M. N. Murty, and P. J. Flynn. Data clustering: A review. *In ACM Computing Surveys*, vol.31(3), pp.264-323, 1999.

[15] P. Salembier and L. Garrido. Binary partition tree as an efficient representation for image processing, segmentation, and information retrieval. *In IEEE Transactions on Image Processing*, vol.9(4), pp.561-576, 2000.

[16] F. Van der Meer. The effectiveness of spectral similarity measures for the analysis of hyperspectral imagery. *In International Journal of applied earth observation and geoinformation*, vol.8, pp.3-17, 2006.

[17] F. Calderero, F. Marqués. Region-merging Techniques Using Information Theory Statistical Measures. *In IEEE Transactions on Image Processing*, vol.19, pp.1567-1586, 2010.

[18] F. Calderero, F. Marques and A. Ortega. Performance Evaluation of Probability Density Estimators for Unsupervised Information Theoretical Region Merging. *In IEEE Proceedings of ICIP 2009*, pp.4397-4400, Egypt, 2009

[19] S. Lee and M. Crawford. Unsupervised multistage image classification using hierarchical clustering with a Bayesian similarity measure. *In IEEE Transactions on Image Processing*, vol.14(3), pp.312-320, 2005.

[20] Y. Tarabalka, J.A. Benediktsson, J. Chanussot. Spectral-Spatial Classification of Hyperspectral Imagery Based on Partitional Clustering Techniques. *In IEEE Transactions on Geoscience and Remote Sensing*, vol.47(8), pp.2973-2987, 2009.

[21] Y. Tarabalka, J. A. Benediktsson, J. Chanussot, and J. C. Tilton. Multiple Spectral–Spatial Classification Approach for Hyperspectral Data. *In IEEE Transactions on Geoscience and Remote Sensing*, vol. 48, no. 11, pp.4122-4132, 2010.

[22] J.A. Gualtieri and J. Tilton. Hierarchical Segmentation of Hyperspectral Data. *In Proceedings os AVIRIS Earth Science and Applications Workshop*, pp.5-8, 2002.

[23] P. Coupe, P. Yger, S. Prima, P. Hellier, C. Kervrann, and C. Barillot. An Optimized Blockwise Nonlocal Means Denoising Filter for 3-D Magnetic Resonance Images, *In IEEE Transactions on Medical Imaging*, vol. 27(4), pp.425-441, 2008.

[24] M. Dimiccoli and P. Salembier. Hierarchical region-based representation for segmentation and filtering with depth in single images. *In IEEE Procedings of ICIP'09*, pp.3533-3536, Egypt, 2009

[25] Y. Escoufier. Le Traitement des Variables Vectorielles. *In Biometrics (International Biometric Society)* vol.29 (4): 751-76, 1973.

[26] C.M. Cuadras, S. Valero, P. Salembier and J. Chanussot. Some measures of multivariate association relating two spectral data sets. *In Proceedings of Compstat 2010*, France.

[27] C.M. Cuadras. Multidimensional and Dependencies in Classification and Ordination. *In K. Fernandez and A. Morineau (Ed.), Analyses Multidimensionelle des Donnees*, pp.15-25, France.

[28] T.F. Cox and M.A. Cox. Multidimensional Scaling. *In K. Fernandez and A. Morineau (Ed.),Chapman & Hal*, London, 1994.

[29] T.W. Anderson. An Introduction to Multivariate Analysis. *In Third Edition Wiley*, New York, 2003.

[30] C.R. Rao, H. Toutenburg, A. Fieger, C. Heumann, T. Nittner and S. Scheid. Linear Models: Least Squares and Alternatives. *In Springer Series in Statistics*, 1999

[31] E. Cramer and W.A. Nicewander. Some symmetric, invariant measures of multivariate association. *In Psychometrika*, vol.44, pp.43-54, 1979.

[32] J.C. Gower. Some distance properties of latent roots and vector methods used in multivariate analysis *in Biometrika* , vol.53, pp.325-338, 1966.

[33] C.M. Cuadras, A. Arenas and J. Fortiana. Some computational aspects of a distance-based model for prediction. *In Communications in Statistics: Simulation and Computation* , vol.25, pp.593-609, 1996.

[34] M.H. Kutner, C.J. Nachtsheim, and J. Neter. Applied Linear Regression Model. *In 4th ed., McGraw-Hill/Irwin*, 2004.

[35] K.M. Rajpoot and N.M. Rajpoot. Wavelet based segmentation of hyperspectral colon tissue imagery. *In Proceedings 7th IEEE International Multitopic Conference INMIC*, pp.38-43, 2003.

[36] I. Silverman, S.R. Rotman and C.E. Caefer. Segmentation of Hyperspectral Images from the Histograms of Principal Components. *In Imaging Spectrometry MII, Sylvia S. Shen , Editor, Proceedings of SPIE*, vol.4816, 2002.

[37] G. Noyel, J. Angulo and D. Jeulin. Morphological segmentation of hyperspectral images. *In Image Anal. Stereol.*, vol.26, pp.101-109, 2007.

[38] M. Servais, T. Vlachos and T.Davies. Motion-compensation using variable-size block-matching with binary partition trees. *In IEEE Procedings of ICIP'05*, vol.1, pp.I-157, Sept. 2005.

[39] V. Vilaplana, F. Marques and P. Salembier. Binary Partition Tree for Object Detection. *in IEEE Transactions on Image Processing*, vol.17, pp.2201-2216, 2008.

[40] V. Vilaplana and F. Marques. On building a hierarchical region-based representation for generic image analysis. *In IEEE Proceedings of ICIP'07*, vol.4, pp.325-328, 2007.

[41] T. Adamek and N.E. O'Connor. Using dempster-shafer theory to fuse multiple information sources in region-based segmentation. *In IEEE Proceedings of ICIP 2007*, pp.269-272, 2007.

[42] G. Scarpa, M. Haindl, and J. Zerubia. A hierarchical finite-state model for texture segmentation. *In IEEE Proceedings of ICASSP '07*, vol.1, pp.1209-1212, 2007.

[43] Z. Liu, J. Yang and N. Peng. An efficient face segmentation algorithm based on binary partition tree. *In Signal Processing Image Communication*, vol.20(4), pp.295-314, 2005

[44] H. Lu, J.C. Woods and M. Ghanbari. Image segmentation by binary partition tree. *In Electronics Letters*, vol.42, pp.966-967, 2006

[45] S. Cooray, N. O'Connor, S. Marlow, N. Murphy and T. Curran. Semi-Automatic Video Object Segmentation Using Recursive Shortest Spanning Tree and Binary Partition Tree. *In Workshop on Image Analysis for Multimedia Interactive Services*, 2001.

[46] J. Pont-Tuset and F. Marques. Contour Detection using Binary Partition Trees. *In IEEE Proceedings of ICIP'10*, pp.1609-1612, 2010.

[47] C. Ferran Bennstrom and J. R. Casas. Binary partition tree creation using a quasi-inclusion criterion. *In Proceedings of 8th International Conference on Information Visualization*, 2004.

[48] T. Adamek, Noel E. N. O'Connor, and Noel Murphy. Region-based segmentation of images using syntactic visual features. *In in Proceedins of 6th International Workshop on Image Analysis for Multimedia Interactive Services*, 2005.

[49] H. Lu, J. C. Woods, and M. Ghanbari. Binary Partition Tree for Semantic Object Extraction and Image Segmentation. *In IEEE Transactions on Circuits and Systems for Video Technology*, vol.17(3), pp.378-383, 2007.

[50] L. Breiman, J. Friedman, R. Olshen and C. Stone. Classification and Regression Trees. *In Wadsworth International Group*, Belmont, CA.

[51] J.S. Cardoso and L. Corte-Real. Toward a generic evaluation of image segmentation. *In IEEE Transactions on Image Processing*, vol.14(11), pp.1773-1782, 2005.

[52] J.S. Cardoso. Metadata Assisted Image Segmentation. *In Ph.D. dissertation in Faculdade de Engenharia da Universidade do Porto*, 2006.

[53] D. Martin. An empirical approach to grouping and segmentation. *In Ph.D. dissertation, UC Berkeley*, 2003

[54] D. Martin, C. Fowlkes, D. Tal, and J. Malik. A database of human segmented natural images and its application to evaluating segmentation algorithms and measuring ecological statistics. *In Proceedings of the 8th International Conference on Computer Vision (ICCV-01)*, vol.2, pp.416-423, 2001

[55] J.P. Barthelemy and B. Leclerc. The median procedure for partitions. *In DIMACS Series In Discrete Mathematics and Theoretical Computer Science*, vol.19, pp.3-34, 1995.

[56] H. Lu, J.C. Woods and M. Ghanbari. Binary Partition Tree Analysis Based on Region Evolution and Its Application to Tree Simplification. *In IEEE Transactions on Image Processing*, vol.16, pp.1131-1138, 2007.

[57] L. Garrido and P. Salembier and D. Garcia. Extensive Operators in Partition Lattices for Image Sequence Analysis. *In Proceedings of EURASIP Signal Processing 1998*, pp.157-180, 1998.

[58] O.J Morris, M. Lee and A.G. Constantinides. Graph theory for image analysis: an approach based on the shortest spanning tree. *In IEEE Proceedings of Communications, Radar and Signal Processing*, vol.133, pp.146-152, 1986.

[59] H. Ling and K. Okada. Diffusion distance for histogram comparison. *In Proceedings of Conference on Computer Vision and Pattern Recognition*, vol.1, pp.246-253, 2006.

[60] Y. Rubner, C. Tomasi, and L. J. Guibas. The earth mover's distance as a metric for image retrieval. *In Internationall Journal of Computer Vision*, vol.40(2), pp.99-121, 2000.

[61] A .Buades, B. Coll and J.M. Morel. A non local algorithm for image denoising. *In IEEE Computer Vision and Pattern Recognition 2005*, vol.2, pp.60-65, 2005.

[62] Y. Boykov et G. Funka-Lea. Graph cuts and efficient and image segmentation. *In International Journal of Computer Vision*, 70(2), 109-131, 2006.

[63] Y .Boykov et V. Kolmogorov. Computing geodesics and minimal surfaces via graph cuts. *In International Conference on Computer Vision*, pp.26-33, Nice, France, October 2003.

[64] Y. Boykov et V. Kolmogorov. An experimental comparison of min-cut/max- flow algorithms for Energy Minimization in Vision. *in IEEE Transactions on Pattern Analysis and Machine Intelligence*, vol.26(9), pp.1124-1137, 2004.

[65] Y. Boykov, O. Veksler, et R. Zabih. Fast approximate energy minimization via graph cuts. *In IEEE Transactions on Pattern Analysis and Machine Intelligence*, vol.23(11), pp.1222-1239, 2001.

[66] J. Shi and J.Malik .Normalized Cuts and Image Segmentation. *In IEEE Transactions on pattern analysis and machine intelligence*, vol.22(8), pp.888-905, 2000

[67] J. Zu and R. Lealhy . An optimal Graph Theoretic Approach to Data Clustering: Theory and Its Application to Image Segmentation. *in IEEE Transactions on pattern analysis and machine intelligence*, vol.15(11), pp.1011-1113, 1993

[68] V.N. Vapnik. Statistical learning theory. *In New York: Wiley*, 1998.

[69] S. Valero and P. Salembier and J. Chanussot. Comparison of merging orders and pruning strategies for binary partition tree in hyperspectral data. *In IEEE Proceedings of ICIP'10*, pp.2565- 2568, 2010.

[70] S. Valero, P. Salembier, and J. Chanussot. New hyperspectral data representation using binary partition tree. *In IEEE Proceedings of IGARSS'10*, pp.80-83, 2010.

[71] C.M. Cuadras, S. Valero, D. Cuadras, P. Salembier and J. Chanussot. Distance-based measure of association with applications in relating hyperspectral images. *Communications in Statistics - Theory and Methods*, vol.41, pp. 2342-2355, 2012.

[72] D. Landgrebe. Hyperspectral Image Data Analysis as a High Dimensional Signal Processing Problem. *In (Invited), Special Issue of the IEEE Signal Processing Magazine*, vol.19(1), pp.17-28, 2002.

[73] G.F. Hugues. On the mean accuracy of statistical pattern recognizers. *In IEEE Transactions on Information Theory*, vol.14, pp.55-63, 1986

[74] P. Comon. Independent component analysis, a new concept? *In Signal Processing, Elsevier,* vol.36(3), pp.287-314, 1994

[75] D.A. Landgrebe, Signal Theory Methods in Multispectral Remote Sensing, *In John Wiley and Sons, Hoboken*, New Jersey, 2003

[76] C. Lee and D. Langrebe. Decision boundary feature extraction for neural networks. *In IEEE Transactions on Neural Networks* vol.9, pp.75-83, 1997

[77] C. Lee and D.A. Landgrebe. Feature extraction based on decision boundaries. *In IEEE Transactions of Patttern Anal. Machine Intell.*,vol.15, pp.388-400, 1993

[78] N. Gorreta. Proposition d'une approche de segmentation d'images hyperspectrales .*In Ph.D thesis*, Université – Montpellier II, 2009.

[79] F. Tsai, C.-K. Chang, and G.-R. Liu. Texture analysis for three dimension remote sensing data by 3D GLCM. *In Proc. of 27th Asian Conference on Remote Sensing*, pp.1-6, 2006.

[80] X. Huang and L. Zhang. A comparative study of spatial approaches for urban mapping using hyperspectral rosis images over pavia city, northern italy. *In International Journal of Remote Sensing*, vol. 30(12), pp.3205-3221, 2009

[81] R. L. Kettig and D. A. Landgrebe. Classification of multispectral image data by extraction and classification of homogeneous objects. *In IEEE Transactions on Geoscience Electronics*, vol.14(1), pp.19-26, 1976.

[82] L. Zhang and X. Huang. Object-oriented subspace analysis for airbone hyperspectral remote sensing imagery. *In Neurocomputing*, vol.73(4-6), pp.927-936, 2010.

[83] S. v. d. Linden, A. Janz, B. Waske, M. Eiden, and P. Hostert. Classifying segmented hyperspectral data from a heterogeneous urban environment using Support Vector Machines. *In Journal of Applied Remote Sensing*, (1:013543), 2007.

[84] A. Darwish, K. Leukert, and W. Reinhardt. Image segmentation for the purpose of object-based classification. *In IEEE Proceedings of IGARSS '03*, pp.2039-2041, 2003.

[85] Y. Tarabalka. Classification of Hyperspectral Data Using Spectral-Spatial Approaches. *In Ph.D thesis*, University of Iceland and Grenoble Institute of Technology, 2010

[86] Y. Tarabalka, J. Chanussot, and J. A. Benediktsson. Segmentation and classification of hyperspectral images using watershed transformation. *In Pattern Recognition*, vol.43(7), pp. 2367-2379, 2010

[87] L. O. Jimnez, J. L. Rivera-Medina, E. Rodrguez-Daz, E. Arzuaga-Cruz, and M. Ramrez-Vlez. Integration of spatial and spectral information by means of unsupervised extraction and classification for homogenous objects applied to multispectral and hyperspectral data.*In IEEE Transactions on Geoscience and Remote Sensing*, vol.43(4), pp.844-851, 2005.

[88] G. Camps-Valls, L. Gomez-Chova, J. Muñoz-Mari, J. Vila-France and J. Calpe-Maravilla. Composite kernels for hyperspectral image classification. *In IEEE Geoscience and Remote Sensing Letters*, vol.3(1), pp.93-97, 2006.

[89] M. Fauvel. Spectral and Spatial Methods for the Classification of Urban Remote Sensing Data. *In Ph.D thesis*, Grenoble Institute of Technology, 2007.

[90] J. Angulo, and S. Velasco-Forero. Semi-supervised hyperspectral image segmentation using regionalized stochastic watershed. *In Proceedings of SPIE symposium on Defense, Security, and Sensing: Algorithms and Technologies for Multispectral, Hyperspectral, and Ultraspectral Imagery XVI* ,SPIE Vol. 7695, 12 p., Orlando, United States, 2010

[91] J. Angulo, S. Velasco-Forero, J. Chanussot. Multiscale stochastic watershed for unsupervised hyperspectral image segmentation. *In IEEE Proceedings of IGARSS'2009*, vol. 3, pp.93-96, Cape Town, South Africa, 2009.

[92] G. Mercier and M. Lennon. Support vector machines for hyperspectral image classification with spectral-based kernels.*In IEEE Proceedings of Geoscience and Remote Sensing Symposium, IGARSS '03*. vol.1, pp.288-290, 2003

[93] R. C. Dubes and A. K. Jain. Random field models in image analysis. *In Journal of Applied Statistics*,vol.20(5), pp.121-154, 1993.

[94] O. Pony, X. Descombres, and J. Zerubia. Classification d'images satellitaires hyperspectrales en zone rurale et periurbane. *Technical report, INRIA Sophia Antipolis*, France, 2000.

[95] G. Rellier, X. Descombes, X. Falzon, and J. Zerubia. Texture feature analysis using a Gauss-Markov model in hyperspectral image classification. *in IEEE Transactions on Geoscience and Remote Sensing*, vol.42(7), pp.1543-1551, 2004.

[96] Q. Jackson and D. Landgrebe. Adaptive bayesian contextual classification based on Markov random fields.*In IEEE Transactions in Geoscience and Remote Sensing*, vol. 40(11), pp.2454-2463, 2002.

[97] A.A. Farag, R.M. Mohamed, and A. El-Baz. A unified framework for MAP estimation in remote sensing image segmentation. *In IEEE Transactions in Geoscience and Remote Sensing*, vol. 43(7), pp.1617-1634, 2005.

[98] F. Bovolo and L. Bruzzone, A context-sensitive technique based on support vector machines for image classification. *In Proceedings of Pattern recognition and machine intelligence*, pp. 260-265, 2005

[99] D. Liu, M. Kelly, and P. Gong. A spatial-temporal approach to monitoring forest disease spread using multi-temporal high spatial resolution imagery. *In Remote Sensing of Environment.*, vol.101(2), pp.167-180, Mar. 2006.

[100] Y. Tarabalka, M. Fauvel, J. Chanussot, J. A. Benediktsson. SVM and MRF-based method for accurate classification of hyperspectral images. *In IEEE Geoscience and Remote Sensing Letters*, vol.7(4), pp.736-740, 2010.

[101] J. Li, J. Bioucas-Dias and A. Plaza. Semi-Supervised Hyperspectral Image Segmentation Using Multinomial Logistic Regression with Active Learning. *in IEEE Transactions on Geoscience and Remote Sensing*, vol. 48(11), pp.4085-4098, 2010

[102] J. Li, J. Bioucas-Dias, and . Plaza. Supervised Hyperspectral image segmentation using active learning. *In IEEE Proceedings of GRSS Workshop on Hyperspectral Image and Signal Processing: Evolution in Remote Sensing (WHISPERS'10)*, Reykjavik, Iceland, 2010

[103] J.Serra. Image Analysis and Mathematical Morphology. *In Ac. Press, Volume 1*, 1982

[104] I. Pitas and C. Kotropoulos. Multichannel L filters based on marginal data ordering.*In IEEE Transactions on Signal Processing*. vol.42, pp.2581-2595, 1994.

[105] A. Plaza, P. Martinez, R.Perez and J.Plaza. Spatial/spectral endmember extraction by multidimensional morphological operations. *In IEEE Transactions on Geoscience and Remote Sensing*, vol.40(9), pp.2025-2041, 2002.

[106] S. Velasco-Forero and J. Angulo. Spatial structures detection in hyperspectral images using mathematical morphology. *In IEEE Proceedings of WHISPERS'10 (2nd IEEE GRSS Workshop on Hyperspectral Image and Signal Processing)* ,Reykjavík, Iceland, 2010

[107] S. Velasco-Forero and J. Angulo Supervised ordering in Rp: Application tomorphological processing of hyperspectral images.*Accepted in IEEE Transactions on Image Processing*, 2011

[108] M. Pesaresi and J.A. Benediktsson,. A new approach for the morphological segmentation of high-resolution satellite imagery. *In IEEE Transactions on Geoscience and Remote Sensing,* vol. 39(2), pp.309-320, 2001.

[109] J. A. Palmason, J. A. Benediktsson, and K. Arnason. Morphological transformations and feature extraction for urban data with high spectral and spatial resolution. *In IEEE Proceedings of IGARSS*, vol.1, pp.470-472, 2003

[110] F. Dell'Acqua, P. Gamba, A. Ferrari, J. A. Palmason, J. A. Benediktsson, and K. Arnason. Exploiting spectral and spatial information in hyperspectral urban data with high resolution. *In IEEE Geoscience and Remote Sensing Letters*, vol.1(4), pp.322-326, 2004.

[111] J. A. Benediktsson, J. A. Palmason, and J. R. Sveinsson. Classification of hyperspectral data from urban areas based on extended morphological profiles. *In IEEE Transactions on Geoscience and Remote Sensing*, vol. 43(3), pp.480-491, 2005.

[112] J. A. Palmason, J. A. Benediktsson, J. R. Sveinsson, and J. Chanussot. Classification of hyperspectral data from urban areas using morphological preprocessing and independent component analysis. *In IEEE Proceedings of International Geoscience and Remote Sensing Symposium 2005, IGARSS '05*, vol.1, pp.176-179, 2005.

[113] M. Dalla Mura. Advanced techniques based on mathematical morphology for the analysis of remote sensing images. *Ph.D. thesis*, University of Iceland and University of Trento, 2011

[114] A. Plaza, P. Martinez, J. Plaza, and R. Perez. Dimensionality reduction and classification of hyperspectral image data using sequences of extended morphological transformations. *In IEEE Transactions on Geoscience and Remote Sensing*, vol.43(3), pp.466-479, 2005.

[115] M. Fauvel, J. Chanussot, and J. A. Benediktsson. Kernel principal component analysis for feature reduction in hyperspectral images analysis. *In Proceedings of 7th Nordic Signal Processing Symposium NORSIG 2006*, pp. 238-241, 2006.

[116] G. Noyel. Filtrage, reduction de dimension, classification et segmentation morphologique hyperspectral. *Ph.D. thesis*, Ecole de Mines de Paris University, 2008

[117] S. De Jong, T. Hornstra and H. Maas. An integrated approach to the classification of mediterranean land cover types : the SSC method. *In International Journal for Applied Earth Observation and Geoinformation*, vol 3(2), pp.176-183, 2001

[118] H. G. Akçay and S. Aksoy. Automatic detection of geospatial objects using multiple hierarchical segmentations. *In IEEE Transactions on Geoscience and Remote Sensing*, vol.46(7), pp.2097-2111, July 2008.

[119] J.M. Beaulieu and M.Goldberg. Hierarchy in picture segmentation: A stepwise optimization approach". *In IEEE Transactions on Pattern Analysis and Machine Intelligence*, vol.11(12), pp.150-163, 1989

[120] J.Tilton. Image segmentation by region growing and spectral clustering with a natural convergence criterion. *In IEEE Proceedings of International Geoscience and Remote Sensing Symposium (IGARSS)*, pp.1766-1768, 1998

[121] J.Tilton. A split-remerge method for elimination processing window artifacts in recursive hierarchical segmentation. *In Technical Repors GSC 14994-1, NASA*, 2005

[122] A.Plaza and J.Tilton. Hierarchical classification with single level shape features Segmentations of Remotely Sensed Hyperspectral Images. *In IEEE Proceedings of IGARSS*, 2005.

[123] L. Garrido, P. Salembier, and D. Garcia. Extensive operators in partition lattices for image sequence analysis. *In Signal Processing: Special issue on Video Sequence Segmentation*, pp.157-180, 1998.

[124] A.Cracknell. Synergy in remote sensing: What's in a pixel?. *In International Journal of Remote Sensing*, vol.19, pp.2025-2047, 1998

[125] T. Pavlidis. Structural Pattern Recognition. *New York: Springer*, 1980.

[126] J.M. Molion and W.G. Kropatsch. Graph based Representations. *in Proceedings of GbR'97, 1st IAPR Int Workshop on Graph based Representations, Springer Verlag, Computing Suppl., 12*, 1998.

[127] K. Haris, S.N. Efstratiadis, N. Maglaveras, A.K. Katsaggelos .Hybrid image segmentation using watersheds and fast region merging. *In IEEE Transactions on Image Processing*, vol.7(12), pp.1684-1699, 1998

[128] S.L. Horowitz and T. Pavlidis. Picture segmentation by a directed split and merge procedure. *In Proceedings of Second Intern. Joint Conf. on Pattern Recognition*, pp.424-433, 1974.

[129] A. Klinger. Patterns and search statistics *In Optimizing Methods in Statistics (J. S. Rustagi, Ed.), Academic Press,* New York, 1971.

[130] E. Shusterman and M. Feder. Image compression via improved quadtree decomposition algorithms. *In IEEE Transactions on Image Processing*, vol.3(2), pp.207-215, March 1994.

[131] G.J. Sullivan and R.L. Baker. Efficient quadtree coding of images and video.*In IEEE Transactions on Image Processing*, vol.3(3), pp.327-331, 1994

[132] J. Cichosz and F. Meyer. Morphological multiscale image segmentation. *In Proceedings of Workshop on Image Analysis for Multimedia Interactive Services*, pp.161-166, Louvain-La-Neuve, Belgium, 1997.

[133] S. Beucher and C. Lantuéjoul. Use of watersheds in contour detection. *In International workshop on image processing, real-time edge and motion detection* , 1979.

[134] F. Meyer and S. Beucher. Morphological segmentation. *In Journal of Visual Communications and Image Representation*, vol.1(1), pp.21-46, 1990.

[135] P. Salembier, A. Oliveras, and L.Garrido. Anti-extensive connected operators for image and sequence processing. *In IEEE Transactions on Image Processing* ,vol.7, pp.555-570, 1998

[136] P. Monasse and F. Guichard. Fast computation of a contrast invariant image representation. *In IEEE Transactions on Image Processings*, vol. 9(5), pp.860-872, 2000.

[137] P. Salembier and L. Garrido. Connected Operators Based on Region-Tree Pruning Strategies. *In Proceedings Int. Syrup. on Math. Morphology*, pp.169-178, 2000.

[138] A. Alonso-Gonzalez, C. Lopez-Martinez and P. Salembier. Filtering and segmentation of polarimetric SAR images with Binary Partition Trees. *In IEEE Proceedings of Geoscience and Remote Sensing Symposium (IGARSS)*, pp.4043-4046, 2010

[139] P. Salembier, F. Marqués, M. Pardás, R. Morros, I. Corset, S. Jeannin, L. Bouchard, F. Meyer and B. Marcotegui. Segmentation-based video coding system allowing the manipulation of objects. *In IEEE Transactions on Circuits and Systems for Video Technology* ,vol.7, pp.60-73, 1997.

[140] L. Guigues, J.P. Cocquerez and H. Le Men. Scale-Sets Image Analysis.*in International Journal of Computer Visio*n, vol. 68(3), pp.289-317, July 2006.

[141] L.Garrido. Hierarchical Region Based Processing of Images and Video Sequences: Application to Filtering, Segmentation and Information Retrieval. *In Ph.D. thesis*, Politechnical University of Catalunya, 2002

[142] D. Knuth. The art of computer programming, vol.3 (Sorting and Searching). *In Addison-Wesley*, 1973.